Universität Potsdam

Doctoral thesis

Cosmic-ray transport and signatures in their local environment

A thesis submitted in fulfilment of the requirements for the degree of "Doctor rerum naturalium" (Dr. rer. nat.)

in the

Institut für Physik und Astronomie
Mathematisch-Naturwissenschaftliche Fakultät

Author:
Vasundhara Shaw

Supervisors:
Dr Andrew M. Taylor-Castillo
Prof. Martin Pohl

Published online on the
Publication Server of the University of Potsdam:
https://doi.org/10.25932/publishup-62019
https://nbn-resolving.org/urn:nbn:de:kobv:517-opus4-620198

Declaration of authorship

I, Vasundhara Shaw, declare that this thesis titled, 'Cosmic ray transport and signatures in their local environment' and the work presented in it are my own in collaboration with my supervisor, Andrew Taylor and co-supervisor, Arjen Van Vliet. I confirm that:

* No part of this work was or will be submitted for any degree or diploma or certificate or other qualification at this University or elsewhere.
* Unless otherwise stated, this thesis is the result of my own work.
* Any published work that has been consulted has been accurately referenced.
* Any quotations mentioned in the thesis have been accurately cited.
* The work in Chapter 2 and Chapter 3 has been published collectively in *Monthly notices of Royal Astronomical Society*, (Vasundhara Shaw, Arjen van Vliet and Andrew M. Taylor, 517, 2534–2545 (2022)) [1].
* The work in Chapter 4 will be published in a peer-reviewed journal in the future.

Abstract

The origin and structure of magnetic fields in the Galaxy are largely unknown. What is known is that they are essential for several astrophysical processes, in particular the propagation of cosmic rays. Our ability to describe the propagation of cosmic rays through the Galaxy is severely limited by the lack of observational data needed to probe the structure of the Galactic magnetic field on many different length scales. This is particularly true for modelling the propagation of cosmic rays into the Galactic halo, where our knowledge of the magnetic field is particularly poor.

In the last decade, observations of the Galactic halo in different frequency regimes have revealed the existence of out-of-plane bubble emission in the Galactic halo. In gamma rays these bubbles have been termed Fermi bubbles with a radial extent of ≈ 3 kpc and an azimuthal height of ≈ 6 kpc. The radio counterparts of the Fermi bubbles were seen by both the S-PASS telescopes and the Planck satellite, and showed a clear spatial overlap. The X-ray counterparts of the Fermi bubbles were named eROSITA bubbles after the eROSITA satellite, with a radial width of ≈ 7 kpc and an azimuthal height of ≈ 14 kpc. Taken together, these observations suggest the presence of large extended Galactic Halo Bubbles (GHB) and have stimulated interest in exploring the less explored Galactic halo.

In this thesis, a new toy model (GHB model) for the magnetic field and non-thermal electron distribution in the Galactic halo has been proposed. The new toy model has been used to produce polarised synchrotron emission sky maps. Chi-square analysis was used to compare the synthetic skymaps with the Planck 30 GHz polarised skymaps. The obtained constraints on the strength and azimuthal height were found to be in agreement with the S-PASS radio observations.

The upper, lower and best-fit values obtained from the above chi-squared analysis were used to generate three separate toy models. These three models were used to propagate ultra-high energy cosmic rays. This study was carried out for two potential sources, Centaurus A and NGC 253, to produce magnification maps and arrival direction skymaps. The simulated arrival direction skymaps were found to be consistent with the hotspots of Centaurus A and NGC 253 as seen in the observed arrival direction skymaps provided by the Pierre Auger Observatory (PAO).

The turbulent magnetic field component of the GHB model was also used to investigate the extragalactic dipole suppression seen by PAO. UHECRs with an extragalactic dipole were forward-tracked through the turbulent GHB model at different field strengths. The suppression in the dipole due to the varying diffusion coefficient from the simulations was noted. The results could also be compared with an analytical analogy of electrostatics. The simulations of the extragalactic dipole suppression were in agreement with similar studies carried out for galactic cosmic rays.

Allgemeine Zusammenfassung

Unsere Galaxie wird ständig von hochenergetischen geladenen Teilchen unterschiedlicher Energie bombardiert, die als kosmische Strahlung bezeichnet werden und deren Ursprung nicht bekannt ist. Satelliten- und erdgestützte Messungen haben bisher ergeben, dass es in unserer Galaxie Beschleuniger für kosmische Strahlung gibt, z. B. die Überreste explodierender Sterne (Supernova-Überreste), aber bei den höchsten kosmischen Strahlungsenergien bleiben die Quellen ein Rätsel. Fortschritte zu erzielen ist eine Herausforderung, auch weil die kosmische Strahlung durch Magnetfelder abgelenkt wird, was bedeutet, dass die beobachtete Richtung mit der Richtung der Quelle übereinstimmen kann oder auch nicht. Unsere Galaxie weist starke Magnetfelder auf, deren Beschaffenheit noch nicht gut verstanden ist, insbesondere in der Komponente außerhalb der Scheibe (dem galaktischen Halo). Darüber hinaus haben Beobachtungen in den letzten zehn Jahren blasenartige Strukturen im galaktischen Halo mit enormen Gesamtenergien aufgedeckt, die auch als galaktische Halo-Blasen bezeichnet werden. All dies motiviert uns, den galaktischen Halo zu untersuchen.

In meiner Doktorarbeit schlagen wir ein neues, vereinfachtes Magnetfeldmodell für galaktische Halo-Blasen vor. Das Modell umfasst sowohl strukturierte als auch turbulente Komponenten des Magnetfelds. Das vereinfachte Modell wurde mit Beobachtungsdaten verglichen, um den am besten passenden Parametersatz zusammen mit den Unsicherheiten zu erhalten.

Ich untersuchte die Propagation der ultrahochenergetischen kosmischen Strahlung durch das vereinfachte Modell und untersuchte dessen Auswirkungen auf die Ankunftsrichtungen der ultrahochenergetischen kosmischen Strahlung für zwei potenzielle Quellen, Centaurus A und NGC 253.

Außerdem habe ich sowohl numerisch als auch analytisch abgeschätzt, wie stark ein Dipol der extragalaktischen kosmischen Strahlung durch verschiedene Konfigurationen der turbulenten Magnetfelder des vereinfachten Modells unterdrückt wird.

Die Ergebnisse all dieser Arbeiten werden in dieser Arbeit im Detail vorgestellt.

Acknowledgements

A journey has come to an end with this thesis. I have been lucky enough to meet and interact with a number of people who have made this journey rich and pleasant.

First and foremost, I would like to thank my supervisors, Andrew and Arjen. Both of them were instrumental in helping me develop a scientific temper. Their guidance has helped me to develop my ability to think critically about issues not only in physics but also in everyday life, which is an essential skill not only in science but in life in general.

I would also like to thank Mike Peel who patiently answered my questions about radio data analysis and always provided very useful feedback.

I would also like to thank Pau, discussing topics in physics with him was always enlightening. Additionally, I wish to thank members of the theory group especially Marc and Leonel some of my closest friends. I learned a lot of computational skills from both of them and thoroughly enjoyed several long hours of discussions. I would also like to thank Michelle, Xin-Yue and Olivier for spending their time discussing physics and providing companionship at work.

I would also like to thank Martin, my advisor, at the university for his continuous guidance, and support during my PhD. Additionally, a hearty thank you to the members of theory group Walter, Pavlo, Parth and others who made were also influential people in my time at DESY.

Lastly, I would like to thank Karl Jansen for allowing me to work for his group whilst finishing my PhD thus ensuring my employment. I am also grateful to the members of CQTA for including me as an active member in their group.

List of publications

The material in Chapter 2 and Chapter 3 was published collectively in *Monthly notices of Royal Astronomical Society*, (Vasundhara Shaw, Arjen van Vliet and Andrew M. Taylor, 517, 2534–2545 (2022)) [1].

The material presented in Chapter 4 is being prepared for submission in a peer-reviewed journal.

Contents

List of Figures

1 Introduction

Figure 1.1: A composite image of the Galaxy NGC 5775 and its magnetic field made by superimposing optical image from the Hubble Space Telescope from the radio data from the Karl G. Jansky Very Large Array (VLA) telescope (**Image Credit: NRAO, NASA, ESA, Hubble**).

Magnetic fields are ubiquitous to astrophysical systems. In a galaxy they contribute majorly to the total pressure which balances the interstellar medium (ISM) against gravity. They also impact the flow of gas in halos and spiral arms of the disc of a Galaxy. They affect star formation, and are responsible for cosmic ray density and distribution. Magnetic fields are a key ingredient in particle acceleration, for instance in active galactic nuclei (AGN) and gamma ray bursts (GRB). Additionally, magnetic fields are responsible for deflecting cosmic rays arising from sources both within and outside our Galaxy [2]. Despite them being omnipresent, little is understood about their origin and structure especially in Galaxies such as ours, the Milky Way.

1.1 Magnetic fields in galaxies and Galaxy clusters

Spiral galaxies like the Milky Way can have magnetic fields with typical values of $\approx 3\mu$G in the disc and $\approx 6\mu$G in the out of disc plane component or the Galactic halo [3, 4]. This number can be derived by imposing equipartition among magnetic fields, non-thermal

particles like comic rays (CRs) , thermal particles as well as the gravitational potential and can be approximated to $\approx 1\,\mathrm{eV/cm^3}$ [2, 5]. The magnetic field in the Galaxy can be divided into two types: large-scale structured/regular fields which remain coherent up to a few kpc distances and small-scale turbulent magnetic fields whose coherence length (L_{coh}), the propagation distance over which magnetic field behaves coherently will be a few 10s to 100s of pc.

Albeit, the origin of magnetic fields in galaxies is poorly understood, it is known from observations that magnetic fields exist both in different Galaxy types and galaxy clusters.

Observations of Galactic and extragalactic magnetic fields

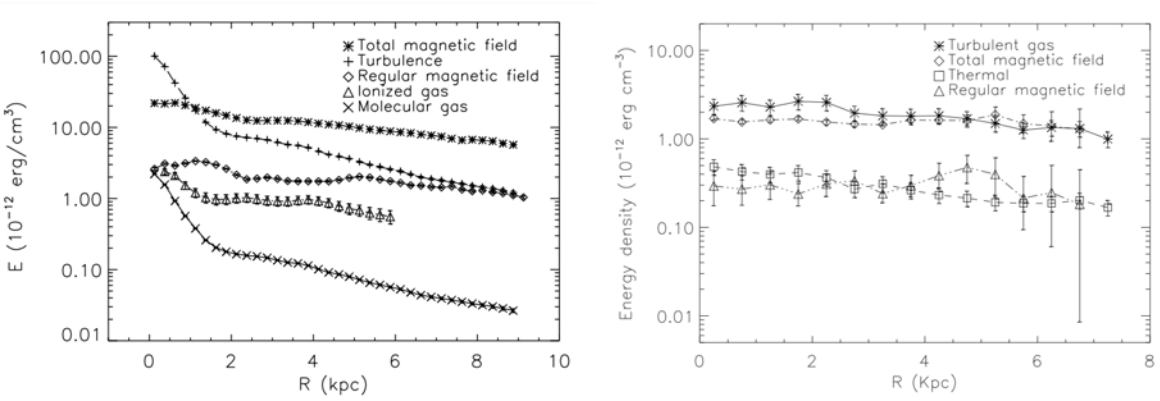

. s

Figure 1.2: The figures above show the contribution of turbulent magnetic fields being considerably larger than the structured/regular/large-scale magnetic field strength for two different galaxies NGC 6946 (left) and M33 (right). The figure on the left obtained from [6] and on the right from [7]

Listed below is a comprehensive list discussing the observations of magnetic fields both within galaxy clusters and galaxies. The following points have been compiled using the overview of magnetic fields provided in [8].

1. Extragalactic observations of spiral galaxies suggest magnetic field strengths of 5 – 10 μG with L_{coh} ~ size of the Galactic disc (few 10s of kpc) indicating the presence of large-scale structured fields [9, 10].
2. As also seen from observations of external galaxies the turbulent magnetic fields are suggestive of being stronger than the structured fields [6, 7]. In Figure 1.2 the energy density in the turbulent magnetic field component is more than the regular or large-scale structured magnetic field for NGC 6946 (right) and M33 (left).
3. Magnetic fields in spiral galaxies showcase symmetries both with respect to the galaxy's equatorial plane and spin axis [11, 12].

4. In contrast to spiral galaxies, magnetic fields in elliptical galaxies tend to have L_{coh} smaller than the Galactic scale and are turbulent in nature. Barred and irregular galaxies also have shown observational signatures of magnetic fields [2].
5. Magnetic fields of the order of a few μG have also been observed in Galaxy clusters with the L_{coh} being comparable to the size of the clusters [13].

Origin of Galactic magnetic fields

The origin of Galactic magnetic fields (GMFs) is not well understood. Magnetic fields (at μG levels) in the universe seem to be coherent over length scales of the order of the size of Galaxies and galaxy clusters [2, 8, 14, 15]. Evidence also seems to suggest large-scale coherent structures of magnetic fields over super-cluster scales [16]. Theoretically it has been suggested that such fields might owe their origin to the amplification of initial *seed* fields $\sim 10^{-20}$ G via dynamo action. Seed fields are said to be generated in the very early universe at redshift of 5 or more [2, 17]. Other theories favour the existence of even stronger large-scale primordial fields $\sim 10^{-9}$ G that could be formed during inflation or early phase transition in the universe in protogalaxies or quasars at redshift > 6 [8, 15, 18–23]. Recent observational evidence seems to suggest that the intergalactic medium in voids in the universe could have magnetic fields of 10^{-16} G coherent over Mpc scales [14, 24]. Magnetic fields within Galaxies can be explained by field amplification and ordering via the dynamo mechanism. Seed fields $\leq 10^{-12}$ G in initial stages of Galaxy formation could have undergone dynamo action such that kinetic energy is continuously converted into magnetic energy by the turbulent motion of the interstellar medium (ISM) resulting in the amplification of magnetic fields. This results in magnetic fields of coherence length $L_{\text{coh}} \approx$ the size of the galaxy [25, 26]. The key ingredients to sustain a Galactic dynamo are conducting ISM material with turbulent motion and differential rotation of the galactic system. Since these systems are common to most galaxies, it has been speculated that Galactic dynamo may be a responsible mechanism for maintaining large-scale coherent magnetic fields [27]. Note that the mechanisms responsible for the generation of magnetic fields are not the focus of this thesis and hence will not be discussed further.

1.2 Measuring magnetic fields

There are several ways to detect magnetic fields. Each technique is discussed in this section with suitable examples from observations. Galactic magnetic fields broadly can

be classified as large-scale structured or regular magnetic fields with coherence lengths ($L_{\rm coh}$) of a few kpcs and small-scale random magnetic fields $L_{\rm coh}$ ~ few 10s to 100s pc.

There are several ways to measure the observational tracers of magnetic fields in our Galaxy: ***1:*** indirect method which involves measuring the strength and/or direction of magnetic fields which is either parallel to or perpendicular to the direction of the line of sight (LOS[†]) of the observer or in the plane of the sky[‡] and ***2:*** a direct method where one can measure magnetic fields will be via the Zeeman effect (discussed below).

In this section the basics of polarisation are discussed, followed by Zeeman splitting in Section 1.2.1, synchrotron radiation is discussed in depth in Section 2.2.2 and Chapter 2. Faraday rotation has been discussed both in Section 1.2.3 in this chapter and in Section 2.2.4 in Chapter 2. Effects of optical and infrared polarisation is discussed in Section 1.2.4.

Basics of polarisation of electromagnetic waves

Most techniques used to study magnetic fields at different scales involve polarisation of some form. Polarised emissions at different wavelengths give valuable information of not only the strength of the magnetic field but also the direction and geometry. Polarisation of electromagnetic (EM) waves can be expressed via 4 Stokes parameters namely I, Q, U and V which carry information about the complete state of an EM wave. The total intensity for any radiation is given by I. $+V$ and $-V$ gives the information of the right-handed and left-handed circularly polarised component respectively. Q and U are vector-like quantities, the linearly polarised component's orientation is given by $2\Psi = \tan^{-1}(U/Q)$ and the polarised intensity ($I_{\rm pol} = \sqrt{Q^2 + U^2}$). Subsequently, one can estimate the linear polarisation fraction which tells the degree of polarisation present in the radiation, it can be expressed as $p^{\rm L}_{\rm frac} = I/I_{\rm pol}$. Similarly, the circular polarisation fraction can be given by $p^{\rm Cir}_{\rm frac} = V/I$.

Linearly polarised waves can be expressed as the instantaneous sum of right and left-handed circularly polarised waves with the relative phase given by Ψ. If the magnitude of left and right-handed polarisations are unequal then the polarised wave is said to be elliptical. An elliptically polarised wave can be decomposed into a linearly polarised wave superimposed on a left or right-handed circularly polarised wave. The majority of astronomical sources have very little polarisation and in that case I is always positive since it represents purely randomly polarised radiation.

[†] A line of sight is the direction from the observer (Earth in this case) to the source that is being observed.
[‡] A schematic representation of line of sight calculation is shown in Chapter 2

1.2.1 Zeeman effect

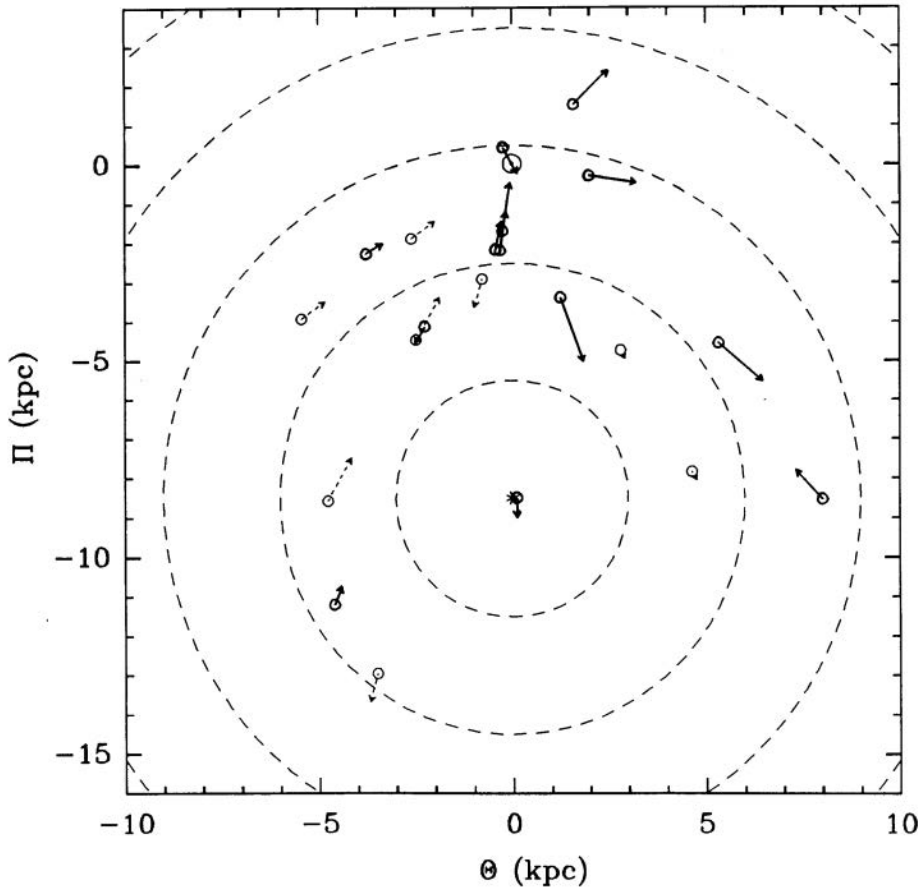

Figure 1.3: Figure above obtained from [28] shows the OH maser sources (in circles) as seen in the Galactic plane [28], the magnitude of the magnetic field and the line-of-sight direction for each source has been shown by the length and direction of arrows respectively.

For an atom with total angular momentum $\vec{J}$, spin $\vec{S}$ and orbital angular momentum $\vec{L}$, there will be $2j + 1$ energy levels where j is the quantum number related to the total angular momentum. The energy liberated in the splitting of neighbouring levels is given by $\Delta E = g\mu B$ where, g is the Lande factor[§] and μ is the Bohr magneton[¶]. This effect is called the Zeeman splitting which involves splitting of spectral lines into two or more components of slightly varying energies when an electromagnetic source is placed in regular uniform magnetic field. Zeeman splitting is called a direct observational tracer of magnetic fields, once ΔE is measured it is easy to deduce the value of the magnetic field B. In contrast to the indirect observational tracers that probe line of sight magnetic fields (like synchrotron radiation and Faraday rotation), Zeeman splitting probes the regular magnetic field at the source. Within the Galaxy, Zeeman effect measurements

[§] Lande factor is a specific example of *g-factor*, it's a dimensionless quantity that characterises the angular momentum and spin of an electron.

[¶] Bohr magneton is a natural unit to express the magnetic moment of an electron given by $\mu_B = \frac{e\hbar}{2m_e}$.

can provide information about the magnetic fields in star forming regions of the Galactic center. Zeeman splitting can be measured in water and OH masers and observations of such OH masers to map the large-scale magnetic field of the Galaxy [28]. Figure 1.3 obtained from [28] shows the Galactic plane with OH maser sources shown in circles. The strength of the magnetic field and the line-of-sight direction is shown by the length and direction of the arrows respectively.

1.2.2 Synchrotron radiation

Charged particles, mostly cosmic ray electrons moving at relativistic speeds, spiral around magnetic field lines generating non-thermal radiation. This radiation is also known as synchrotron radiation and is analogous to cyclotron radiation but at relativistic speeds. Synchrotron radiation both polarised and unpolarised have remained a popular tool to study both large-scale and small-scale magnetic fields [5]. Synchrotron radiation is one of the key tools used in this dissertation and shall be discussed at length in Chapter 2, Section 2.2.2.

1.2.3 Faraday rotation

Faraday rotation (FR) or Faraday effect is a magneto-optical effect which can cause rotation of a plane polarised wave when passing through a magnetised plasma. It arises from modes of radio waves that propagate as elliptically polarised waves in the opposite sense [29]. Upon passage through a magneto-active medium the linearly polarised radio wave (with frequency ν) can be decomposed into equal components of left and right-handed polarised radiation. In the case where $\nu_g/\nu \ll 1$, here ν_g is the gyro-frequency, the refractive index n of these two modes are :

$$n^2 = 1 - \frac{(\nu_p/\nu)^2}{1 \pm (\nu_g/\nu)\cos\Theta}, \tag{1.1}$$

here ν_p is the plasma frequency and is given by:

$$\nu_p = \left(\frac{e^2 n_{th}}{4\pi\epsilon_0 m_e}\right)^{1/2} = 8.98\, n_{th}^{1/2}\ \text{Hz} \tag{1.2}$$

or, in wavelength the above 1.1 can be written as:

$$n^2 = 1 - \frac{(\lambda/\lambda_p)^2}{1 \pm (\lambda/\lambda_g)\cos\Theta}, \tag{1.3}$$

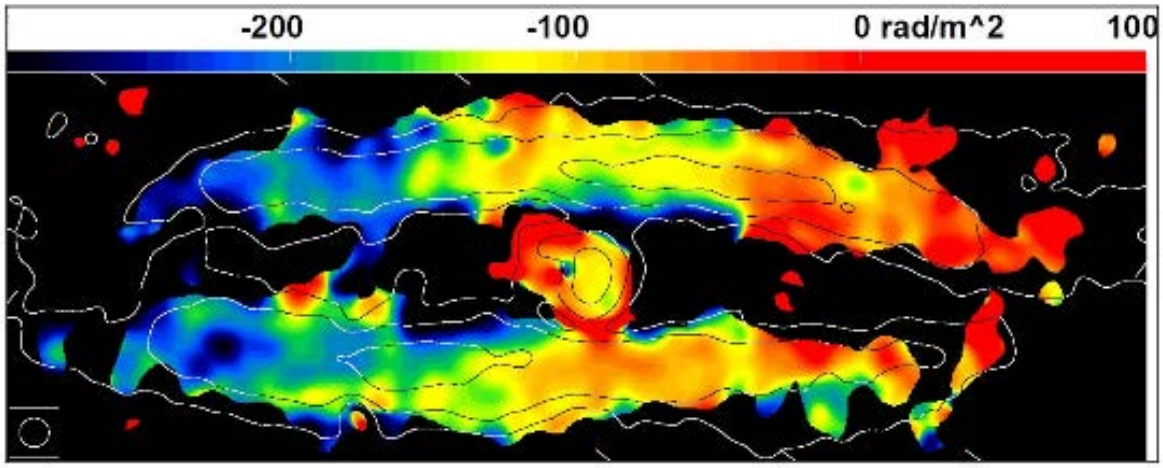

Figure 1.4: Polarised radio emission seen in M31 (contours) at 4.85 GHz and Faraday rotation measure (in colour) at 4.85 GHz and 8.35 GHz. The figure was obtained from [30].

here, e particle charge , $n_{\rm th}$ is the thermal electron density and is measured in m^{-3}, Θ is the angle between the magnetic field direction and the wave propagation direction and $m_{\rm e}$ is the mass of the particle. For a thermal electron density of $n_{\rm th} \sim 0.01$ cm^{-3} or 3×10^4 m^{-3}. The value of $\nu_{\rm p}$ will be 0.3 kHz.

The two elliptically polarised waves have different phase velocities, hence, one sense of the elliptical polarisation will be faster than the other in propagation. On addition of the two elliptically polarised components at depth l through the region the resulting linearly polarised radiation is rotated from the initial polarisation direction.

From equation 1.1 one can calculate the difference in the refractive index $\Delta n = \frac{\nu_{\rm p}^2 \nu_{\rm g}}{\nu^3} \cos\Theta$ if $\nu_{\rm p}/\nu << 1$, $\nu_{\rm g}/\nu << 1$. The phase difference $\Delta\Phi = \frac{2\pi\nu\Delta n}{\rm c} {\rm d}l$ where dl is the distance through the region. In addition, of the two elliptically polarised waves the direction of linearly polarised electric vector is rotated by $\Delta\Theta = \Delta\Phi/2$ [29].

One can re-write $\nu_{\rm g}\cos\Theta$ in terms of $B_\parallel$ which is the component of magnetic fields along the line of sight. The Faraday rotation angle can be written as :

$$\Theta = \lambda^2 8.12 \int_0^l n_{\rm th} B_\parallel dl \tag{1.4}$$

here, Θ is the measured rotation angle in radians, λ is the wavelength of the observation in meters, l is the distance travelled by the wave from the source to observer in parsec and $B_\parallel$ is the line of sight parallel magnetic field measured in Gauss.

The quantity $RM = \frac{\Theta}{\lambda}^2$ is the rotation measure, measured in rad m^{-2}. It provides information about the weighted mean direction of the magnetic field along the line of

sight. If $\frac{\Theta}{\lambda}^2$ is negative then the magnetic field is directed away from the observer and vice-versa if positive. Both Galactic and extragalactic sources emit polarised waves in the radio regime.

By measuring the rotation angle for a particular frequency and the dispersion measure ($\mathrm{DM} = \int n_{\mathrm{th}} \mathrm{d}l$) for the linearly polarised source one can obtain the value of the weighted magnetic field along the line of sight given by

$$< B_{\parallel} > \propto \frac{\text{rotation measure}}{\text{dispersion measure}} \propto \frac{RM}{DM} \propto \frac{\int n_{\mathrm{th}} B_{\parallel} \mathrm{d}l}{\int n_{\mathrm{th}} \mathrm{d}l}. \tag{1.5}$$

In regard to observational evidence for dynamo, Faraday rotation measure has been very useful. Observations of large-scale RMs seem to hint at magnetic fields generated by dynamo in M31 (also see Figure 1.4) and NGC 253 for instance. Faraday rotation only becomes significant at wavelengths of a few centimetres, though in the central regions of Galaxies, Faraday rotation is strong at wavelengths 1-3 cm.

1.2.4 Optical and infrared polarisation

Optical and infrared polarisation can be used as tracers for detecting magnetic fields behind dusty molecular clouds by studying the dichroic extinction* of elongated dust grains. These grains tend to align along magnetic fields within these clouds such that their major axis is perpendicular to the magnetic fields. The dense cloud cores can be opaque at optical wavelengths but polarisation measurements at infrared, far-infrared can still provide information of either magnetic fields in those regions. At such lower frequencies scattering is not expected and thus the polarisation that originates in the dust particle emission is aligned by magnetic fields [31]. Linear polarisation occurs due to the thermal emission of dust grains that are magnetically aligned. This type of polarisation observations prove as an excellent source of exploring the magnetic field morphology. Polarisation observations of molecular clouds are utilised to study the role of magnetic fields in the evolution and formation of clouds and star formation. In the optical regime starlight polarisations can be useful to understand the magnetic field structure of the interstellar magnetic fields. In the infrared regime the dust grains also emit polarised emissions which gives information about magnetic fields in the dust clouds of the Milky Way. Figure 1.5 shows observations of starlight polarisation for about 5000 stars, and it can be seen that polarisation vectors averaged over many clouds tend to align itself

* Dichroic extinction is the extinction by aligned grains of interstellar dust, which causes polarization of starlight.

with the Galactic plane. Starlight polarisation has been useful in estimating distances of large-scale structures for example like the North Polar Spur [32] [33].

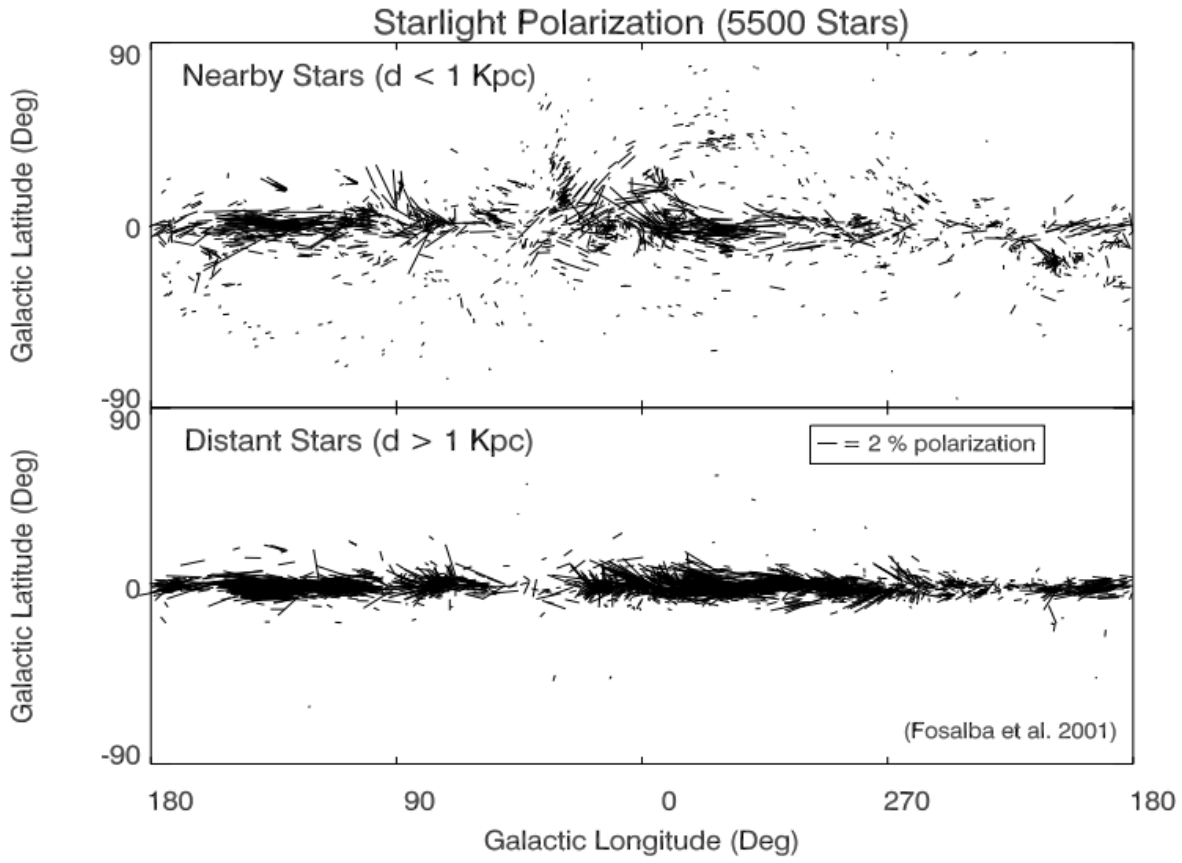

Figure 1.5: Starlight polarisation vectors from a sample of 5500 stars. The top figure shows the vectors in local clouds and the lower figure shows polarisation averaged over several clouds in the Galactic plane. The figure was obtained from [33].

1.3 High Galactic latitude emission observations in the Milky Way

1.3.1 Extended halo observations in external Galaxies

In the past couple of decades observations of the Galaxy ranging from gamma-ray to radio to X-ray wavelengths have revealed existence of large-scale structures which in the past were only observed in external galaxies.

The observations of external galaxies (like starburst galaxies) mainly carried out in radio, gamma, and X-ray led to the discovery of out of the plane extended emission. Observations

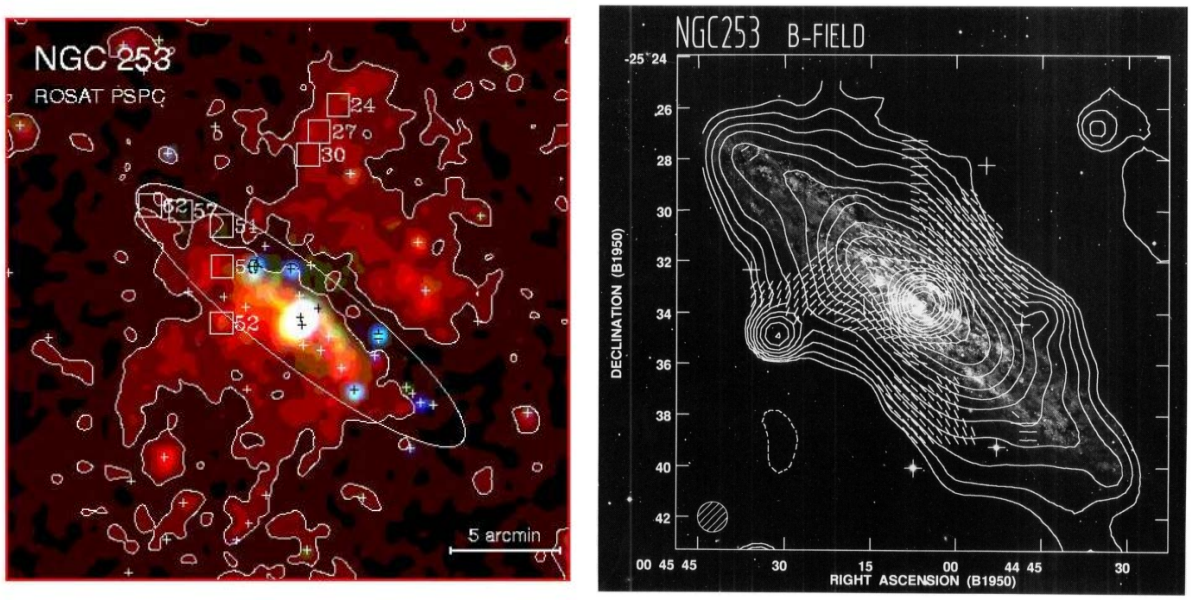

Figure 1.6: Left NGC 253 as seen in the X-ray band in edge-on view. The contours mark the halo as seen by ROSAT, figure obtained from [34].
Right NGC 253 as seen in the radio band in edge-on view. The contours denote the magnetic field lines, figure obtained from [9].

of such extended emissions are not unusual, an example of this is the starburst galaxy NGC 253, bubble-like extended emission out of the Galactic plane into the halo can be seen in X-ray and radio band respectively in Figure 1.6 [9, 34]. These images of NGC 253 in different frequency regimes seem to favour the presence of large extended emissions in its halo. In Figure 1.6 the contours denote the magnetic field lines which appear to have somewhat of a bubble-like shape which has been used as motivation in Galactic magnetic field models of the Milky Way and will be discussed further on in this chapter [35, 36]. It should be noted that for NGC 253 the star formation rate is much higher than in the Milky Way. 50% of all star formation happens in the nuclear zone of NGC 253, which could also possibly lead to such extended Galactic halo bubble-like structures [37, 38].

The Continuum HAlos in Nearby GalaxiES (CHANG-ES) survey of 35 edge on Galaxies reveal extended halos in the external Galaxies. This radio survey was conducted at two frequencies *C-band* (6 GHz with bandwidth of 2 GHz) and *L-band* (1.5 GHz with bandwidth of 500 MHz), utilising the broad bandwidth capabilities of Karl G. Jansky Very Large Array (i.e., the Expanded Very Large Array) [39, 40]. For these external galaxies a magnetic field profile motivated by [41] was utilised and field strengths of upto 5 μG were obtained for halo heights or latitude extents of about 10 kpc [10].

More recently, [42] showed the halo in external galaxies can be further extended, and their findings indicate strong evidence of extended circumgalactic medium existing in 12 $L^{\star}$ spiral external Galaxies utilising the Sunyaev-Zeldovich measurements. These galaxies

were between 3 Mpc to 10 Mpc away in distance. Their findings suggest the presence of hot material at temperatures of $\approx 3 \times 10^6$ K out to the virial radius of the Galaxies (R_{virial} ≈250 kpc). The presence of such outflows could potentially result in magnetic fields and hot gases present out and beyond the virial radius of these external Galaxies.

1.3.2 Galactic Halo Bubbles observation in the Milky Way

In the previous section it was highlighted that there is a growing body of evidence suggesting the presence of extended out of the plane emissions in the halos of external Galaxies. In this section, attention will be drawn to multi-frequency observations of emissions in the Galactic halo of the Milky Way.

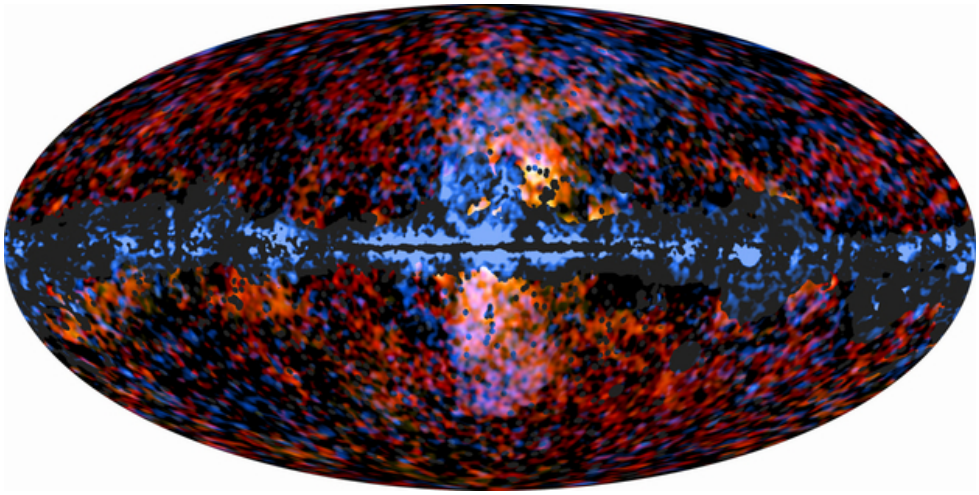

Figure 1.7: Superimposed image containing the Planck data shown in red and yellow which corresponds to the Haze emission at frequencies of 30 GHz and 44 GHz respectively extending out to high latitudes. The Fermi data (blue) shows two extended bubble-like gamma ray emissions, figure obtained from [43].

Discovery of Fermi bubbles

In 2010, Fermi Large Area Telescope (Fermi-LAT), a space observatory used to conduct gamma-ray astronomy detections from low Earth orbit, discovered bi-polar non-thermal gamma ray emissions (100 MeV — 500 GeV) at high Galactic latitudes of 55° from the Galactic disc both in the Northern and Southern Hemisphere ([44–46]). These bubble-like emissions were termed as the Fermi bubbles (see left Figure 1.7). These gamma ray bubbles are extending up to ≈ 3 kpc radially and ≈ 8 kpc in the z-direction (Figure 1.7), and have a total energy of $\approx 10^{(54-55)}$ ergs. The exact origin of these bubbles still remains unknown. They could be a result of cosmic ray acceleration by the supermassive black

hole (Sagittarius A*) at the center of our Galaxy [45] or, they could be associated with the prolonged accumulation of cosmic rays due to star formation in the Galactic center [47].

Radio counterparts of the Fermi bubbles and eROSITA observations

Though the detection of extended emission in the Galactic halo was a first in gamma-ray wavelengths, we had seen high Galactic latitude emission for a while in radio data . The Wilkinson Microwave Anisotropy Probe (WMAP) was a NASA spacecraft mission which operated between 2001 and 2010. The main aim of this experiment was measuring the small temperature differences (for frequencies between 23 GHz to 94 GHz) across the sky in the Cosmic Microwave Background (CMB), it being the remaining thermal signatures from the Big Bang. Apart from measuring the temperature fluctuations, WMAP also observed high Galactic latitude synchrotron emissions later named as the WMAP haze [48]. Later the Planck space observatory (2009-2013) operated by European Space Agency (ESA) whose main mission was also to measure CMB anisotropies at much broader frequency ranges of 30 GHz to 857 GHz verified the results of WMAP and observed high galactic latitude synchrotron emissions now known as the Planck haze [43].

Spatial correlations between this radio haze (WMAP/Planck-haze) and the Fermi bubbles suggest that this emission might have a common origin [45, 49]. This radio haze along with the Fermi bubbles can be seen in Figure 1.7.

Additionally, in 2013 the ground based radio telescope S-band Polarization All-Sky Survey or S-PASS (at 2.3 GHz) later revealed this radio haze to have a more bubble-like structure at 2.3 GHz [4]. The haze and bubbles together will be addressed as radio bubbles henceforth.

Recently, in 2020 the X-ray instrument eROSITA which is a part of Russian–German Spektr-RG space observatory, observed extended emission out in the Galactic halo up to 14 kpc in height (latitude extent) and radially expanding up to 7 kpc from the GC [50]. These high latitude thermal observations or X-ray bubbles are also called the eROSITA bubbles, it was estimated that the total thermal energy content in the eROSITA bubbles was $\approx 10^{56}$ ergs. The Fermi and eROSITA bubble spatial extents can be seen in Figure 1.8, the eROSITA bubbles are further extended out to higher Galactic latitudes encompassing the Fermi bubbles.

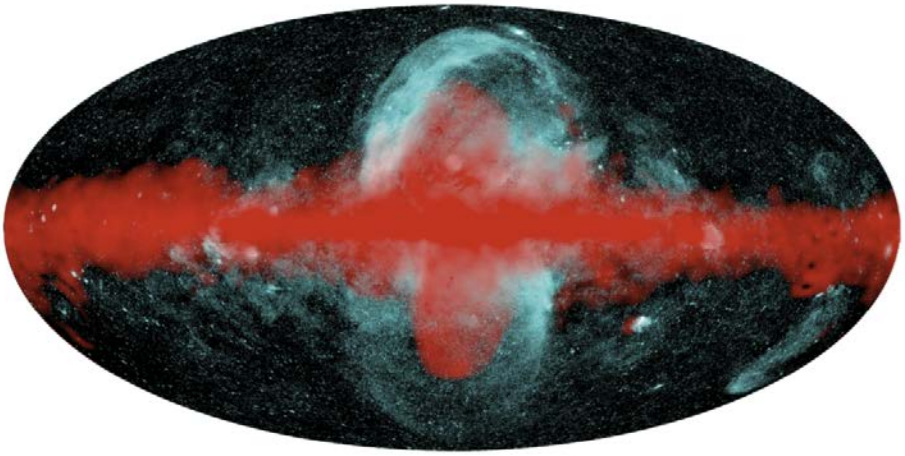

Figure 1.8: A sketch depicting the morphology of Fermi bubbles (in red) versus eROSITA bubbles (in blue), figure obtained from [50]. Together they will be addressed as the Galactic Halo Bubbles (GHBs).

1.4 Motivation to study magnetic fields in the Galactic Halo Bubbles

The aforementioned multi-frequency observations of the Galactic halo indicating the presence of the Galactic Halo Bubbles serves a strong motivation to investigate magnetic fields in this region. Additionally, one can call upon equipartition of energy between different physical processes to further consolidate the need to study Galactic halo bubbles some of which are listed below.

Equipartition between magnetic fields and thermal particles

The FERMI-LAT observations in the gamma regime suggest the values of 10^{54-55} ergs for the total energy content in the Fermi bubbles [45]. Furthermore, the observations made by eROSITA estimated that the total energy in the eROSITA bubbles is $\approx 10^{56}$ ergs for thermal electrons. However, along with these observations, there is a theoretical motivation to study the Galactic halo and that comes from the equipartition of energy argument which assumes thermal particles, cosmic rays and magnetic fields are close to equipartition in the Galactic halo with a value of roughly 1 eV/cm^3 [29, 51]. The plasma β_{plasma} which is the ratio of the energy density in the thermal electrons to magnetic pressure is assumed to be 1 [20] by the argument of equipartition of energies. These total energy content values of the Fermi/eROSITA bubbles or collectively the Galactic Halo Bubbles (GHBs) are a clear indication that the Galactic halo is a far more interesting place than what it was thought to be. Additionally, there is a growing body of evidence [52] which hints that the

energy densities in the extended Galactic halo (virial radius 0f ~ 250 kpc) of the Galaxy can be as high as 0.1 eV/cm^3. Assuming that the magnetic field couples with the hot gas that permeates the extended Galactic halo, there is a possibility of equipartition to exist between the magnetic fields and warm thermal gas given by:

$$U_{\rm mag} \approx U_{\rm thermal}, \text{ or,}$$

$$\frac{B^2}{8\pi} \approx nkT \tag{1.6}$$

with n being the gas density and kT being the temperature of the gas in the extended halo and it is assumed that $\beta_{\rm plasma} = 1$. For $kT \geq 300$ eV the magnetic field strengths expected would be between 0.05 to 0.3 μG [53, 54]. Note that the value of $\beta_{\rm plasma}$ is not well constrained and could lie between 1 – 100 [54, 55].

Equipartition between magnetic fields and cosmic rays

For the local Galactic halo or the Galactic halo bubble region equipartition can be assumed between cosmic rays and magnetic fields. The strength of magnetic field can then be estimated in different parts of the Galaxy. Within our own Galaxy the energy density in cosmic ray protons or relativistic protons seems to be 100 times more than the cosmic ray electrons. However, this ratio of energy between relativistic protons and electrons given by $\beta_{\rm pe}$ is not universal. For example in the Crab nebula the value of $\beta_{\rm pe}$ has to be smaller for dynamical reasons [29]. Therefore, the total energy in cosmic rays is given by:

$$W_{\rm CR} = (1 + \beta_{\rm pe}) V \int_{E_{\rm min}}^{E_{\rm max}} E \frac{{\rm d}n_e}{{\rm d}E} {\rm d}E, \tag{1.7}$$

here, E is the energy of the cosmic rays, $E\frac{{\rm d}n_e}{{\rm d}E}$ is the cosmic ray number density in log E bins and V is the total volume of interest. Similarly, the total magnetic field energy will be given by:

$$W_{\rm mag} = V \frac{B^2}{8\pi}.$$

For equipartition to hold, $W_{\rm B} = W_{\rm CR}$ and utilising this equipartition argument the inferred magnetic field strength from the S-PASS observations in the GHBs can be anywhere between 6 – 10 μG. This also depends on the proton-electron ratio, $\beta_{\rm pe}$.

The aforementioned scenarios suggest that should equipartition hold between magnetic fields and thermal gasses the drop in the magnetic field strengths at extended halo distances of 300 kpc might have a more power law like dependence. Note that the

equipartition has no strong physical justification it is rather a conjecture. It is conjectured that magnetic fields get stretched and tangled in plasmas due to the motion of gases, this can plausibly result in an equipartition between the energy density of these turbulently moving plasma and magnetic fields. These turbulent motions in the plasma might also be a source of accelerating high energy particles which in turn might come into equipartition with the turbulent moving plasma. Thus, the aforementioned observational results and inferred deductions provide strong motivation to study the magnetic fields in the Galactic Halo Bubbles.

1.5 Current models of Galactic magnetic fields

As discussed in Section 1.2 there are a variety of methods that allow observational probes of Galactic magnetic fields. To probe large-scale Galactic magnetic fields Faraday rotation (FR) of Galactic sources like pulsars or extra-galactic sources like fast radio bursts and polarised synchrotron radiation from non-thermal Galactic cosmic rays can be the most useful [5]. Faraday rotation is sensitive to the magnetic-field component parallel to the line of sight, $B_{\parallel}$. On the other hand synchrotron radiation probes the component perpendicular to the line of sight, $B_{\perp}$.

Our understanding of the magnetic field in the disc region of the Galaxy is much better than that of the halo region due to the larger amount of observational data present at varying frequencies [56]. Some early works done in 1990 [57] suggested based on hydrostatic equilibrium that the scale-height or halo height of the halo which included CRs, magnetic fields and part of the ISM should be more than 1 kpc. Models of synchrotron emissivity based on observations of Haslam [58, 59] further improved the value of the scale-height to be around 4.5 kpc in solar vicinity [5] [60]. This value of the scale-height was found to be in agreement with the estimates based on hydrostatic equilibrium done by Kalberla in 1998 [61]. Recent efforts have been made to model the magnetic fields in the Galaxy, for example [35, 62–66].

It should be noted that most current models in the literature assume a scale height (or latitudinal extent of the halo) that is smaller than the halo heights suggested by recent non-thermal observations.

In regard to the geometry of the magnetic fields in the halo, even with the limited observational data, there is evidence of toroidal magnetic field structures (axisymmetric), which are orientated in opposite directions on either side of the Galactic plane (antisymmetric) in the Galactic halo [11, 12, 62, 63, 65, 67]. Additionally, as discussed in Section 1.3.2

observations of X-shaped magnetic fields from external galaxies [13, 68] have motivated similar field halo field models for the Milky Way [35, 36].

Widely used models like JF12 [35] (discussed in next section) have also made efforts towards the modelling of the Galactic halo magnetic field. One drawback of JF12 is that it masks out the Fermi bubble regions in its evaluation of the model agreement with the data, whereas S-PASS observations [4] tell us that the magnetic field strength in this region is not negligible. Therefore, it is important to consider modelling the Galactic halo including the Fermi/eROSITA bubble or Galactic halo bubble regions.

Thus, informed by observations a new toy model for the Galactic halo bubble region was one of the main topics of investigation during this PhD thesis. This new model will be introduced and discussed in detail in Chapter 2.

1.5.1 Example of existing GMF models

One of the more widely used models for magnetic fields in the Milky Way is the Jansson and Farrar or the JF12 model [35]. The main focus of the JF12 model was the Galactic disc. The Galactic halo fields in it are rather weak when compared with the inferred magnetic field values of $6 - 10$ μG from the S-PASS observations [4].

The JF12 model divides the Galactic magnetic field into 3 structured components namely: *1)* the toroidal halo field, *2)* the X-field and; *3)* the disc field. In Figure 1.9, cross-sections in $x - y$ and $x - z$ planes are shown for the toroidal halo and X-field components of the magnetic fields, along with disc field only in the $x - y$ plane (see bottom plot in Figure 1.9) since the field does not extend in the z-direction.

The JF12 halo consists of :

1. Toroidal halo - The toroidal halo model consists of two asymmetric, purely azimuthal toroidal fields in the Northern and Southern Hemisphere at roughly ≈ 4 kpc. The radial extent of the field in the Northern Hemisphere is almost half of the extent in the Southern Hemisphere. The field strengths are roughly 1.4 μG in both north and south.
2. X-field - The X-field was motivated based on the observations from external galaxies [13, 68] as seen also in the radio observations of NGC 253 (see Figure 1.6). The field is axisymmetric and poloidal.
3. Disc field - The disc field was motivated from [69] which in turn was based on the structure NE2001 [70] thermal electron density model.

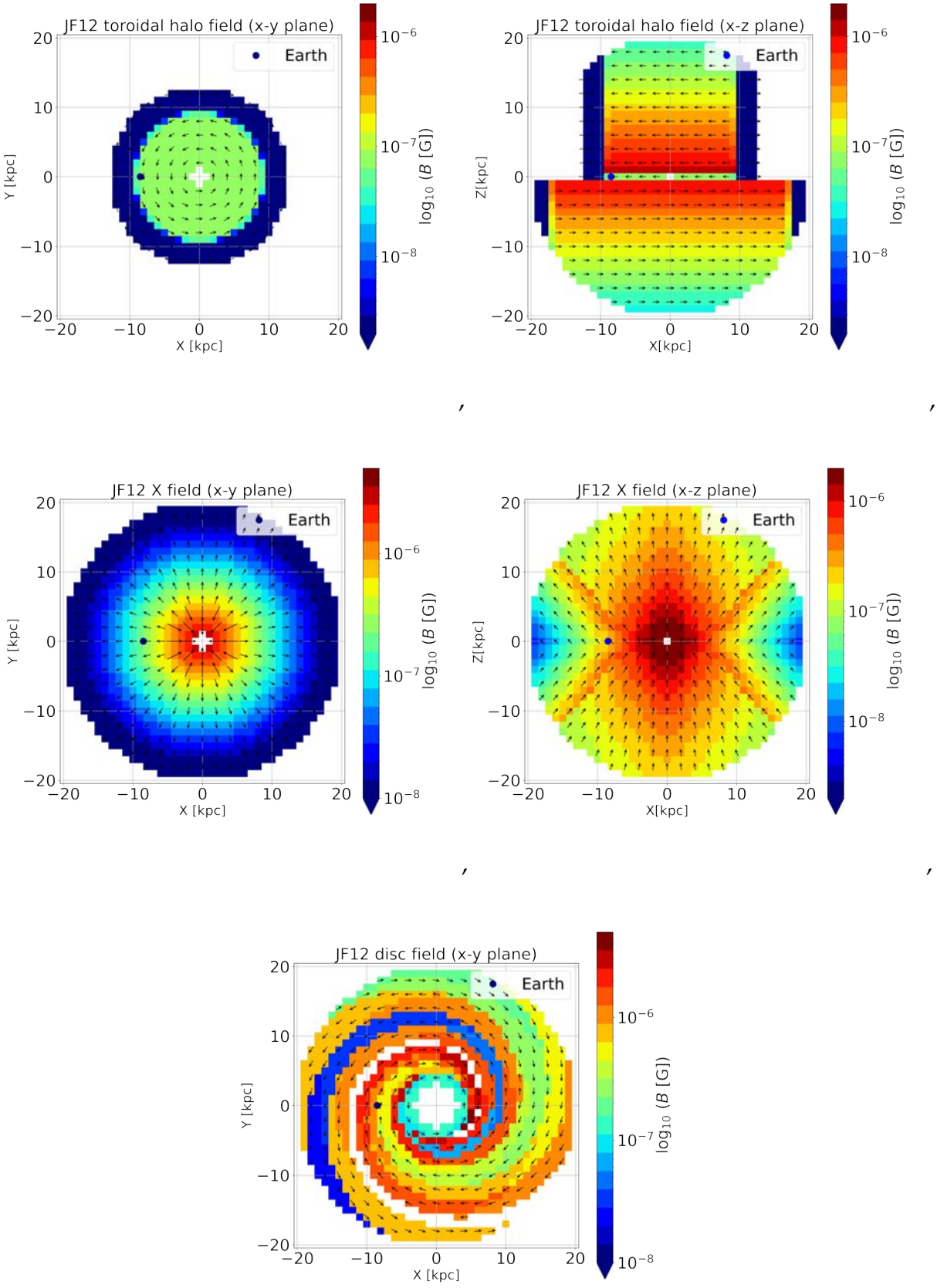

Figure 1.9: Top: The toroidal field from the JF12 model in the $x-y$ at $z = 1$ kpc and $x-z$ at $y = 1$ kpc plane. The toroidal magnetic field is asymmetric and has strengths $\approx 1-2\mu$G.
Middle: The X field from the JF12 model in the $x-y$ at $z = 1$ kpc and $x-z$ sat $y = 1$ kpc plane. This field is called so based on its "X" shape with magnetic strengths of $\approx 2\mu$G.
Bottom: The disc field from the JF12 model in the $x-y$ plane at $z = 1$ kpc [35].

Apart from the large-scale fields the JF12 model also has turbulent fields of varying coherence lengths.

The total energies in the Galactic halo based on multi-frequency observations hint to be roughly between 10^{55} – 10^{56} ergs [45, 50]. In comparison to these values, the total magnetic field energy content in the halo field component of the JF12 model is 4×10^{54} ergs and 3×10^{54} ergs for the toroidal halo and X-field respectively [71]. For this thesis, the focus solely lies in the Galactic halo bubble region which can be described together with the Fermi and eROSITA bubbles. JF12 not only masks the Fermi-bubbles but also adopts magnetic field strengths and spatial extensions both weaker and smaller than those suggested by the S-PASS observations [4] of these bubble regions. Contrary to JF12, the GHB magnetic field model not only focuses on GHBs but also uses the S-PASS observations as a motivation for the magnetic field modelling.

Another model that will be utilised for comparison purposes is the Xu and Han model for the Galactic halo and will be addressed as the XH19 model [72]. This model primarily focusses only on the Galactic halo with an azimuthal cut-off of ≈ 1 kpc. The cross-sections for the XH19 model in the $x - y$ and $y - z$ plane is shown in Figure 1.10

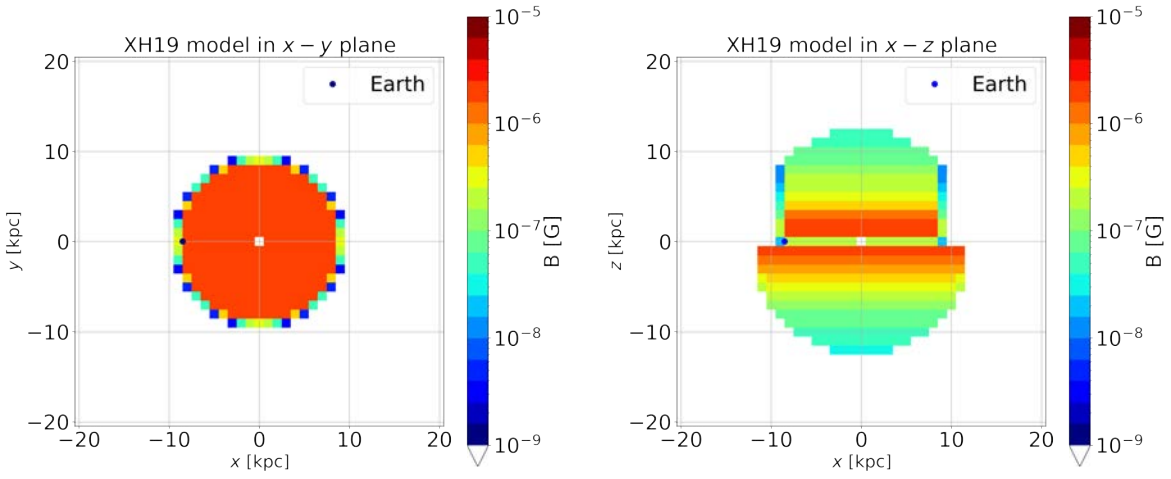

Figure 1.10: Cross-sections in the $x - y$ at $z = 1$ kpc and $x - z$ at $y = 1$ kpc for the XH19 model [72].

1.6 Introduction to Cosmic rays

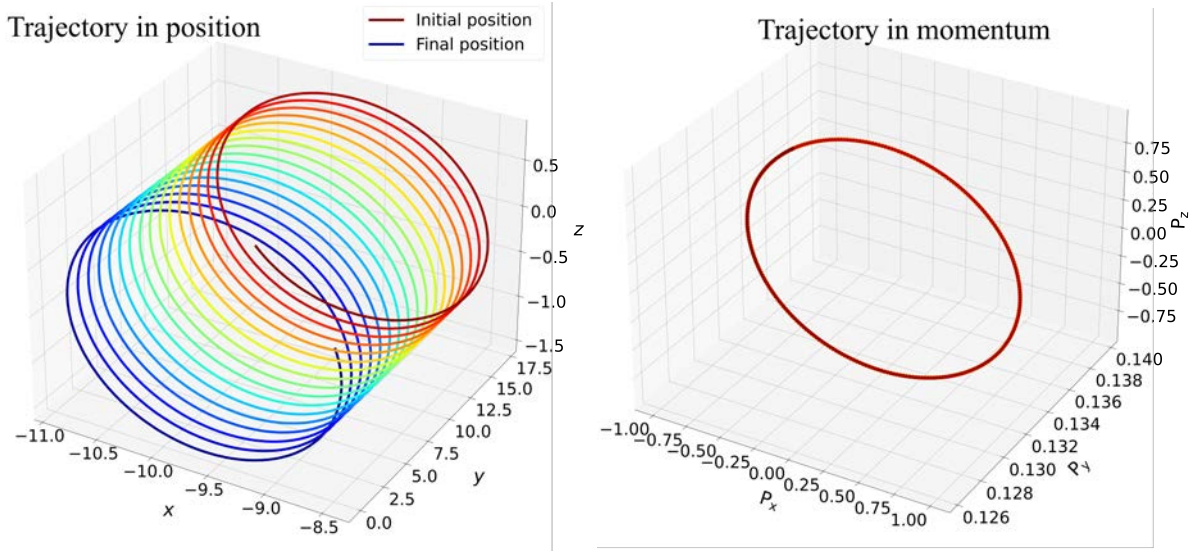

Figure 1.11: A particle in a uniform magnetic field traces a helical path in physical space (left). This same particle will trace a circle in momentum space (right) since all it does is gyrate along magnetic field lines.

Cosmic rays (CRs) also known as non-thermal particles are highly energetic charged particles which can originate both in Galactic and extragalactic objects. Charged particles tend to deflect when they encounter magnetic fields. In the case of uniform magnetic fields they follow a helical path around the field. Charged particles propagating through a magnetic field precesses around the field lines by means of the Lorentz force. The radius of gyration of these charged particles is called the Larmor radius or gyro-radius and is given by:

$$r_{\mathrm{L}} = \frac{\beta E}{ZeB}, \tag{1.8}$$

here, E is the energy of the charged particle in units of eV, Ze is the charge of the particle and B is the magnetic field strength. Figure 1.11 shows the effect of a uniform field in a single direction on a particle travelling through, it can be seen that the particle traces a helical path in position whereas, its momentum vectors follow a circular path around the magnetic field. For reference, a proton at 40 EeV will have a Larmor radius of 7 kpc for typical field strength of 6 μG.

Discovery of cosmic rays and their potential sources

The first real discovery of cosmic rays took place in 1912. That year, Victor Hess made seven balloon flights, the highest of which, on 7 August, reached an altitude of 5350 metres. All of the detectors on board the balloon measured a strong increase in ionization

at altitudes above ≈ 4000 m. Hess's conclusion was that the atmosphere was being hit from above by radiation of high penetrating power, which could not be the result of radioactive emanations. As one of the flights took place during an eclipse, he concluded that the radiation was not coming from the sun [73]. It is worth noting that one of the flights of Hess which was instrumental in the discovery of cosmic rays took place in Bad Saarow/Pieskow in Brandenburg which is not very far from DESY, Zeuthen also in Brandenburg, Germany.

In 1915, Egon Schweidler presented the first theoretical study of possible sources of cosmic rays. He excluded the upper atmosphere, the Moon, the planets, the Sun, and other fixed stars as sources of cosmic rays on the basis of existing knowledge of ionising radiation. His conclusion was that the less extreme conditions favoured the hypothesis of the distribution of radioactive substances in space.

CRs are ionised nuclei that comprise mostly of protons followed up by electrons, positrons etc [74]. Even though the origin of cosmic rays remains a mystery, the common notion based on information from the cosmic ray spectrum is that they are both of Galactic (including our Sun) and extragalactic origin. CRs observed at earth range between 10^9 to 10^{21} eV. The earth's atmosphere is constantly showered by these relativistic particles of extra-terrestrial origin. GeV (10^9) eV energy particles fall at a rate of 10,000 per m^2 per sec whereas, 1000 GeV particles have a rate of 1 particle per m^2 per sec denote PAO. Within our solar system, the Sun is known to be a source of cosmic rays with energies up to a few GeV (1 GeV ~ 10^9 eV).

Outside our solar system supernovae or short gamma ray bursts or GRBs (example: immensely energetic explosion from merging of two neutron stars) could possibly be the source of Galactic cosmic rays. Cosmic rays could also arrive from extragalactic sources like starburst galaxies. These galaxies have a higher star formation rate in their Galactic nucleus region than the Milky Way. For example 50 % of all star formation in NGC 253 occurs in this Galactic nucleus region. This number drops to only 10% for the Milky Way. A starburst galaxy which might be a potential source of highly energetic CRs is NGC 253 due to its high star formation rate [37, 38] (see left Figure 1.12). Another potential source of CRs could be active galactic nuclei (AGN). They are compact regions at the center of galaxies comprising supermassive black holes (few million to a billion solar masses). This compact region is abnormally bright and the black hole at the center is accompanied by an accretion disc which is a circular structure formed when material (stars) fall towards a gravitationally strong object like a black hole, dust torus and a jet which is common though not universal for all AGNs. An example of an AGN which is thought to be a possible source of CRs is Centaurus A or Cen A [54, 75] (see right Figure 1.12). Note, that

both NGC 253 and Cen A as potential sources of ultra-high-energy cosmic rays (energies $> 10^{18}$ eV) will be investigated in Chapter 3.

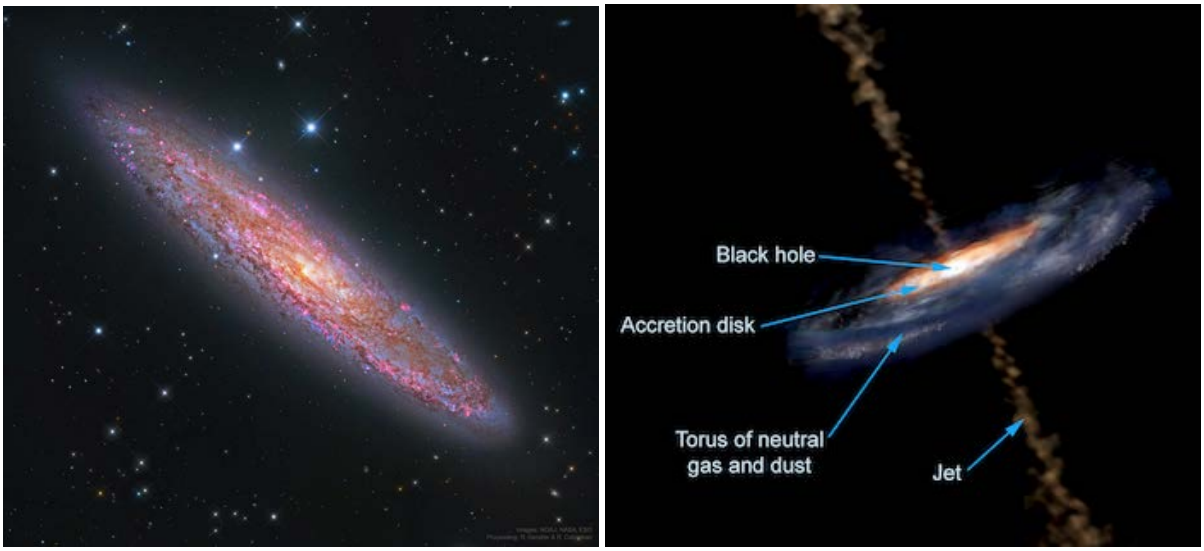

Figure 1.12: Left: starburst galaxy NGC 253 or the Sculptor Galaxy produces 50% of all its stars in the Galactic nucleus region (**Image Credits: NASA, ESO and NOAJ**).
Right: a schematic representation of an AGN with its different features like the accretion disk, jet and the torus of neutral dust and gas (**Image Credit: Aurore Simonnet, Sonoma State University**).

1.6.1 The cosmic ray spectra

The cosmic ray spectrum mostly described by a power-law as shown below :

$$\frac{\mathrm{d}n}{\mathrm{d}E} \propto E^{-\alpha}, \tag{1.9}$$

here, $\frac{\mathrm{d}n}{\mathrm{d}E}$ is the particles per energy bin and α is the power-law index. The spectra of cosmic rays as observed at earth is shown in Figure 1.13, at GeV energies the CRs in the ISM diffuse towards the Earth through the solar wind and hence, there is a departure from the overall fit.

In Figure 1.13 there is a break in the spectrum at energies of about 3×10^{15} eV; here the spectral index changes form 2.7 to 3.1, this break is referred to as the “knee” which was first discovered in 1958 by Kulikov and Khristiansen [77]. There is also a “second knee” which is more subtle. The spectral index goes back to 2.7 beyond the energies of 10^{18} eV. This feature is called the ’ankle’. The "knee(s)" mark a major transition region from potentially Galactic to extragalactic sources (see Section 1.8 for more discussion).

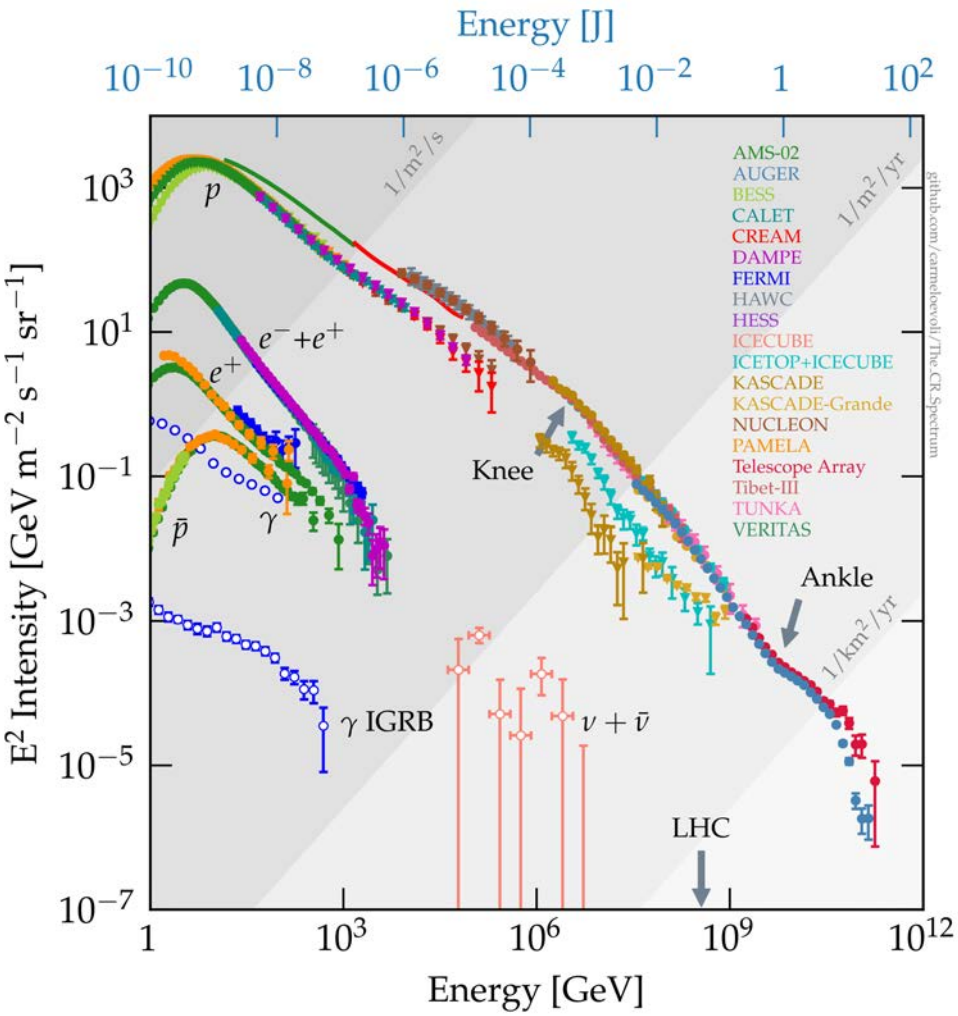

Figure 1.13: The updated cosmic ray spectrum as detected at earth from various instruments. The figure was obtained from [76]

The spectrum gets suppressed at about 5×10^{19} eV. This suppression was formerly theoretically proposed in 1966 independently by Greisen [78] and Zatsepin & Kuzmin [79] and is commonly known as the GZK limit. This is the theoretical upper limit on the energy of cosmic ray protons originating in extragalactic objects. Kenneth Greisen, Georgiy Zatsepin and Vadim Kuzmin predicted that for highly energetic cosmic ray species like protons and nuclei at energies $\geq 5 \times 10^{19}$ eV or 50 EeV will interact with the CMB photons resulting in pion production which would last until the energy of the CR went below the minimum energy required to produce pions. Based on the mean path of the interaction Greisen, Zatsepin and Kuzmin predicted that cosmic rays with energies greater than the threshold arriving at distances greater than 50 Mpc would not be detected at Earth. This is also called the GZK horizon. One of the ways to differentiate between the Galactic versus extragalactic sources of CRs can be addressed by looking at the Larmor radius of such particles. Information about the sources/accelerators of

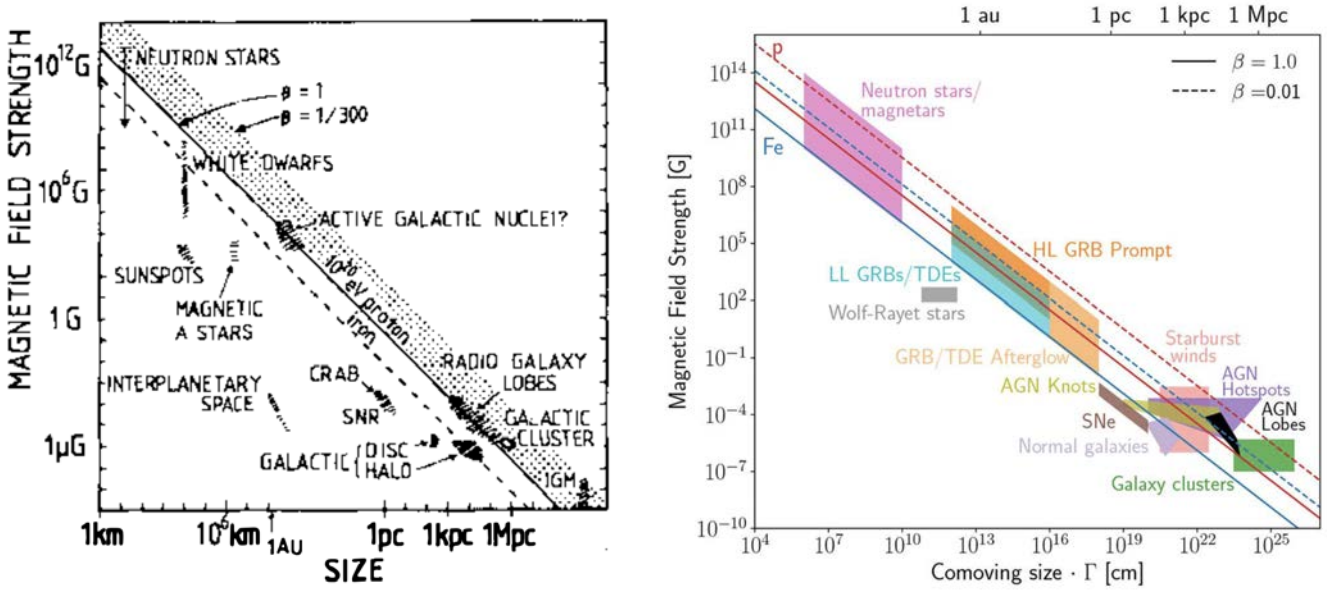

Figure 1.14: Left: The Hillas figure obtained from [80] showing the size (L) and magnetic field strengths (B) of possible cosmic particle accelerators. Objects below the solid black line cannot accelerate particles to 10^{20} eV.
Right: The updated version of Hillas plot obtained from [81] including shock velocities (β) which are possible sites of cosmic ray acceleration.

CRs becomes less clear for higher energies. The Hillas criteria can be used to obtain information about possible sources of CRs of higher energies. A simple dimensional argument of the possible acceleration sites, giving the maximum energy obtainable from the magnetic field and the size of the site, gives the following,

$$E^{\max} \sim 10^{18} Z \, \frac{L}{\text{kpc}} \, \frac{B}{\mu\text{G}} \text{eV} \,, \tag{1.10}$$

where, L is the radius of the accreting region, B is the magnetic field in the accreting region and Z is the charge of the particle that is getting accreted. This expression was first proposed by Michael Hillas in 1984 [80] and is known as the Hillas criterion. In more specific cases of shock acceleration the Hillas criterion can be modified to $E^{\max} = \beta \, 10^{18} Z \, \frac{L}{\text{kpc}} \, \frac{B}{\mu\text{G}} \text{eV}$, here β is the shock velocity in units of speed of light, c. Using these criteria, possible accelerators capable of achieving the particle energies observed at the upper end of the 10^{20} eV spectrum are: active galactic nuclei (AGN) ($R_{\text{kpc}} \sim 10^{-5}$,$B_{\mu\text{G}} \sim 10^{7}$); gamma-ray bursts (GRBs) ($R_{\text{kpc}} \sim 10^{-7}$,$B_{\mu\text{G}} \sim 10^{9}$).

In Figure 1.14, the original and the updated plot after 35 years for different source classes obtained utilising the Hillas criterion is shown [81]. The solid lines mark where Eq. 1.10 is fulfilled for CR nuclei of the indicated energy. From this figure one can state that the probable accelerators for particles of 10^{20} eV could be AGNs or GRBs and starburst regions

(see Figure 1.14). New source classes have been added to the new Hillas plot, including tidal disturbance events. These were not discovered at the time the Hillas criterion was originally proposed.

1.7 Observations of (ultra)-high energy cosmic rays (UHECRs)

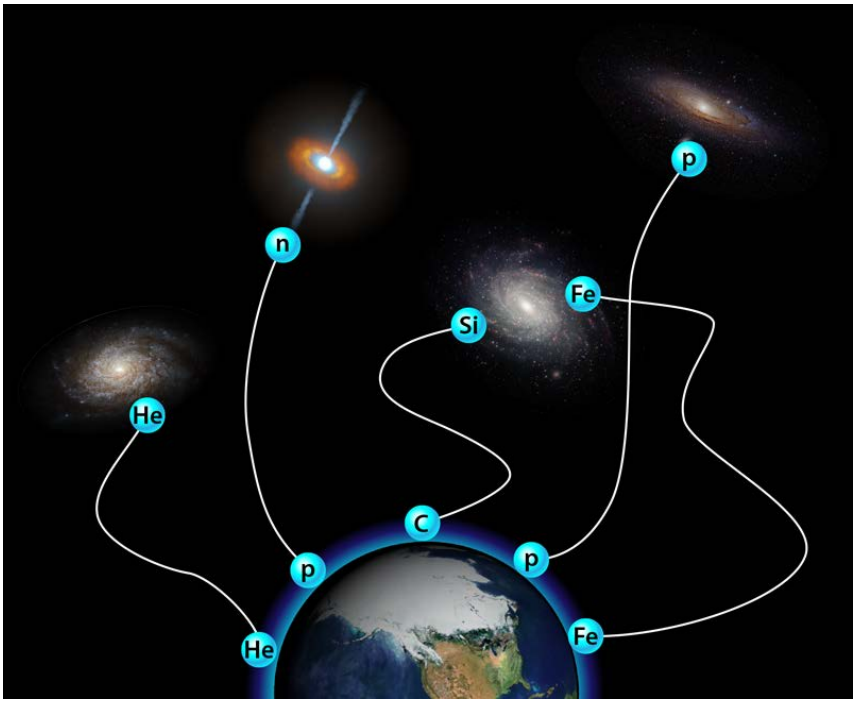

Figure 1.15: PAO observations suggest that UHECRs might be of varied composition and arriving from several potential sources from active Galactic nuclei to starburst Galaxies. The altered trajectories of the UHECRs depicts the difficulty in localising its sources from observations made on Earth (**Image Credits : NASA Archives**).

The origin of UHECRs is one of the biggest unsolved problems of high energy astrophysics. There is not sufficient information to concur confidently what sources are behind such highly energetic cosmic rays (energy $\geq 10^{18}$ eV). The intergalactic and Galactic magnetic fields make the problem even more difficult as source localisation gets harder. In Figure 1.15, potential sources of different UHECR species with their deflected trajectories are shown, these sources could be active Galactic nuclei or starburst Galaxies or gamma ray bursts.

There are several observatories which observe cosmic rays ranging from the high energy (10^{11} – 10^{17} eV) to ultra-high energy ($\geq 10^{18}$ eV). The High-Altitude Water Cherenkov gamma-ray Observatory (HAWC) [82] in Mexico observes cosmic rays and photons between 10^{11} – 10^{14} eV. The KArlsruhe Shower Core and Array DEtector (KASCADE) is

a scintillator array that can measure cosmic rays between the energies of 10^{14} to 10^{17} eV [83].

For the purposes of this thesis, most of the focus will be given to UHECRs between the energies of $\geq 10^{18}$ eV which most likely are of extragalactic origin based on their possible Larmor radii. Two observatories that observe these UHECRs are Pierre Auger Observatory (PAO) in the Southern Hemisphere in Argentina [84] and the Telescope Array Project (TA) in the Northern Hemisphere in the US [85]. PAO and TA cover approximately 3000 km^2 and 700 km^2 of instrumented areas respectively [86]. PAO consists of hybrid detectors comprising large water Cherenkov tanks and TA comprises scintillators. These observatories observe cosmic ray air showers and obtain a flux of about 100 particles per square kilometre per year. Air showers consists of secondary particles that are formed by the interaction of UHECRs with air molecules. A single air shower is mostly incapable of providing any information about the direction or composition of the cosmic rays that arrive at earth and therefore large numbers of observations are required in order to '*guesstimate*' their origin. The surface detectors installed at these observatories not only detect these air showers but also reconstruct the energy and direction of the UHECRs which give rise to the secondary particles (mostly muons). On the other hand, to measure the composition of the air-showers the fluorescence detectors are required which operate on moon-less nights (10% of duty cycle) and thus have far fewer statistics.

Both PAO and TA do not measure the primary cosmic ray or the cosmic ray as it was before entering Earth's atmosphere. They instead measure the air showers created by interactions between the primary cosmic ray and the Earth's atmosphere. This cascade of secondary particles generated contain of three main components (Figure 1.16); the innermost component are the hadrons, followed by muons and the outermost component being electrons/positrons pairs ($e^{\pm}$), and photons (γ). As can be seen from Figure 1.16, the shower fronts develop horizontally as the cascade evolves until the interactions are not possible due to the small size of the reduced size of the secondary particles. The shower front is more or less intact in this whole process due the relativistic speeds of the particles. The difference in the arrival time between these particles can then be used to determine the initial direction of the primary cosmic ray before entering Earth's atmosphere.

1.7.1 Large and small-scale anisotropies in the arrival direction of UHECRs

The biggest challenge in the field of multi-messenger astrophysics is understanding the production mechanisms and unveiling the potential sources of UHECRs and very high

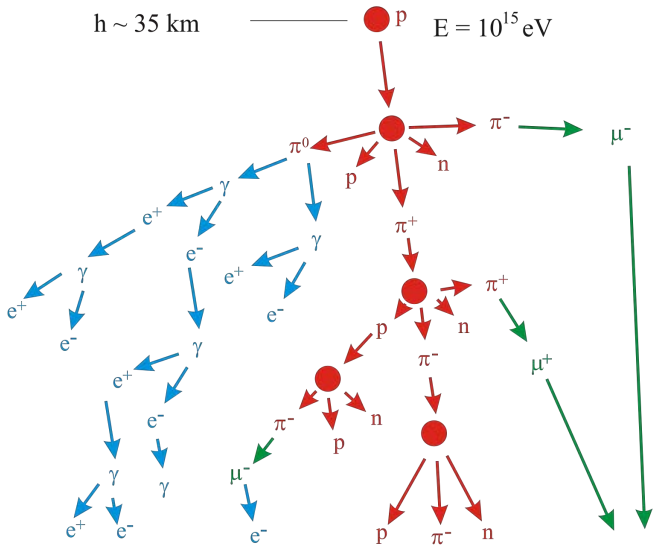

Figure 1.16: Schematic representation of a cosmic ray air shower for a proton of energy E = 10^{15} eV entering at height of 35 kms. The air showers that comprise hadronic components are shown (red), muons (green) and electron/positron pairs ($e^{\pm}$) along with photons (γ) in blue, figure obtained from [87].

energy (VHE) neutrinos (PeV and above energies), the latter likely being a successor of UHECRs which is not a topic of interest for this thesis. The mystery of the origin of high energy particles can only be solved by observing both the UHECRs and VHE neutrinos since theoretically they should be produced simultaneously. Neutrinos arising in extragalactic sources are not subjected to deflections due to magnetic fields between the source and observer. However, we have yet to observe a VHE neutrino arising from a potential extragalactic source of UHECR [88].

For this thesis, the focus lies solely on arrival directions of UHECRs. Since UHECRs are subjected to the GZK effect, there is a limitation on their possible sources due to the energy-loss they undergo by interacting with the extragalactic background light. Depending on the species of cosmic rays the longest possible horizon could be between 250 Mpc (iron) to 5 Mpc (helium). In Figure 1.17 the energy-loss length for nitrogen and iron are depicted. The figure was created using CRPropa3 [89, 90]. The values of the cross-section were obtained by TALYS [91]. Despite some knowledge of the potential source distribution, it is harder to identify UHECR sources due to the deflections they undergo in extragalactic and Galactic magnetic fields.

Large-scale anisotropies

The arrival directions of UHECRs as seen on earth is not entirely isotropic. In 2017 the Pierre Auger collaboration [92, 93] measured a large-scale dipole anisotropy for UHECRs

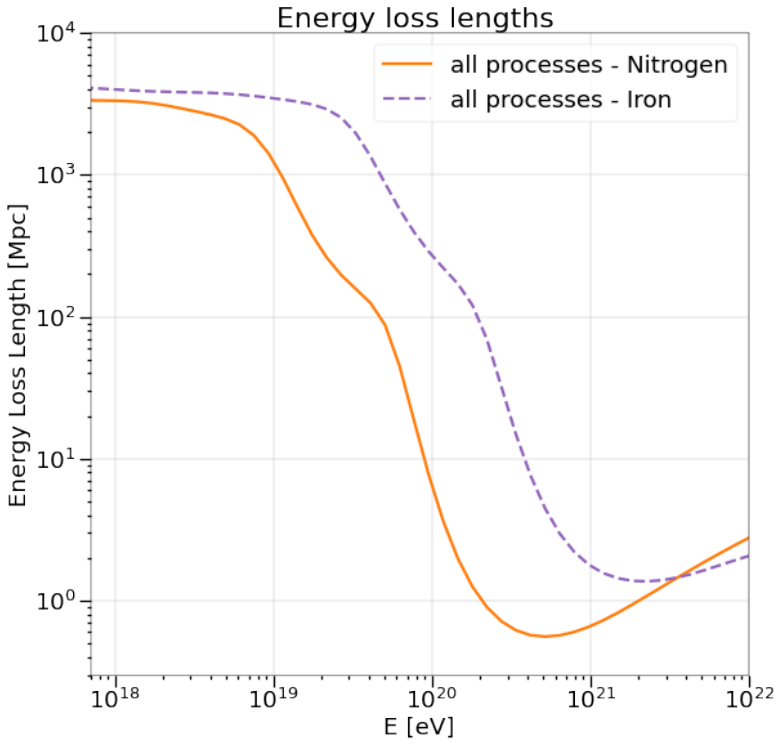

Figure 1.17: The energy-loss lengths for two cosmic rays species, nitrogen in orange and iron in purple. The cross-section values were obtained from TALYS [91] and the figure was created using CRPropa3 [89, 90].

with a confidence level of $\approx 4.2\sigma$ at the energy of ≥ 8.5 EeV with a dipole amplitude $d = 0.073^{+0.011}_{-0.009}$ [94]. The skymap seen by PAO is shown in Figure 1.18, it shows that the UHECR flux is not isotropic but a dipole. The inferred dipole direction is approximately 115° away from the Galactic center with the direction in longitude and latitude (l, b) given by 233°, −13° [95]. It can be speculated that most of the cosmic rays observed at this energy (8 EeV) are potentially extragalactic in origin. It is worth noting that this cosmic ray dipole does not align with the CMB dipole or any potential known source.

The Telescope Array collaboration also searched for the large-scale dipole anisotropy in the Northern Hemisphere [96]. With 11 years of operation, they found a dipole amplitude of 3.3 ± 1.9% though with lower significance.

Small and intermediate scale anisotropies

Both Pierre Auger Observatory and Telescope Array collaboration have also been in search of small-scale (few degrees) and intermediate scale (few 10s of degrees) anisotropies. Despite the 17 years of operation with 120,000 km^2 sr yr of accumulated exposure

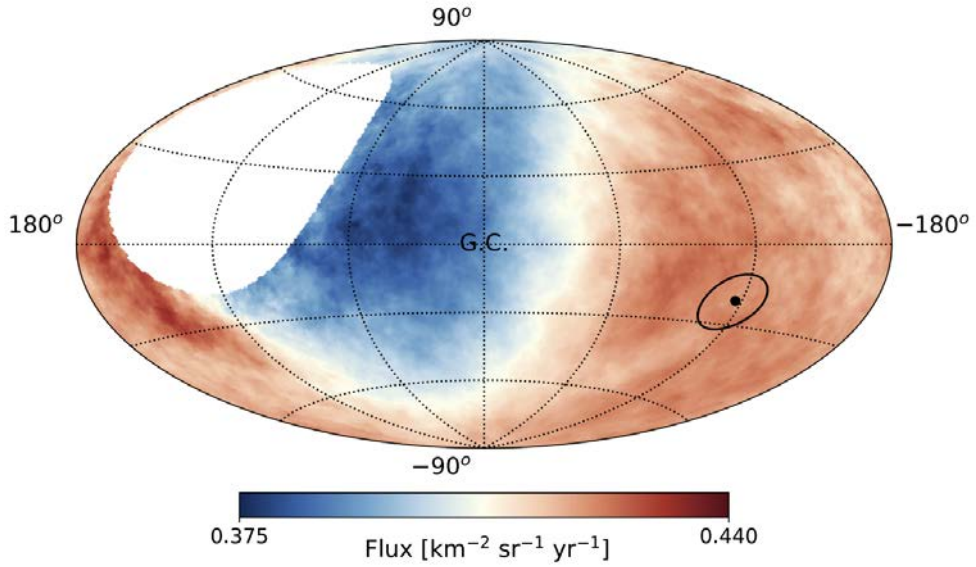

Figure 1.18: A map showing UHECR flux measured by the Pierre Auger Observatory above 8 EeV (in Galactic coordinates) with a 45° top-hat function smoothing. The dipole direction pointing away from the Galactic center is indicative of the dipole being extragalactic.

measurements made, PAO still do not reach the 5σ level. However, 1200 events from 31 EeV and above indicate an excess centred around the Centaurus A (Cen A) region at an angular scale of 27° with significance of 3.9σ [95, 97, 98].

Several extragalactic source catalogues have also been tested for correlation between PAO measurements and potential sources [95]. The highest significance was found with the starburst galaxies catalogue when compared with isotropic flux of cosmic rays for threshold energies of roughly 40 EeV [97]. One of the most prominent sources from the starburst catalogue is NGC 253 (see Figure 1.19) potentially responsible for the hotspot observed by PAO at the Galactic South pole [1, 38, 95, 97, 99]. Another prominent potential source of UHECRs could be the AGN Cen A [54]. Both of these sources will be discussed in detail in Chapter 3.

1.7.2 Status of UHECR arrival directions

Pierre Auger Observatory recently published results from the 17-year data taking process of the *Phase 1* operations. For energy ranges > 32 EeV they measured arrival directions of 2635 UHECRs and investigated for anisotropies. They report deviation in the isotropy at 4.1σ level for UHECRs with energies of ~ 40 EeV [93, 100]. More recently, the PAO and TA collaboration published a joint analysis for the UHECR arrival directions [86]. They found a correlation between the arrival directions of $12\%^{+4.5\%}_{-3.1\%}$ of detected UHECRs for energies $E \geq 38$ EeV by Auger (or $E \geq 49$ EeV by TA) and the positions of close by

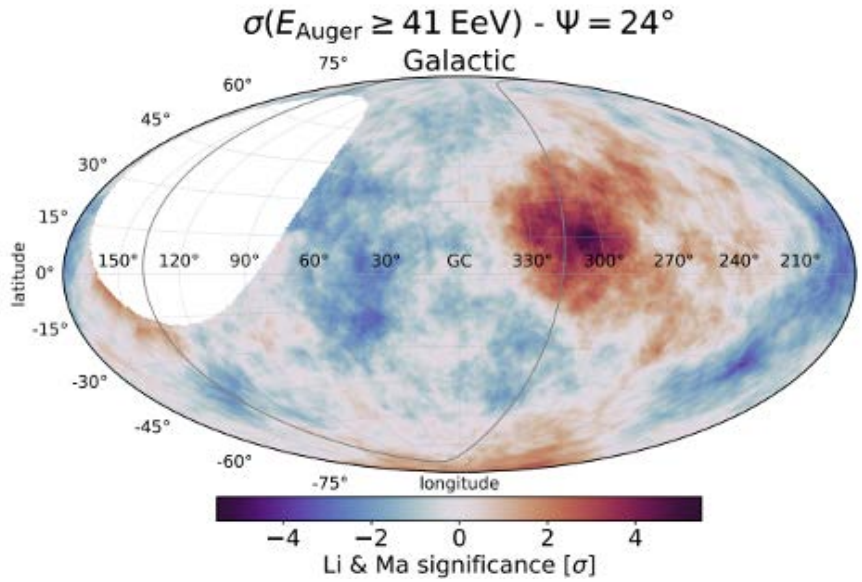

Figure 1.19: The southern Galactic pole hotspot as seen by the PAO which could be potentially linked to the starburst Galaxy NGC 253 [1, 38, 99] while the hotspot in Northern Hemisphere linked to potential UHECR source Cen A [54].

starburst galaxies on an angular scale of $\approx 15°$ with 4.7σ significance. This value is higher than the previously known significance value of 4.2σ.

In the future the observational area of TA will increase by a factor 4 which will result in a reduction of statistical uncertainties for measurements of UHECR flux in the Northern Hemisphere. PAO will also undergo a significant instrumentation upgrade for AugerPrime [101, 102] with new scintillation and radio detectors being added to the existing water-Cherenkov and fluorescence detectors. AugerPrime in the future will be able to separate UHECR species on an event by event basis giving more insight into potential source candidates.

1.8 Cosmic ray distribution in the Galaxy

The "*knee*" in cosmic ray energy spectrum in Figure 1.13 marks what possibly is the transition zone between Galactic and extragalactic cosmic rays. Galactic cosmic rays thus occupy the lower energy range of this spectrum. The principal candidates for the Galactic accelerators of cosmic rays could be supernova remnants or powerful binary systems. The *knee* could be itself a result of reaching the maximum energy of such accelerators [103]. The reason that cosmic rays above the *knee* are thought to be extragalactic is because as their energies increase and their Larmor radii also increase for given magnetic field

strengths, the cosmic rays above a critical energy can then escape the magnetic fields in the Galaxy [104]. For instance, in a μG magnetic field a CR with $E = 10^{18}$ eV will have a Larmor radius at the kpc scale making it highly unlikely to remain contained within the Galaxy. However, the transition region between Galactic and extragalactic sources of CRs is still not well understood and is a topic of active debate.

Understanding the distribution of CRs is essential for studying the magnetic fields in the Galaxy since a lot of indirect methods of probing magnetic fields rely on knowledge of the non-thermal particles or relativistic particle (or CRs) distribution. To study the distribution of cosmic rays within the Milky Way, gamma-ray observations can be useful. This is because diffuse gamma-ray emission[†] above 100 MeV is contributed to by neutral pion-decay. These pions are the result of hadronic interactions between ISM and CR nuclei. Given that the gas distribution is known, the observation of diffuse Gamma ray emission can give information of the spatial distribution of CRs at around 1 GeV per nucleon [103]. Fermi-LAT's sensitivity and broad energy range led to the discovery of different components of this diffuse gamma-ray emission one of them being the giant GeV bubble-like structures in the Milky Way's halo, now known as the **Fermi bubbles** [45].

Galactic cosmic ray electrons

Knowledge of the non-thermal electron distribution is critical in the modelling of Galactic magnetic fields, which are both required inputs for the determination of synthetic synchrotron maps. At energies below 10^{15} eV the CRs might be accelerated via Fermi shock acceleration which usually takes place in supernova remnants. In the Fermi shock acceleration model, the acceleration of the charged particle takes place in the shocks of collision-less plasma in which particles interact with one another via the magnetic fields. The particle undergoes acceleration between the upstream and downstream regions of the shock thereby enhancing its energy to the point that the particle ends up leaving the shock front because the particle becomes too energetic.

The indirect evidence of acceleration of these particles can be seen in several astrophysical sources. For example observations of supernova remnants show emission that can be associated to synchrotron radiation. This can be accompanied by either inverse Compton scattering on photons assuming leptonic processes or proton-proton interaction if hadronic processes are assumed. However, the information about the sources/accelerators of CRs become less clear for higher energies. Note that synchrotron radiation occurs at lower

[†] Diffuse gamma-ray emission occurs due to proton-proton collision which results in pion-decay which in turn results in gamma rays.

energies at radio and x-rays frequencies whereas inverse Compton scattering and proton-proton collision will occur at higher energies with very high energy gamma rays being its signature.

There are direct measurements of non-thermal electron distribution around earth made by CR detectors like AMS[105], DAMPE [106] and CALET [107] to name a few. Conversely, indirect methods have to be called upon to study the spatial distribution of CRs within our Galaxy including the Galactic halo. However, information on electron distribution in the Galaxy is still unknown. Currently, there are a few ways to model the spatial distribution of these relativistic electrons; for example, either on theoretical grounds using the GALPROP diffusive transport code ([108, 109]) or on more phenomenological grounds as done in the WMAP data analysis ([67]). Non-thermal particles in particular electrons will be further discussed in Chapter 2.

1.9 Focus of this thesis

The work carried out during my PhD focuses primarily on the study of magnetic fields and the propagation of ultra-high energy cosmic rays in the Galactic Halo Bubbles (GHB) region of the Galaxy, motivated in Section 1.4. The work I have done during this thesis has been divided into three main chapters. The focus of each chapter is listed below:

1. Chapter 2 - introduces a new toy model for the magnetic fields and non-thermal electron distribution in the Galactic halo bubble region. The toy model was used to produce synthetic polarised synchrotron emission skymaps, which were then compared using chi-squared analysis with Planck 30 GHz polarised synchrotron observations. The resulting constraints were noted and compared with existing literature.
2. Chapter 3 - focuses on the propagation of UHECRs through the toy model proposed in the previous chapter. The constraints obtained in Chapter 2 were used to generate three versions of the toy model for the upper-bound, lower-bound and best-fit parameter sets. UHECRs were backtracked through the three versions of the toy model and the magnification maps and arrival direction skymaps for two potential sources, Centaurus A and NGC 253, were examined. The maps obtained were qualitatively compared with the UHECR arrival direction skymaps from the Pierre Auger Observatory and the deductions noted.
3. Chapter 4 - examines the propagation of UHECRs with an extra-galactic dipole through the turbulent magnetic fields of the toy model. The suppression of the

extragalactic dipole during its propagation by the changing turbulent fields or diffusion coefficients is a result of solving the transport equation. An analogous problem to this is also seen in electrostatics and comparisons were drawn between the cosmic ray and the electrostatic problem. The numerical simulations and the electrostatic analogy were found to be in agreement. Furthermore, the results of this study were found to be compatible with the existing literature.

In Chapter 5, a final set of conclusions and the future development of each topic investigated in this thesis have been provided.

Author's note: the work I will present in Chapters 2, 3 and 4 was carried out by me throughout the course of my PhD under the supervision of my supervisors. Any external pieces of software or codes that were utilised have been mentioned at necessary places throughout the text.

Modelling and constraining magnetic fields in Galactic halo bubbles

2

One of the unresolved problems in astrophysics is the origin and structure of the Galactic magnetic field (GMF) in the Milky Way. Even though GMFs play an important role in a Galaxy, our understanding of them is limited. Galactic magnetic field can be broadly divided into Galactic disc magnetic fields and Galactic halo magnetic fields. Between

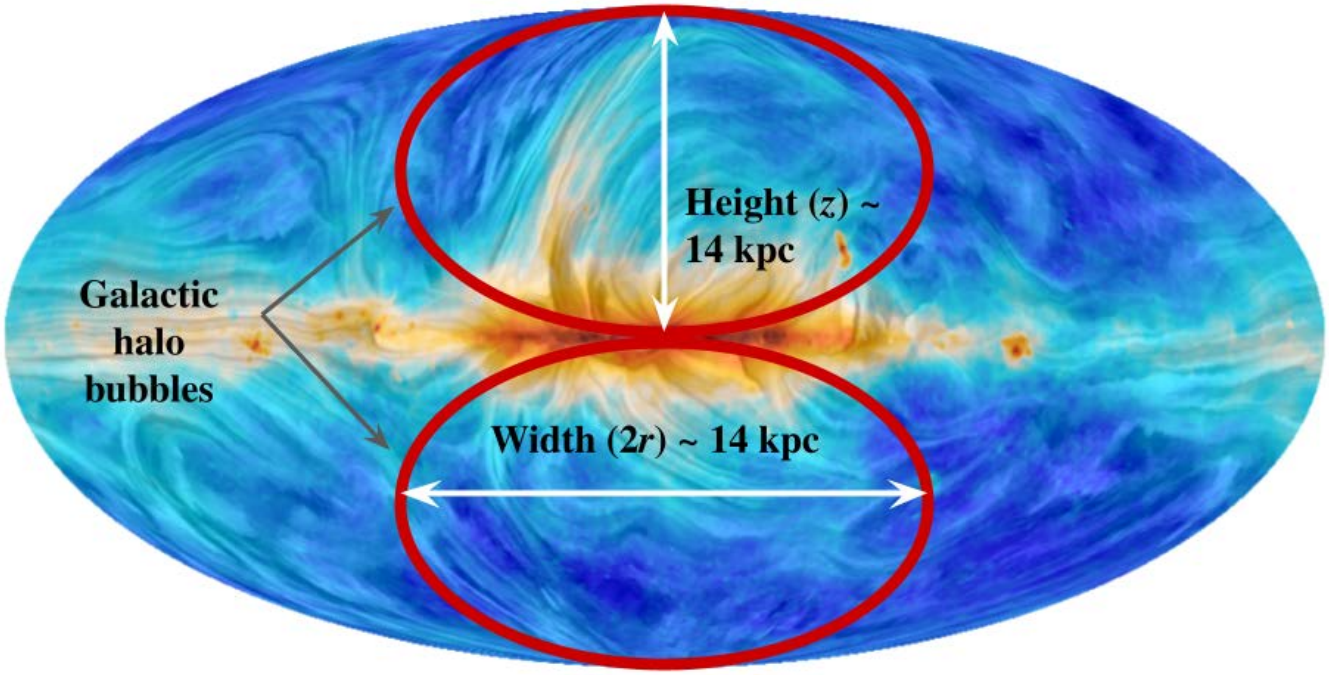

Figure 2.1: The Planck 30 GHz skymap with the magnetic field contours and a schematic representation of the Galactic halo bubbles [45, 50, 110, 111].

these two components of the Galactic magnetic field, the magnetic fields in the Galactic disc are comparatively more data rich than the Galactic halo [2, 5, 56], thus leading to the Galactic halo being less constrained. As mentioned in Chapter 1, Section 1.3.2, during the last decade the Galactic halo has been revealed in different frequency regimes, namely by Fermi [45], S-PASS [4] and eROSITA [50] observations in gamma, radio and X-ray respectively. This chapter introduces **a new toy model of the magnetic fields and non-thermal electron distribution for the Galactic halo bubbles which was developed as a part of this thesis**. This will be followed by comparing polarised synchrotron emission with the Planck 30 GHz skymap and a discussion about current models that look into the Galactic halo. A schematic representation of the region of the sky covered by the GHB toy model in presented in Figure 2.1.

2.1 Galactic halo bubbles toy model

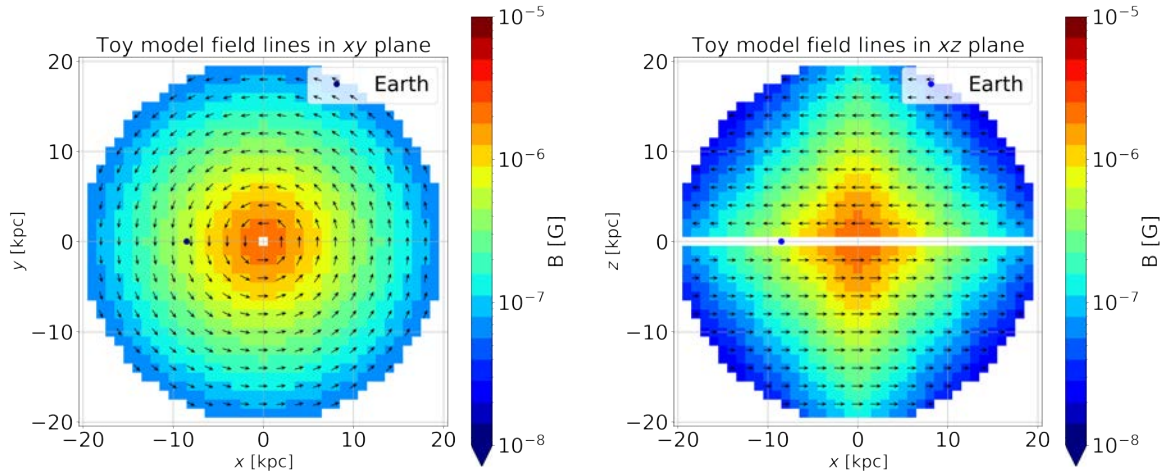

Figure 2.2: Cross-section of GHB model for the Galactic magnetic field in the Galactic halo region in the XY (for z = 1 kpc) and XZ (for y = 1 kpc) plane (with the Galactic plane in the XY plane at z = 0) showing their drop in two dimensions. The plot was made from the best-fit value of the GHB model discussed in detail in Section 2.4.4 for $B_{\rm str} \approx 4\ \mu$G , $R_{\rm mag}$ = 5 kpc and $Z_{\rm mag}$ = 6 kpc (see table 4.1).

In this section, a simple GHB toy model, henceforth called the GHB model is proposed that includes the magnetic field (both structured and turbulent) and a distribution of non-thermal electrons.

2.1.1 GHB model - Structured Fields

The structured or large-scale magnetic field adopted in the GHB model is axisymmetric and toroidal in nature with fields pointing in opposite directions above and below the Galactic plane. The strength of the structured fields is given by the following expression:

$$B_{\rm tor}(r,z) = B_{\rm str} e^{(-|z|/Z_{\rm mag})} e^{(-z_{\rm min}/|z|)} e^{(-|r|/R_{\rm mag})}, \tag{2.1}$$

here, r and z are the radial and azimuthal positions where the strength $B_{\rm tor}$ is measured. The three parameters in the structured model are:

1. $B_{\rm str}$**-** the mean strength of the structured or large-scale magnetic field,
2. $R_{\rm mag}$**-** the radial cut-off distance for the structured fields,
3. $Z_{\rm mag}$**-** the azimuthal cut-off distance for the structured fields.

The model spans radially up to 14 kpc centred at the Galactic center (GC) at (0,0,0). A visualisation of the GHB structured magnetic field in the xy and xz cross-sections is shown in Figure 2.2. Note: the exponential profile for the magnetic fields in the GHB might not be the right prescription based on observational evidences suggesting a larger extended halo both in the Milky Way and other external galaxies [42, 52]. This will be discussed in more detail in Section 2.5.

2.1.2 GHB model - Turbulent Fields

Any magnetic field model for the Galaxy is incomplete without its turbulent components which are small-scale fluctuations in nature and have randomly oriented direction vectors. This type of field is particularly difficult to constrain due to the lack of observational probing techniques. The observational difficulty of constraining turbulent magnetic fields will be discussed in further detail in Section 2.4.1. Turbulent motion results from currents of different scale sizes. A turbulent field can be modelled as a superposition of multiple plane waves or Fourier modes. The energy density of the field can be given by a proportionality relation:

$$\frac{\mathrm{d}\delta B^2}{\delta k} = \frac{B_{\mathrm{tur}}^2}{k_{\mathrm{min}}}\left(\frac{k}{k_{\mathrm{min}}}\right)^{-\gamma}$$

here k is the wave number given by $k = 2\pi/L$ with L being the wavelength and B_{tur} is the root-mean-square value. Assuming that the wavelength of the turbulent field is constrained between the limit $k_{\mathrm{min}} < k < k_{\mathrm{max}}$ (that is scale sizes $L_{\mathrm{min}} < L < L_{\mathrm{max}}$), γ is the turbulence cascade index. The integrated energy density in the turbulent field can be written as:

$$\delta B^2 = \int_{L_{\mathrm{min}}}^{L_{\mathrm{max}}} \frac{\mathrm{d}\delta B^2}{\mathrm{d}L}\mathrm{d}L = \frac{B_{\mathrm{tur}}^2}{L_{\mathrm{max}}}\int_{L_{\mathrm{min}}}^{L_{\mathrm{max}}}\left(\frac{L}{L_{\mathrm{max}}}\right)^{\gamma-2} dL \tag{2.2}$$

$$\delta B^2 = \frac{B_{\mathrm{tur}}^2}{\gamma - 1}\left[1 - \left(\frac{L_{\mathrm{min}}}{L_{\mathrm{max}}}\right)^{\gamma-1}\right] \tag{2.3}$$

Usually (for typical values of γ, considered) this integral is insensitive to L_{min} , being dominated by the longest mode values, so where one truncates the lower end of the integral has only a small effect. The artificial enhancement of B_{tur}^2 due to the truncation that was adopted is $[1 - (1/2)^{\gamma-1}]^{-1}$, which for $\gamma = 5/3$ is 2.7, corresponding to B_{tur} being artificially enhanced by ~60% due to the early truncation of the turbulent spectrum adopted [112].

Then for an isotropic homogeneous magnetic field, coherence length ($L_{\rm coh}$) can then be defined as with the integral being dominated by $k_{\rm min}$ or $L_{\rm max}$:

$$L_{\rm coh} = \frac{\langle L \rangle}{2} = \frac{\int_{L_{\rm min}}^{L_{\rm max}} L \, {\rm d}L \left(\frac{{\rm d}\delta B^2}{{\rm d}L} \right)}{\int_{L_{\rm min}}^{L_{\rm max}} {\rm d}L \left(\frac{{\rm d}\delta B^2}{{\rm d}L} \right)}, \tag{2.4}$$

Coherence length for such a field will be thus given by:

$$L_{\rm coh} = \frac{1}{2} L_{\rm max} \frac{\gamma - 1}{\gamma} \frac{1 - (L_{\rm min}/L_{\rm max})^{\gamma}}{1 - (L_{\rm min}/L_{\rm max})^{(\gamma - 1)}}, \tag{2.5}$$

here, γ is the turbulence cascade index, $L_{\rm max} \propto k_{\rm min}^{-1}$ and $L_{\rm min} \propto k_{\rm max}^{-1}$ minimum and maximum scale sizes of the magnetic eddies with $k = 2\pi/L$. For values of $\gamma \gg 1$ or a narrowband of $L_{\rm min} \sim L_{\rm max}$, correlation length $L_{\rm coh} \simeq L_{\rm max}/2$. For a broad range of values between $L_{\rm min}$ and $L_{\rm max}$ such that $L_{\rm min} \ll L_{\rm max}$, then $L_{\rm coh} \simeq L_{\rm max}/5$ for Kolmogorov spectrum or $L_{\rm coh} \simeq L_{\rm max}/6$ for a Kraichan spectrum [113].

To keep the problem simple, a 5/3 Kolmogorov power law spectrum with an RMS value of $B_{\rm tur}$ as the only free parameter was used. These magnetic fields were generated using CRPropa 3* ([89, 90]). For computational reasons the dynamic range of the wavelength of the turbulent fields (that is the values of minimum and maximum wavelengths) was restricted to $L_{\rm min} = 200$ pc and $L_{\rm max} = 400$ pc. This narrow range of the wavelength is similar to what was adopted by [112]. For the fixed values of $L_{\rm min} = 200$ pc and $L_{\rm max} = 400$ pc and $\gamma = 5/3$, the $L_{\rm coh} = 148$ pc from Eq. 3.9. This value was fixed for all simulations carried out for this and the next chapter. This value, although very large, does sit in the range of values considered ([41, 114–117]).

Several realisations of the turbulent fields were investigated, a few of which are shown in Figure 2.3. These realisations were discarded since in all the power spectra (or the energy density B^2) one or more modes (in the x, y, z directions) did not follow the Kolmogorov 5/3 spectrum. For these plots the power spectrum is plotted in x, y and z directions, after averaging over the other two directions. The step size of 1 pc was chosen and integrated up to $\approx 9 \times 10^4$ pc.

The turbulent fields in the GHB model extend only out to 14 kpc radially from the Galactic center, chosen to encompass the Galactic bubble region reported in [50]. After exploration with different seed values, the realisation which closely followed a power-law spectrum

* **Note:** In Chapter 3 an in depth discussion over CRPropa3 has been presented.

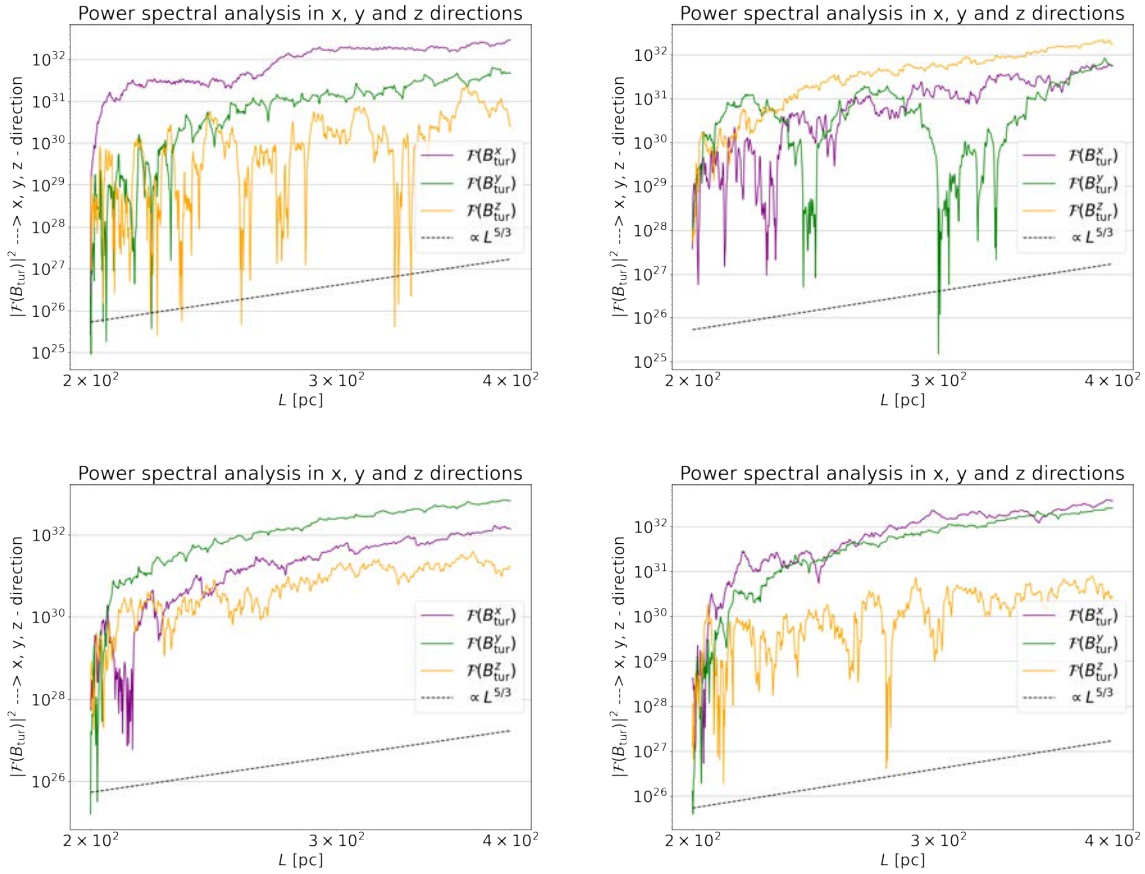

Figure 2.3: The figures above show the energy density in the turbulent magnetic fields with the same value so of $L_{min} = 200$ pc, $L_{max} = 400$ pc, $L_{coh} = 150$ pc but different seeds (chosen arbitrarily). The x axis shows the wavelength of the field and y axis the turbulent field energy density. Realisations like these of the turbulent field were discarded since power spectra do not seem to follow the 5/3 Kolmogorov spectrum in one or more modes in x, y and z direction implying the existence of anisotropic turbulent magnetic fields.

of index 5/3, with a similar amount of power in each direction (that is, was reasonably isotropic) was utilised and is shown in Figure 2.4.

2.1.3 GHB model : Non-thermal electron distribution

In order to calculate synthetic synchrotron maps, both a non-thermal electron distribution and a magnetic field model are required. The current magnetic field models like the JF12 [35] model considered both the WMAP analytical expression [67] and simulated electron distribution model from the GALPROP [108, 118] model as non-thermal electron distribution' utilising the latter. The WMAP [67] model is an analytical expression whereas the GALPROP model is a software based model, obtained from a solution to the diffusive transport equation assuming a specific spatial distribution for the sources and for which no large Galactic halo is considered to exist. Since the distribution of Galactic cosmic

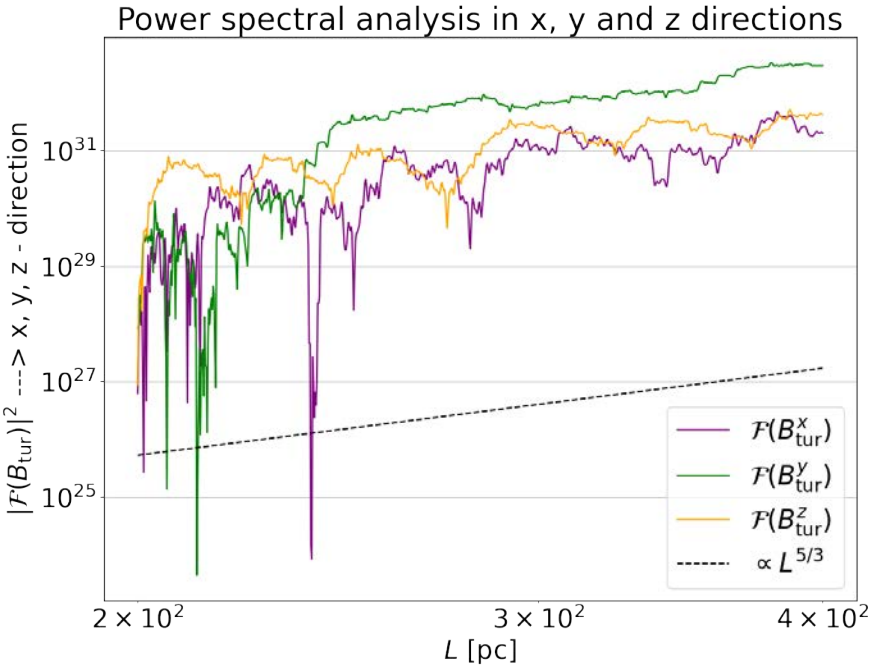

Figure 2.4: Power spectra of turbulent magnetic fields, evaluated along three orthogonal directions, namely the x, y and z directions. Though this realisation has significant fluctuations at lower value of λ the 5/3 Kolmogorov spectrum seems to be in agreement for all 3 modes at $\lambda \geq 230 - 250$ pc.

rays within our galaxy still largely remains a mystery, a simple analytical distribution of Galactic cosmic ray electrons[†] was adopted to avoid further layers of complexity.

The WMAP electron density distribution model that was adopted has the form:

$$\frac{\mathrm{d}n_\mathrm{e}}{\mathrm{dlog}E_\mathrm{e}} = C_\mathrm{norm} \left(\frac{E_\mathrm{e}}{\mathrm{E}_{10\ \mathrm{GeV}}} \right)^{-p+1} e^{-r/R_\mathrm{el}} \mathrm{sech}^2 \left(\frac{z}{Z_\mathrm{el}} \right), \tag{2.6}$$

where $\frac{\mathrm{d}n_\mathrm{e}}{\mathrm{dlog}E_\mathrm{e}}$ is the differential electron density in logarithmic energy bins, in units of cm^{-3}, and $p = 3$ is the spectral index of the electron spectrum. The parameter C_norm, describes the electron density for electrons with an energy of 10 GeV, and R_el & Z_el describe the radial and azimuthal spatial cut-offs. For reference, in Figure 2.5 spatial distribution of the electron density both in logarithmic (left) and linear (right) spaces have been shown.

[†] The words Galactic cosmic ray electrons and non-thermal electrons will be used interchangeably throughout this text.

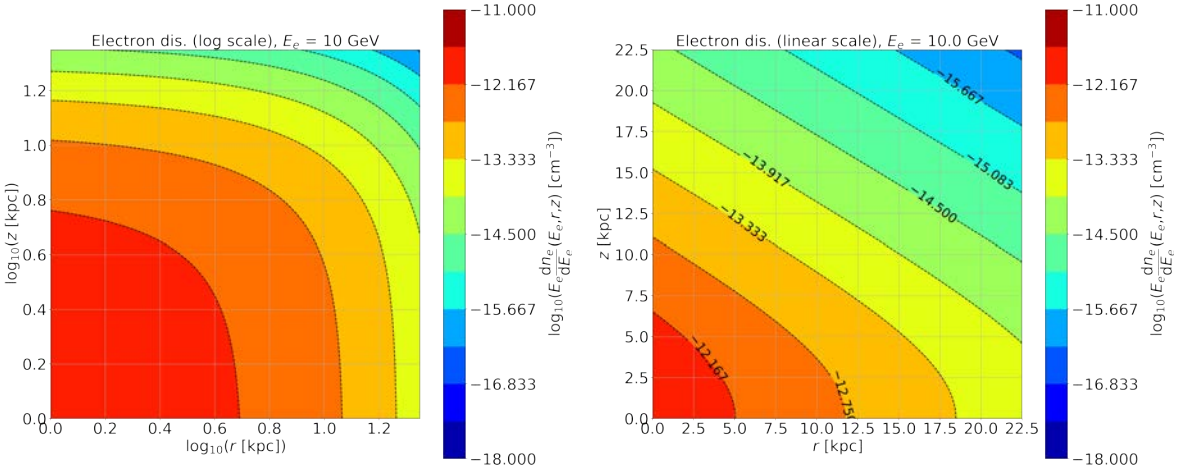

Figure 2.5: An example of the electron distribution in log (left) and linear (right) scale for an electron energy of E_e of 10 GeV, R_{el} = 5 kpc and Z_{el} = 7 kpc in log-scale on right. C_{norm} value for this plot is $10^{-12.43}$ cm^{-3} (see table 4.1).

2.2 Magnetic field tracer - Synchrotron radiation

Synchrotron radiation or magneto-bremsstrahlung radiation is the radiation produced due to charged particles that gyrate at relativistic speeds around a static magnetic field. It is analogous to cyclotron radiation in which the charged particles spiral around the magnetic field at non-relativistic speeds.

2.2.1 Synchrotron radiation - total intensity

Charged particles (say electrons) traversing through magnetic fields at relativistic speeds ($v \to c$) are subject to gyration by virtue of the Lorentz force given by:

$$\frac{\mathrm{d}\vec{\beta}}{\mathrm{c\,d}t} = \frac{1}{r_\mathrm{L}}\vec{\beta} \times \hat{B} \tag{2.7}$$

here, c is the velocity of light, $\vec{\beta}$ is the vector denoting particle velocity and $\hat{B}$ is the total magnetic field as unit vector respectively, Ze is the charge of the electron, m_e is the mass of the electron, Γ_e is the Lorentz factor.

For a magnetic field strength B, r_L is the particle's Larmor radius, defined by Eq. 1.8 in Section 1.6 in Chapter 1. The electron gyrates along this magnetic field line at a constant pitch angle θ and constant velocity with its gyro-frequency given by : $\nu_g = \frac{\mathrm{e}B}{2\pi\, m_\mathrm{e}\, \Gamma_\mathrm{e}}$, where

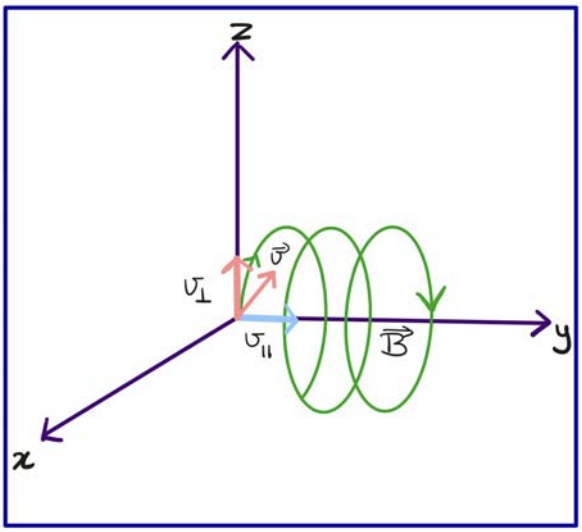

Figure 2.6: An electron gyrating along magnetic field line $\vec{B}$ with the velocity vector $\vec{v}$ decomposed as $v_\perp$ and $v_\parallel$. The electron traces a helical path as it traverses around the magnetic field.

$m_e c^2 = 0.511$ MeV is the rest-mass energy of the electron and Γ_e is the electron Lorentz factor.

The number flux of synchrotron emission from a mono-energetic electron distribution ($E_\gamma \frac{dN_\gamma}{dE_\gamma dt}$) in a uniform magnetic field [119] can be written as :

$$E_\gamma \frac{dN_\gamma}{dE_\gamma dt} = \underbrace{\frac{\sqrt{3}\alpha}{2\pi} \frac{m_e}{\hbar} \frac{B_\perp}{B_{crit}}}_{\tau^{-1}} F\left(\frac{E_\gamma}{E_\gamma^{peak}}\right), \tag{2.8}$$

where the photon energy peaks at $E_\gamma^{peak} = \frac{3}{2}\Gamma_e^2 \frac{B_\perp}{B_{crit}} m_e$ and $B_{crit} = \frac{m_e^2 c^3}{e\hbar} = 4.414 \times 10^{13}$ G is the maximum or critical magnetic field existing in astrophysical systems, e.g.,: neutron stars, τ^{-1} being the timescale in terms of units, $h = 4.136 \times 10^{-15}$ eV s is Planck's constant and $\hbar = h/2\pi$, and $\alpha \approx \frac{1}{137}$ is the electromagnetic fine structure constant.

$F(x) = x \int_x^\infty K_{5/3}(z) dz$‡ with Bessel function $K_{5/3}$ that describes the shape of the photon spectrum [120]. Eq. 2.8 can be expressed as the energy-loss rate by:

$$\frac{dE_e}{dt} = \int_0^\infty dE_\gamma E_\gamma \frac{dN_\gamma}{dE_\gamma dt}, \tag{2.9}$$

‡ Setting $\mu = 0$, $\int_0^\infty F(x)dx = \Gamma\left(\frac{7}{3}\right)\Gamma\left(\frac{2}{3}\right) = 1.62$ by use of the recurrence relations for Γ-functions by Abramovitz and Stegun (1965).

which gives,

$$\frac{\mathrm{d}E_\mathrm{e}}{\mathrm{d}t} = E_\gamma^\mathrm{peak}\,\frac{\sqrt{3}\alpha}{2\pi}\frac{m_\mathrm{e}}{\hbar}\frac{B_\perp}{B_\mathrm{crit}}\int_0^\infty \underbrace{F\left(\frac{E_\gamma}{E_\gamma^\mathrm{peak}}\right)}_{\frac{8\pi}{9\sqrt{3}}}\mathrm{d}E_\gamma\,. \tag{2.10}$$

Inserting the value of E_γ^peak in the above equation gives:

$$\frac{\mathrm{d}E_\mathrm{e}}{\mathrm{d}t} = \frac{8\pi\alpha}{9}\frac{E_\mathrm{e}^2}{h}\left(\frac{B_\perp}{B_\mathrm{crit}}\right)^2\frac{3}{2}. \tag{2.11}$$

Note, that the above formula is consistent with standard literature [119, 120] when considering an average over all pitch angles $B_\perp^2 = \frac{2}{3}B^2$, ($B_\perp = B\sin\theta$). Once the pitch angle averaging is included in the calculation, the energy loss rate can be expressed as:

$$\frac{\mathrm{d}E_\mathrm{e}}{\mathrm{d}t} = \frac{8\pi\alpha}{9}\frac{E_\mathrm{e}^2}{h}\left(\frac{B}{B_\mathrm{crit}}\right)^2. \tag{2.12}$$

The cooling time τ_e, which is the time taken by electrons producing synchrotron radiation to cool down by 1 E_e fold is given by [121]:

$$\tau_e = \frac{E_\mathrm{e}}{\mathrm{d}E_\mathrm{e}/\mathrm{d}t} \tag{2.13}$$

$$= \frac{9}{8\pi\alpha}\left(\frac{B_\mathrm{crit}}{B_\perp}\right)^2\frac{h}{E_\mathrm{e}}. \tag{2.14}$$

The above equations can be used to calculate the total synchrotron emission (I) obtained by a distribution of electrons (e.g.: power law) $\frac{\mathrm{d}n_\mathrm{e}}{\mathrm{dlog}E_\mathrm{e}}$ see Eq. 2.6 (with n_e being the number density) as:

$$I = \int_{\log E_\mathrm{e}^\mathrm{min}}^{\log E_\mathrm{e}^\mathrm{max}} \mathrm{dlog}E_e\,\frac{\mathrm{d}n_\mathrm{e}}{\mathrm{dlog}E_\mathrm{e}}\int_{E_\gamma^{min}}^{E_\gamma^{max}}\mathrm{dlog}E_\gamma E_\gamma\frac{\mathrm{d}N_\gamma}{\mathrm{d}E_\gamma\mathrm{d}t}. \tag{2.15}$$

2.2.2 Emission from a single line of sight

The aim of this section is to provide an analytical estimate for synchrotron emission which could provide a useful insight in the expected synchrotron emission from a region of the sky. For similar magnetic field strengths and electron distribution the value obtained from this analytical estimate should be approximately of the same order of magnitude

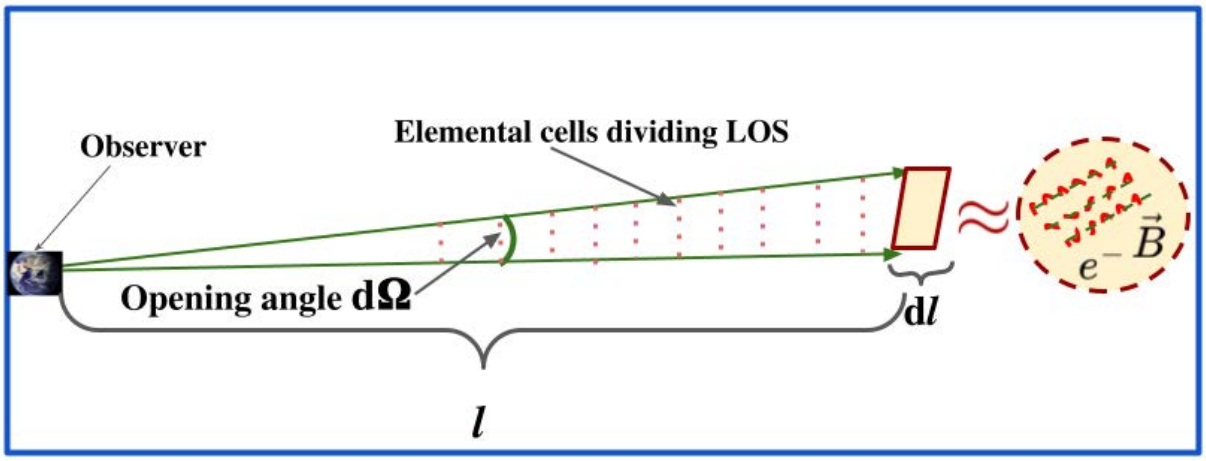

Figure 2.7: A schematic representation of calculating emission from individual cells (in pink) from a large synchrotron emitting region shown as a rectangular cell (approximated to an emitting blob) with the opening angle of dΩ.

obtained from the skymap. Thus, the analytical estimate acts as a helpful cross-check for the skymaps calculated later on in this chapter.

In reality non-thermal synchrotron emission occurs from sources at large distances. This can be understood from the cartoon representation of synchrotron emission in an astrophysical environment shown in Figure 2.7. Assuming that all synchrotron emission occurs isotropically from an emitting surface, there exists a line of sight along which the synchrotron emission can be observed. The observer sits at a distance l from the emitting surface (Figure 2.7) with a viewing solid angel dΩ. The goal is to estimate the entire emission of a volume along a line of sight. This can be done by dividing this cone into smaller cells with distance dl between them that is integrated over later. One can approximate one cell as a single blob, that is homogeneously filled with a number of electrons that isotropically emit synchrotron radiation.

For an electron with the energy of approximately $E_\mathrm{e} \approx 30$ GeV and a magnetic field of $B \approx 3\ \mu$G, the synchrotron power emitted by one electron will be given by:

$$\frac{\mathrm{d}E_\mathrm{e}}{\mathrm{d}t} = \frac{8\pi\alpha}{9}\frac{E_\mathrm{e}^2}{h}\left(\frac{B}{B_\mathrm{crit}}\right)^2 = 3\times10^5\ \mathrm{eV/s}. \tag{2.16}$$

The total power/luminosity L within a given solid angle dΩ of the sky can then be approximated by the power of a single electron multiplied with the number of radiating electrons. One can estimate this number by the product of a constant CR density, $E_\mathrm{e}\frac{\mathrm{d}n_\mathrm{e}}{\mathrm{d}E_\mathrm{e}} \approx 5\times10^{-14}\mathrm{cm}^{-3}$, with the volume of a cell $\frac{\mathrm{d}V}{\mathrm{d}\Omega}$ per solid angle on the sky. It is given by:

$$\frac{\mathrm{d}L}{\mathrm{d}\Omega} = \frac{\mathrm{d}E_\mathrm{e}}{\mathrm{d}t}\, E_\mathrm{e}\, \frac{\mathrm{d}n_\mathrm{e}}{\mathrm{d}E_\mathrm{e}}\, \frac{\mathrm{d}V}{\mathrm{d}\Omega}. \tag{2.17}$$

In this example the thickness of the cell at distance $l = 1$ kpc is fixed arbitrarily and $\mathrm{d}l = 0.1$ kpc. It is noted that for a constant density assumption the total emission of the cone will be dominated by the outermost shell, given the spherical growth of the volume with the second power of l, $\frac{\mathrm{d}V}{\mathrm{d}\Omega} = l^2 \mathrm{d}l$. This yields:

$$\frac{\mathrm{d}L}{\mathrm{d}\Omega} \approx 5 \times 10^{45}\ \mathrm{eV\ s^{-1} sr^{-1}}. \tag{2.18}$$

In order to obtain the number instead of the power, both per time and solid angle $\frac{\mathrm{d}L}{\mathrm{d}\Omega}$ is divided by the average energy of the synchrotron photons $E_\gamma \approx \Gamma_\mathrm{e}^2 \frac{B_\perp}{B_\mathrm{crit}} m_e \approx 2 \times 10^{-4}$ eV.

Thus, the number of photons emitting this luminosity per solid angle can be given by:

$$\frac{\mathrm{d}N_\gamma}{\mathrm{d}t\mathrm{d}\Omega} = \frac{\mathrm{d}L}{\mathrm{d}\Omega}\, \frac{1}{E_\gamma} \approx 3 \times 10^{49}\ \mathrm{s^{-1} sr^{-1}}$$

here, N_γ is the number of photons emitted.

Assuming that this rate of photon emission is emitted isotropically by the cell into the surface $A = 4\pi l^2$, a detector at distance l measures a brightness of $\frac{\mathrm{d}N_\gamma}{\mathrm{d}t\mathrm{d}\Omega\mathrm{d}A}$ which is given by:

$$\frac{\mathrm{d}N_\gamma}{\mathrm{d}t\mathrm{d}\Omega\mathrm{d}A} = \frac{\mathrm{d}N_\gamma}{\mathrm{d}t\mathrm{d}\Omega}\, \frac{1}{4\pi l^2} \approx 2 \times 10^{5}\ \mathrm{cm^{-2} s^{-1} sr^{-1}}$$

This value of brightness was cross-checked with simulations for estimating synchrotron brightness from a single cell (for the same distance of $l = 1$ kpc, $\mathrm{d}l = 0.1$ kpc) for the same fixed magnetic field and non-thermal and electron distribution and the results from the simulation were found to be similar to the theoretically expected value.

2.2.3 Synchrotron Polarisation-theory

The expression given by Eq. 2.15 only focusses on the total intensity of synchrotron radiation. In principal one can observe polarised synchrotron radiation at low frequencies.

Westfold states in his 1959 paper [120] that any radiation connected to magnetic fields would exhibit polarisation of some sort. One of the conclusion from this paper was that the acceleration vectors of the electrons emitting synchrotron radiation change constantly due to the gyration of the electrons along the magnetic field which results in the elliptical

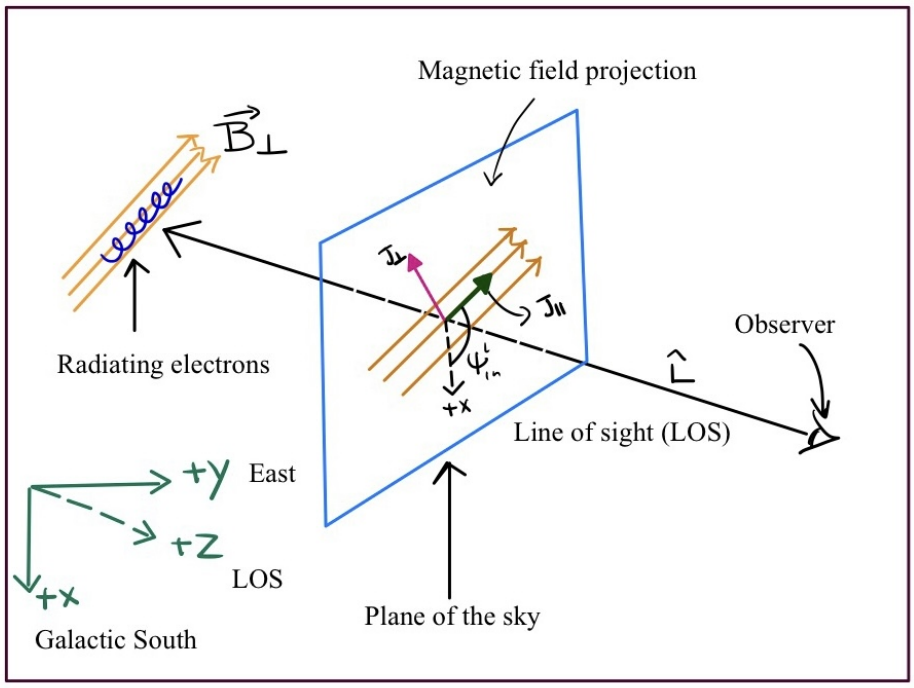

Figure 2.8: A sketch of the magnetic field projection. The emission happens in two directions, one is parallel to the line-of-sight perpendicular ($B_\perp$) magnetic field and the other is perpendicular to the magnetic field. $J_\parallel$ is lying parallel to the magnetic field and $J_\perp$ is perpendicular to it. The coordinate system adopted from Planck [122] is shown in green, the polarisation angle $\Psi^l_{\rm in}$ is measured from the Galactic south (+X) at each point along the line-of-sight.

polarisation of the radiation received from a single electron. The sense of polarisation (right or left-handed) is determined by whether the line of sight sits inside or outside the cone of radiation. However, for a distribution of particles that vary smoothly with the pitch angle, the elliptical component cancels out and so the emission cones will contribute equally on each side of the line of sight. The radiation is then linearly polarised [119]. The polarised radiation can then be decomposed into two states, the perpendicular ($J_\perp$) and the parallel ($J_\parallel$) state of polarisation. In Figure 2.9, the functional shape of the two components $J_\perp$ and $J_\parallel$ show the photon spectrum from a mono-energetic electron.

Below are expressions of the polarised components of radiation for both perpendicular and parallel polarisation states (for a power law electron distribution) at each point along the line of sight. The direction $J_\parallel$ is parallel to the direction of magnetic field $\vec{B}_\perp$ and direction $J_\perp$ is perpendicular to the magnetic field $\vec{B}_\perp$. Here, only the magnitudes of the parallel and perpendicular states at each point along the line of sight are given:

The expressions Eq. 2.19 and Eq. 2.20 are provided in terms of the critical magnetic field strength, $B_{\rm crit} = \frac{m_e^2 c^3}{e\hbar} = 4.414 \times 10^{13}$ G, where $m_e c^2 = 0.511$ MeV is the rest-mass energy of

the electron, $h = 4.136 \times 10^{-15}$ eV s is Planck's constant and $\hbar = h/2\pi$, Γ_e is the electron Lorentz factor and $\alpha \approx \frac{1}{137}$ is the electromagnetic fine structure constant.

$$J_{\perp}^{l} = \frac{1}{\tau} \int_{\log E_{\rm e}^{\rm min}}^{\log E_{\rm e}^{\rm max}} {\rm d}\log E_e \, \frac{{\rm d}n_{\rm e}}{{\rm d}\log E_e} \left[F\left(\frac{E_\gamma}{E_\gamma^{\rm peak}}\right) + G\left(\frac{E_\gamma}{E_\gamma^{\rm peak}}\right) \right], \tag{2.19}$$

and

$$J_{\parallel}^{l} = \frac{1}{\tau} \int_{\log E_{\rm e}^{\rm min}}^{\log E_{\rm e}^{\rm max}} {\rm d}\log E_e \, \frac{{\rm d}n_{\rm e}}{{\rm d}\log E_e} \left[F\left(\frac{E_\gamma}{E_\gamma^{\rm peak}}\right) - G\left(\frac{E_\gamma}{E_\gamma^{\rm peak}}\right) \right], \tag{2.20}$$

where

$$\tau^{-1} = \frac{\sqrt{3}\alpha}{4\pi} \frac{B_\perp}{B_{\rm crit}} \frac{m_e c^2}{\hbar}, \qquad E_\gamma^{\rm peak} = \frac{3}{2}\Gamma_e^2 \frac{B_\perp}{B_{\rm crit}} m_e c^2,$$

and the Bessel functions are,

$$F(x) = x \int_x^\infty K_{5/3}(x')dx' \;\&\; G(x) = xK_{2/3}.$$

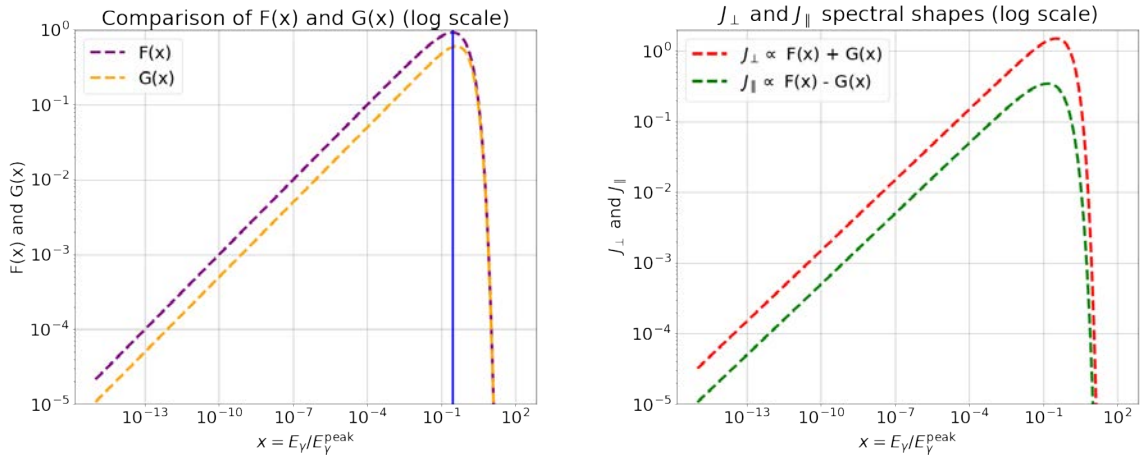

Figure 2.9: Left: the shape of the functions F(x) and G(x) describing the photon spectrum for a mono-energetic electron, the functional form which includes $K_{5/3}$ and $K_{2/3}$ Bessel functions respectively. The blue line marks the peak value of the F(x) function.
Right: the brightness spectra for a single high-energy electron for polarisation in perpendicular and parallel direction as seen in Longair [29] as well. The quantity on the x axis is dimensionless. It is the ratio of the photon energy E_γ and the peak photon energy $E_\gamma^{\rm peak}$.

In Figure 2.9, the spectral shape of the functions F(x) and G(x) which comprises Bessel function $K_{5/3}$ and $K_{2/3}$ respectively has been shown. The blue line in the top figure denotes

the $E_\gamma = E_\gamma^{\rm peak}$. The photon spectrum from a mono-energetic electron in perpendicular and parallel direction to $\vec{B}_\perp$ with functional form of F(x) + G(x) and F(x) - G(x) is shown in Figure 2.9.

In the case of a mono-energetic electron-energy distribution with density n_e, one can calculate the total radiated power density by summing Eq. 2.19 and Eq. 2.20 and integrating over the photon energy distribution:

$$\frac{{\rm d}E_{\rm e}^{\rm tot}}{{\rm d}t} = \frac{2\alpha}{3} n_e \left(\frac{B_\perp}{B_{\rm crit}}\right)^2 \frac{E_e^2}{\hbar}, \tag{2.21}$$

where, the result $\int_0^\infty F(x){\rm d}x = 8\pi/(9\sqrt{3})$ [120] has been used. The above expressions can be used to compute the pitch angle averaged synchrotron cooling time ($\langle B_\perp^2 \rangle = 2/3B^2$) for electrons in this unit system, given by $\tau_c = \frac{E_{\rm e}}{{\rm d}E_{\rm e}/{\rm d}t}$ [121]. Note that the conventions adopted here match those used by the Planck collaboration shown also in Figure 2.10 based on the *Healpix*[§] software by [123, 124].

The next important quantities to consider are the total intensity $I_{\rm tot}$ and the polarised intensity $I_{\rm pol}$.The total intensity integrated along the line of sight can then be defined as:

$$I_{\rm tot} = \frac{1}{4\pi} \int_0^l {\rm d}l (J_\perp^l + J_\parallel^l) \tag{2.22}$$

Here ${\rm d}l = \frac{{\rm d}V}{{\rm d}A} = \frac{{\rm d}\Omega\ {\rm d}l\ l^2}{{\rm d}\Omega\ l^2}$.

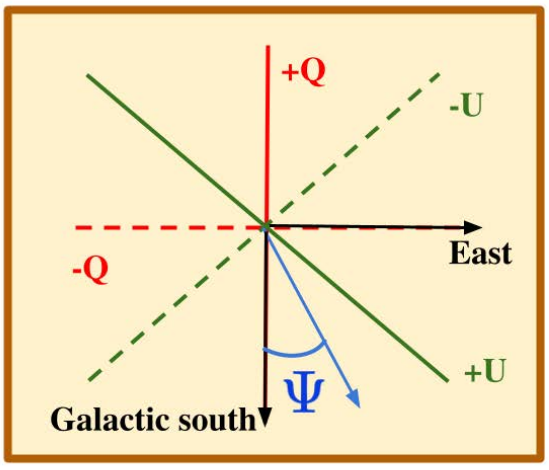

Figure 2.10: The Planck convention is to measure the polarisation angle ψ from the Galactic south. This convention has been adopted for all polarised synchrotron calculations throughout this text.

[§] https://healpix.jpl.nasa.gov/

The Stokes parameters at each point along the line of sight can be written in terms of the intrinsic polarisation angle $\Psi^l_{\rm in}$, which is the angle between the line-of-sight perpendicular component of the magnetic field $B_\perp$ and Galactic south at each step. The reason for choosing the Galactic south is because of the Planck convention as shown in Figure 2.10 (see Planck convention). The Stokes parameters at each point along the line of sight can be written in terms of the angle $\Psi^l_{\rm in}$ which is the angle between the line of sight's perpendicular component of the magnetic field and the Galactic south at each step. The $Q^l_{\rm in}$ and $U^l_{\rm in}$ values will then be:

$$Q^l_{\rm in} = (J^l_\perp - J^l_\parallel)\cos(2\Psi^l_{\rm in}) \tag{2.23}$$

$$U^l_{\rm in} = (J^l_\perp - J^l_\parallel)\sin(2\Psi^l_{\rm in})\ . \tag{2.24}$$

The integrated values along a line of sight can be defined as $Q^{\rm tot}_{\rm in}$ and $U^{\rm tot}_{\rm in}$ as:

$$Q^{\rm tot}_{\rm in} = \frac{1}{4\pi}\int_0^L {\rm d}l\ Q^l_{\rm in}, \tag{2.25}$$

(2.26)

$$U^{\rm tot}_{\rm in} = \frac{1}{4\pi}\int_0^L {\rm d}l\ U^l_{\rm in} \tag{2.27}$$

(2.28)

The polarised flux ($I_{\rm pol}$) can then be expressed as :

$$I_{\rm pol} = \sqrt{Q^{\rm tot2}_{\rm in} + U^{\rm tot2}_{\rm in}}. \tag{2.29}$$

The intrinsic polarisation angle $\Psi_{\rm in}$ is the angle between the Galactic south and the local magnetic field component perpendicular to the line of sight. It can be defined as:

$$\tan(2\Psi_{\rm in}) = \frac{U^{\rm tot}_{\rm in}}{Q^{\rm tot}_{\rm in}}. \tag{2.30}$$

An illustrative understanding of polarised synchrotron emission

One can visualise perpendicular and parallel components of polarised synchrotron emission as an ellipse. The major axis of such an ellipse is the emission in the perpendicular direction, $J_\perp$, and minor axis direction, $J_\parallel$. A good way to develop an intuition for this

concept is to consider some simple test cases. Two tests were done with such ellipses with fixed magnitudes of $J^l_\perp$, $J^l_\parallel$ along line of sight. Different values of $\Psi^l_{\rm in}$ were taken for these cases.

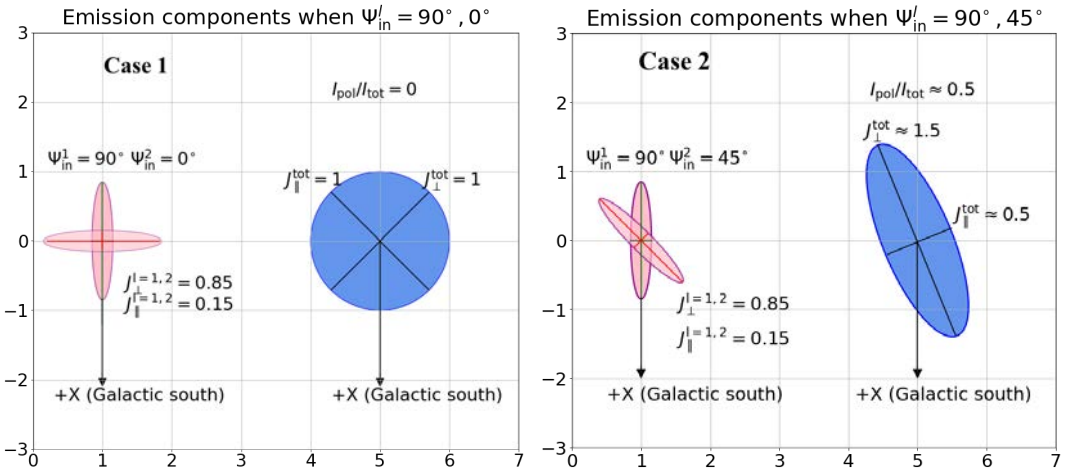

Figure 2.11: Left: ellipses showcasing **case 1** for fixed magnitudes $J^1_\perp = J^2_\perp$ and $J^1_\parallel = J^2_\parallel$ along line of sight with only changing $\Psi^l_{\rm in} = 90°, 0°$ The resulting emission is unpolarised.
Right: ellipses showcasing **case 2**, the emission components when the two ellipses are of the same size but different angles with $\Psi^1_{\rm in} = 90°$ and $\Psi^2_{\rm in} = 45°$. The resulting emission is polarised.

Case 1: in Figure 2.11 was for $\Psi^1_{\rm in} = 0°$ and $\Psi^2_{\rm in} = 90°$, 1 and 2 are denoting steps along the line of sight.

The values of $Q^{\rm tot}_{\rm in} = 0$ and $U^{\rm tot}_{\rm in} = 0$ in both the cases. The resultant value of polarised and total intensities will be:

$$I_{\rm pol} = \sqrt{(Q^{\rm tot}_{\rm in})^2 + (U^{\rm tot}_{\rm in})^2} = 0, \tag{2.31}$$

$$I_{\rm tot} = (J^1_\perp + J^1_\parallel) + (J^2_\perp + J^2_\parallel). \tag{2.32}$$

One can now obtain the resultant values of $J^{\rm tot}_\perp$ and $J^{\rm tot}_\parallel$ which are the resultant magnitudes of emissions in perpendicular and parallel directions:

$$I_{\rm tot} = J^{\rm tot}_\perp + J^{\rm tot}_\parallel, \tag{2.33}$$

$$I_{\rm pol} = J^{\rm tot}_\perp - J^{\rm tot}_\parallel. \tag{2.34}$$

This gives:

$$J^{\rm tot}_\perp = (I_{\rm tot} + I_{\rm pol})/2, \tag{2.35}$$

$$J^{\rm tot}_\parallel = (I_{\rm tot} - I_{\rm pol})/2. \tag{2.36}$$

For case 1 the values of $J_{\perp}^{\mathrm{tot}} = J_{\perp}^{\mathrm{tot}}$ and hence, the resultant intensity distribution is circular (that is the emission is fully unpolarised).

Case 2: similar calculations as the above were done for Figure 2.11 where the values of $J_{\perp}^{l}$ and $J_{\parallel}^{l}$ are fixed, but the intrinsic polarisation angles now are $\Psi_{\mathrm{in}}^{1} = 90°$ and $\Psi_{\mathrm{in}}^{2} = 45°$. Non-zero values are obtained for both $Q_{\mathrm{in}}^{\mathrm{tot}}$ and $U_{\mathrm{in}}^{\mathrm{tot}}$ because of the change of the different values of Ψ_{in}^{l}. This gives partially polarised emission its resultant ellipse (in blue). It will lie in between the red ellipses as shown in the figure. Corresponding to this ellipse the values of $J_{\perp}^{\mathrm{tot}} \approx 1.5$ and $J_{\parallel}^{\mathrm{tot}} \approx 0.5$. The resultant polarisation fraction $I_{\mathrm{pol}}/I_{\mathrm{tot}} \approx 0.5$.

2.2.4 Faraday Rotation

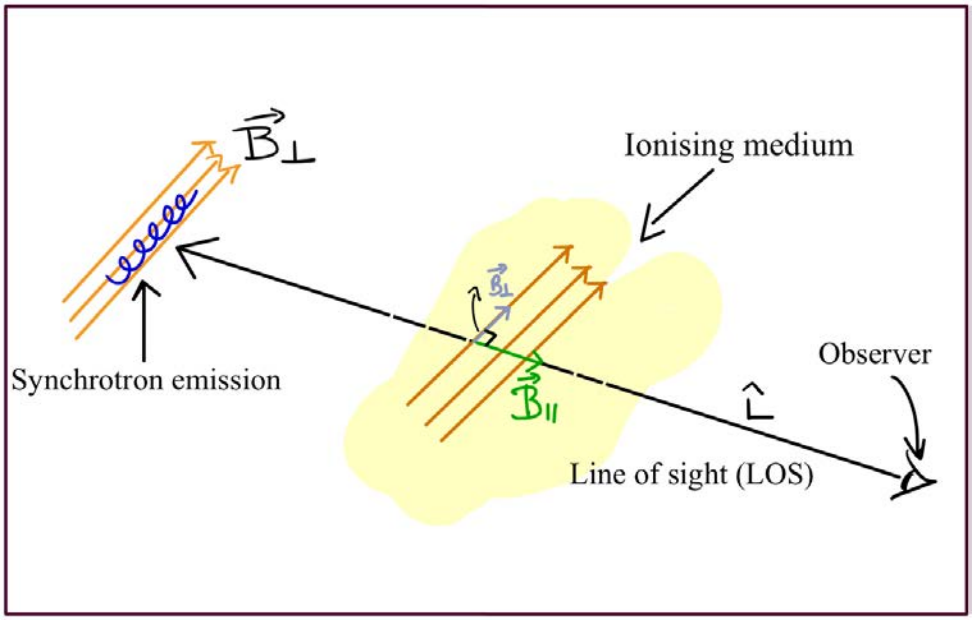

Figure 2.12: Faraday rotation of the polarised synchrotron radiation. Linearly polarised synchrotron radiation undergoes rotation by virtue of Faraday rotation when passing through hot plasma.

This discussion is an extension of Faraday rotation from Chapter 1, Section 1.2.3. It aims to form a link in the previously discussed synchrotron radiation to Faraday rotation. The intrinsic polarisation angle (Ψ_{in}.) of an EM wave gets rotated when passing through a magnetised plasma with thermal electron density n_{th}, thereby resulting in a rotation of the observed polarisation angle (Ψ_{obs}). This phenomenon is called Faraday rotation, it is sensitive to the line-of-sight magnetic field $B_{\parallel}$ which is in contrast to synchrotron radiation that probes the perpendicular component of the line-of-sight magnetic field, $B_{\perp}$ (see Figure 2.12.). The new observed polarisation angle Ψ_{obs}^{l} is integrated over the intrinsic polarisation angle Ψ_{in}^{l} and the rotation at each point along the line-of-sight, l. It

is given by:

$$\Psi^l_{\rm obs} = \Psi^l_{\rm in} + \underbrace{\lambda^2 k_0 \int_0^l {\rm d}l\ n_{\rm e} B_\parallel}_{\Theta_{\rm RM}}, \tag{2.37}$$

with the rotation measure RM given by:

$$RM = \frac{\Theta}{\lambda^2}$$

here, $k_0 = 8.12 \times 10^3$ (in SI units Longair [29]) is a constant. Faraday rotation of the polarised synchrotron radiation also results in altering the Stokes parameters $Q^l_{\rm obs}$ & $U^l_{\rm obs}$ and the new observed values are given by:

$$Q^l_{\rm obs} = (J^l_\perp - J^l_\parallel)\cos(2\Psi^l_{\rm obs}) \tag{2.38}$$

$$U^l_{\rm obs} = (J^l_\perp - J_\parallel{}^l)\sin(2\Psi^l_{\rm obs}) \tag{2.39}$$

This will also change the resultant observed polarised intensity $I^{\rm obs}_{\rm pol}$. Therefore, the new polarised intensity will be given by:

$$I^{\rm obs}_{\rm pol} = \sqrt{(\int_0^L {\rm d}l\ Q^l{}_{\rm obs})^2 + (\int_0^L {\rm d}l\ U^l_{\rm obs})^2}\,. \tag{2.40}$$

These calculations are consistent with the literature [108]. The next useful quantity is the fractional polarisation or degree of linear polarisation (as seen in equation[2.55] in Rybicki and Lightman [119]). The general expression for polarisation fraction Π for a power law distribution of electrons is given by:

$$\Pi = \frac{I^{\rm obs}_{\rm pol}}{I_{\rm tot}} \tag{2.41}$$

If now a uniform magnetic field is considered then the above expression is equivalent to the expression given in Rybicki and Lightman [119]:

$$\Pi = \frac{p+1}{p+7/3} \approx 0.75 \tag{2.42}$$

Here, $p = 3$ is the power law index of the electron distribution. Synchrotron radiation of the electrons in a uniform magnetic field is highly polarised. This implies that theoretically polarisation of synchrotron radiation will always be at a 75% level, though in reality it is

seen from observations that this polarisation fraction is between 15% to 20% [125].

2.3 Test model case

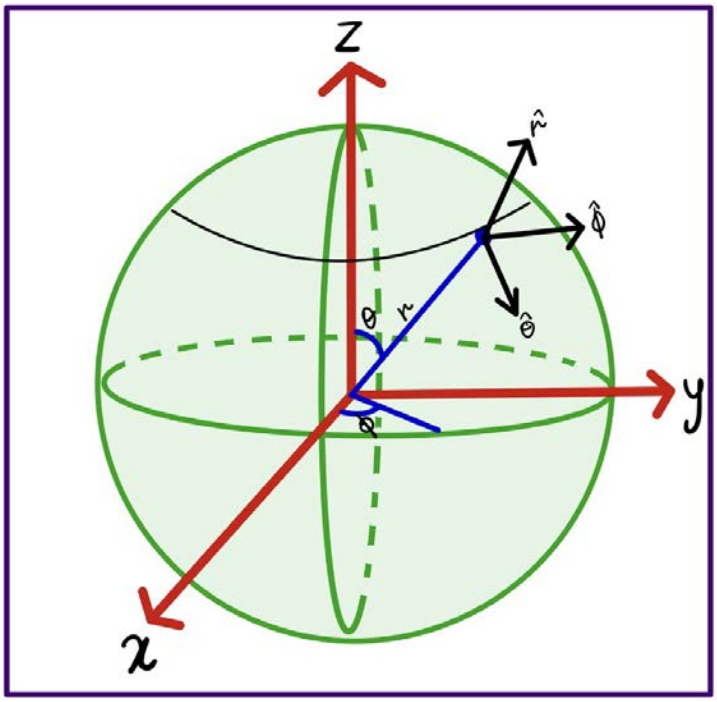

Figure 2.13: Figure above shows the spherical coordinates θ and ϕ and the Cartesian coordinates. The skymaps are made by converting these θ and ϕ in latitude and longitude.

A few tests were carried out on simpler cases of magnetic field configurations before going into the polarised synchrotron emission calculations for the Galactic halo bubble model.

2.3.1 Uniform field orientated in x-direction

A simple case to understand how magnetic field geometries determine synchrotron skymaps can be performed by assuming a uniform magnetic field orientated in a single direction (say the x direction in this case). Since the magnetic field is orientated only along the x direction, and the observer is located on Earth (-8.5,0,0 kpc from the GC), the magnetic field ($\vec{B}$) will be parallel to the line of sight of the observer, with little or no contribution in the perpendicular direction. As mentioned in the previous sections, synchrotron radiation is sensitive to the component of the magnetic field perpendicular to the line of sight, $B_\perp = B \sin \alpha$ (where α is the pitch angle of the synchrotron electron) which

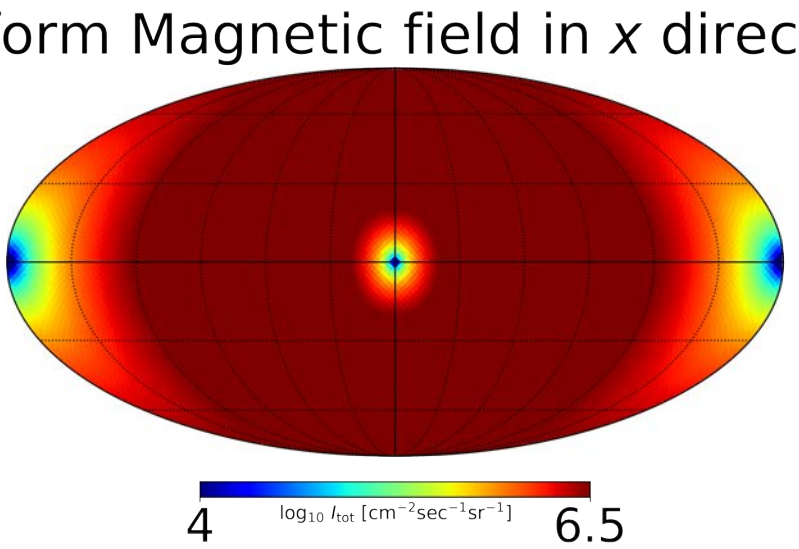

Figure 2.14: The skymap shows the synchrotron emission due to a uniform magnetic field orientated in the x direction. For an observer sitting on Earth (where $[x, y, z]$ = [-8.5,0,0]), the minimum amount of emission is observed when the observer's line of sight is orientated along the x axis. Since synchrotron radiation is sensitive to the magnetic field perpendicular to the line of sight, emission will be lowest in that direction. As the line of sight changes, the brightness of the synchrotron also increases, with maximum brightness seen for cases where the line of sight is orthogonal to the original magnetic field direction.

means that the synchrotron emission is suppressed for $\alpha = 0$. Therefore, theoretically, one would expect synchrotron emission to be strongly suppressed along the x axis, but as the pitch angle α increases, $B_\perp$ also increases, resulting in a skymap with a cold spot around the centre and increasing brightness in the $y - z$ directions. This is also the result of the simulated map in Figure 2.14. In Figure 2.13, the Cartesian x, y and z directions are shown with the spherical coordinates θ and ϕ, the latter two are then converted to latitude and longitude and plotted on skymaps. The magnetic field $\vec{B}$ is parallel to the x axis when the line-of-sight is orientated along the x axis. As a result, the perpendicular component $B_\perp$ is close to zero. This results in very low emission around $l = 0°$ and $b = 0°$. But as one moves away from the centre of the galaxy, the synchrotron emission starts to increase as the strength of $B_\perp$ increases, with the maximum emission for the case of $\alpha \approx 90°$. Thus, the synchrotron emission obtained in such a case gives a sky map with minimum emission at the centre (l = 0° & 180°, b = 0°), with increasing emission radially away from the centre.

2.4 Simulating synthetic polarised synchrotron skymaps and comparison to observations

A synthetic polarised synchrotron emission map was produced for each parameter set for the GHB model. Before going into the details of the simulations carried out to compute the synthetic polarised synchrotron emission, it is useful to discuss the observational data used to compare these synthetic maps.

2.4.1 Post-processing of data

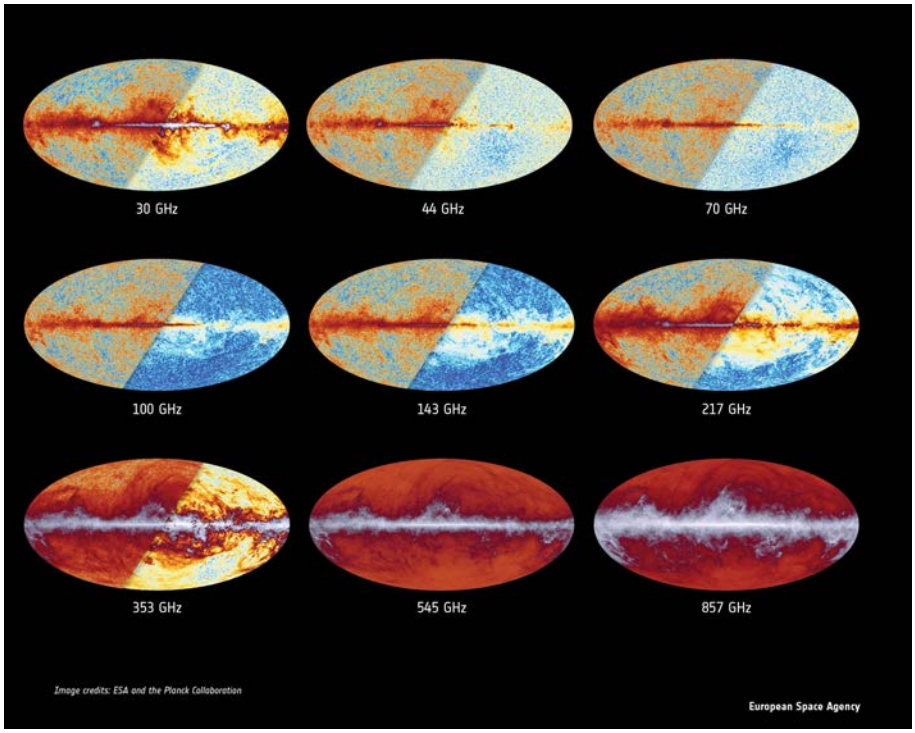

Figure 2.15: Planck skymaps at its 9 different observational frequencies. The first 7 frequency channels are also sensitive to polarisation and the last two only observe total intensities.

There are a number of radio observations which can be utilised to probe magnetic fields in the GHB region, namely:

1. **S-PASS** - the S-band Polrisation All Sky Survey (S-PASS) is a project to map polarised synchrotron emission at 2.3 GHz with the Parkes radio telescope in the Southern Hemisphere in Australia, and operated by CSIRO-CASS [4]. The 2.3 GHz frequency regime of S-PASS makes it more prone to depolarisation due to Faraday rotation. Another disadvantage with the S-PASS data-set is its insensitivity to large sections of the Galactic halo due to its ground-based location in the Southern Hemisphere.

2. **WMAP** - the Wilkinson Microwave Anisotropy Probe (WMAP) was an all sky coverage satellite mission launched by NASA. It operated between 2001 and 2010 with an objective to measure temperature differences across the sky in the cosmic microwave background (CMB). WMAP had an observational frequency range between 22 GHz to 90 GHz.
3. **Planck** - was a European Space Agency satellite mission to study the CMB with an all sky coverage. The satellite was launched in 2009 and turned off in 2013. The main objective of the Planck mission was to study the signatures of the Big Bang by analysing the CMB and testing the different models for the evolution of the Universe. However, in order to do so, the Planck satellite had to map all the Galactic foreground emissions and also untangle them from the CMB emissions. The main objective of the Planck mission was to study the signatures of the Big Bang by analysing the CMB and testing the different models for the evolution of the Universe. However, in order to do so, the Planck satellite had to map all the Galactic foreground emissions and also untangle them from the CMB emissions. For this thesis Planck satellite data was utilised. Planck has 9 main observational frequency domains between 30 GHz to 857 GHz. The skymaps from all of these can be seen in Figure 2.15. The frequency range that Planck observed varied from 30 GHz corresponding to 1 cm to 857 GHz which corresponds to 1/3 of a millimetre. Different physical phenomena dominate at each frequency interval with the CMB being dominant between 70 GHz to 200 GHz. Of these 9 domains only the first 5 provided both polarised and total intensity data whereas the latter two can only be utilised for unpolarised data [110, 122, 124, 125] (see Planck).

The most useful frequency regime where synchrotron radiation dominates lies between 10 and 30 GHz as shown in Figure 2.16 [126]. The polarised synchrotron emission data at these frequencies are not subjected to Faraday rotation effects and are mainly synchrotron dominated. Thus, making the 30 GHz Planck data-set the most useful to study the polarised synchrotron emission. It has a peak frequency of 28.4 GHz, with a bandwidth of 9.8 GHz. The contribution from the CMB at this frequency is insignificant for all intents and purposes. This frequency is best suited for polarised synchrotron emission since Faraday rotation at such high frequencies is negligible. It should be noted however, that the 30 GHz Planck data cannot be used to probe synchrotron intensity directly, since it receives considerable contributions from both thermal bremsstrahlung and anomalous microwave emission, as well as synchrotron radiation in equal amounts [122, 124, 125, 127].

In creating the polarised synchrotron skymaps, three regions of the sky were removed

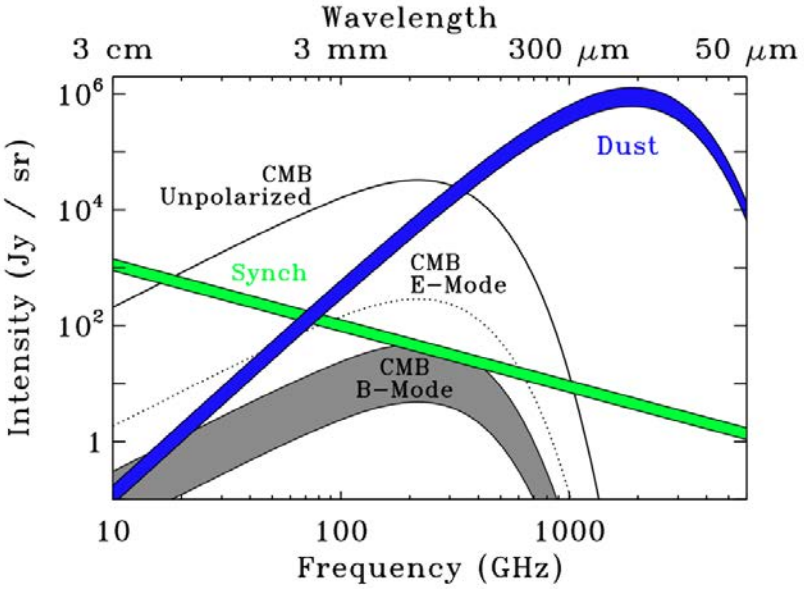

Figure 2.16: CMB and polarised foregrounds as seen at different frequencies. It can be seen that synchrotron dominates at lower frequencies between 10-30 GHz, this figure was obtained from [126].

from the analysis. The map with the cuts listed below is shown in Figure 2.17, the regions of the sky that were cut and the motivation behind it is listed below:

* **Galactic Disc** - Since the focus of this work was solely in modelling magnetic fields in the Galactic halo bubble region the Galactic disc region (between latitude (b) = $(-15°, 15°)$) was cut out from the final skymaps.
* **Longitude cut** - The regions of the sky with longitudes $\geq \pm 90°$ from the Galactic center (that is, all directions pointing away from the Galactic center direction) were also removed from this analysis. These cuts were motivated by the radio observations made from [45] and [50]. It ensured that only the Galactic halo bubble region with radial expanse up to 14 kpc or regions between longitude = $\pm 90°$ was incorporated in this analysis.
* **NPS region** - The final region to be blocked out for the analysis was the North Polar Spur (NPS) region. The motivation to block the NPS region was starlight polarisation observations [32] which suggests at higher latitude emission from the NPS region might have a Galactic center origin but rather local. In order to ensure that the cut was impartial the template by [128] was utilised.

Additionally, the region around Centaurus A or Cen A (for details about Cen A see Section 1.6 in Chapter 1) which has the brightest pixels in the skymap created utilising the publicly available Planck data was also masked. This masking was carried out for the Stokes Q and U maps separately before producing the polarised synchrotron intensity map (see Figure 2.17).

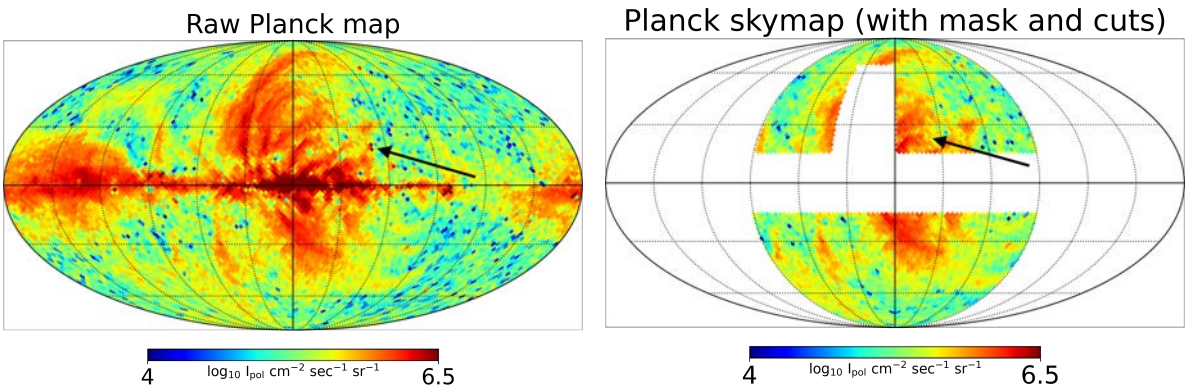

Figure 2.17: Left: Planck polarised 30 GHz data without masking Centaurus A region (see black arrow) and the cuts. **Right:** The same data with masking Centaurus A region and the longitude, latitude and NPS cut.

2.4.2 Simulation setup

The GHB model consists of 5 free parameters; in Table 4.1 the names and description of all the parameters has been provided. The radial and azimuthal cut-offs for both the electron distribution and magnetic field were kept identical with $R_{\rm Mag} = R_{\rm el}$ and $Z_{\rm Mag} = Z_{\rm el}$ respectively. This assumption is based on the fact that synchrotron radiation depends on both the magnetic field and non-thermal electron distribution and the absence of either one of these two components will not result in production of synchrotron radiation. Thus, it may happen that in reality either the spatial extent of the magnetic field and electron distribution differ, but synchrotron radiation can only be utilised to probe magnetic fields when it is present along with non-thermal electron distribution.

A spatial parameter scan for $R_{\rm Mag}/R_{\rm el}$ and $Z_{\rm Mag}/Z_{\rm el}$ was carried out between 2 kpc to 19 kpc, with a scanning step size of 1 kpc. Contrary to the linear scan for the spatial parameters both $B_{\rm str}$ and $B_{\rm tur}$ were scanned logarithmically with 30 bins per decade between 2 μG and 18 μG. Similarly, the normalisation factor for the electron distribution $C_{\rm norm}$ was scanned logarithmically between 10^{-14}cm^{-3} and 10^{-11}cm^{-3}, adopting 10 bins per decade.

Note that it is assumed that both the magnetic field and electron distribution in the models proposed in this thesis have an exponential profile, whereas in reality it is highly probable that both electron distribution and magnetic fields have a power-law decay [42, 54, 108, 129, 130]. However, the focus of this study was primarily on the region of the sky that is dominated by synchrotron emission and thus the actual distribution of the magnetic field and non-thermal electron distribution beyond the observational scale heights of the Galactic halo bubbles was not accounted for in this study. Synchrotron

emission is dominated by local emission along the line-of-sight, any emission beyond the cut-off distances can be safely ignored.

2.4.3 Explanation of smoothing method

A grid search over the 5 free parameters ($B_{\rm str}$, $R_{\rm Mag}/R_{\rm el}$, $Z_{\rm Mag}/Z_{\rm el}$, $B_{\rm tur}$ and $\log_{10} C_{\rm norm}$) sampling in total 8×10^6 parameter sets was carried out in order to obtain the best-fit parameters and constraints for the GHB model using the chi-squared fitting method. A synthetic skymap was generated for each of the parameter sets using *Healpix* [123], with a resolution of Nside = 32. For each parameter combination synthetic polarised maps were created from the stokes Q and U maps resulting in a total of 8×10^6 polarised synchrotron maps.

The Planck 30 GHz skymap has a lot of small-scale fluctuations (see Figure 2.17), which was not the focus of this study. In order to be sensitive to only the large-scale features, a Gaussian smoothing of a fixed radius was utilised which approximately corresponds to the size of these large-scale features. The principle of smoothing is simple, for each data point on the map a new value is generated which is some function of the original value at that point and its neighbouring points. For Gaussian smoothing the function is a Gaussian kernel defined in 1-D by:

$$P(x) = \frac{1}{\sqrt{(\pi\sigma^2)}} e^{-\frac{x^2}{2\sigma^2}} \tag{2.43}$$

here, x is the data point and σ^2 is the variance.

The *Healpix* [123] smoothing kernel was utilised for smoothing the Planck 30 GHz data-set and the 8×10^6 synthetic polarised synchrotron emission skymaps that were obtained from the various parameter combinations for each bin of the grid. The size of the kernel was fixed to 15° in order to match the size of the large-scale features of the skymap which were of interest whilst smoothing the small-scale fluctuations.

2.4.4 Chi-square analysis and the constraints obtained on the GHB model

The smoothened synthetic polarised data maps were then compared with the smoothened Planck 30 GHz skymap using a simple chi-square test. Since the region of interest was only the GHB, a 15° cut in latitude was carried out along with removing regions of the

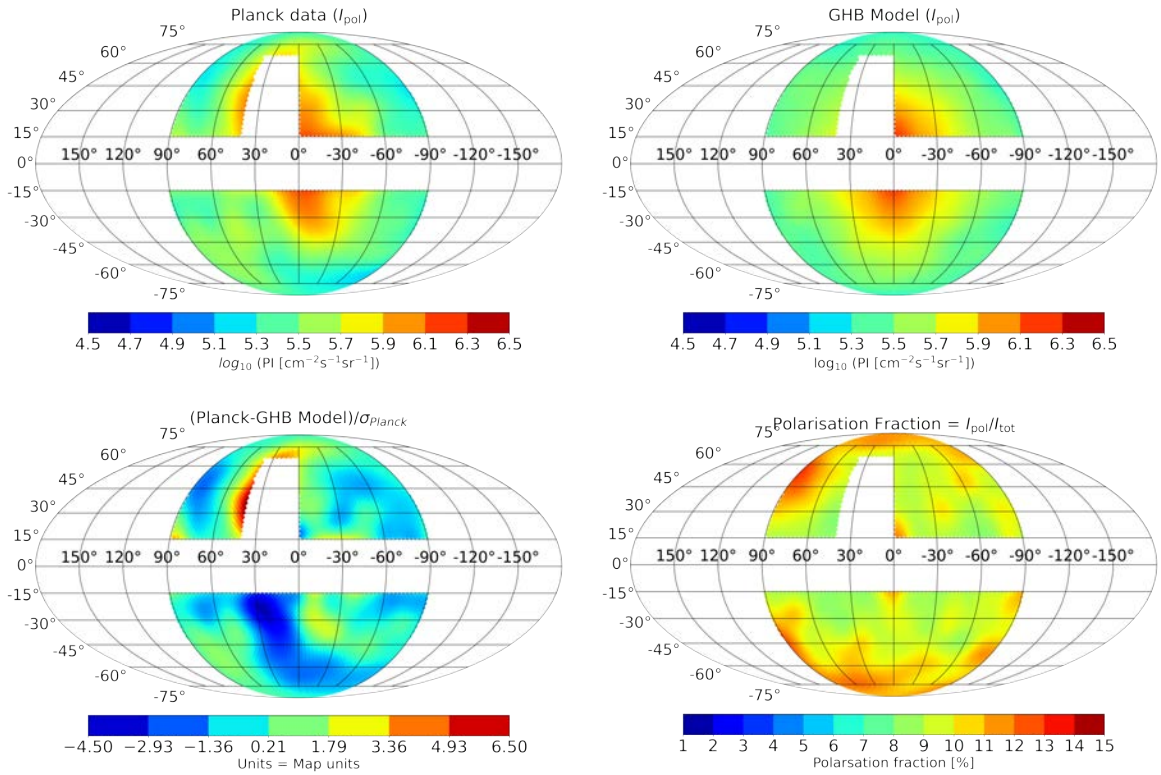

Figure 2.18: Top: Planck polarised intensity skymap (**left**) and simulated polarised intensity (**right**) for the best-fit parameters (see Table 4.1). **Bottom:** Residual of the observation and the simulated data (**left**) and the polarisation fraction for the GHB model (**right**).

sky beyond a longitude of 90°. The NPS region was also removed, which was motivated by observations [32, 128]. With the remaining region the number of grid points with data were counted (N) and the chi-square per degree of freedom ($\chi^2_{\rm DOF}$) was given by:

$$\chi^2_{\rm DOF} = \frac{(I^{\rm Planck}_{\rm pol} - I^{\rm Sim}_{\rm pol})^2}{N - p} \tag{2.44}$$

here, $I^{\rm Planck}_{\rm pol}$ is the smoothened Planck data, $I^{\rm Sim}_{\rm pol}$ is the smoothened synthetic skymap, $p = 5$ is the fixed number of parameters. Note that an ideal model should have the $\chi^2_{\rm DOF} \approx 1$ which implies that a model and data are in full agreement. However, in reality most models cannot replicate all features of an observational data. In the case of the GHB model, it is a toy model and more of a proof-of-concept. The smallest or the best-fit $\chi^2_{\rm DOF}$ obtained from the chi-square analysis for the GHB model was $\chi^2_{\rm DOF} \approx 1.7$. 1σ constraints were obtained on the magnetic field and electron distribution model parameters. A tabulated list of the best-fit values along with the uncertainties has been provided in Table 4.1. For the structured magnetic field strength, $B_{\rm str} \approx 4$ μG was the best fit value, the upper extreme and lower extreme value obtained were ≈ 12 μG and ≈ 2 μG respectively. In case of turbulent fields, $B_{\rm tur}$, the mean value was ≈ 7 μG with lower and upper extreme

Table 2.1: Table of best-fit parameters with uncertainties for the full GHB model

Best-fit value with 1σ constraint		
Parameter	Best-fit value	Description
$B_{\rm str}$	4^{+6}_{-2} μG	Structured field strength
$B_{\rm tur}$	7^{+10}_{-3} μG	Turbulent field strength
$R_{\rm Mag} = R_{\rm el}$	5^{+1}_{-0} kpc	Radial cut-off
$Z_{\rm Mag} = Z_{\rm el}$	6^{+1}_{-0} kpc	Azimuthal cut-off
$\log_{10}\,(C_{\rm norm}[{\rm cm}^{-3}])$	$-11.7^{+0.6}_{-0.9}$	Electron normalisation at 10 GeV

values being ≈ 3 μG and ≈ 17 μG, respectively. In the case of the spatial extent, the best-fit value for the radial ($R_{\rm Mag}/R_{\rm el}$) and azimuthal ($Z_{\rm Mag}/Z_{\rm el}$) extent was ≈ 5 kpc and ≈ 6 kpc respectively. The upper extreme value was +1 kpc for both spatial parameters, however, the lower extreme value remained the same as the best-fit value. This was mainly due to the large step-size adopted in the parameter scan. For the electron normalisation $\log_{10} C_{\rm norm}$, the mean value obtained was ≈ -11.7 and the upper and lower extreme values were ≈ -11.0 and ≈ -12.7, respectively. The Figure 2.18 shows the smoothened skymap from the best-fit parameter values and the polarised Planck data along with the polarisation fraction and residuals. The polarisation fraction obtained by the best-fit GHB-model, given in Figure 2.18, was calculated taking the ratio of the polarised to the total intensity. The polarisation fraction for the best-fit GHB model is comparable to the values as seen in the observation data of [67] and [4].

2.4.5 Polarised synchrotron emission from other halo models

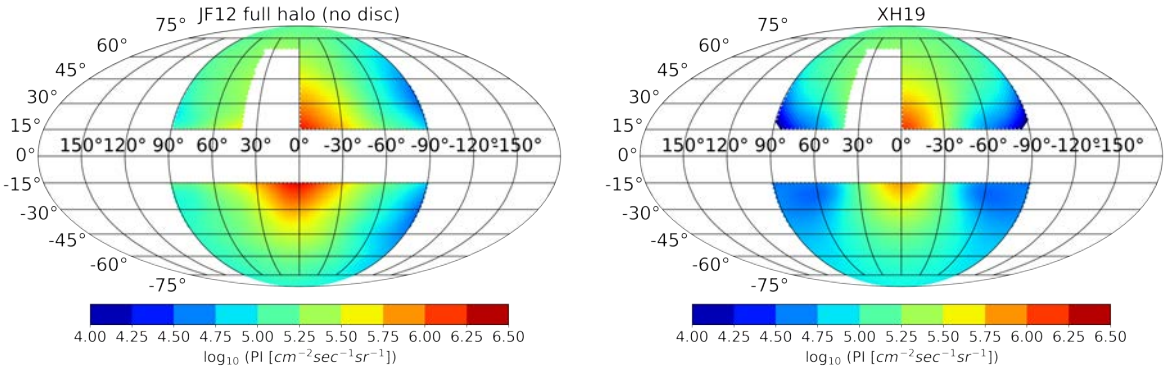

Figure 2.19: Top: Simulated polarised intensity for the JF12 full halo (no disc) (**left**) and XH19 model (**right**) with the same electron distribution (see Eq. 2.6), smoothing and angular cuts as in the results in Figure 2.18.

From the chi-square analysis described above, a $\chi^2_{\rm DOF}$ = **1.7** was obtained by comparing

polarised synchrotron emission from the **GHB model** and Planck polarised 30 GHz data (see Figure 2.18).

For the sake of comparison given the same electron distribution, smoothing kernel and angular cuts (see Section 2.4.1 and Section 2.4.3), polarised synchrotron emission skymaps from the XH19 and JF12 full halo (no disc) (see Figure 2.19) were calculated as well. These skymaps were then compared with the Planck polarised 30 GHz data for the same region and **a $\chi^2_{\rm DOF}$ = 11.0 for the XH19 model and $\chi^2_{\rm DOF}$ = 6.0 for the JF12 full halo model** was obtained. The lower value of the $\chi^2_{\rm DOF}$ from the GHB model implies that it is better fit to the observation data. The large $\chi^2_{\rm DOF} \gg 1$ values from these two models indicate a poorer fit to data in comparison to the low value of $\chi^2_{\rm DOF}$ obtained from the GHB model. The poor fit of the JF12 full halo no disc and XH19 models could be attributed to either the complete lack of any turbulent magnetic fields like in the XH19 model or a weak turbulent magnetic field model as seen in the case of JF12 full halo.

From these statistical comparisons it can be concluded that the GHB model description is sufficiently well-suited to explain the Planck polarised emission data.

2.4.6 Imprints of different kinds of magnetic fields - Turbulent vs structured

For the polarised synchrotron emission calculations the line-of-sight is kept until 14 kpc, with an isotropic turbulent magnetic field. To avoid further layers of complexity, a spatial cut-off in the turbulent magnetic field similar to the structured magnetic fields of the GHB model was not considered in this study. Nevertheless, for theoretical purposes the effect of an isotropic turbulent magnetic field in comparison to one with an exponential spatial cut-off was also investigated.

As a recapitulation, the turbulent field in the GHB model follows a 5/3 Kolmogorov spectrum with $L_{\rm min}$ = 200 pc and $L_{\rm max}$ = 400 pc. Two kinds of turbulent fields were looked into: ***1)*** isotropic turbulent fields (i.e. it has no spatial truncation) and ***2)*** turbulent fields with an exponential spatial cut-off which is given as $B_{\rm tur} e^{-|z|/Z_{\rm Mag}} e^{-|r|/R_{\rm Mag}}$. For $B_{\rm tur} \approx 6\ \mu G$,$R_{\rm Mag} = Z_{\rm Mag} \approx 6$ kpc the turbulent field without and with the cut-off as a function of line sight is shown in Figure 2.20 in the left column. The cut-off values were motivated from the best-fit values given in Table 4.1. For the sake of completeness, synthetic skymaps obtained from these two turbulent magnetic field models were then compared with skymaps obtained from the structured part of the GHB magnetic field model with $B_{\rm str} = 6\ \mu$G, $R_{\rm Mag} = Z_{\rm Mag} = 6$ kpc. The turbulent field imprints itself differently

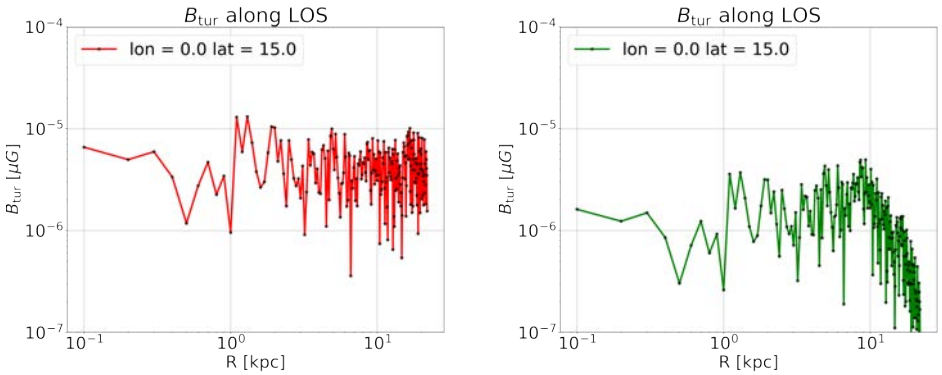

Figure 2.20: On the **left** is the strength of turbulent magnetic fields without a spatial cut-off and on **right** magnetic field strength is plotted with an exponential spatial cut-off as a function of line of sight (lon = 0°, lat = 15°) respectively.

depending on whether it's an isotropic-filled field in a rectangular box of 14 kpc or when it has an exponential spatial cut-off which is similar to the structured fields of the GHB model. For the case when there is a spatial cut-off in the turbulent fields, the field strength will drop off beyond the cut-off distance and the skymap also shows a drop in the brightness due to the cut-off. However, when there is no exponential cut off in the turbulent fields it imprints emission much more uniformly across the skymap. The structured field which has a regular geometry showcases the bubble structures in the polarised synchrotron emission. These effects of different magnetic field types and geometry can be understood in Figure 2.21. The figure showcases the effect of the spatial exponential cut-off in turbulent fields and how polarised synchrotron emission exhibits itself in the case of a pure turbulent and pure structured magnetic field configuration.

This study showcases that not only turbulent magnetic fields contribute significantly to the polarised synchrotron emission, but also that their spatial geometry has a considerable effect on the synthetic polarised synchrotron skymaps.

2.4.7 Smoothing maps at different stages

Briefly summarising the smoothing technique adopted in 2.4.3, the synthetic polarised synchrotron skymap ($I_{\rm pol}$) for each parameter combination was calculated using the Stokes Q and U maps for each bin on the grid followed by the Gaussian smoothing. The Planck polarised 30 GHz skymap was also calculated the same way. The 8×10^6 synthetic polarised synchrotron emission skymaps were then compared with the Planck polarised skymap (see 2.4.4) by doing a chi-square analysis. The constraints obtained are provided in Table 4.1.

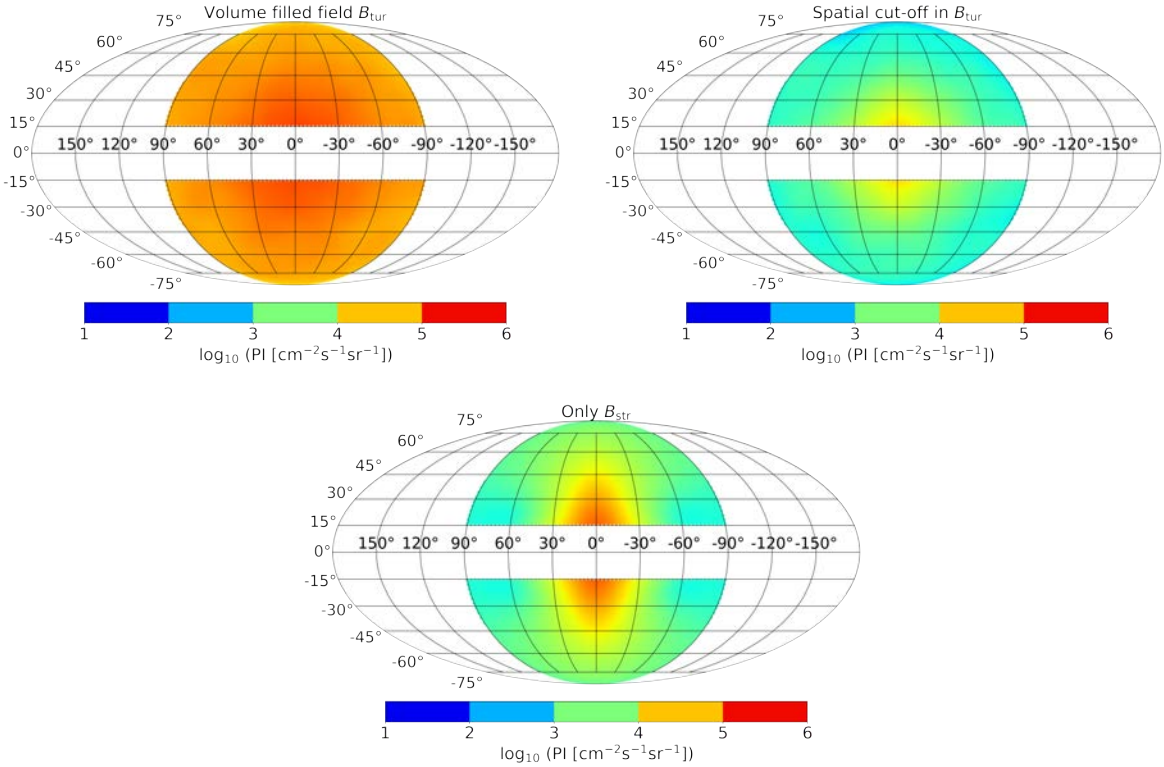

Figure 2.21: The polarised synchrotron skymap (bottom) only made with the purely structured magnetic field component of the GHB model clearly showcases reduced emission overall due to lack of any turbulent magnetic field model. In the top right figure is the polarised skymap with only turbulent fields but having a spatial cut-off similar to the structured magnetic field of the GHB model. The top left figure shows the skymap obtained utilising only the turbulent magnetic field of the GHB model which is isotropic similar to the one adopted in the GHB model. Not only do the turbulent magnetic fields significantly contribute to the polarised synchrotron emission, their geometry also dictates the morphology of the emission.

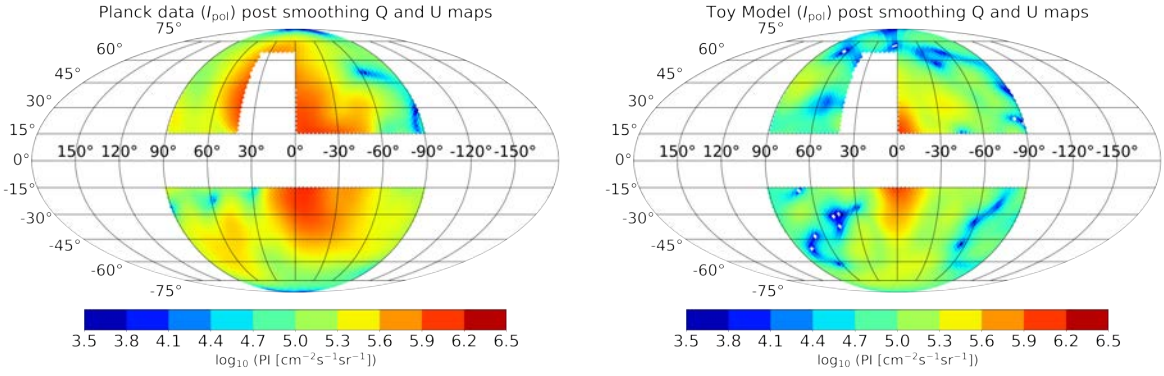

Figure 2.22: Left: The Planck polarised synchrotron skymap created by first smoothing the Planck Stokes Q and U maps by a 15° Gaussian kernel and then estimating the polarised emission.
Right: The GHB model skymap for the best-fit parameter values listed in Table 4.1. This skymap was created in the same manner as the Planck map on the left.

However, it is interesting to note the effect that smoothing and comparing different kinds of maps have. Below are listed two different types of methods of comparing synthetic data with observational data apart from the one adopted in Section 2.4.3.

1. **Smooth first method** - Estimating chi-squared per degree of freedom when the Stokes Q and U maps are smoothed first and then the polarised synchrotron skymaps are calculated. As an example case the Q and U maps for both the Planck 30 GHz data and the best-fit parameter model were first smoothed with the same Gaussian kernel as used in Section 2.4.3, and then the polarised synchrotron emission was calculated. The skymaps for both Planck and synthetic data are shown in Figure 2.22. The new χ^2_{DOF} was found to be much worse at 3.8 compared to the χ^2_{DOF} of 1.7 for the case where the polarised synchrotron emission was calculated first, and the smoothing was done afterwards followed by a chi-square analysis.
2. **Comparing Q and U maps separately** - Another method that can be utilised to compare the polarised synchrotron maps from the GHB toy model and Planck data is to compare the Stokes maps Q and U separately for data and observations and then calculating chi-squares for these maps separately.

Both of the aforementioned methods will be carried out in the future and the new results obtained will then be compared with the constraints obtained in Section 2.4.4, Table 4.1.

2.5 Conclusion and outlook

Note that results from this work were published as a part of the peer-reviewed article [1].

The radio observations [4] of the Fermi bubbles clearly suggest the presence of non-thermal particles at high Galactic latitudes. The GHB magnetic field and non-thermal electron distribution model for the Galactic halo bubble region proposed in this thesis is an attempt to better describe the polarised synchrotron emission 30 GHz data as seen by the Planck satellite.

Utilising the GHB model (both magnetic field and non-thermal electrons) to generate synthetic polarised synchrotron emission skymaps and comparing them against the 30 GHz Planck data, several parameter combinations were explored. Through this study significant evidence was found for the presence of an extended magnetic field component in the Galactic halo bubbles region. The best-fit value obtained for the azimuthal extent of the magnetic field ~ 6 kpc was found to be compatible with spatial extents also reported by Fermi-LAT observations [46]. Likewise, a large value of ~ 7μG was found for the total magnetic field strength in the GHBs, this was found to be consistent with the radio observations by S-PASS [4].

If equipartition between the magnetic fields and thermal particles exist such that the plasma beta $\beta_{\rm plasma} = \frac{U_{\rm thermal}}{U_{\rm mag}}$, then one would expect that the total magnetic field (structured and turbulent combined) energy is approximately around the value reported by the eROSITA [50] data at 10^{56} ergs. The best-fit parameter set for the GHB model yields a total magnetic field energy at $\approx 10^{55}$ ergs which is smaller than the eROSITA values. In comparison, the total energy content in the JF12 model was found to be 4×10^{54} ergs and 3×10^{54} ergs for the toroidal halo and X-field respectively [71].

Additionally, even though only very loose constraints were obtained on the turbulent fields the parameter grid search strongly favours the Galactic halo to be turbulent field dominated. This finding also seems to be consistent with magnetic field strengths estimated for other local galaxies from observations [7, 131].

There is a growing body of evidence suggesting the presence of thermal gas out to the virial radius of the Galaxy ($R_{\rm virial} \approx 300$ kpc) [52]. Models motivated by such data suggests that for $U_{\rm thermal} \approx 0.1$ eV, magnetic fields of around $\approx 0.3 \mu$G are required assuming that there exists equipartition between thermal gas and magnetic fields [53]. The presence of an extended halo has also been seen in multiple external galaxies [42] which implies that having large extended magnetised haloes in galaxies might not be unusual. Based on these observational evidences utilising a power law profile for magnetic fields in the halo is probably a more realistic description of the halo. The GHB model proposed in this thesis will be improved and extended in the future by exploring power-law profiles for the Galactic halo.

This study successfully demonstrates that the model proposed in this thesis is able to better describe the observational 30 GHz Planck data. Its is important to test this model with other observational data at different frequency ranges to further improve this model and tighten the constraints. Through processes like synchrotron radiation, the magnetic field component perpendicular to the line of sight (direction from observer to source) can be probed. Polarised synchrotron (parametrised via Stokes Q and U) probes the large-scale morphology and strength of structured magnetic fields. Turbulent magnetic fields also imprint themselves in polarised synchrotron radiation. However, in order to constrain the turbulent magnetic fields, unpolarised synchrotron data (Stokes I) needs to be utilised [41]. Unlike its predecessors like Haslam observations (408 MHz) is only unpolarised [132] and the S-PASS data (2.3 GHz) suffers greatly from Faraday rotation [4] whereas Planck data [111] suffers from contamination from other physical processes in the total intensity data. The latest all sky radio survey C-BASS observes both polarised and unpolarised synchrotron emission at 5 GHz [133, 134] and parts of the data are expected

to be released in late 2023[¶]. It will reveal both the degree of polarisation (ratio of polarised to unpolarised radiation) and polarisation angle.

The radio polarisation data obtained from C-BASS can be utilised to model the structured magnetic fields and further improve and expand the GHB model. Unpolarised C-BASS data will be crucial in modelling different realisations of turbulent magnetic fields. Templates based on existing observations for different radiation processes [134] like synchrotron and thermal bremsstrahlung can be used as filters to study the contribution of unpolarised synchrotron radiation alone, providing new insight into the turbulent magnetic field structure. This is a well-established methodology previously used to study Galactic foregrounds [135–137]. This work will be pursued as an extension to the work presented in this thesis.

[¶] see talk by Harper at the Galactic science and CMB foregrounds workshop

Propagation of UHECRs through the GHB model

3

Ultra-high energy cosmic rays or UHECRs cannot propagate freely on their way from the extragalactic source to the observer (Earth). As they travel from the extragalactic source to an observer, they experience energy losses due to their interaction with the extragalactic background light and deflections from both the extragalactic and Galactic magnetic fields. As a result, the composition, and spectrum of the UHECRs and their initial injection directions at the source are altered by these propagation effects, and this is reflected in the observations of the UHECRs. The effect of the magnetic fields from the GHB model on the arrival directions of UHECRs will be the sole focus of this work.

3.1 Propagation of particles through magnetic fields

Charged particles travelling through a magnetic field at speeds close to the speed of light are precessed around the magnetic field lines by virtue of Lorentz force:

$$\frac{\mathrm{d}\vec{\beta}}{\mathrm{c}\,\mathrm{d}t} = \frac{1}{r_{\mathrm{L}}}\vec{\beta} \times \hat{B} \tag{3.1}$$

here, the particle velocity ratio is given by unit vector $\vec{\beta} = \vec{v}/c$, r_L is the particle's Larmor radius and $\hat{B}$ is the magnetic field unit-vector. The Larmor radius is given by:

$$r_L = \frac{\beta E}{ZeB}, \tag{3.2}$$

here, E is the energy of the charged particle in units of eV, Ze is the charge of the particle and B is the magnetic field strength. For example a proton at 40 EeV will have a Larmor radius of 7 kpc for a typical field of 6 μG. The angle between the perpendicular velocity vector $\hat{\beta}$ and the magnetic field is called the pitch angle. The particle gyrates with the Larmor radius around the center of the circular orbit, the center of which is called the guiding center.

Broadly, magnetic fields can be classified by large-scale coherent fields or structured magnetic fields and small-scale random fields or turbulent magnetic fields. To understand the motion of charged particles in magnetic fields of different length scales the principles of adiabatic invariance can be called upon.

The velocity vector $\vec{v}$ can be decomposed into components which are perpendicular and parallel to $\vec{B}$ as $v_\perp$ and $v_\parallel$ respectively, such that:

$$\frac{\mathrm{d}v_\parallel}{\mathrm{d}t} = 0, \tag{3.3}$$

$$\frac{\mathrm{d}v_\perp}{\mathrm{d}t} \sim \vec{v} \times \vec{B}. \tag{3.4}$$

The force parallel to the velocity vector as shown in Eq. 3.3 will be zero because force due to a magnetic field on a particle will always be perpendicular to the direction of motion and thus the parallel component is zero. Eq. 3.4 shows that the magnetic field B only affects the velocity of the particle perpendicular to it.

The Larmor radius given in Eq. 3.2 can be re-written in terms of the particle mass m and perpendicular velocity $v_\perp$ and the Lorentz factor Γ as:

$$r_\mathrm{L} = \Gamma \frac{m v_\perp}{ZeB}$$

A charged particle of mass m spiralling around a uniform magnetic field is equivalent to a current carrying loop. The current (i) in such a loop can be given by the charge passing a particular point in the loop per second, $i = Zev_\perp/2\pi r_\mathrm{L}$ with Ze being the charge in the loop and r_L being the Larmor radius of the particle effectively acting as the radius of the loop. The magnetic moment in the loop with area $A = \pi r_\mathrm{L}^2$ can then be given by:

$$\mu_B = i\, A = \frac{Zev_\perp}{2\pi} \pi r_\mathrm{L}^2,$$

where, $w_\perp$ is the kinetic energy of the charged particle. The magnetic moment in the relativistic case with Lorentz factor (Γ), can be given by:

$$\mu_B = \Gamma \frac{m v_\perp^2}{2B} = \frac{w_\perp}{B} \tag{3.5}$$

here, $w_\perp$ is the particle's kinetic energy. Assuming that there is a small perturbation ΔB in the magnetic field flux density B in one orbit. An electromotive force $E_\mathrm{emf} = -\frac{\mathrm{d}B}{\mathrm{d}t}$ is induced in the loop due to the changing magnetic field which results in the charged particle to accelerate.

The work done on the charged particle in one orbit by E_emf can be given by

$$Ze\, E_\mathrm{emf} = Ze\, \frac{\mathrm{d}B}{\mathrm{d}t} = Ze\, \pi r_\mathrm{L}^2 \frac{\Delta B}{\Delta T},$$

where $\Delta T = 2\pi r_L/v_\perp$, is one time period. The change in the kinetic energy can then be given by:

$$\Delta w_\perp \frac{Zer_L v_\perp}{2}\Delta B,$$

putting the value of r_L in the above equation, we get:

$$\Delta w_\perp = \frac{w_\perp}{B}\Delta B.$$

The corresponding change in the magnetic moment ($\Delta\mu$) can then be given by using a Taylor expansion* for first two terms which gives:

$$\Delta\mu = \Delta\left(\frac{w_\perp}{B}\right) = \frac{\Delta w_\perp}{B} - \frac{w_\perp \Delta B}{B^2} = \frac{\Delta w_\perp \Delta B}{B^2} - \frac{\Delta w_\perp \Delta B}{B^2} = 0, \tag{3.6}$$

The above equation thus implies that the *magnetic moment acts as a pseudo invariant quantity or pseudo adiabatic invariant quantity for a slowly changing magnetic field.*

If a particle moves *slowly* from a weak field to a strong field region $\vec{B}$ will increase, thereby increasing $v_\perp$ but in order to keep the total energy conserved $v_\parallel$ must decrease. Therefore, as a particle goes from a stronger to a weaker $\vec{B}$ field regime its Larmor radius changes, but for slowly changing magnetic fields the magnetic moment will remain a pseudo adiabatic invariant† [29, 138].

3.1.1 UHECR Larmor radius and the first adiabatic invariant

In the physical world, fields are seldom uniform and tend to have fluctuations or turbulence at different scale sizes. For example in the case of hydrodynamics, turbulence can be described as currents, knowns as eddies, which can be of different sizes. The energy density in each eddy of a particular size is assumed to follow a power law. It can be given by the differential quantity:

$$\frac{\mathrm{d}\delta B^2}{\delta k} = \frac{B_{\mathrm{tur}}^2}{k_{\mathrm{min}}}\left(\frac{k}{k_{\mathrm{min}}}\right)^{-\gamma} \tag{3.7}$$

here k is the wave number given by $k = 2\pi/L$ with L being the wavelength and B_{tur} is the root-mean-square value. For a detailed explanation on turbulent fields see Chapter 2.

* Taylor expansion can be given by $f(x+\Delta x) = f(x) + f'(x)/1!\,(\Delta x) + f''(x)/2!\,(\Delta x)^2 + \ldots$

† Note: there are two other adiabatic invariant quantities, the *longitudinal invariant* of a trapped particle in a magnetic mirror, this property is used in Fermi acceleration and the *flux invariant* which states that the magnetic flux through the guiding center orbit is conserved. These two will not be further discussed in this thesis.

Fluctuating magnetic fields are generally present together with large-scale structured fields or mean-fields. The information about the magnetic field is generally encoded in the UHECR arrival directions. The effect that structured versus turbulent magnetic fields have on UHECR arrival directions is very different and will be discussed in detail in this chapter.

For a slowly varying magnetic field the radius of curvature of a particle's path is such that it conserves the magnetic flux enclosed by the orbit such that $\Delta(Br_{\rm L}^2) = 0$, this is the same as stating $\Delta(w_\perp/B) = 0$. In Figure 3.1, cases where adiabatic invariant remains

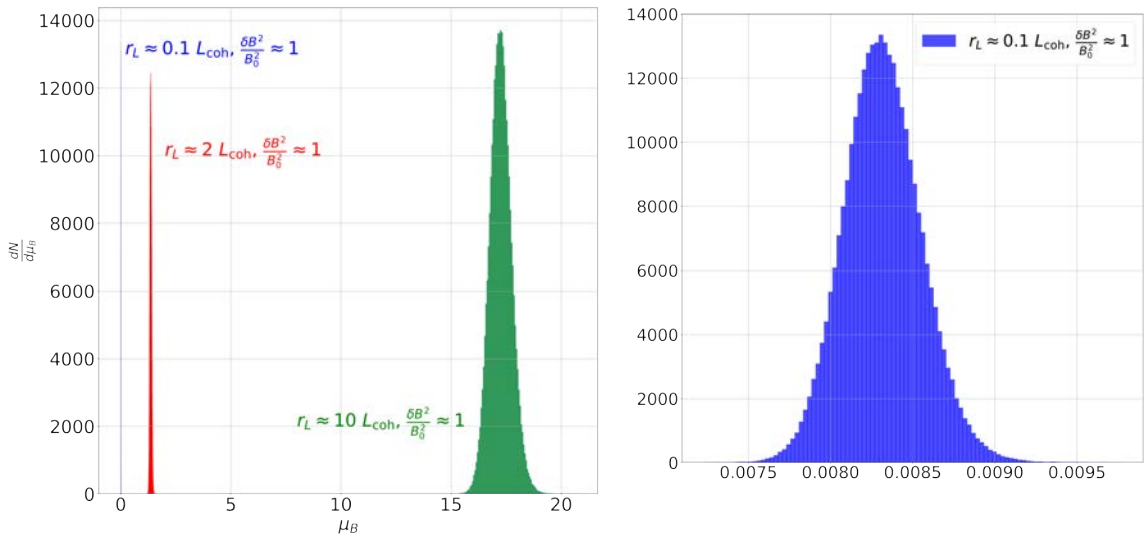

Figure 3.1: Histograms shown in above figure showcases the distribution of the μ_B values for different ratios of r_L and $L_{\rm coh}$. The plot was created for a proton particle of fixed energy at energies of 2, 30, and 100 EeV with a uniform mean field, B_0 and fluctuating turbulent field given by δB. The histograms above are only for the **strong turbulent field regime** here the ratio between δB^2 and B_0^2 is ≈ 1 is fixed. The histograms are discussed below:
1. The Gaussian distribution of the μ_B values for $r_{\rm L} \gg L_{\rm coh}$ indicates that the adiabatic invariant in this case is not conserved. This is because in this case the particle *feels fluctuations in the field* and its pitch angle changes constantly due to this. This is because the energy density in the turbulent magnetic field is comparable to the mean field.
2. The delta like distribution for $r_{\rm L} \ll L_{\rm coh}$ showcases that the adiabatic invariant is almost conserved since the distribution of the μ_B values is very narrow. A zoomed version of the histogram corresponding to this case is shown on the right in the above figure the Gaussian distribution here is very narrow giving the delta-like appearance in the left plot.
3. The pitch angle scattering regime lies when $r_{\rm L} \sim L_{\rm coh}$, in this case the adiabatic invariant also undergoes some level of fluctuations. In general in this case the adiabatic invariant cannot be conserved since there is a significant change in the pitch angle of the particle in one single Larmor radius. The scattering of particles by the random superposition of the small-scale fluctuations results in random changes in the pitch angle of the particle.

conserved and where the conservation is not maintained is discussed. To create this figure a proton particle at energies of 2, 30, and 100 EeV was propagated through a magnetic field configuration which had a uniform mean magnetic field B_0 combined with

fluctuating turbulent field given by δB. Three cases were analysed for strong field regime with $\delta B/B_0 \approx 1$, namely:

1. $r_{\mathrm{L}} \gg L_{\mathrm{coh}}$ - In this scenario the adiabatic invariant is not conserved and the values of μ_B follow a Gaussian distribution. This is because in this case the particle's pitch angle changes constantly due to the high level of turbulent magnetic fields. Note that the only time the adiabatic invariant can be conserved in this case is when the level of fluctuations are smaller than the mean field then the particle will follow the mean field only. This can be seen in the trajectory plot in the bottom panel in Figure 3.2.
2. $r_{\mathrm{L}} \sim L_{\mathrm{coh}}$ - known as the pitch angle scattering regime is the case when the Larmor radius of the particle is comparable to the coherence length of the field. In general in this case the adiabatic invariant cannot be conserved since there is a significant change in the pitch angle of the particle in one single Larmor radius. The scattering of particles by the random superposition of the small-scale fluctuations results in random changes in the pitch angle of the particle resulting in it drifting across the field. The histogram for this case has a more peaked Gaussian. In Figure 3.2 in the top-right figure the drifting due to pitch angle scattering is shown for one case.
3. $r_{\mathrm{L}} \ll L_{\mathrm{coh}}$ - In this case for the strong field regime the adiabatic invariant is almost conserved since the distribution of the μ_B values is very narrow and looks more like delta distribution in comparison to the above-mentioned cases. The particle's Larmor radius is much smaller than the coherence length, and therefore it follows the geometry of the fluctuating field. The trajectory of this is shown in the top-left panel of Figure 3.2.

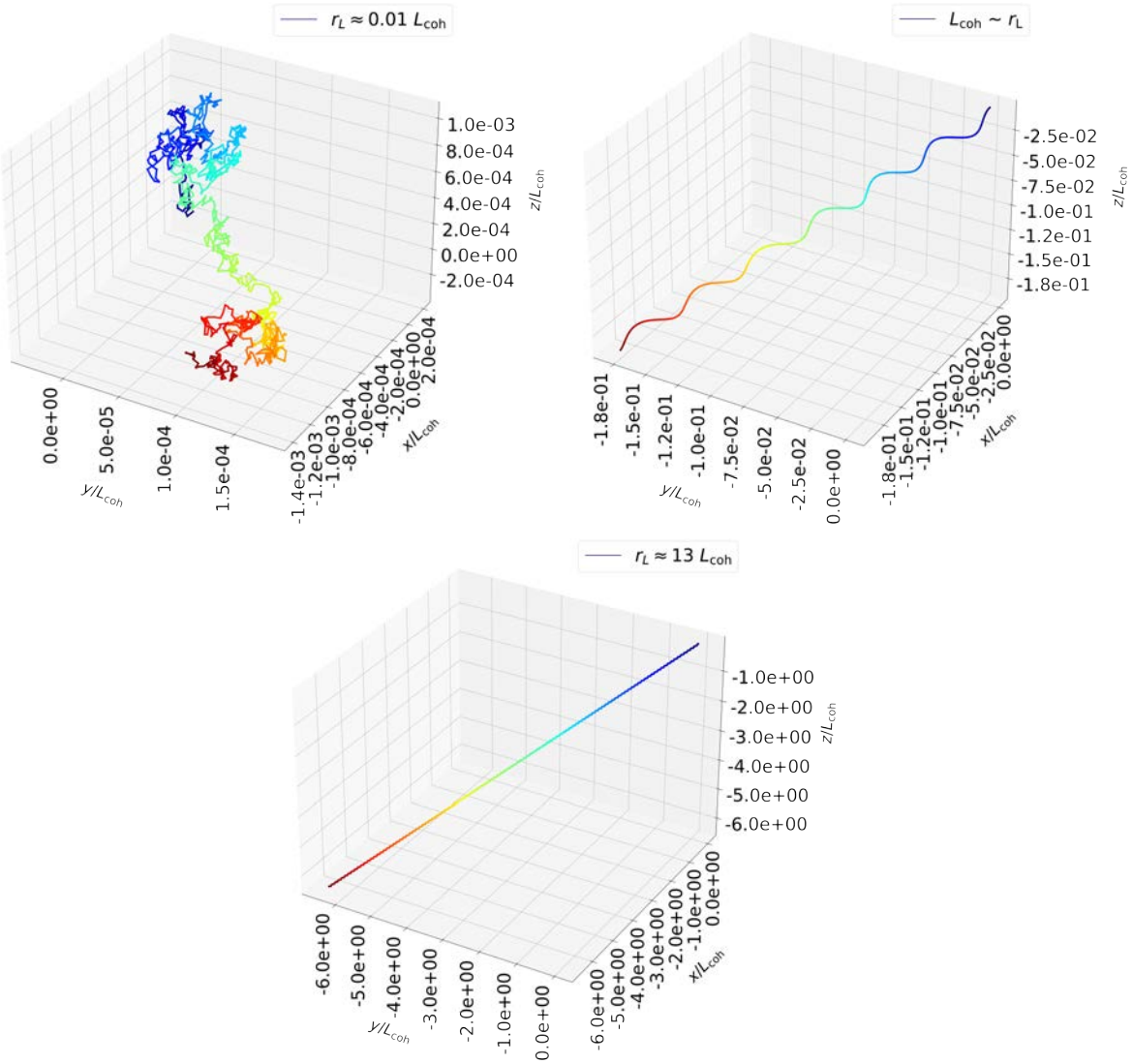

Figure 3.2: Figure above shows trajectories of a charged particle for three cases, namely:
1) Top-left: when $r_{\rm L} \ll L_{\rm coh}$, the particle follows the shape of the small-scale fluctuating fields, as the orientation of the field changes the particle trajectory also changes.
2) Top-right: shows the particle smoothly following the fluctuating field, this is the pitch angle scattering regime when the Larmor radius is comparable to the size of the fluctuations $r_{\rm L} \sim L_{\rm coh}$, the particle drifting in the magnetic field.
3) Bottom: for $r_{\rm L} \gg L_{\rm coh}$, the particle will gyrate around the mean-field and *does not feel* any fluctuations and follows the mean field.

3.2 The GHB magnetic field model

In Chapter 2, the Galactic halo bubble (GHB) magnetic field model was introduced. As a recapitulation the GHB model comprises two components, namely:

1. Toroidal structured magnetic field described by:

$$B_{\rm tor}(r,z) = B_{\rm str} e^{(-|z|/Z_{\rm mag})} e^{(-z_{\rm min}/|z|)} e^{(-|r|/R_{\rm mag})}, \tag{3.8}$$

here, r and z are the radial and azimuthal positions where the strength $B_{\rm tor}$ is measured. The 3 free parameters in this model are the mean strength of the structured magnetic field, $B_{\rm str}$ and the radial and azimuthal spatial cut-off distances $R_{\rm mag}$ and $Z_{\rm mag}$, respectively.

2. Turbulent or random magnetic field component parameterized by the root-mean-square or RMS strength given by $B_{\rm tur}$. The coherence length $L_{\rm coh}$ was fixed at 150 pc with the $L_{\rm min}$ = 200 pc and $L_{\rm max}$ = 400 pc.

Note: the coherence length for such a field will be given by (see also Chapter 2 for more detail):

$$L_{\rm coh} = \frac{1}{2} L_{\rm max} \frac{\gamma - 1}{\gamma} \frac{1 - (L_{\rm min}/L_{\rm max})^{\gamma}}{1 - (L_{\rm min}/L_{\rm max})^{(\gamma-1)}}, \tag{3.9}$$

here, $L_{\rm max}$ and $L_{\rm min}$ are the minimum and maximum scale sizes [139]. A more in-depth discussion of the above-mentioned two components is provided in Chapter 2. In the last chapter, constraints over these parameters were obtained by doing chi-squared analysis for the synthetic polarised synchrotron emission skymaps for various parameter combinations of the GHB model with Planck 30 GHz polarised synchrotron data. This chapter will focus on using the minimum/lower-bound, best-fit and maximum/upper-bound parameter values of GHB model and propagating UHECRs through them. The parameter set utilised has been provided in Table 3.1.

Table 3.1: Table of best-fit, minimum/lower-bound and maximum/upper-bound parameter values obtained for the GHB model. Note that these values were obtained by carrying out a chi-square analysis between the synthetic polarised synchrotron emission skymaps of the GHB model and the 30 GHz Planck polarised skymaps.

Parameter	Best-fit	Minimum	Maximum
$B_{\rm str}$	4 μG	2 μG	10 μG
$B_{\rm tur}$	7 μG	4 μG	17 μG
$R_{\rm Mag}$	5 kpc	5 kpc	6 kpc
$Z_{\rm Mag}$	6 kpc	6 kpc	7 kpc

3.2.1 Simulation framework

To study the effect of the GHB magnetic field model on the propagation of UHECRs through the Galaxy, the publicly available cosmic ray propagation code CRPropa3 [89, 90] was used. It is a Monte Carlo based simulation package. The basic concept of CRPropa3 is having all aspects of cosmic ray propagation, such as photo-disintegration or the

maximum trajectory length, split up into independent simulation *Modules*. Their task is to modify a cosmic ray one after the other and in small steps. The propagation then consists of repeatedly looping a cosmic ray through a list of active modules until a module signals that the propagation is finished. The modules are independent in that they do not require each other and can basically be used in any combination.

Backtracking of particles

For this work the backtracking feature of CRPropa3 was utilised. The backtracking feature of CRPropa3 is based on the Lorentz pusher and consists of both the Boris and the Cash Karp pusher [140–142]. Backtracking of cosmic rays involves starting with an isotropic distribution of cosmic rays at the Galactic center (GC) or Earth and pushing them from GC/Earth through the magnetic fields of the Galaxy up until a termination sphere with a termination radius of R_{term} which marks the of edge of the Galaxy. It is important to note that CRPropa3 conserves the total energy of each particle during the propagation. The directions obtained at the termination sphere are then converted to the following:

1. **Magnification maps** - these maps show the sky as it would appear at the termination sphere. To create these histograms, the cosmic ray distributions were binned into angular bins (with respect to observer at Earth or GC) at the termination sphere with 180 bins for both latitudes ($\cos\theta$) and longitudes. The histogram values in the maps are normalized to the histogram values obtained for simulations without any magnetic fields present (giving rise to uniform sky brightness).
2. **Arrival direction skymap** - are skymaps as seen by an observer at Earth or any particular spatial location. These maps were created by backtracking UHECRs through the GHBs until a termination radius of 30 kpc starting with an isotropic distribution in momentum and delta distribution in position at Earth. The CR arrival directions for 5° region around the source were binned and converted to the directions seen by an observer, and the maps were normalised to the peak value of the histogram in the source region for the case involving no magnetic fields.

Trajectory of a particle with and without magnetic fields

In order to visualise how the backtracking scheme works in CRPropa, 40 (40 EeV nitrogen) UHECR isotropically distributed (i.e., isotropic in momentum and delta in position) were backtracked from the GC to R_{term} = 20 kpc for the case when there were no magnetic fields present and when there was a uniform magnetic field (B_x = 2 μG) present but only

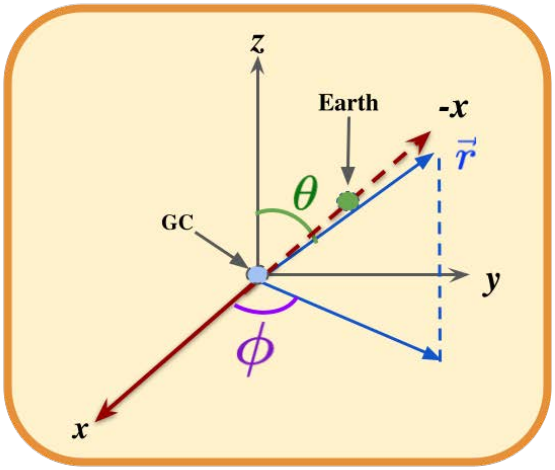

Figure 3.3: The cartesian x, y, z with the spherical coordinate system with r being the radial vector, θ is the angle between azimuthal direction z and r and ϕ is the angle between x and y. A uniform magnetic field in x direction exists only along the x axis (in red).

in the x. In Figure 3.3, the Cartesian and spherical projections are shown, with the x axis marked in red along which the magnetic field was orientated. In Figure 3.4, the Galaxy has been shown by the light green sphere with the GC at the origin. On the left-hand side the no magnetic field case is shown here the particles travel ballistically due to lack of any fields, on the right-hand side of the figure the particles gyrate around the magnetic field B_x and terminate at the poles having a Larmor radius (r_L) of approximately 3 kpc.

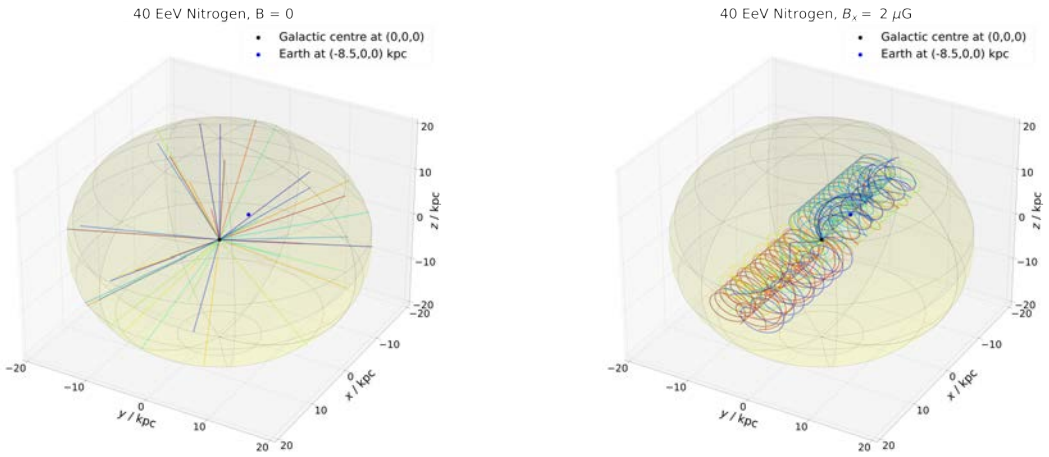

Figure 3.4: Plots above show trajectories of 40, 40 EeV Nitrogen UHECRs. In the case when there are no magnetic fields the particles terminate ballistically at the termination radius of 20 kpc (**left**). In the second case magnetic fields of 2μ G are present in the +z direction. The UHECRs with $r_L \approx 3$ kpc in this case gyrate around the .field lines and terminate at the edge of the sphere (**right**). Since, the magnetic field is in the ± z-direction the particles also terminate in that direction.

Difference between final position and final momentum direction of UHECR

As stated previously backtracking of UHECRs is always done starting with an isotropic distribution of cosmic rays at Earth/GC. This distribution is isotropic in momentum directions and a delta distribution in positions of UHECRs. Note that CRPropa3 can provide both the position of a particle and the momentum direction of a particle at the termination sphere.

To understand how the final position and momentum direction distribution of UHECRs after propagation look like, a simpler magnetic field model was utilised. UHECRs were propagated through a uniform magnetic field orientated along the x axis. This is the same magnetic field configuration adopted in Chapter 2 for estimating synchrotron emission.

10^5 UHECR nitrogen at 40 EeV were propagated through a uniform magnetic field orientated along x direction with an arbitrary field strength choice of 12 μG starting with isotropic momentum distribution and delta distribution in position at the GC.

In Figure 3.5 on the top-left the initial position map is shown since the initial distribution of particle distribution in position is a delta, the map is isotropic. In the same figure on the top-right, the position map for the final positions of the particles at the termination sphere have been shown. The two coloured hotspots mark the final position of the UHECRs at which they enter and leave the magnetic field. Due to the projection of 3-D coordinate system on a 2-D map the hotspots appear at lon = 0°, lat = 0° and lon = 180°, lat = 0°. This is an expected result, since the magnetic field is only orientated along the x axis, the final particle positions will also be along this axis. The final position map produces the same result as shown in the trajectory plot on the right in Figure 3.4; the trajectory plot shows that the particles get clocked when they enter and leave the field resulting in the two hotspots also in final position map.

In Figure 3.5, on the bottom-left the isotropic distribution of the initial momentum directions is shown as a magnification map. For a single particle velocity orientated in the y direction and the field in the x direction the particle will experience a force in the z direction, similarly when the particle moves in the z direction and the field is in the x direction the particle will experience force in the y direction by the cross-product rule. The particle therefore circles in the $y - z$ plane. This is also shown in the trajectory plot on the right in Figure 3.4. The momentum directed in the x direction remains unaffected resulting in a magnification map that looks isotropic.

With the test case now being discussed, the effect of the GHB model on the propagation of UHECRs will be studied. In order to understand the combined effect of structured and

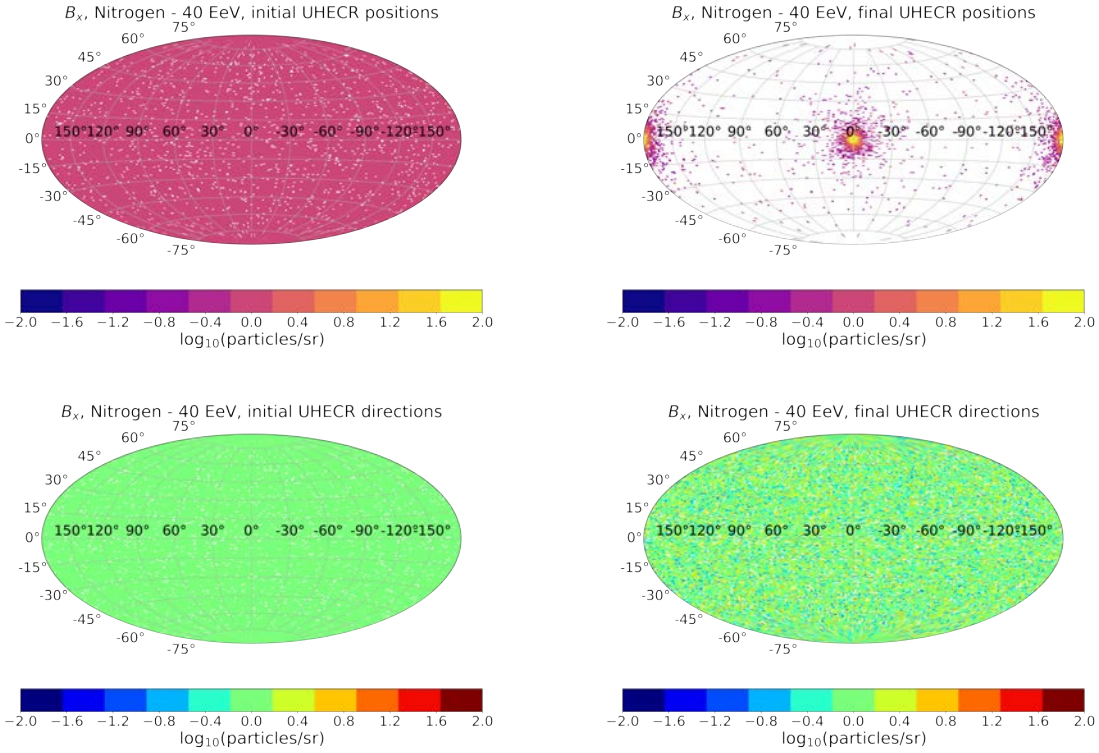

Figure 3.5: Top: The initial and final positions map of UHECRs before and after propagation through the uniform field in the x direction. The initial positions (**left**) of the UHECRs at the starting position (GC) is a delta distribution for each particle and hence the map shows the isotropic feature. The final positions (**right**) of the UHECRs at the termination sphere will show two hotspots marking the entry and exit of the UHECRs through the $+x$ and $-x$ direction respectively. The particles are only clocked once when they enter the field and when they exit the field.
Bottom: The magnification maps for initial and final directions as seen at the termination sphere shows the log binned histogram of initial and final momentum directions normalised to 1. On the **left** is the isotropic magnification map for the initial directions since the distribution at GC is isotropic both in position and momentum. On the **right** are the final momentum directions since the field is uniform in the x-direction, and the particles are gyrating in the $y-z$ direction their momentum in the x direction remains unaffected resulting in an overall isotropic distribution for the final momentum directions.

turbulent magnetic fields on the UHECR propagation, it is useful to study their effects separately and combined on the trajectory of an UHECR and the magnification maps. This will be done in the following fashion:

1. In Section 3.2.2 the selection of UHECR sources and the energy and species of the UHECRs utilised for this study is introduced motivated by observations.
2. In Section 3.2.3 the effect of the pure structured component of the GHB model will be studied on the trajectory of 40 EeV nitrogen UHECR and the magnification map of 1 million backtracked UHECRs of the same species. The parameter values adopted for this will correspond to the best-fit values of the structured field component provided in table 3.1.
3. In Section 3.2.4 the same effect as above will be studied for the pure turbulent

component of the GHB model with the best-fit parameter value provided in table 3.1.

4. Finally, in Section 3.2.5 the full GHB model structured plus turbulent, will be utilised to propagate UHECRs. The magnification maps and arrival direction skymaps for two potential sources (motivated in Section 3.2.2) will be investigated for the best-fit, minimum and maximum parameter values (see table 3.1).

3.2.2 Selection of sources of UHECRs and motivation behind choosing nitrogen as UHECR composition

UHECRs encounter two types of magnetic fields upon leaving their sources one being extragalactic and the other Galactic, both of whose structure, origin, and strengths are not well known. The extragalactic magnetic fields are considered to be weak in comparison to GMFs ([143, 144]), with ***speculated*** coherence lengths of $L_{\rm coh} \sim 1$ Mpc[‡] for $B <$ nG.

UHECRs with energy $E > 10^{19}$ eV in weak (< nG) extragalactic magnetic fields with $r_L > 10$ Mpc experience a deflection of $\theta \approx L_{\rm coh}/r_L < 6^\circ$ for each coherence length. Thus, the angular deflection expected from UHECRs propagating from local (< 4 Mpc) sources a few coherence lengths away is $\lesssim 10^\circ$. In comparison, within the Galactic magnetic field structure, the strength of the mean magnetic field in the halo can be of the order of 5 μG. An UHECR with rigidity, $R = E/Ze$ of 10 EV in a 5 μG magnetic field, will have a Larmor radius of $r_L \approx 2$ kpc. Within this rigidity range UHECRs from a local source (within 4 Mpc) will pick up the largest angular deflection from their original source direction upon propagating through the large-scale structured component of the Galactic magnetic fields. Thereby making the arrival directions (the distribution of cosmic rays on the sky as seen by an observer) of these UHECRs observed on earth for example by PAO [§] not their true source directions thus making identification of UHECRs' sources difficult. However, the skymaps of the arrival directions of UHECRs as seen by PAO can be used as a motivation to choose potential sources. In Figure 3.6, the arrival directions of 40 EeV or 6 EV UHECRs as measured by PAO are shown [93, 95]. This skymap shows two hotspots which are around the region of Centaurus A or **Cen A** in the **Northern Hemisphere** with its coordinates being at longitude (lon) = −50.49°, and latitude (lat) = 19.42° and **NGC 253** in the **Southern Hemisphere** lon = 97.36°, lat = −87.96° A detailed discussion about these two potential source types has been provided in Chapter 1 in Section 1.6. The analysis

[‡] 1 pc = 3×10^{18} cm
[§] https://www.auger.org/

by the PAO collaboration hints that at this energy range the UHECRs are dominated by **nitrogen** in composition [145].

Drawing on the observations by PAO for the work done in this thesis, both Cen A and NGC 253 were treated as potential sources of UHECRs and the choice of species of UHECRs and their energy range was chosen to be nitrogen at 40 EeV.

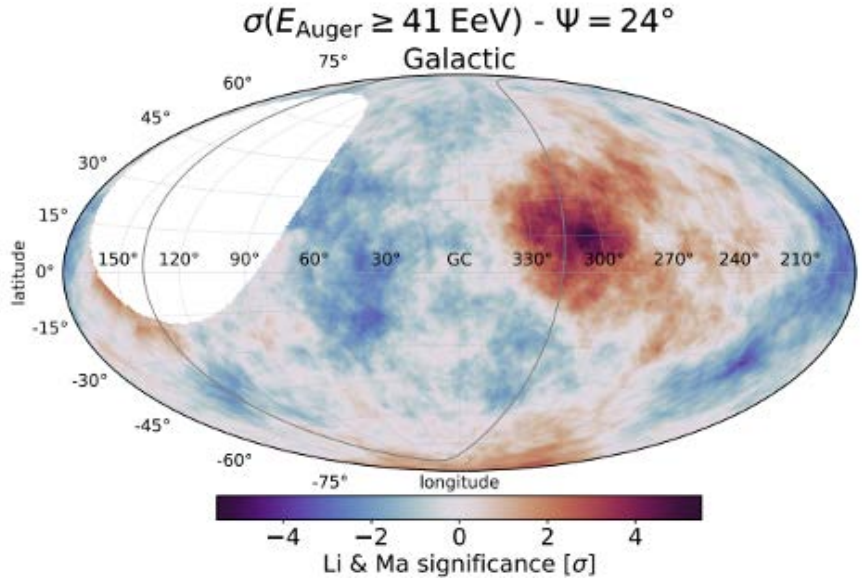

Figure 3.6: Arrival direction skymap as observed by PAO for E ≥ 38 EeV for a top hat smoothening of 24°. The two hotspot regions are speculated to be associated with Cen A and NGC 253 [93]. At this energy range most of the UHECR composition is nitrogen dominated [145].

3.2.3 Case 1 - GHB structured fields

Utilising the structured component of the GHB magnetic field model (see table 3.1) for magnetic field strength of $B_{\text{str}} \approx 4$ μG and spatial parameters $R_{\text{Mag}} = 5$ kpc and $Z_{\text{Mag}} = 6$ kpc trajectory plot of UHECR nitrogen at 40 EeV shows the position and momentum directions in Figure 3.7. The particle was backtracked starting from Earth up until the termination radius of $R_{\text{term}} \approx 20$ kpc. The toroidal nature of the structured component of the GHB magnetic field implies that it is not completely uniform in one direction. Therefore, the particle only covers a fraction of the circular orbit for the velocity while in the position it completes a fraction of the spiral part whilst moving through the magnetic field. Structured magnetic fields affect the propagation of UHECRs in different ways to turbulent fields (the latter being discussed in the Section 3.2.4). This effect will also be evident in magnification maps of the final momentum directions of these particles. In order to create such a map, 1 million UHECRs (nitrogen at 40 EeV) starting with an

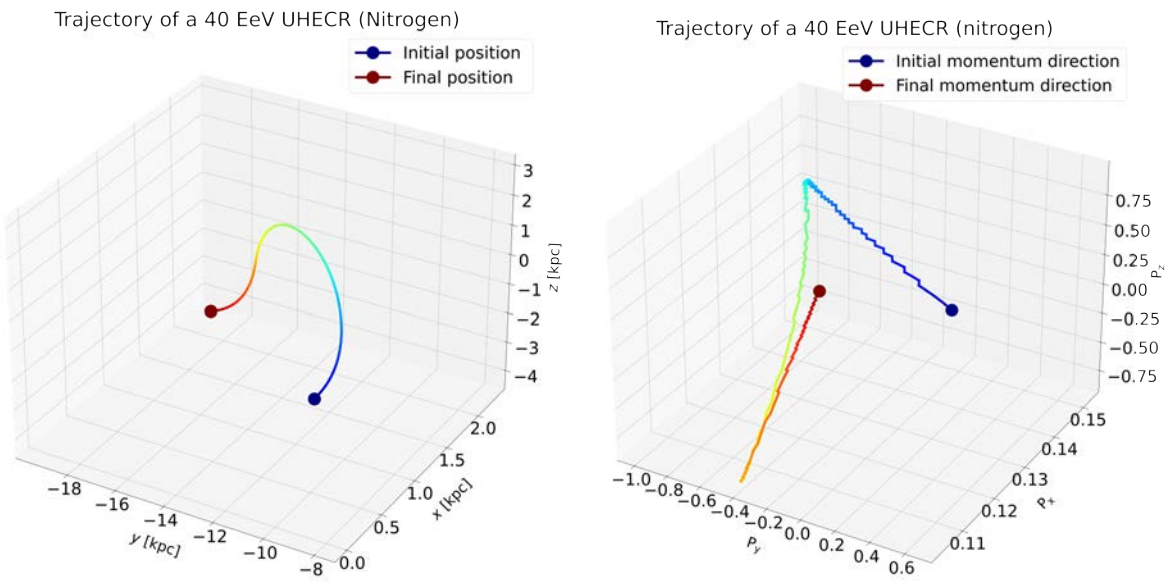

Figure 3.7: Figure shows trajectory of a 40 EeV nitrogen cosmic ray particle for both position (left) and momentum direction (right) for only structured field $B_{\text{str}} \approx 4\ \mu$G respectively. Since the field is not uniform but has a toroidal spatial geometry. The particle does not complete a full Larmor radius in velocity and changes direction as it propagates through the large-scale field. The change in direction of the particle dictates both its position and momentum direction.

isotropic distribution in momentum and delta distribution in position at Earth were backtracked through only the structured component of the GHB ($B_{\text{str}} \approx 4\ \mu$G) using CRPropa3. The pure structured fields ($B_{\text{str}} \approx 4\ \mu$)G of the GHB model have large-scale geometry which deflects the UHECRs greatly thereby pushing them mostly to the sides where the strength of the structured fields are weak. This results in a deficit of UHECRs in the GHB region where the field strength is strongest and an abundance beyond the GHB region for longitudes $> \pm 90°$ (see **right** Figure 3.8). Note that for very large statistics it is possible to fill in the white void regions of the pure structured field map, however this requires extremely long computation time¶.

In the context of arrival direction skymaps the structured magnetic fields result in the **coherent deflection** of the arrival directions from the original position. As already shown in this section large-scale fields push or deflect particles resulting in a deflection from the original particle trajectory. This effect will be discussed in greater detail in the next section Section 3.2.5.

¶ **Note:** According to Liouville's theorem if there is an isotropic extragalactic distribution of UHECRs then at Earth one also observes an isotropic distribution of UHECRs. However, the vice-versa of this scenario is not true because during backtracking of UHECRs starting with an isotropic distribution in momentum and delta distribution in position at Earth. In this case the UHECRs that would not reach Earth have not been taken into account. This is discussed in greater detail in Chapter 4 in Section 4.3.1.

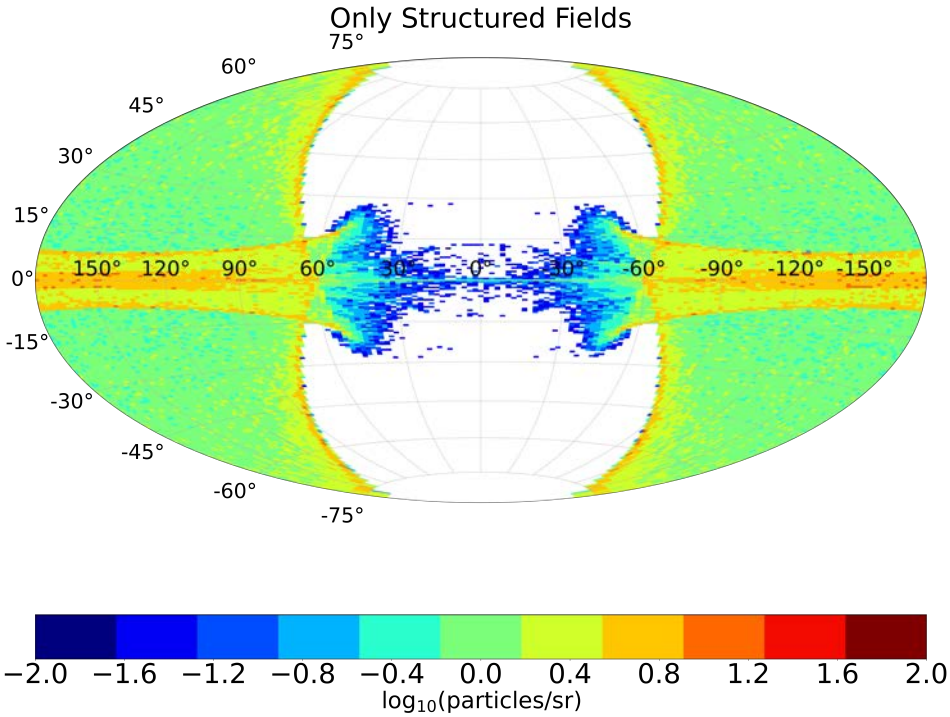

Figure 3.8: The magnification map for UHECRs for 40 EeV UHECR (nitrogen) created for only the structured component ($B_{\text{str}} \approx 4\ \mu$) of the GHB model. The large-scale toroidal geometry of the GHB model deflects the UHECRs greatly and pushes the final directions to the edges of the map. The white region is the area where the structured magnetic field is the strongest and the UHECRs are *unable to live* in this region.

3.2.4 Case 2 - GHB turbulent fields

Similar to the previous section the effect of turbulent magnetic fields was also studied for the trajectory of a single UHECR (nitrogen) at 40 EeV for the RMS value of $B_{\text{tur}} = 7\ \mu$G backtracked from Earth. The trajectories of the particles for both the position and momentum direction has been shown in Figure 3.9. In case of turbulent magnetic fields the UHECR nitrogen continuously changes velocity directions and ceases to have any circular orbit, thus the particle never completes a Larmor radius. Likewise, in the positions the particle random walks as well due to the constantly changing momentum directions.

Similar to the case of pure structured fields, 1 million UHECRs (nitrogen at 40 EeV) starting with an isotropic distribution in momentum and delta distribution in position at Earth were backtracked through the purely turbulent component of the GHB magnetic field ($B_{\text{tur}} \approx 7\ \mu$G). In Figure 3.10 the magnification map at the termination sphere due to only the turbulent component of the GHB magnetic field model is shown. These maps are normalised relative to results obtained without magnetic fields with the same total number of events. In the turbulent field ($B_{\text{tur}} \approx 7\ \mu$)G, case we start with an initial isotropic distribution of UHECR directions. The final arrival directions of the UHECRs

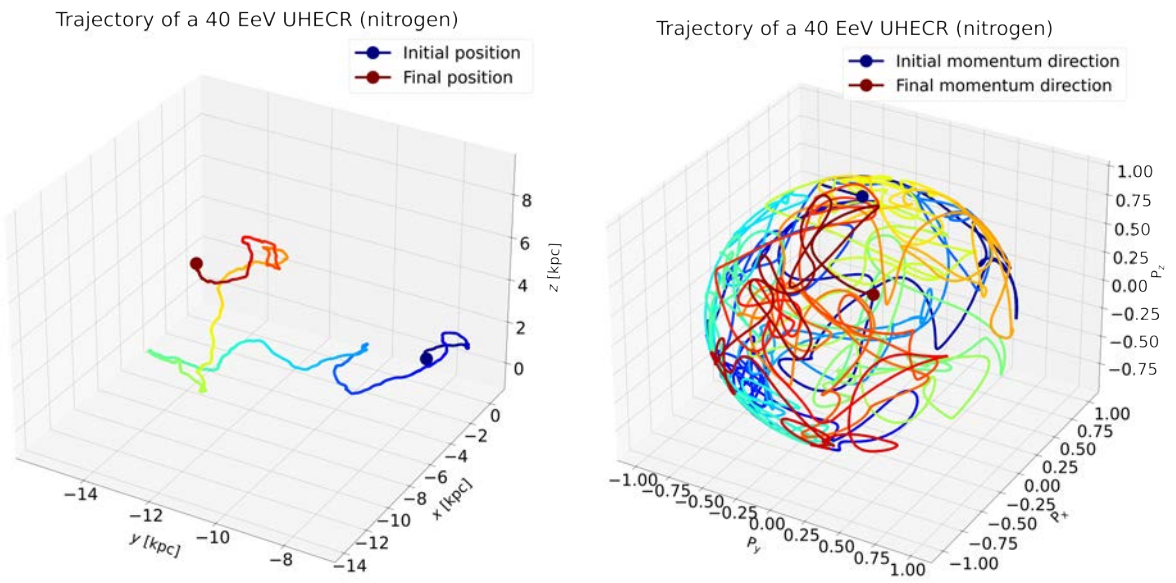

Figure 3.9: Trajectory of a 40 EeV nitrogen cosmic ray particle for position (left) and momentum (right) for only turbulent field $B_{\text{str}} \approx 7\ \mu$G. The particle continuously changes its momentum direction due to the random distribution of magnetic field direction which leads it to do a random walk in position.

after propagating through the GHB turbulent magnetic field model are also isotropic. This is because of the lack of any large-scale field geometry, the small-scale nature of turbulent magnetic fields are unable to deflect the UHECR particles by large deflection angles. This results in a magnification map which is isotropic (see Figure 3.10).

In the context to the arrival directions skymaps the turbulent magnetic fields result in what is called as the **spreading effect**. The particle random walks in momentum directions resulting in the arrival directions being spread out on the skymap. This effect will be discussed in greater detail in the next section Section 3.2.5.

3.2.5 Case 3 - Full GHB model fields

Starting with an isotropic momentum distribution and delta distribution in position at Earth, 4×10^7 nitrogen cosmic rays with rigidity $R = 6$ EV were pushed through the GHB magnetic field model to a termination radius of 30 kpc from the Galactic center (GC). This dimension of the simulation box was chosen such that the results remain insensitive to it. This ensured that the Larmor radius of the UHECR at this distance was an order of magnitude larger than the box size, for the strongest magnetic field case considered. The cosmic ray species choice of nitrogen was based on the composition measurements by PAO [146] and the rigidity choice was motivated by the arrival-direction correlations with

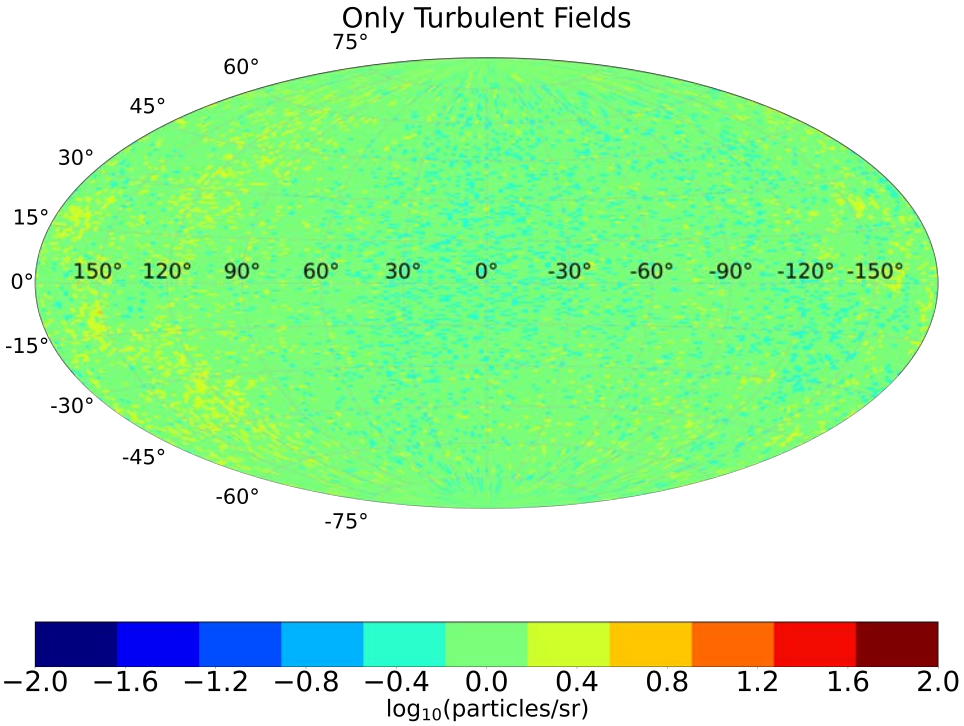

Figure 3.10: The magnification map for 40 EeV UHECR nitrogen created by normalising the final arrival directions to the initial directions of the UHECRs. This map was created for only the turbulent component ($B_{\text{tur}} \approx 7\ \mu$) of the GHB model and since we start from an isotropic distribution at Earth the final arrival direction in the skymap looks isotropic as well. This is because the small-scale turbulent magnetic fields are unable to deflect particles by a large deflection angle.

nearby galaxies measured by PAO [93, 95]. The same simulation was also repeated for 40 EeV UHECR protons which will be discussed in Section 3.4.

3.2.6 Magnification maps and arrival direction skymaps from the GHB model

In Figure 3.11 the magnification map and the arrival direction skymap obtained for the best-fit, minimum or lower bound and maximum or upper bound parameter set is shown. The list of values utilised for each parameter set is provided in table 3.1. The explanation of each column of the Figure 3.11 is as follows:

1. In the **Left column:** magnification maps in (log(particles/sr)) show the regions where cosmic rays are suppressed in blue and enhanced in orange regions. These maps were created based on the best fit (**top**) 'Minimum' (**bottom**) and 'Maximum' (**middle**) values respectively obtained in Chapter 2, (see table 3.1) for values with the two potential sources of UHECRs Centaurus A (Cen A) and NGC 253 denoted by coloured ★. For reference a magnification map for the JF12 toroidal halo was also

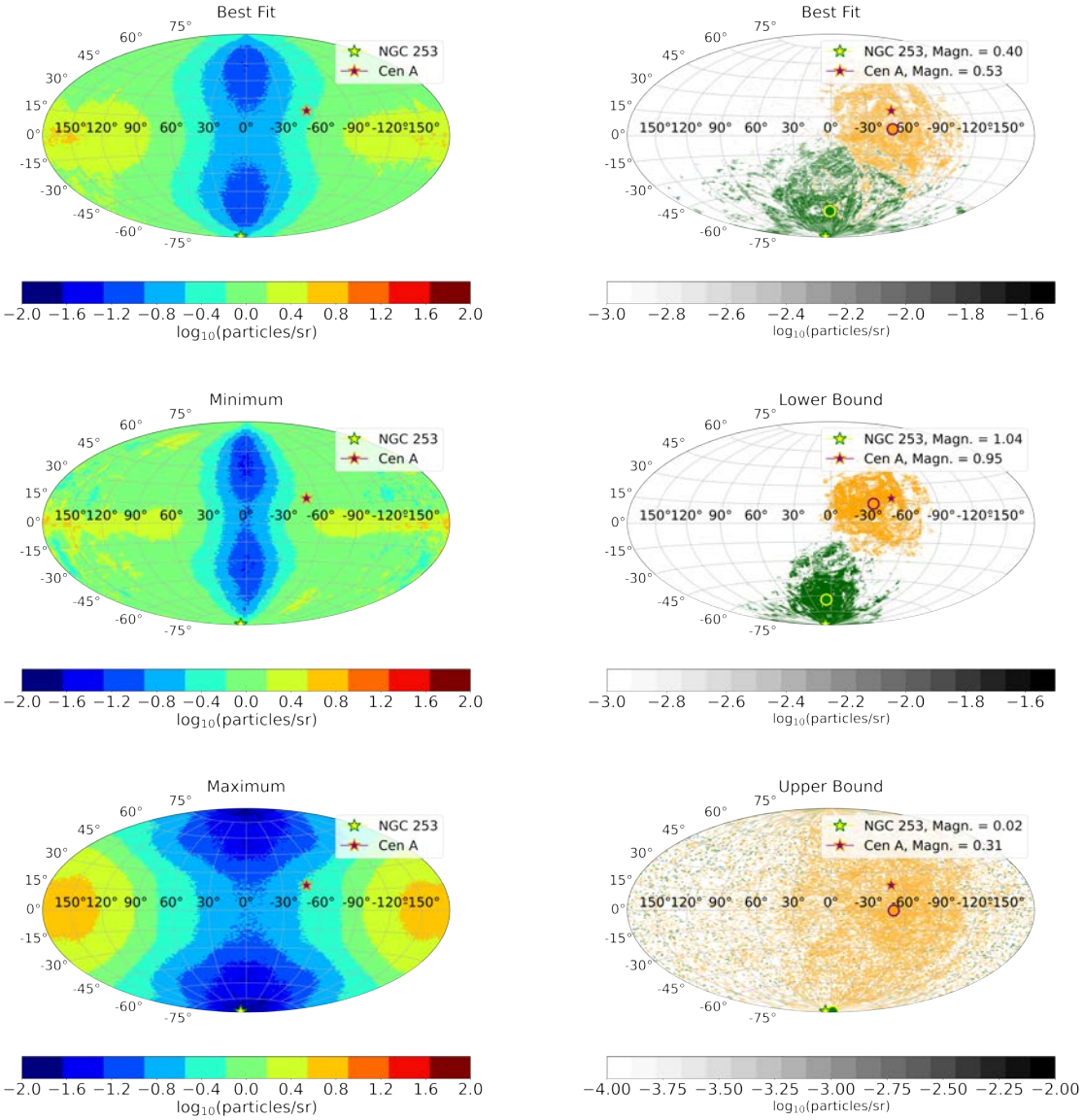

Figure 3.11: Left: magnification maps of the extragalactic sky obtained by backtracking an isotropic distribution of UHECRs (with $R \approx 6 \times 10^{18}$ V) from Earth. These maps were normalised by the results obtained without magnetic fields for the same number of events. **Right**: the binned arrival directions of the cosmic rays (with $R \approx 6 \times 10^{18}$ V) from two potential UHECR candidate sources: Cen A and NGC 253. In the legend for both sources, the ratio ('Magn.') of the number of backtracked cosmic rays within 5° from the source location for the GHB magnetic field model, to the equivalent number obtained when no magnetic fields are present is provided. The number of particles in each bin were again normalised by the peak value of a binned histogram obtained in the absence magnetic fields, as represented by the grey colour bars. The mean direction in each plot is denoted by a ●. **Top row:** results obtained for best-fit values of the GHB magnetic field parameters, **middle row:** lower bound GHB magnetic field parameters & **bottom row:** upper bound GHB magnetic field parameter (see table 3.1).

created for comparison purposes (see bottom Figure 3.13). Note that these maps may get affected due to magnetic fields in the Galactic disc and lower Galactic latitudes ($|b| < 15°$). However, since the focus of this work is the GHB, no disc magnetic field model was utilised.

2. In the **Right column:** arrival direction skymaps of cosmic rays for two potential sources of UHECRs Cen A and NGC 253 are shown. Similar to the magnification maps, the **top**, **middle**, and **bottom** maps show the 'Best-fit', 'Minimum' and 'Maximum' cases, respectively. Like the magnification maps, the magnification numbers/normalised numbers of the number of hits are provided in each map as 'Magn.' in the legend.

3.3 Understanding results

As shown previously, UHECR deflections are dependent on both the structured and turbulent magnetic field components in separate ways. There are three primary effects that are worth noting:

1. **Suppression effect:** Cosmic rays from specific parts of the sky can undergo significantly large suppressions for the 'Maximum' parameter case for the GHB model in comparison to the 'Best-fit' and 'Minimum' cases (see Table 3.1). The enhancements and suppressions of UHECRs can also be seen in the magnification maps for specific potential sources, namely Cen A (lon = −50.49°, lat = 19.42°) and NGC 253 (lon = 97.36°, lat = −87.96°). Due to the sky coordinates both Cen A and NGC 253 lie in the suppression regions of the sky for both 'Best-fit' and 'Maximum' parameter cases. It should be noted that in the case of NGC 253 the CRs are suppressed down to ≈ 2% of the level that would arrive for the no magnetic field case, and ≈ 31% for Cen A.
2. **Spreading effect:** Turbulent magnetic fields result in the spreading of the CRs around their original source position, this effect was measured by looking at the mean spread (σ_{source}) for each source and each parameter set. The value of σ_{source} was estimated as the average spread between the mean direction and the arrival directions of the UHECRs. The table below shows these value for 'Best-fit', 'Minimum' and 'Maximum' cases respectively.

   * Best fit - $\sigma_{\text{NGC 253}} = 32°$, $\sigma_{\text{Cen A}} = 33°$
   * Minimum - $\sigma_{\text{NGC 253}} = 16°$, $\sigma_{\text{Cen A}} = 21°$
   * Maximum - $\sigma_{\text{NGC 253}} = 80°$, $\sigma_{\text{Cen A}} = 59°$

   When compared with the JF12 toroidal halo field model (Section 3.3.1, Figure 3.13) for the same rigidity particles the mean spreads were the following for NGC 253 and Cen A:

   * $\sigma_{\text{NGC 253}} = 10°$ and $\sigma_{\text{Cen A}} = 20°$.

The inclusion of a disc field (JF12 disc field in this case) had a less than 1° effect on these results which was found to be consistent with previous studies [71, 113].
The GHB model produces potentially considerably larger (up to 5-10 times bigger) spreads than the JF12 model. One of the main reasons for this difference between the JF12 toroidal halo model and the GHB model is that the latter consists of larger levels of turbulent magnetic fields than structured fields, as derived from the parameter scan in Chapter 2, (see 3.1 for values adopted).
Comparing these with PAO observations, it should be noted that the GHB model presented here obtains $\sigma_{\text{Cen A}} = 33°$ which is found to be comparable with the PAO observations to the size of the hotspots in Figure 3.6, [93, 98].

3. **Coherent deflection:** The structured fields on the other hand are responsible for the effect that dictates the mean direction in which the cosmic rays collectively deflect from the original source direction. The **new** mean **shifted** source positions (lon, lat) for the two potential sources NGC 253 and Cen A for the three cases are as follows:

   * Best fit - NGC 253: (2°,−63°) & Cen A: (−50°,5°)
   * Minimum - NGC 253: (7°,−63°) & Cen A: (−35°,15°)
   * Maximum - NGC 253: (−39°,−88°) & Cen A: (−50°,−0.2°)

   In comparison the new mean shifted positions obtained for the JF12 halo model for NGC 253 was (−0.8°,−34°) and for Cen A was (−44°,−1°).

A schematic representation of deflections for UHECRs from NGC 253

In order to understand the deflection of UHECR due to a toroidal magnetic field, one can focus on sources lying in the Galactic south, for example NGC 253 shown by a ★ in Figure 3.12. Ampere's right-hand thumb rule states that a current flowing in a circular loop induces a current perpendicular to the magnetic field in that loop. In the case of the toroidal field as shown in the schematic diagram in Figure 3.12, the current $\vec{J}$ (in purple) is directed perpendicular to the direction of the field. For UHECRs coming from the Galactic south (z) the current of the particles shown by the velocity/momentum vectors $\vec{v}_z$ (in pink) will interfere with the current, $\vec{J}$. By virtue of Fleming's hand rule the force directed on the UHECRs will be in the x-y direction as shown in the figure. Therefore, particles coming from the Galactic south will get deflected towards the equator lower latitudes as is the case with the arrival direction skymap in Figure 3.11 and the ones coming from the Galactic north will experience the same effect.

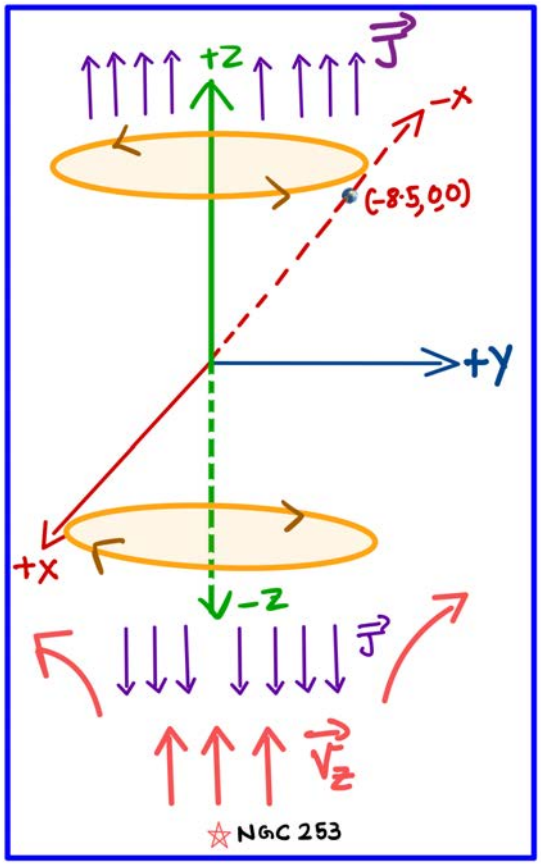

Figure 3.12: A schematic representation explaining deflections from the toroidal component of the GHB model with the Earth at -8.5,0,0 kpc from the GC and a cross-section of the toroidal field is shown in orange. A source like NGC 253 situated at the $-z$ direction experiences the current $\vec{J}$ (in purple) due to the toroidal magnetic fields, by Fleming's hand rule, the velocity vectors $\vec{v}_z$ (in pink) of the UHECRs coming from NGC 253 thus get pushed in the $x-y$ plane, resulting in the hotspot potentially linked to it [93, 95].

3.3.1 Comparison to other magnetic field models

As stated earlier, the arrival directions of cosmic rays (nitrogen at 40 EeV), for the JF12 toroidal halo and JF12 toroidal halo and X-field combined model, shown in Figure 3.13 were also calculated for the two candidate sources, Cen A and NGC 253. These maps were also normalised by the same method given in Section 3.2.5. The mean shifted positions obtained from only the JF12 toroidal halo model for the two sources are (−0.8°,−34°) for NGC 253 and (−44°,−1°) for Cen A, and the new mean spread from Cen A and NGC 253 are $\sigma_{\text{NGC 253}} = 10°$, and $\sigma_{\text{Cen A}} = 20°$.

The mean shifted positions obtained from the JF12 toroidal halo and X-field model for the two sources are (lon = −29°, lat = −27°) for NGC 253 and (lon = −72°, lat = −0.4°) for Cen A, and the mean spread from NGC 253 and Cen A are $\sigma_{\text{NGC 253}} = 12°$, and $\sigma_{\text{Cen A}} = 18°$.

It can be seen from the top row in Figure 3.13 that the JF12 toroidal halo displaces the

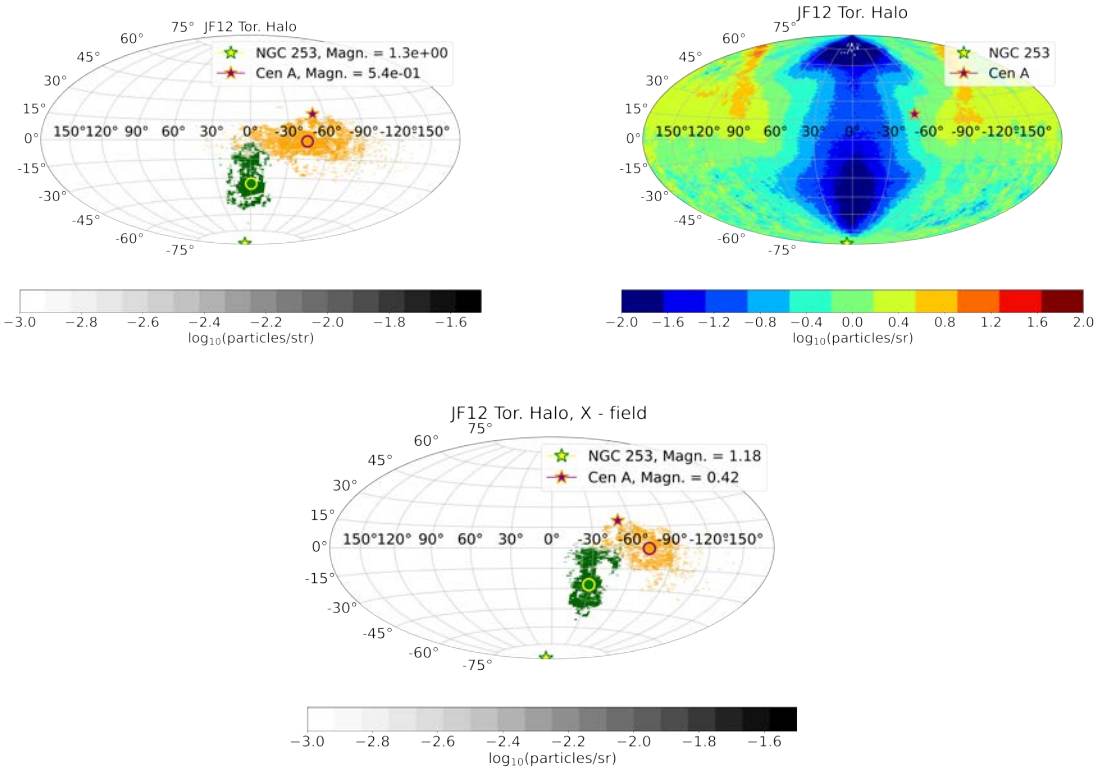

Figure 3.13: Top left: The magnification map for the JF12 toroidal halo with the sources NGC 253 and Cen A marked as ★ similar to the plots shown in Figure 3.11.**Top right**: Arrival direction map of cosmic rays (with $E \approx 40 \times 10^{18}$ eV) deflected from the JF12 toroidal halo model for two potential UHECR sources. It can be seen that the mean shifted direction of the deflection for the JF12 toroidal halo is at a higher latitude than for the best-fit GHB magnetic field model, shown in Figure 3.11.
Bottom: The arrival directions for UHECRs (with $E \approx 40 \times 10^{18}$ eV) from the JF12 toroidal halo and X-field combined. The mean shifted direction for the two potential shifts also in longitude due to the X-fields.

binned arrival directions to much higher latitudes in the case of NGC 253. This behaviour of the JF12 toroidal halo occurs due to the structured field strength in the JF12 toroidal halo being stronger than the turbulent field and hence the mean deflection from the source position is larger.

Additionally, if the JF12 toroidal halo is combined with its X-field, then arrival directions from NGC 253 also shift in latitude [71]. It should be noted that the combined JF12 toroidal halo and X-field are unable to reproduce the Auger hotspot for NGC 253 (see bottom Figure 3.11) [93, 95].

The same method was applied as well to study the UHECR deflections (nitrogen at 40 EeV) for the XH19 model. In this case, the mean shifted positions obtained for NGC 253 and Cen A are (1.2°,–29°) and (–48°,–5.1°), respectively. The high latitude deflections obtained from the XH19 model is due to the presence of structured magnetic fields which results in only the coherent deflection cosmic rays. The absence of turbulent fields results

in a negligible mean spread in the UHECR arrival directions. Thus, assuming that if NGC 253 is indeed a source of UHECRs both of these models are unable to reproduce the hot spot seen by PAO in the Galactic south whereas both the lower bound and best-fit parameter set of the GHB magnetic field model are able to recreate this hotspot. In table 3.2, a tabulated list of the new mean shifted source positions and the mean spreads for different models is provided for the case of UHECR nitrogen species. Note that the mean spreads were not calculated for the XH19 model.

3.4 Deflection of UHECR proton through GHB model

The effect of the GHB magnetic field model was also studied on 40 EeV protons for the 'Best-fit' case and the upper-bound ('Maximum') case (see Fig. Figure 3.14) for the GHB magnetic field model was also computed. The mean spreads obtained are as follows:

* Best fit - $\sigma_{\text{NGC 253}} = 5°$, $\sigma_{\text{Cen A}} = 8°$,
* Maximum - $\sigma_{\text{NGC 253}} = 12°$, $\sigma_{\text{Cen A}} = 17°$.

The mean shifted positions after the coherent deflection through the GHB magnetic field model are:

* Best fit - NGC 253: (10°,–83°) & Cen A: (–47°,20°),
* Maximum - NGC 253: (6°,–61°) & Cen A: (–30°,17°).

These skymaps for the arrival directions of different species (like proton) can therefore be helpful in studying the effect of the magnetic fields in the Galactic halo bubbles on different cosmic ray species. With mean spreads for the 'Best-fit' model of $\sigma_{\text{NGC 253}} = 5°$ and $\sigma_{\text{Cen A}} = 8°$, the deflections for this scenario are significantly reduced compared to the

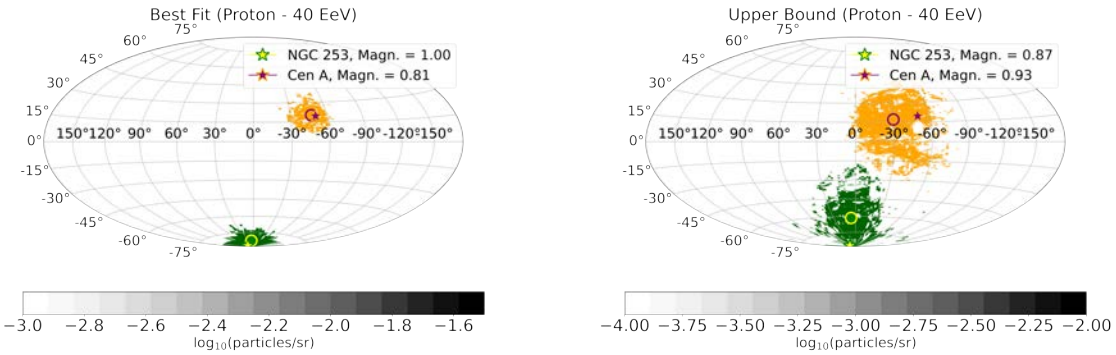

Figure 3.14: Arrival direction map of cosmic ray protons (with $E \approx 40 \times 10^{18}$ eV) for the best fit case (**left**) and upper bound case (**right**) of the GHB magnetic field model.

nitrogen case. The purpose of this study was to make future predictions for AugerPrime [101, 102] whose main goal would be to identify the species of UHECRs on an event by event basis.

3.5 Deflection of UHECRs from potential sources on a grid

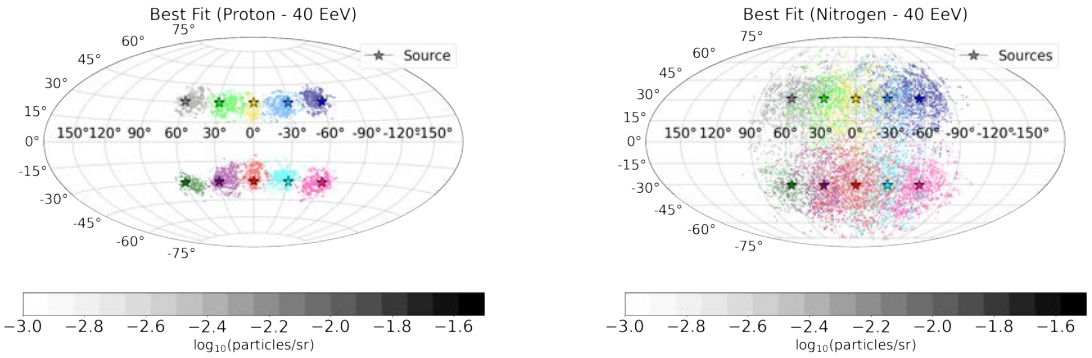

Figure 3.15: Figure above shows cosmic ray arrival directions due to deflections from the best-fit parameter set of the full GHB magnetic field model for 40 EeV proton and nitrogen for potential sources (★) on a grid. The arrival directions of CR protons (left) are more compact than the ones from nitrogen (right) as the former has a larger Larmor radius and remains unaffected by the magnetic fields. These predicted arrival directions can be extremely useful for AugerPrime [101, 102] in the future as it will be able to do an event by event separation of cosmic ray species.

Lastly, 10 potential sources of UHECRs were placed on a grid as shown by the ★ on Figure 3.15. Note that these are arbitrary source choices mostly for a theoretical study. 1 million UHECRs were backtracked from Earth through the best-fit parameter (see first column in 3.1) set of the GHB magnetic field model. The arrival directions were plotted as a ratio of the number of backtracked cosmic rays within a 5° region from the source location (in the presence of the GHB field) to the equivalent number obtained in the absence of GHB fields. The number of particles in each bin is again normalised by the peak value of a binned histogram obtained without magnetic fields, as represented by the grey colour bars. The coloured ★ denotes the potential source position of the UHECR and the binned arrival directions are in the same colour as the star for each source. The mean spreads noted from these 10 sources was between 15° – 20° for the 40 EeV nitrogen and the mean spreads from 40 EeV proton was between 5° – 8°. Thus, the size of the mean spreads can change significantly as the UHECR species is changed. This conclusion is similar to what is seen in Section 3.4. The deflection of the UHECRs for different sources will be different based on their position on the sky. For instance, if one compares the left-most dark blue source with the right-most grey source, the deflections seen on the skymap from the latter are directed towards the right, whereas for the blue source deflections are

directed towards the left. Though not motivated observationally, sources on a grid can be utilised for future observations of UHECR sources. The predicted arrival directions from the grid sources will be useful in the future for comparisons with the observations made by AugerPrime [101, 102], which will be able to separate UHECR compositions on an event by event basis.

3.6 Conclusions and outlook

Note that results from this work were published as a part of the peer-reviewed article [1].

UHECRs were propagated through the GHB magnetic field model for the best-fit, minimum (lower-bound) and maximum (upper-bound) parameter values to study its effect on the magnification maps and arrival direction skymaps. A significant amount of suppression can be seen in the Galactic halo bubble region from the magnification map especially for the maximum cases. This result is significant for potential UHECR sources lying in the GHB region parameterized by the upper-bound parameters as the cosmic rays in this case will be highly suppressed.

Assuming that Cen A is a potential source of UHECRs (see [54, 130]) the spread obtained by the GHB bubble model ($\sigma_{\text{Cen A}} = 33°$) is qualitatively comparable to the 24° spread suggested by PAO [93].

Similar to the spread from Cen A, the spread from NGC 253 for the GHB bubble was ($\sigma_{\text{NGC 253}} = 32°$) also comparable to PAO results. As shown in the case of the JF12 toroidal halo (see Section 3.3.1 Figure 3.13), the new mean shifted position for the deflected cosmic rays from NGC 253 was found situated at a latitude of −34° (also seen in [99]). The number was in contrast with the 'Best-fit' case value of approximately −63° from the GHB magnetic field model. The number from the GHB magnetic field model was found to be in agreement with the PAO observations [99] also assuming that the hotspot originating in the southern Galactic hemisphere originates from NGC 253.

The difference in the hotspots from the GHB magnetic field model and the JF12 toroidal halo arises due to the higher level of turbulent magnetic fields in comparison to the structured magnetic fields in the GHB magnetic field model (see Table 3.1). In comparison, the JF12 toroidal halo has stronger structured magnetic fields which also dictates the extent of the mean spread from the source position.

Table 3.2: The new mean shifted source positions ($< l, b >$) and mean spreads from 40 EeV UHECR nitrogen for the 3 cases of the GHB model and other magnetic field models (JF12 and XH19) for two potential sources of UHECRs, NGC 253 and Cen A.

Model	$\sigma_{\text{NGC 253}}$	$\sigma_{\text{Cen A}}$	$< l, b >_{\text{NGC 253}}$	$< l, b >_{\text{Cen A}}$
Best-fit	32°	33°	2°,−63°	−50°,5°
Minimum	16°	21°	7°,−63°	−35°,15°
Maximum	80°	59°	−39°,−88°	−50°,−0.2°
JF12 tor. halo	10°	20°	−0.8°,−34°	−44°,−1°
JF12 tor. halo + X	12°	18°	−29°,−27°	−72°,−0.4°

The skymaps from the 'Best-fit' and 'Minimum' parameter cases clearly indicate some level of association of the deflected UHECRs with their potential original source position. However, source information is completely lost in the 'Maximum' or upper bound parameter case of the GHB model. The main reason for this distinction between the two scenarios is that structured fields dictate the overall direction of deflection for the cosmic ray particles (**coherent deflection**), whereas turbulent fields in the 'Maximum' case are responsible for the spreading out of the arrival directions around the overall deflected region (**spreading effect**). The large strength of turbulent magnetic fields thus washes out any information about the parent source directions for these particles. Once again, if the PAO skymaps do correlate with the potential UHECR sources Cen A and NGC 253, the data seems to favour smaller (**coherent deflection**) deflections of UHECR arrival directions implying that the strength of the structured magnetic field may be weaker than the turbulent field. The suppression spreading and coherent deflection effects introduce several challenges in associating the UHECRs to their parent sources. This is specially evident for the 'Maximum' parameter set for the GHB model, since source association cannot be established for the UHECR arrival directions.

Note that if the starburst Galaxy NGC 253 is a potential UHECR source and PAO hotspots are correlated to NGC 253 then the 'Maximum' case can be utilised as an observable to constrain the magnetic fields in the GH. The 'Maximum' case has $B_{\text{tur}} \geq 10$ μG (see the 1-σ parameter space study in Chapter 2 Section 2.4.4), with strong turbulent magnetic field values; the PAO skymap cannot be recreated due to the *"washing out"* of UHECR arrival directions (for NGC 253 see Figure 3.11). The cosmic rays underwent large levels of deflection resulting in a mean spread of $\sigma_{\text{NGC 253}} = 80°$ which spans across the entire map (b = ±90°). Similarly, for sources like Cen A, the mean spread is $\sigma_{\text{Cen A}} = 59°$, which also inhibits association of a potential source to these cosmic rays since the spreading of

the arrival directions jumbles any information about the source direction.

In this study the Telescope Array (TA) skymaps [147, 148] could not be utilised since the region of the sky that TA observes lies at larger longitudinal values which does not lie within the GHB region that this work focusses on. The constraints on both the Galactic magnetic field and UHECR potential sources will improve immensely with the first light of AugerPrime [102] which will be able to measure UHECRs on an event by event basis. Additionally, the proposed Global Cosmic Ray Observatory (GCOS) will enhance the exposure region by an order of magnitude thereby enabling higher statistics and will have larger sensitivity [88].

New observations of the circumgalactic medium of external galaxies [42] and thermal X-ray observation of the Milky Way [52] show strong evidence of an extended hot Galactic halo ranging up to ≈ 250-300 kpc with thermal pressure of 0.1 eV/cc. Assuming equipartition were to hold in such a case, field strengths could be as high as ≈ 0.1 μG at these large distances. Should this indeed be the case the propagation of UHECRs within our Galaxy would not only be affected by the Galactic magnetic fields but also by the extended Galactic halo [54]. In the future this idea will be taken forward and the GHB model will be extended to study the effect of magnetic fields in the extended Galactic halo on propagation of UHECRs.

Propagating of an extragalactic UHECR dipole through GHB turbulent magnetic fields

4

In this chapter, the focus will be on the propagation of an extragalactic dipole only through the turbulent magnetic field component of the GHB model introduced in Chapter 2. The suppressed dipole strength measured by the observer will be explained by an analytical electrostatic analogy.

4.1 Evidence for anisotropies in UHECR arrival directions

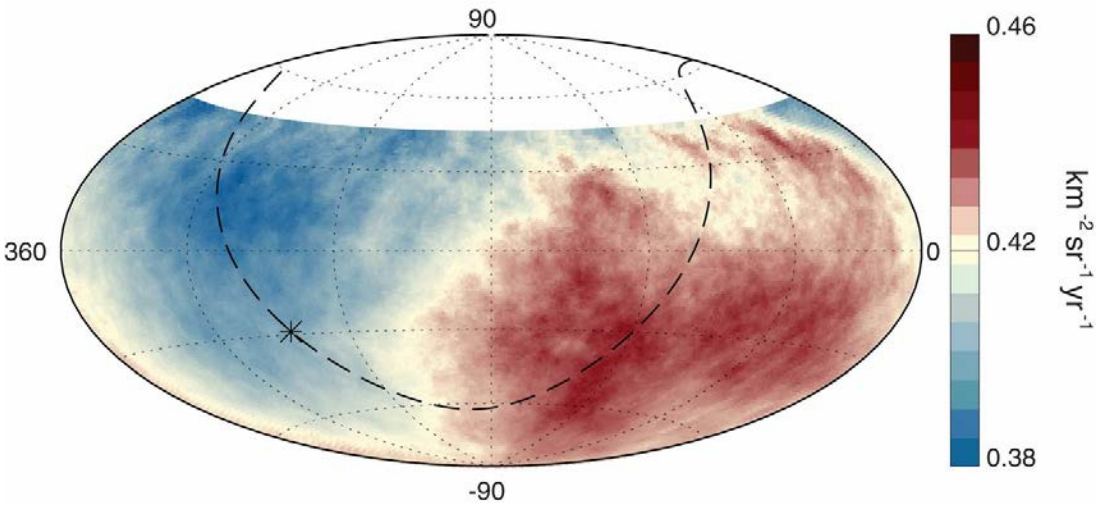

Figure 4.1: The UHECR dipole skymap in equatorial coordinates as seen by PAO at 8.5 EeV with the Galactic plane shown by the dotted line. The dipole observed is roughly at a ≈ 7 % level with 5.2σ confidence level, figure obtained from [92, 93].

Results from PAO [92, 93] indicated the presence of an anisotropy in the form of a large-scale dipole* in the distribution of arrival directions of UHECRs above 8 EeV. The magnitude of the dipole was measured with a confidence level of 5.2σ at ≈ 7 % away from the Galactic centre, suggesting that the origin of such a dipole could be extragalactic [93]. While the reason for an anisotropy in the arrival directions of UHECRs is not well understood, one leading explanation suggests that an anisotropy in the distribution of UHECR sources could result in an anisotropy in the arrival directions of UHECRs [92, 93]. In Figure 4.1 the UHECR arrival directions for energy ≥ 8 EeV measured by PAO show the exposure-weighted average of the flux within a top-hat window of radius 45°. This is done to exaggerate the large-scale features. Figure 4.1 shows that above energies of 8 EeV

* A brief discussion of a pure dipole is presented in Section A.1, Chapter A.

the excess flux comes from a region of right ascension $\approx 100°$, with a corresponding flux deficit in the opposite direction.

4.2 Propagating a dipole through GHB turbulent magnetic fields

We know from observations that the dipole observed by PAO is at a 7% level. This strength is not the true dipole amplitude at the time of injection into the Galaxy. The Galactic magnetic fields affect the extragalactic dipole ($\delta_{\rm EG}$) in two ways: the large-scale structured component changes the extragalactic direction of $\delta_{\rm EG}$ and the small scale turbulent magnetic fields (with RMS value of $B_{\rm tur}$) suppress the strength of the $\delta_{\rm EG}$. The proof that the turbulent magnetic fields indeed play no role in altering the extragalactic direction of the extragalactic dipole is shown in Figure 4.13 in Chapter A.

One of the main conclusions of Chapter 2 was that the magnetic fields within our Galaxy are most likely turbulent dominated. This is not an unusual finding, observations of external galaxies seem to favour the turbulent field dominated configuration of Galactic magnetic fields [7, 131]. If this is indeed the case the strength of the extragalactic dipole whilst propagating through the Galaxy will undergo suppression based on the strength of the turbulent fields. This chapter will focus on investigating the suppression of the extragalactic dipole as it propagates through only the turbulent magnetic field component of the GHB model. A numerical and analytical prediction of the probable strengths of the extragalactic dipole will also be provided with a comparison to existing models.

4.2.1 Effect of turbulent magnetic fields on the dipole - Analytical estimate

One can visualise the galaxy to be in a sphere with a radius of (say) 30 kpc. UHECRs entering the Galaxy with an extragalactic dipole propagate through it interacting with the Galactic magnetic fields. Assuming that there are only turbulent magnetic fields present in the Galaxy the extent to which the UHECRs diffuse within the Galaxy will depend on the strength of the turbulent fields.

Diffusion of particles in random fields

For turbulent magnetic fields the important assumption is that they fluctuate randomly. The power spectrum of such a magnetic field describes the amount of energy that exists in each of the Fourier modes (see Figure 2.4 in Section 2.1.2 Chapter 2) assuming that the phases of the turbulent field are random. For cosmic rays propagating through such a field it means that the particle propagates under the influence of one specific component of the field for a single wavelength until it encounters another wave with a phase orientated randomly to the previous one. This results in isotropic diffusion where the cosmic ray *feels* any given wave for a single wavelength before getting scattered by another wave which is randomly orientated with respect to the last one.

For a single wavelength, the average orientation of the field lines from the large-scale mean field direction due to the magnetic fluctuations is given by $\Theta \sim B_1/B_0$ where, B_0 is the mean field strength and B_1 is the random field amplitude. The change in pitch angle of the particles with Larmor radius $r_{\rm L}$ scales with wavelength $L_{\rm coh}$ of the field, $r_{\rm L} \sim L$. The guiding center of the gyrating particles changes by $r \sim \Theta r_{\rm L}$ which is representative of diffusion of cosmic rays across the magnetic field as well as the change in their pitch angles. Each time the particle sees a new wavelength it gets scattered due to the changing pitch angle. Therefore, in order for a particle to scatter by π radian it has to undergo scattering N times, where $N^{1/2}\Theta = \pi$. The scattering distance covered for N number of scatters can be given by $L_{\rm scat} \approx \pi^2 N r_{\rm L} \approx \pi^2 \frac{r_{\rm L}}{\Theta^2}$. This is called the scattering length for a particle diffusing along a magnetic field. The change in the pitch angle is large enough to result in the particle retaining no memory of its last value. The scattering length $L_{\rm scat}$ can be re-written as:

$$L_{\rm scat} \approx \pi^2 \frac{r_{\rm L}^2}{L_{\rm coh}}. \tag{4.1}$$

For a particle with Larmor radius $r_{\rm L}$ the particle will undergo a deflection of angle Θ in a field with coherence length $L_{\rm coh}$ such that $\Theta = \frac{r_{\rm L}}{L_{\rm coh}}$.

The scattering length can be re-written as a diffusion coefficient D by the following relation:

$$D \sim \frac{c\, L_{\rm scat}}{3}.$$

In the case of isotropic diffusion the diffusion coefficient $D \propto \frac{1}{B_{\rm tur}^2}$, implying that the stronger the magnetic fields the lower the diffusion coefficient and the more particles get diffused [113].

Upon propagation from a source through the Galaxy, cosmic rays undergo diffusion due to either magnetic field fluctuations or some instabilities due to motion of the particles. The scalar diffusion coefficient D describes the motion of these particles. As the cosmic rays diffuse, they undergo energy losses and gains, nuclei decay and other processes. A partial differential equation can be utilised to study the effects of the above-mentioned processes on the spectrum of particles.

The continuity equation tells us about the amount of flux that enters and exits through a given volume, and it can be defined as:

$$\frac{\mathrm{d}n}{\mathrm{d}t} = \nabla \cdot \vec{J_{\mathrm{tot}}} + Q, \tag{4.2}$$

here, 'n' is the number density and $\frac{\mathrm{d}n}{\mathrm{d}t}$ is the rate of change of the number density in a given volume, '$\vec{J_{\mathrm{tot}}}$' is the current density and $\nabla \cdot \vec{J_{\mathrm{tot}}}$ tells us the amount of current that diverges from a given point, 'Q' is the source term inside the given volume . Assuming that the particles do not undergo any advection and at the net change in the number density in a given time is zero Eq. 4.2 can be re-written as:

$$\nabla \cdot \vec{J_{\mathrm{tot}}} + Q = 0,$$

here, $\vec{J_{\mathrm{tot}}} = -D\nabla n$ with D being the diffusion coefficient such that $\nabla \cdot \vec{J_{\mathrm{tot}}} = -D\nabla^2 n$ The steady-state continuity equation for cosmic ray diffusion can then be written by:

$$D_{\mathrm{CR}}\nabla^2 n = Q. \tag{4.3}$$

One can look for an analogous situation similar to cosmic ray diffusion in other physical processes. One such case is for the estimation of electrostatic potential in the presence of charge density given by:

$$\epsilon_r \nabla^2 V = \frac{\rho}{\epsilon_0}, \tag{4.4}$$

here, 'V' is the electrostatic potential, 'ρ' is the volume charge density, 'ϵ_r' is the permittivity of the dielectric material and ϵ_0 is the permittivity of free space.

Note that in Eq. 4.3 and Eq. 4.4, the cosmic ray density n is analogous to the potential V, dielectric constant ϵ_r maps to the diffusion coefficient D_{CR} and UHECR source Q is similar to the ratio $\frac{\rho}{\epsilon_0}$.

4.2.2 Electrostatic equivalent problem to isotropic diffusion of UHECRs

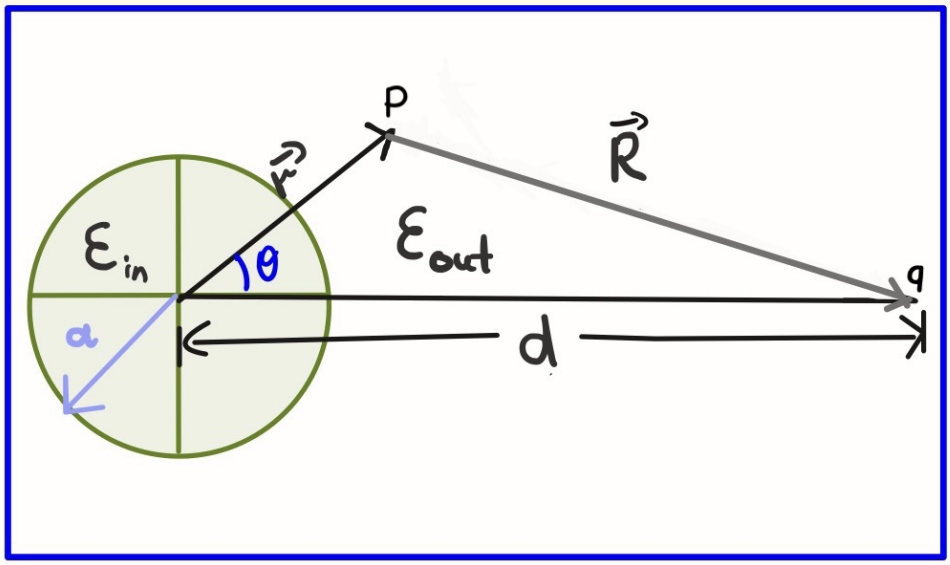

Figure 4.2: A schematic representation of the electrostatic case with the charge q at a distance d from the center of the dielectric sphere of radius a. The dielectric constants inside and outside the sphere being ϵ_{in} and ϵ_{out}. $\vec{R}$ and $\vec{r}$ are the distances measured from the source charge q and center of the dielectric sphere respectively, with P being the point at which the potential is measured [149].

To study the effect of the diffusion coefficient on the CR dipole one can look at an analogous problem of calculating the dipole strength due to a point charge inside a dielectric medium from electrostatics. In Figure A.2, a sketch depicting a dielectric sphere of radius a situated at a fixed distance (d) from a point source (q) is depicted. Here, the dielectric sphere is equivalent to the Galaxy, with the point source being analogous to a UHECR source with d being similar to the distance between the Galactic center and the UHECR source. In Figure A.2 the radial distance '$\vec{R}$' is measured from the charge and can be re-written as a function of distance 'd', radial distance '$\vec{r}$' measured from the center of the dielectric sphere and angle 'θ'.

$$R = \sqrt{r^2 + \mathrm{d}^2 - 2\, r\, \mathrm{d} \cos\theta},$$

or,

$$\frac{1}{R} = \frac{1}{d} \frac{1}{\sqrt{\left(1 - 2\frac{r}{d}\cos\theta + \left(\frac{r}{d}\right)^2\right)}}. \tag{4.5}$$

The above expression is the same as the generating function for the Legendre polynomials:

$$\sqrt{\frac{1}{1 - 2xt + t^2}} = \sum_{n=0}^{\infty} P_{\mathrm{n}}(x) t^n.$$

In the expression Eq. A.2, r/d maps to t and x maps to $\cos\theta$, assuming that $r << d$, the expression above can be written in terms of Legendre polynomials $P_n(\cos\theta)$ as:

$$\frac{1}{R} = \sum_{n=0}^{\infty} \frac{r^n}{d^{n+1}} P_n(\cos\theta). \tag{4.6}$$

The potentials inside and outside of the dielectric sphere can be given by equations Eq. 4.7 and Eq. 4.8 respectively.

$$V_{\text{in}} \approx q\ \frac{1}{\epsilon_{\text{in}}} \sum_{n=0}^{\infty} \mathrm{A} \frac{r^n}{d^{n+1}} P_n(\cos\theta), \tag{4.7}$$

here, potential inside the dielectric medium (V_{in}) is only dependent on the source charge.

$$V_{\text{out}} \approx q\ \frac{1}{\epsilon_{\text{out}}} \sum_{n=0}^{\infty} \left(\frac{r^n}{d^{n+1}} + B \frac{1}{r^{n+1}} \right) P_n(\cos\theta), \tag{4.8}$$

here, '$P_n(\cos\theta)$' is the Legendre polynomial up-to n^{th} order. Note that the potential outside the dielectric sphere experiences an additional reactionary potential due to the dielectric sphere along with potential due to the source and is therefore a function of both. 'A' and 'B' are constants that can be calculated by solving for the boundary conditions for radial and tangential directions. A full derivation of the potential is provided in Section A.2 Chapter A.

Putting values of A and B (for full derivation see Section A.2 in Chapter A) in Eq. 4.7 and Eq. 4.8, the inside and outside potentials can be expressed as:

$$V_{\text{in}} \approx q \sum_{n=0}^{\infty} \frac{2n+1}{n\epsilon_{\text{in}} + (n+1)\epsilon_{\text{out}}} \frac{r^n}{d^{n+1}}\ P_n(\cos\theta) \ \text{ and} \tag{4.9}$$

$$V_{\text{out}} \approx q\ \frac{1}{\epsilon_{\text{out}}} \sum_{n=0}^{\infty} \left(\frac{r^n}{d^{n+1}} + \frac{n(\epsilon_{\text{out}} - \epsilon_{\text{in}})}{n\epsilon_{\text{in}} + (n+1)\epsilon_{\text{out}}} \frac{a^{2n+1}}{d^{n+1}} \frac{1}{r^{n+1}} \right) P_n(\cos\theta). \tag{4.10}$$

For the simplest case, $n = 0, 1$ and $\theta = 0$ the tangential $E^{\theta}_{\text{in/out}} = 0$ since $\sin\theta$ is 0. Note that here $r = a$ is set at the boundary and Legendre polynomials $P_n(\cos\theta)$ values for $n = 0, 1$ are 1 and $\cos\theta$ respectively. Then the potential and dielectric field inside the sphere can be given by:

$$V_{\text{in}} = q\left(\frac{1}{\epsilon_{\text{out}}} \frac{1}{d} + \frac{3}{\epsilon_{\text{in}} + 2\epsilon_{\text{out}}} \frac{a}{d^2} \right), \tag{4.11}$$

and,

$$V_{\text{out}} = q\frac{1}{\epsilon_{\text{out}}}\Big(\frac{1}{d} + \frac{a}{d^2} + \frac{a}{d^2}\frac{\epsilon_{\text{out}} - \epsilon_{\text{in}}}{\epsilon_{\text{in}} + 2\epsilon_{\text{out}}}\Big). \tag{4.12}$$

Since the aim of this study is to mimic the real-world scenario of an observer sitting inside the Galaxy, the region of interest lies inside the dielectric sphere. Thus, the dielectric field inside the dielectric sphere in the r direction can be given by:

$$E_{\text{in}}^{\text{die}} = \epsilon_{\text{in}}\frac{\delta V_{\text{in}}}{\delta r}$$

or,

$$E_{\text{in}}^{\text{die}} \approx \frac{3\epsilon_{\text{in}}}{2\epsilon_{\text{out}} + \epsilon_{\text{in}}}\frac{1}{d^2}. \tag{4.13}$$

Now, that the electrostatic description for the dielectric field is ready the cosmic ray counterpart to the Eq. 4.13 can be written as:

$$\nabla n = J_{\text{EG}} \approx \frac{3D_{\text{in}}}{2D_{\text{out}} + D_{\text{in}}}\kappa, \tag{4.14}$$

here, ∇n or J_{EG} is the extragalactic cosmic ray current which is analogous to the dielectric field $E_{\text{in}}^{\text{die}}$, D_{in} and D_{out} maps onto ϵ_{in} and ϵ_{out} respectively and κ is similar to the constant factor $1/d$.

The Eq. 4.14 is similar to equation 5 in [149] (see Eq. 4.15 below) which focuses on the propagation of Galactic cosmic rays that potentially originate in supernova remnants within the Galaxy, this is a problem similar to the one being addressed here. In this paper, the author, Zirakashvili studied the streaming of Galactic cosmic rays as they propagate from a region of a higher diffusion coefficient to a region of a lower diffusion coefficient, the former being the region surrounding the Galactic interstellar medium and the latter being inside the Local bubble in which the Sun is located approximately centrally.

$$J_{\text{obs}} = \frac{3D_{\text{in}}\,J_{\text{CR}}}{2D_{\text{out}} + D_{\text{in}}}. \tag{4.15}$$

Here, J_{obs} is the cosmic ray current inside the Local bubble and is analogous to the extragalactic cosmic ray current J_{EG} and the dielectric field inside the dielectric sphere $E_{\text{in}}^{\text{die}}$. For both Eq. 4.14 and Eq. 4.15, diffusion coefficients inside and outside the Local bubble are D_{in} and D_{out} respectively and physically have the same meaning and are analogous to the dielectric constants ϵ_{in} and ϵ_{out}. The cosmic ray streaming at infinity is given by J_{CR}, the constant is similar to the constant κ and the fixed distance d between the dielectric sphere and the source. The constant will mostly dictate the normalisation of the left-hand side terms in Eq. 4.13, Eq. 4.14 and Eq. 4.15.

Analogy between cosmic ray dipole and electrostatic dipole

The diffusion approximation of Fick's law which states that the flux, $\vec{J}$ of particles moves from a higher to a lower concentration region with its magnitude being proportional to the concentration gradient or spatial derivative and is given by:

$$\vec{J} = -D\vec{\nabla}N(r,t), \tag{4.16}$$

here, $\vec{J}$ is the number of particles that flow through a unit surface in a unit time, $\vec{\nabla}N(r,t)$ is the change in the concentration of the particles at given position (r), time (t) and D is the diffusion coefficient.

Any asymmetry in the distribution of sources results in a net gradient in the density of cosmic rays, by virtue of Fick's law this implies a net flux of CRs. In the isotropic diffusion case, this will result in an anisotropy in the cosmic ray arrival directions with dipole direction pointing in the case of UHECRs away from Galactic center [92, 150, 151]. Thus, the cosmic ray dipole propagating in a medium with an isotropic diffusion coefficient D is given by:

$$\delta_{\rm CR} \simeq D\frac{\nabla n}{n}. \tag{4.17}$$

Note, that apart from anisotropy due to distribution of cosmic rays sources, a weak dipole anisotropy in the direction of motion is also introduced due to the relative motion of the observer with respect to the frame in which cosmic ray distribution was completely isotropic, this is known as the Compton-Getting effect.

The electrostatic analogy discussed above can be used to calculate a quantity equivalent, the electrostatic dipole ($\delta_{\rm ES}$). The behaviour of $\delta_{\rm ES}$ is similar to the cosmic ray dipole and can predict how the latter changes when the diffusion coefficients change within the Galaxy during cosmic ray propagation.

The electrostatic dipole in radial direction and for $\cos\theta = 1$ can be given by:

$$\delta_{\rm ES} \simeq \frac{\nabla V}{V} \simeq \frac{E_{\rm in}^{\rm die}}{V_{\rm in}},$$

here, the change in the cosmic ray number density, ∇n is similar to the dielectric field ($E_{\rm in}^{\rm die}$) and n is analogous to the potential, V in the electrostatics case.

$$\delta_{\rm ES} \propto \frac{1}{d}\,\frac{3\,\epsilon_{\rm out}\epsilon_{\rm in}}{2\epsilon_{\rm out}+\epsilon_{\rm in}}. \tag{4.18}$$

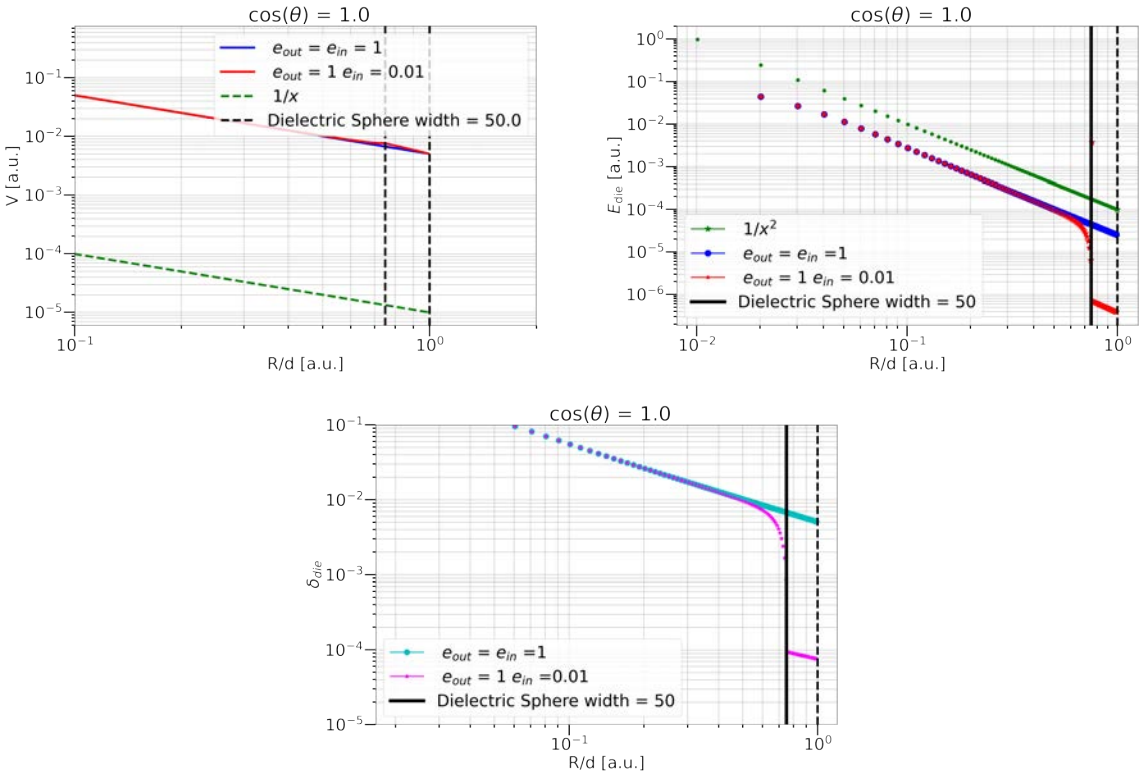

Figure 4.3: Plots showing the potential (**top left**), electric field (**top right**) and dipole (**bottom**) dropping as a function of radial distance R/d (measured from the source) for a simplified case of cos $\theta = 1$. Each plot shows two cases when $\epsilon_{\text{in}} = \epsilon_{\text{out}}$ and $\epsilon_{\text{in}} < \epsilon_{\text{out}}$ (for reference see Figure A.2). For the former case of $\epsilon_{\text{in}} = \epsilon_{\text{out}}$ there is no change in the behaviour of the potential, electric field, or dipole both inside and outside the dielectric sphere. In the latter case where $\epsilon_{\text{in}} < \epsilon_{\text{out}}$ the potential changes ever so slightly, but both the electric field and dipole strength drop inside the dielectric sphere by the factor $\frac{\epsilon_{\text{in}}}{\epsilon_{\text{out}}}$. It is evident from these figures that the dipole strength is driven by the electric field and not the potential.

In Figure 4.3 for cos $\theta = 1$ a 1-D plot of the potential and electric field inside and outside of the dielectric sphere for the two cases (when $\epsilon_{\text{in}} = \epsilon_{\text{out}}$ and $\epsilon_{\text{in}} < \epsilon_{\text{out}}$) is shown as a function of the radial distance R/d measured from the charge q.

Case I: When $\epsilon_{\text{in}} = \epsilon_{\text{out}}$, i.e., the dielectric constant inside and outside the sphere are the same, the potentials inside and outside will also be the same ($V_{\text{in}} = V_{\text{out}} = V$) and follow a $1/R$ drop from the source (q). Similarly, the dielectric field drops as a function of $1/R^2$ for this case and is the same both inside and outside ($E^{\text{die}}_{\text{in}} = E^{\text{die}}_{\text{out}} = E_{\text{die}}$).

Case II: When $\epsilon_{\text{in}} < \epsilon_{\text{out}}$, the dielectric field inside the dielectric sphere experiences a large amount of suppression. The potential, in this case, does not undergo much change since it's dominated by the dielectric strength outside ϵ_{out} (see expression for V_{in} and V_{out} in Eq. 4.11, Eq. 4.12 respectively).

Figure 4.4 shows the 2D plots for the potential, dielectric field and the electrostatic dipole. In the top left plot in Figure 4.4 it can be seen that the equipotential lines seem to get more

concentrated inside the dielectric sphere due to a lower value of dielectric constant ϵ_{in} inside than outside. The top right plot of Figure 4.4 shows the dielectric field, since the dielectric field is perpendicular to the equipotential lines, the dielectric field lines tend to avoid entering the dielectric sphere with the field being suppressed inside the sphere by the ratio of $\frac{\epsilon_{\text{in}}}{\epsilon_{\text{out}}}$. The dielectric field in this case also results in driving the dipole strength

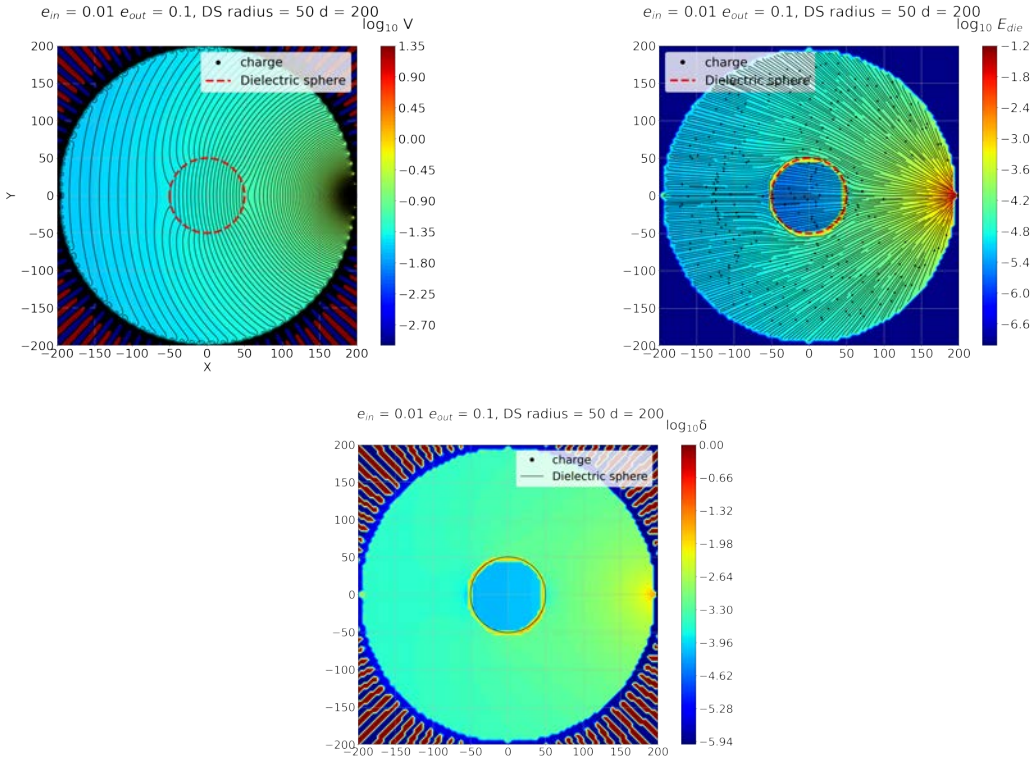

Figure 4.4: The figure (**top-left**) shows the potential dropping as a function of distance from the source, with the equipotential lines more closely packed inside the dielectric sphere than outside. The dielectric field lines (**top-right**) being orthogonal to the equipotential lines, the field avoids entering the dielectric sphere and is hence suppressed. The dipole (**bottom**) is plotted as the ratio of the dielectric field and the potential, it can be seen that the dipole strength is driven by the electric field.

(bottom plot in Figure 4.4) and therefore, the strength of the dipole gets suppressed similarly as the electric field.

Utilising the analytical description from electrostatics, the dipole strength for cosmic rays inside the dielectric sphere can be re-written in relation to the electrostatics case as:

$$\delta_{\text{in}}^{\text{CR}} \propto \kappa \, \frac{3 \, D_{\text{out}} D_{\text{in}}}{2 D\text{out} + D_{\text{in}}}. \tag{4.19}$$

The above expression is a general relation that is applicable when both the diffusion and the number density of the UHECRs are known. Now that the analytical description of an extragalactic dipole propagating through a region of changing magnetic fields is ready,

the next step is to compare it with simulations of UHECRs propagating through changing magnetic fields.

4.3 Propagating extragalactic dipole through the Galactic turbulent fields

Simulating propagation of UHECRs requires pushing the cosmic rays through magnetic fields by solving a Lorentz pusher scheme like the one used in Chapter 3. There are two ways of carrying out this propagation either by backtracking as also done in Chapter 3 or forward tracking. Both of these methods are discussed below.

4.3.1 Backtracking versus forward tracking and test of Liouville theorem

As a recapitulation, in the backward tracking method, isotropic distribution (i.e., isotropic in momentum) of UHECRs starting at Earth is backtracked through the Galactic magnetic fields until they reach a termination distance that is representative of the edge of the Galaxy.

In forward tracking, we start from an isotropic momentum distribution of UHECRs on a sphere enclosing the Galaxy also known as the injection sphere, and push the UHECR particles inwards through the Galactic magnetic fields and stop the simulation once the observer sees them. In Chapter 3, backward tracking of cosmic ray particles utilising CRPropa3 [89, 90] was carried out, in this chapter however, forward tracking of UHECRs will be utilised. The reason for using forward tracking as opposed to backtracking of UHECRs is discussed below.

For an extragalactic isotropic momentum distribution of UHECRs, the observed arrival direction anywhere within the Galaxy will also always be isotropic. This is a result of the Liouville theorem [150].

To test this theorem, a simulation was set up using CRPropa3 [89, 90]. One billion UHECR protons 8.5 EeV with an isotropic momentum distribution were directed inwards ballistically into the Galaxy and an observer of an exaggerated size of 500 pc was fixed at an arbitrary position (say the Galactic center) within the Galaxy. The resulting UHECRs observed were approximately of the order of 10^6. A histogram of the distribution of the longitudes shown in Figure 4.5 shows a flat distribution implying that irrespective of the

position of the observer the arrival directions seen anywhere in the Galaxy are isotropic provided the injected distribution of UHECRs is isotropic in momentum space. Note that though no magnetic fields were used for this simulation for a very large (>10^9) number of injected UHECRs, the arrival directions seen by an observer within the Galaxy will also be isotropic. A similar longitude plot including the GHB turbulent magnetic field component is shown in Figure 4.9.

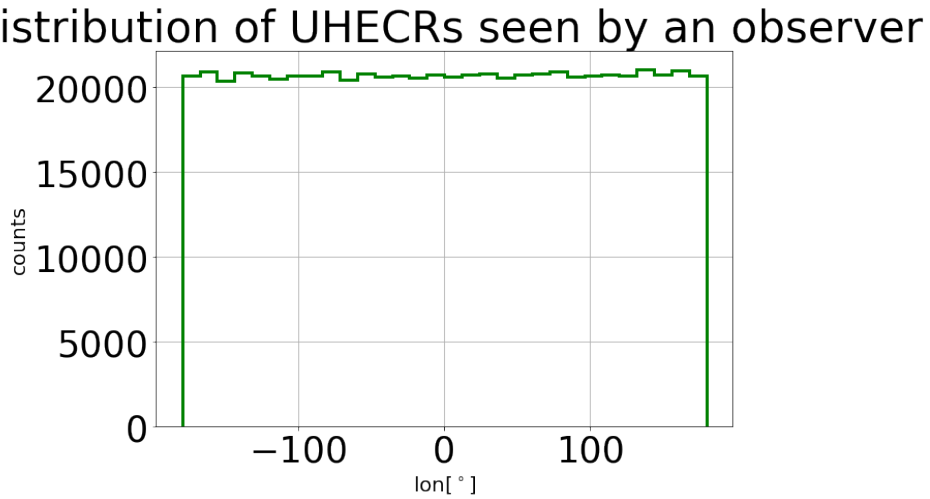

Figure 4.5: Isotropic distribution of arrival directions in longitudes of UHECR protons seen by an observer when the injected distribution of the protons is isotropic in momentum directions. This is called the Liouville theorem [150].

For an ideal simulation, the size of the observer should be as small as possible in order to mimic the earth as an observer sphere. However, it can be seen from Figure 4.5, that in order to observe UHECRs of the order of 1 million in the absence of Galactic magnetic fields, the injected number of UHECRs should be a few orders of magnitude higher. With the introduction of magnetic fields, the observed number of UHECRs gets even smaller. This is one of the major drawbacks of forward tracking making it computationally very expensive.

In reality, cosmic rays from all directions enter the galaxy and what is observed by PAO [92, 93] is a fraction of UHECRs that hit the observer (Earth). This means that if backtracking of an isotropic momentum distribution of UHECRs is carried out from an observer, one does not consider the UHECRs that do not reach Earth. The final arrival direction maps in this case will be anisotropic as also seen from the magnification maps from Figure 3.11 in Chapter 3. When backtracking UHECRs from Earth the initial directions are isotropic in momentum directions, but this is not true for positions as we assume that Earth is acting like a source of UHECRs. This makes the backtracking of UHECRs highly anisotropic which results in an anisotropic arrival direction map as well.

The main focus of this chapter lies in the propagation of an external cosmic ray dipole

through turbulent magnetic fields. For this reason, it was necessary to have an isotropic momentum distribution of UHECRs with a weight of a dipole at the injection surface, in order to mimic the observations that are made at Earth [92, 148]. Therefore, forward tracking of cosmic rays was utilised for investigating the effect of diffusion on the extragalactic dipole.

In the previous section an analytical analogous estimate of dipole strength for the electrostatics case was discussed. This case will be used as a tool to understand the dipole suppression for UHECRs. Before simulating the propagation of the extragalactic dipole through the Galaxy with different turbulent fields i.e., diffusion coefficients, there were three kinds of estimates that required to be carried out. The estimates below were required to numerically simulate the scenario of UHECRs with an extragalactic dipole propagating through the diffusive medium of the Galaxy, such that the diffusion coefficient is different outside and inside the Galaxy. This is similar to the electrostatic analogy discussed in Section 4.2.2. The simulations would be carried out for different values of scattering lengths/diffusion coefficients, so first the value of the scattering length for each magnetic field strength must be estimated. This is followed by an estimation of the uncertainties of the values obtained. As already highlighted in Section 4.3.1, the size of the observer is important to take into account and therefore needs to be studied for each magnetic field scenario. Thus, the next section will focus on the following:

1. **Estimation of scattering length** - The estimation of the diffusion coefficients or the scattering length of UHECRs requires simulating their trajectories. This will be discussed in detail in Section 4.3.2.
2. **Estimation of uncertainties** - Each dipole amplitude that was computed requires the estimation of uncertainties as well. For this, a small experiment with Gaussian distribution of random numbers was carried out, and it will be discussed in Section 4.3.3.
3. **Estimation of the size of the observer** - Lastly, to propagate UHECR protons at 8.5 EeV through the GHB turbulent magnetic field with varying RMS values, one needs to also estimate the size of the observer. The effect of observer size or observer sphere was investigated and is discussed in Section 4.3.4.

4.3.2 Estimating scattering lengths for the UHECRs for each GHB turbulent field strength

With the analytical electrostatic estimates on hand, the focus of the following sections will be propagating the UHECRs through the turbulent component of the GHB model

and describing the change in the dipole amplitude. As already stated previously in Section 4.2.1, small-scale deflections of UHECRs due to the magnetic fields within the Galaxy can be given by $\delta\Theta \sim L_{\rm coh}/r_L$, here $L_{\rm coh}$ is the coherence length of the turbulent magnetic field and r_L is the Larmor radius of the UHECRs. For N number of deflections where $N = L_{\rm scat}/L_{\rm coh}$, with $L_{\rm scat}$ being the length scale at which the UHECR scatters in a magnetic field, the net deflection can be given as $\Theta = \sqrt{N}\delta\Theta$, Assuming that for a sufficient number of scattering $\Theta \sim \pi$ radians, the expression for the scattering/diffusion length can be re-written as:

$$L_{\rm scat} \approx \pi^2 \frac{r_L^2}{L_{\rm coh}}. \tag{4.20}$$

The diffusion coefficient $D \sim L_{\rm scat}$ c/3 with 'c' being the speed of light. Throughout this text the word scattering length and the diffusion coefficient will be used interchangeably.

UHECRs protons for a fixed energy of 8.5 EeV were considered for this study. A range of logarithmically binned turbulent magnetic field strengths between 2-20 μG with $L_{\rm coh}$ = 150 pc were utilised to compute the scattering length for the 8.5 EeV protons. Test simulations were carried out for several values of coherence lengths but for the sake of consistency with Chapter 3, the value of 150 pc was chosen. Ideally, the simulation should be repeated for multiple coherence length values, but this proves to be computationally intensive due to long simulation hours.

Utilising CRPropa3 [89, 90] the simulation was set up for a single source scenario with the particles propagating through the Galaxy for multiple maximum trajectory lengths (or simulation time) between 10 kpc to 6000 kpc. Upon propagation once the particles had completely isotropised such that the average mean square of the deflection angle $< \Delta\phi^2 >$ had plateaued the trajectory length value was noted. Note that ϕ is the angle between the initial and final momentum direction of the particle. Then the scattering length $L_{\rm scat} \propto D_{\phi\phi} \simeq \frac{<\Delta\phi^2>}{2\Delta t}$, this expression comes from the rotational version of Fick's law which states that charged particles diffuse randomly obeying the Eq. 4.16.

Scattering lengths for 15 magnetic field strengths with a fixed value of $L_{\rm coh}$ at 150 pc were computed similarly, and the results have been summarised in table 4.1. Note that due to computation time, these trajectories were calculated only for a few thousand particles, in the future this number will be increased. In Figure 4.6, the scattering length as a function of the turbulent magnetic field is shown. It can be seen that the simulations produce the expected inverse square dependence between the two quantities with $L_{\rm scat} \propto \frac{1}{(B_{\rm tur})^2}$ (see Eq. 4.20).

Table 4.1: Table of turbulent magnetic field strengths ($B_{\rm tur}$) and corresponding particle scattering lengths ($L_{\rm scat}$).

$B_{\rm tur}$ μG	$L_{\rm scat}$ kpc
2.2	2500
2.7	1800
3.2	1300
3.9	1000
4.6	700
5.6	500
6.7	400
8.0	300
9.6	220
11.5	150
13.8	120
16.6	90
19.9	70
23.9	60

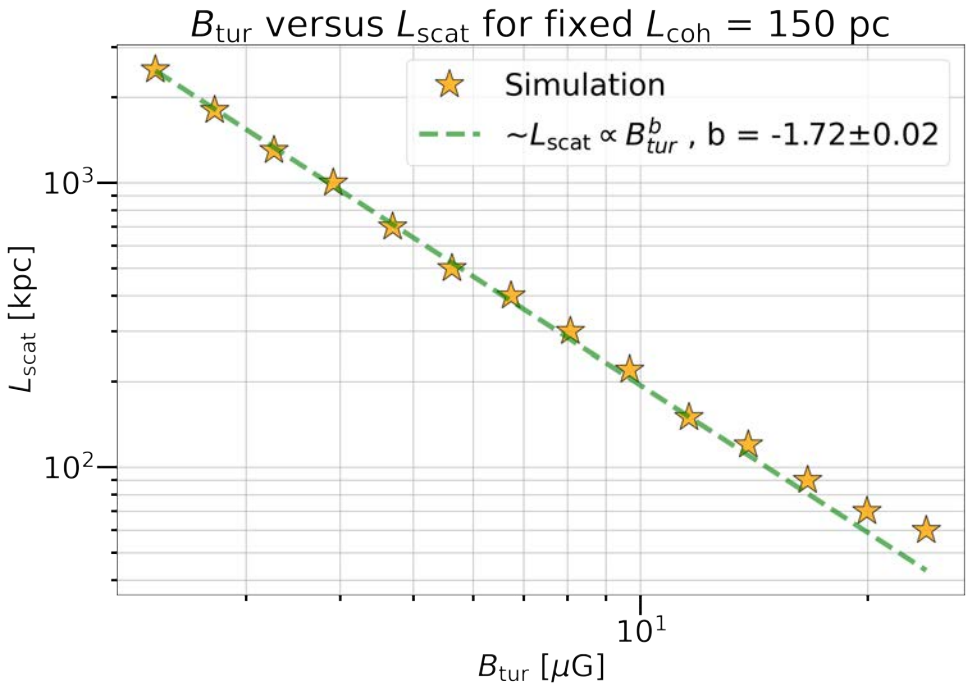

Figure 4.6: The scattering length $L_{\rm scat}$ varying inversely as a function of $(B_{\rm tur})^2$ for two fixed values of coherence lengths ($L_{\rm coh}$ = 150 pc).

The linear dependence of the coherence length with the scattering length was also investigated and is shown on the right in Figure 4.7. Due to long simulation hours, this figure was made only for 5 data points and will be improved in the future by the addition of more data points. The diffusion coefficient can be given by:

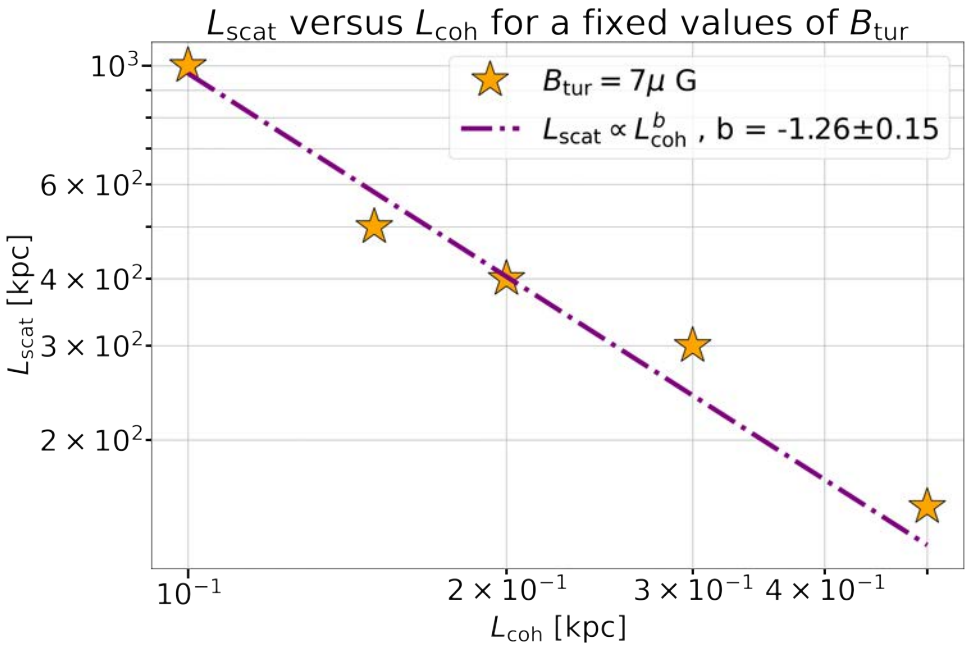

Figure 4.7: The scattering length L_{scat} varying inversely as a function of L_{coh} for fixed value of B_{tur} = 7 μG.

$$D \propto L_{scat}\, c/3,$$

and the scattering length scales inversely with the coherence length such that $L_{scat} \propto 1/L_{coh}$. Thus implying that the diffusion coefficient D, also scales as $1/L_{coh}$. The dipole amplitude (δ) has a linear scaling with the diffusion coefficient such that $\delta \propto D$ thus it will scale inversely with the coherence length and this is also what is obtained from the simulation results shown in Figure 4.8.

4.3.3 Estimation of uncertainties

The calculation of the dipole strength using a weighted sum method is given by Eq. 4.22 and will be discussed in detail in the next section. In the absence of an extragalactic dipole, the arrival directions of the UHECRs are randomly oriented so that they have an isotropic distribution. For a sufficiently high number of statistical data points, the distribution of UHECR arrival directions is similar to a Gaussian distribution of random numbers.

To test this isotropic momentum distribution, UHECRs at 8.5 EeV were tracked forward without an extragalactic dipole through the turbulent magnetic fields of the GHB model and the arrival directions were noted. The Figure 4.9 shows the distribution of these UHECRs arrival directions in latitude (lat) with an isotropic Gaussian distribution and the arrival directions in longitude (lon) which show a flat distribution, indicating that

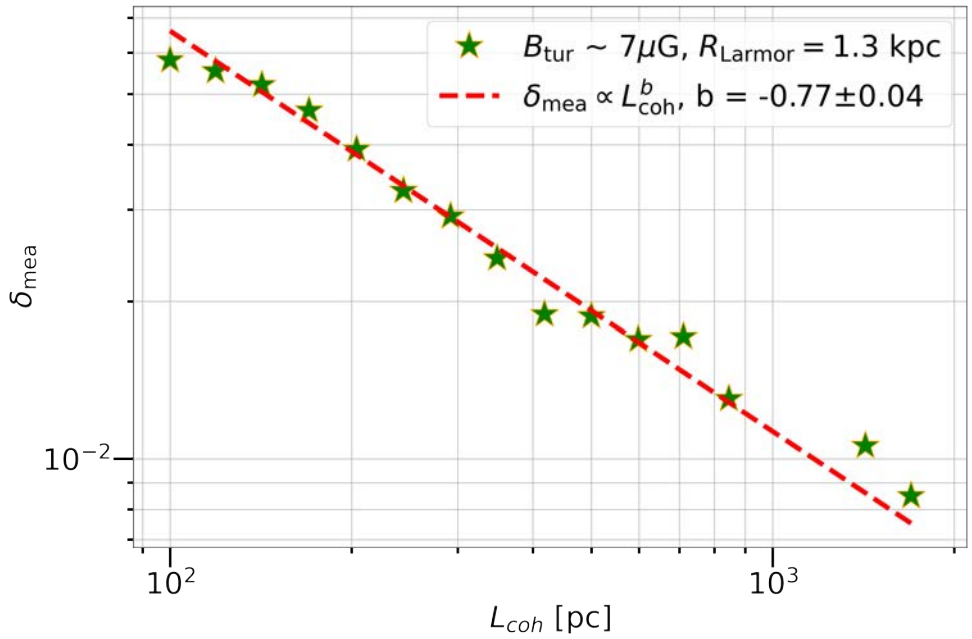

Figure 4.8: The change in dipole as a function of coherence length show that the two are inversely proportional. The black ★ are the data point with the solid red line being the fit. This figure was created for a single value of B_{tur} at 7 μG.

UHECRs are isotropically distributed in all directions of the sky. The flat longitude distribution is a verification of Liouville's theorem, as also discussed in Section 4.3.1.

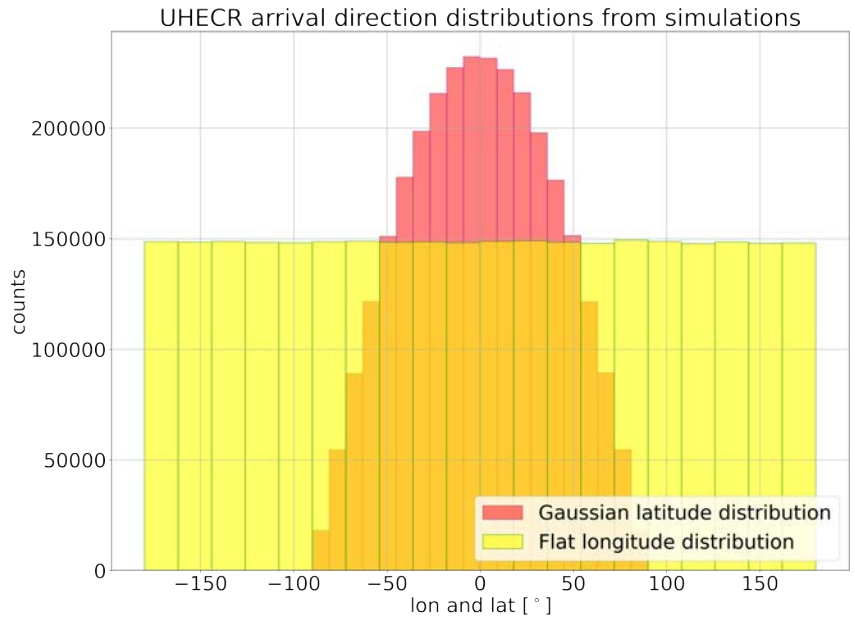

Figure 4.9: The Gaussian distribution of the UHECR arrival direction in latitude and the flat distribution in longitude show that, in the absence of an extragalactic dipole, the UHECRs have an isotropic distribution after propagating through the Galaxy when only turbulent magnetic fields are present.

The strength of the dipole (δ_{Noise}) was calculated from the simulation by:

$$\delta_{\text{Noise}} = \frac{\sum \hat{p_f} \cdot \hat{d}_f}{N} \tag{4.21}$$

here, N is the total number of particles, $\hat{p_f}$ is the final momentum directions (arrival directions) and $\hat{d}_f$ is the dipole direction at (lon = 0°, lat = 0°). The noise dipole was calculated for (2×10^6) UHECRs and the standard deviation σ_{sim} was noted.

Simultaneously, an experiment for the case of a fixed number of statistics (2×10^6) in a random Gaussian distribution was conducted. Its standard deviation σ_{exp} was computed by normalising the Gaussian distribution by the total number of particles. The standard deviations (σ_{exp}) for the same number as the UHECRs was calculated. The values of σ_{sim} and σ_{exp} were the same for the same number of statistics in both the simulation and the experiment.

In Figure 4.10, the Gaussian distribution of random numbers is shown as the histogram with the orange region marking the $2\sigma_{\text{exp}}$ region in between. The dashed purple lines corresponds to $2\sigma_{\text{sim}}$ calculated from the simulation, 95% of the simulation results lie with the $2\sigma_{\text{exp}}$ region from the Gaussian experiment. Note that throughout the number of data points in both simulation and experiment were kept equal.

This test was also repeated for different levels of statistics for both simulation and experiment and for a fixed number of data points $\sigma_{\text{sim}} = \sigma_{\text{exp}}$. This study verifies that treating the non-weighted distribution of UHECR arrival directions as a Gaussian distribution for sufficiently large number of particles is correct.

4.3.4 Estimation of the size of the observer/observer sphere

In order to obtain meaningful results whilst not losing a lot of computational resources, a simulation was carried out to estimate the size of the observer or observer sphere. From an injection radius of 50 kpc (few billion) UHECR protons (8.5 EeV) with an isotropic distribution in momentum directions and an extragalactic dipole of $\delta_{\text{EG}} = 7\%$ were directed inwards through turbulent magnetic fields of the GHB model as used in Section 4.3.2. This test was repeated for 5 values of B_{tur} at 2, 7, 5, 10, 15 and 18 μG. The UHECRs were pushed from the injection sphere inwards through the concentric observer spheres of varying radii of 1 and 48 kpc.

Note that all the concentric spheres were smaller in radii than the injection sphere. This setup can be visualised as concentric spheres (see Figure 4.11). In Figure 4.11 the outermost

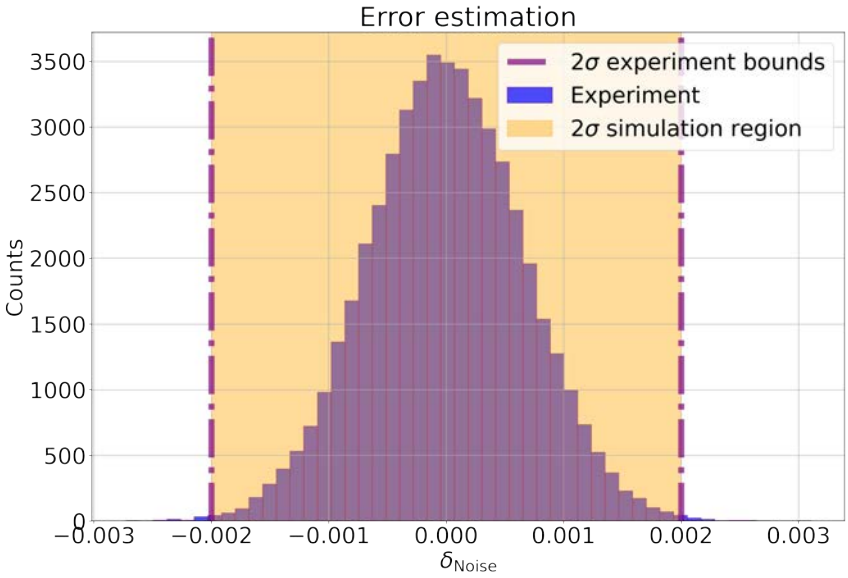

Figure 4.10: The figure shows the random number experiment showing Gaussian distribution as a histogram with 50 bins for 2 million numbers with the 2σ region from the experiment in between the dashed purple line. The light orange region comprises the 2σ points from the simulation.

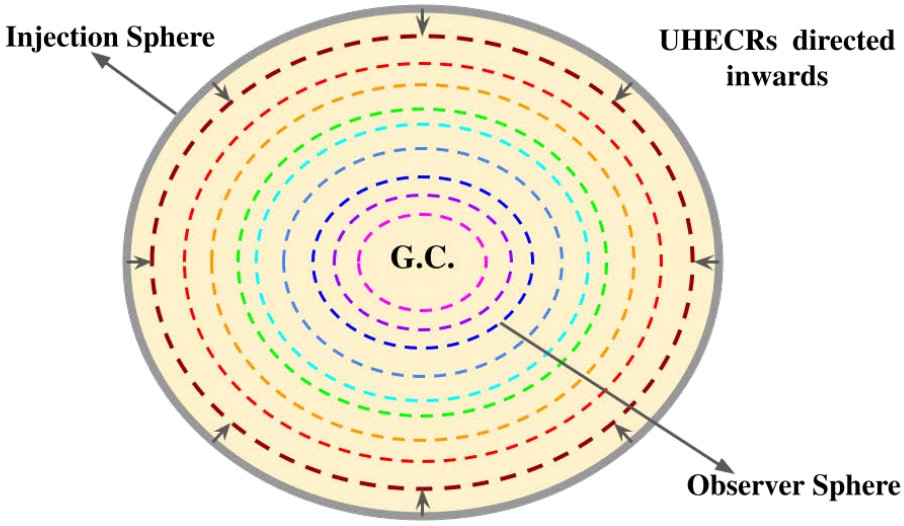

Figure 4.11: A schematic representation showing the difference between observer and injection sphere. Since observers cannot ideally be shown as single points for computation reasons they are represented as observer spheres of varying radii in CRPropa. Note that all spheres are centred on the Galactic center. For determining the ideal size of the observer sphere isotropic distribution (in momentum) of UHECRs was injected inwards towards the GC. Each particle then gets detected once by every observer sphere before reaching the final sphere where the simulation stops.

shell in grey is the injection sphere and the observer spheres in coloured dashed lines lie as concentric spheres within it. The Galactic center is at the center of all the concentric spheres. As the particles got pushed through the different observer spheres they got detected only once while entering the surface. The simulation stopped once the particles

hit the termination sphere which was fixed at 100 kpc for all cases expect one which will be discussed below.

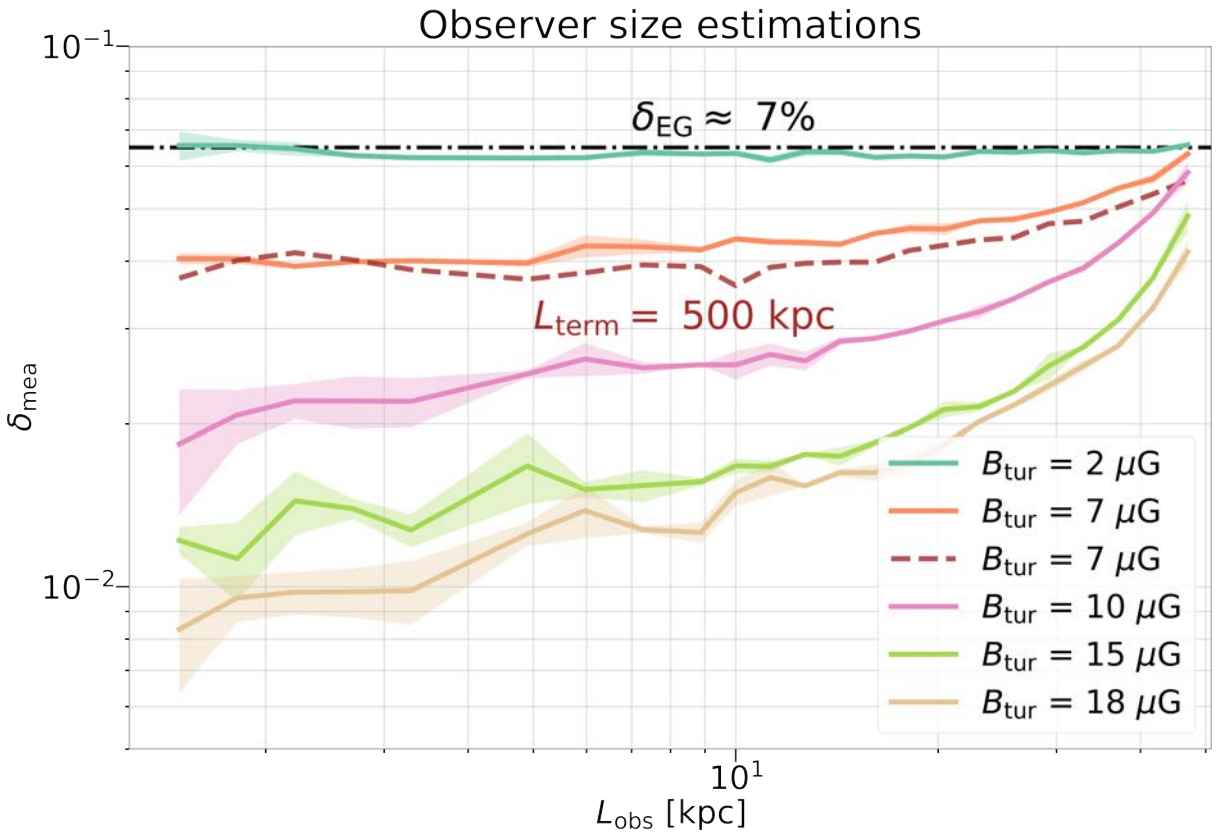

Figure 4.12: Figure showing the measured dipole strength (δ_{mea}) changing as a function of the observer sphere for 5 different magnetic field strengths. The value of δ_{mea} reaches a plateau for $B_{tur} \leq 10\ \mu$G but for field strengths larger than this the plateau does not seem to appear implying that the size of the observer sphere for stronger magnetic fields should be below 1 kpc at least.

The particles propagating through each configuration of the GHB turbulent field model underwent diffusion and thus resulting in the suppression of the measured dipole δ_{mea} which can be given by:

$$\delta_{mea} = 3\frac{\sum \hat{p_f} \cdot \hat{d_f}\ (1 + \delta_{EG}\ (\hat{p_i} \cdot \hat{d_i}))}{\sum 1 + \delta_{EG}\ (\hat{p_i} \cdot \hat{d_i})} \tag{4.22}$$

here, $\hat{p_i}$,$\hat{d_i}$ are initial and $\hat{p_f}$,$\hat{d_f}$ are the final momentum and dipole direction (unit vector) of the UHECR particle respectively and δ_{EG} is the extragalactic dipole amplitude. The dipole direction $\hat{d_i}$ in x, y and z coordinates can be written as d_i^x, d_i^y, d_i^z and these values were fixed at (1,0,0) respectively. Since only turbulent magnetic fields were utilised in this study the initial and final dipole directions were kept equal ($\hat{d_i} = \hat{d_f}$) as turbulent fields do not alter the extragalactic dipole direction (see Section 4.3.4 below).

The dipole δ_{mea} was measured for different values of turbulent magnetic fields of the

GHB model and a suitable value of $L_{\rm obs}$ was noted when the value of $\delta_{\rm mea}$ plateaued (see Figure 4.12). The level of uncertainties for each magnetic field case is shown as a shaded region in Figure 4.12. To calculate the uncertainties the noise dipole $\delta_{\rm Noise}$ was calculated for each magnetic field case without any extragalactic dipole as weight. For values of $B_{\rm tur} < 10\mu$G, the measured value of dipole $\delta_{\rm mea}$ plateaus between observer sphere sizes of 4 to 6 kpc. Whereas for stronger turbulent magnetic fields > 10 μG or smaller scattering < few 100s of kpc, the measured dipole does not seem to plateau and the uncertainties in the measurement are large, for such cases observer spheres were required to be smaller than 1 kpc preferably between 100 and 500 pc in order to reduce the level of fluctuations in the estimation of the amplitude of $\delta_{\rm mea}$. This also implied that the simulation time and the number of particles that were injected were much larger for cases $B_{\rm tur} > 10$ μG. The stronger the magnitude of $B_{\rm tur}$ the more particles would diffuse resulting in them taking longer in reaching the termination sphere. This resulted in longer simulation time. Additionally, since the particles diffuse more, their chances of hitting the observer narrows down which means that at the injection radius the initial number of particles for the case where $B_{\rm tur}$ = 18 μG has to be larger than the $B_{\rm tur}$ = 2 μG case.

Note that a larger termination sphere size at 500 kpc was also tested shown by the brown dashed line for $B_{\rm tur}$ = 7 μG in Figure 4.12, but no significant change was seen in the value measured dipole. Moreover, setting the termination distance to a very large value adds to simulation time and results in fewer statistics and larger fluctuations. Therefore, the termination sphere size was kept at twice the injection sphere size.

Effect of turbulent magnetic fields on the extragalactic dipole direction

The initial and final dipole direction being same the for turbulent magnetic fields, was also verified by utilising the *Healpix* [123] routine. In Figure 4.13 the initial dipole direction is (lon = lat = 0°) shown in the map. The $\delta_{\rm mea}$ was calculated both from Eq. 4.22 and from the "anafast" function and both yielded the same strengths. Separately, the dipole direction was also calculated using the "$fit-dipole$" function which also yielded lon = 0.3°, lat = 0.2° shown as purple ★ in Figure 4.13. The reason there is little to no shift in dipole direction when propagating it through turbulent magnetic fields is because turbulent fields isotropies the particle directions and only the initial weight (dipole) is left. **Note:** In Figure 4.13 the size of the star does not indicate any magnitude, it is only a visual aid to highlight that the dipole direction remains unchanged when UHECRs are propagated through turbulent fields only.

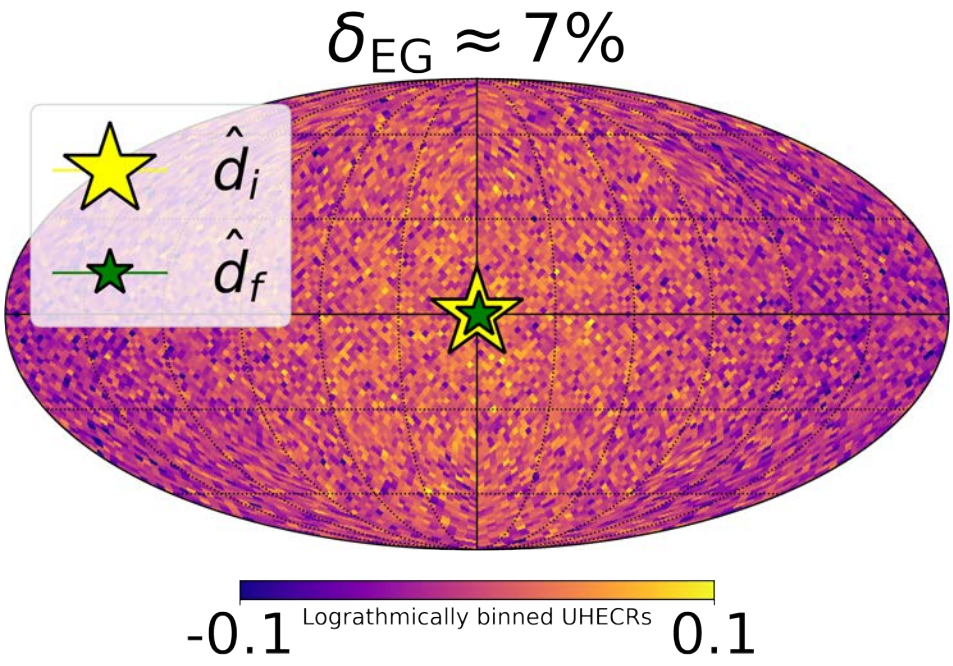

Figure 4.13: The dipole weighted skymap with initial dipole direction ($\hat{d}_i$) in longitude and latitude given in the big orange ★ at lon = lat = 0°. The final dipole direction ($\hat{d}_f$) is shown in the purple ★ at lon = 0.3°, lat = 0.2°. In case of propagating the dipole through turbulent magnetic fields only, no change in direction is observed.

4.3.5 Estimating dipole strength with changing scattering length

Finally, the focus of this section lies in estimating this suppression of the extragalactic dipole and comparing it with the analytical analogy given by Eq. 4.18. To estimate the dipole strength for varying scattering lengths, forward tracking of a few billion particles was carried out utilising CRPropa3. UHECR protons (at 8.5 EeV) with isotropic distribution in momentum directions were injected inwards from an injection radius of 30 kpc towards an observer surface of radius L_{obs} centred at the GC. The termination distance for these simulations was set at twice the injection radius. These particles interacted only with turbulent magnetic fields B_{tur} of the GHB magnetic field model.

Magnetic field strengths between 2 and 24 μG spaced logarithmically for 14 values were utilised. For strengths up to 10 μG, the value of L_{obs} was set to 5 kpc which corresponds to the plateaued region from Figure 4.12 and for strengths higher than 10 μG it was set between 500 pc to 150 pc for increasing field strengths.

The effect of diffusion for B_{tur} = 2 μG will be less than B_{tur} = 16 μG because UHECRs scatter more often in the case of B_{tur} = 16 μG. The maps in Figure 4.15 show the log intensity arrival directions of UHECRs weighted with the extragalactic dipole with the latitude and longitude at 0. Note that in these cases that the number of observed particles

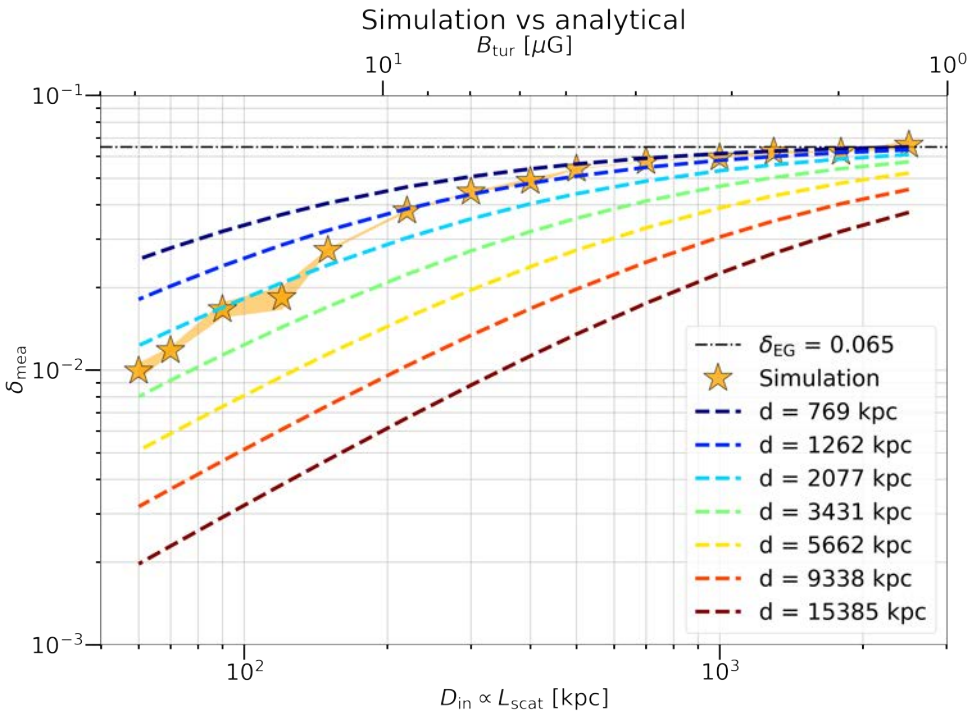

Figure 4.14: The ★ in the figure show the simulation data points denoting the measured dipole strength δ_{mea} varying as a function of the diffusion coefficient D_{in}. For the sake of simplicity the units of D_{in} are kept to be in [kpc] since $D_{in} \propto L_{scat}$. The dashed lines correspond to the analogous electrostatic case where the strength of D_{out}/d is fixed at a 7% level and the value of d is varied to show different source distances.

vary with the 2 μG case having 3 million and the 16 μG case having about 1.5 million observed arrival directions.

In Figure 4.15, the top plot shows the unsmoothed raw skymap for the log binned UHECRs for the B_{tur} = 16 μG case. Though the dipole is still present in this map, it is impossible to see it by eye. The bottom row maps in Figure 4.15 were smoothened with a top-hat function with radius of 45° same as the one adopted by PAO [92], to make the dipole visible to the eye. Post smoothing, it is easier to see the effect of a smaller scattering length or higher rate of diffusion for the skymap made with B_{tur} = 16 μG in comparison to the one made with B_{tur} = 2 μG .

Smoothing of a skymap results in the washing out of features of a certain radius on the skymap. In the case of PAO, they utilise a top-hat function of radius 45° to smoothen their skymap like the one shown in Figure 3.6 [92]. Their top-hat function is defined such that regions of sky smaller than 45° were set to a fixed value. To smoothen the maps the publicly available codes provided by PAO were utilised for the sake of consistency.

In Figure 4.14 a plot of the dipole amplitude as a function of scattering lengths is shown by the solid black ★. The dashed coloured lines correspond to the analogous electrostatics case, the dipole strength from the analogy can be given by Eq. 4.18. Assuming that

$\epsilon_{\text{out}} \to D_{\text{out}}$ and $\epsilon_{\text{in}} \to D_{\text{in}}$, here D_{out} and D_{in} are diffusion coefficients outside and inside the injection sphere respectively, the injected dipole strength δ_{EG} can be written as:

$$\delta_{\text{EG}} \propto \frac{D_{\text{out}}}{d} \tag{4.23}$$

here, d is the distance to the UHECR source and is analogous to the electrostatic problem case. The ratio of $\frac{D_{\text{out}}}{d}$ has been fixed to $\approx 7\%$ and therefore, by changing the value of D_{out}, d can be estimated. The y-axis normalisation of this plot was done by dividing each dashed coloured line with the peak value for $D_{\text{out}} = 50$ kpc and multiplying by $\delta_{\text{EG}} \approx 7\%$.

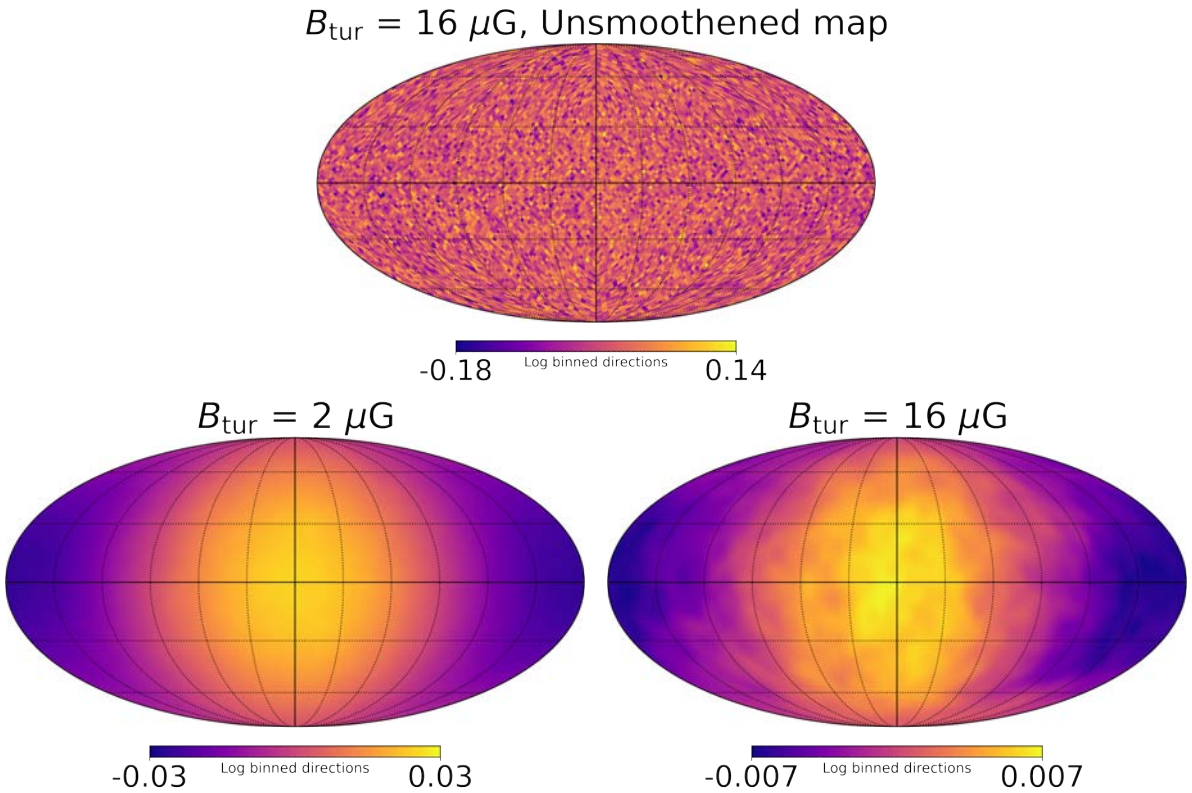

Figure 4.15: Top: unsmoothed skymap for the logarithmically binned UHECR directions weighted with extragalactic dipole for $B_{\text{tur}} = 16$ μG. Due to the large levels of noise its almost impossible to see the dipole by eye.
Bottom: maps with logarithmically binned UHECRs arrival directions with an extragalactic dipole added as a weight. The skymap with $B_{\text{tur}} = 2$ μG (left) is less diffused due to its larger scattering lengths in comparison to the skymap created with $B_{\text{tur}} = 16$ μG (right).

4.4 Conclusions and outlook

This study was done assuming a simple volume-filled description of the turbulent magnetic field from the GHB model proposed in Chapter 2, if the Galactic halo is indeed

turbulent field dominated then the suppression of the $\delta_{\rm EG}$ is imminent.

The work of [149] also used an electrostatic analogy to explain the propagation of Galactic CRs. The simulation results reported in this study serve as a confirmation of [149] and are further verified for UHECRs.

Suppression of the extragalactic dipole from the GMF were reported from a recent phenomenological study [152] which focussed on utilising GMF models present in literature. It is worth noting that most of these models have weaker turbulent magnetic field strengths. Whereas, in our study, we explore a wide range of turbulent magnetic fields and thereby a large range of diffusion coefficients ($L_{\rm scat} \sim D_{\rm CR} \propto \frac{1}{(B_{\rm tur})})^2$.

This is also what is reported by the simulations in this work of propagating an extragalactic dipole through turbulent magnetic fields within the Galaxy. Furthermore, the simulations could be verified and predicted by adapting a simple electrostatic analogy of electric fields due to a point charge within a dielectric sphere. For some fiducial values of 'd' the suppression of the dipole can be estimated given the ratio of the diffusion coefficient outside the Galaxy and the value of 'd' is equal to the strength of $\delta_{\rm EG}$.

The analytical electrostatic analogy holds also for complicated magnetic field scenarios where the strength of turbulent fields is changing constantly. This study could prove immensely useful for the modelling of UHECR sources. If the dipole amplitude in Figure 4.14 is fixed to the dipole strength measured by PAO at 7% level [92], then the actual extragalactic dipole strength could be much higher before it enters the Galaxy. This deduction can be of great importance for source modelling of UHECR, the stronger the $\delta_{\rm EG}$, the more anisotropy lies in the source distribution.

Additionally, the amount of suppression the dipole is experiencing provides insight into the strength of diffusion coefficients, as seen from Figure 4.14, for example, for $d \geq 1000$ kpc the $\delta_{\rm EG}$ drops almost by an order of magnitude for a shift in a decade to the left.

One drawback of this analogy is that one has to assume that the distance 'd' between the point source and the centre of the dielectric sphere is very large in order to observe a dipole. This issue can be circumvented if a uniform electric field is assumed to exist outside the dielectric sphere; the solution to this problem always results in a dipole (see [153]). This idea was beyond the scope of this thesis to cover, however, we are currently working on improving the electrostatic analogy and preparing this work for publication in a peer-reviewed scientific journal.

5 Final conclusions and future prospects

The results from the studies have indicated the need to model Galactic halo magnetic fields and their effect on cosmic ray propagation. In this final chapter, a brief summary and the most important results of the work carried out during this PhD thesis are given, together with the next possible directions in which the work presented in this thesis can be taken.

The discovery of Fermi bubbles [45] unveiled large extended gamma ray bubbles in the Galactic halo. Radio observations [4] of the Fermi bubble region strongly support the presence of non-thermal particles. Additionally, the Planck haze [43] at radio frequencies of a few 10s of GHz has a strong spatial correlation with the Fermi bubbles. More recently, the discovery of eROSITA bubbles [50], albeit in the thermal range has drawn a great amount of attention to the Galactic halo predominantly. Utilising the observational data as a motivation in Chapter 2, a new toy model for the region comprising the Fermi and bubbles was proposed. This region was collectively called the Galactic halo bubble (GHB). This new GHB model consists of three components:

1. A structured magnetic field which has an axisymmetric toroidal geometry with the field pointing in opposite directions above and below the Galactic plane.
2. A simple turbulent magnetic field which follows a 5/3 Kolmogorov power spectrum.
3. An analytical description of the distribution of non-thermal electrons for the GHB region.

Synthetic polarised synchrotron emission skymaps derived from the GHB model were compared to data from the 30 GHz Planck satellite mission to obtain constraints on the GHB model. In order to study only the large-scale properties of the GHB region post-processing of both the Planck data and the synthetic data, in the form of Gaussian smoothing, masking, and truncation of the uninteresting regions of the sky, was carried out. A chi-square analysis was done for the various parameter combinations of the GHB model and the Planck data to obtain the best-fit values and the constraints on the parameters.

One of the main conclusions from the chi-squared analysis was that for the total magnetic field strengths (best-fit values for structured and turbulent magnetic fields combined) and the azimuthal extent of the structured halo fields obtained from this study appear to be in agreement with the radio observations. This study strongly supports the presence of an out-of-the plane component of magnetic fields with the best fit value of the azimuthal

extent of the field being ~ 6 kpc which was found to be compatible with spatial extents also reported by observations [46]. The total field strength derived from the polarised synchrotron study was a large value of ~ 7μG which is also consistent with the S-PASS radio observations [4].

The total magnetic field energy content derived from the GHB model with the best-fit parameter set values was $\approx 10^{55}$ ergs which is smaller than the total energy in thermal electrons reported by eROSITA [50]. In contrast, the total energy from the JF12 model was calculated to be 4×10^{54} ergs and 3×10^{54} ergs for the toroidal halo and X-field respectively [71] which is orders of magnitude below the thermal energy content in eROSITA.

In Chapter 3 the deflections of UHECRs through the Galactic halo bubble toy model was studied. UHECRs starting with an isotropic distribution in momentum and delta distribution in position from Earth were backtracked till the edge of the Galaxy and the initial and final directions of the UHECRs were noted. Utilising these directions two types of maps were created for the minimum/lower-bound, maximum/upper-bound and best-fit parameter sets (for values see Table 3.1), namely:

1. Magnification maps which were made from the log binned histogram of final directions at the edge of the Galaxy normalised by the histogram of the initial directions.
2. Arrival direction skymaps which were made by converting the final directions to the directions as seen by an observer at Earth.

Using the maximum and minimum constraints on the parameter values of the GHB magnetic field model, a range of deflections experienced by UHECRs interacting with the GHB magnetic field structure was investigated. A significant number of predictions were made for both the magnification of different parts of the extragalactic sky and the arrival directions due to the deflections of UHECRs from potential sources.

Assuming that active Galactic nucleus like Centaurus A or Cen A is a potential source of UHECRs (see [54, 130]) the spread obtained by the GHB bubble model ($\sigma_{\text{Cen A}} = 33°$) is qualitatively comparable to the 24° spread suggested by PAO [93]. Similar to the spread from Cen A, the spread from NGC 253 for the GHB bubble was ($\sigma_{\text{NGC 253}} = 32°$) was also comparable to PAO results. Its noteworthy that even the new mean shifted position for UHECR arrival directions from NGC 253 situated at a latitude of −63° (also seen in [99]) seems comparable with the hotspot of PAO (see Figure 1.19).

Additionally, predictions for arrival directions of UHECR protons at 40 EeV for potential sources like Cen A and NGC 253 were carried out along with potential sources on a grid.

This analysis could be useful in the context of AugerPrime [101, 102] which will be capable of carrying out the separation of cosmic ray species on an event by event basis.

In Chapter 4 of this dissertation the propagation of UHECRs with an extragalactic dipole through the turbulent magnetic field component of the GHB toy magnetic field model for varying strengths was investigated.

The level of suppression in the magnitude of the extragalactic dipole measured by the observer (sitting in the Galaxy) after the UHECRs had propagated through the turbulent magnetic field filled Galaxy can be explained by using an electrostatic analogy. The dipole measured in the electrostatic case is analogous to the dipole measured by the observer. For arbitrary values of the distance between the extragalactic source and observer d, the suppression of the dipole could be estimated given the ratio of the diffusion coefficient outside the Galaxy and the value of d is equal to the strength of $\delta_{\rm EG}$. This work was not only applicable to UHECRs but was also a numerical verification for the model of [149] which focussed on Galactic cosmic rays. The results presented in this thesis were also found to be consistent with the phenomenological study with turbulent magnetic fields [152].

The effect of turbulent magnetic fields or diffusion on the propagation of UHECRs with an extragalactic dipole is useful information for simulating UHECR sources and their distribution. Hence, this work can be utilised to model UHECR sources. If the dipole amplitude measured at Earth is fixed at a 7% level then the strength of the extragalactic dipole will be much higher and will require to be taken into account for source modelling.

This study can be further improved by using the electrostatic analogy of a dielectric in a constant electric field and will be the focus of future work.

With the conclusions of the thesis highlighted above, it is important to ask what direction the work done during this thesis can be taken into. Some of these questions are highlighted below with a short description for the future plans in the context of answering each question.

What can be the next step in modelling magnetic field in the Galactic halo? Provided one uses new data releases can new constraints be obtained on the strength and structure of magnetic fields in the local and extended Galactic halo?

Apart from carrying out an analysis with different post-processing schemes and comparing the Stokes Q and U maps for data and simulation new observational data due to release soon will be utilised in the future. The 5 GHz all sky radio survey C-BASS can be utilised

to model the structured magnetic fields and further improve and expand the GHB toy model. Unpolarised C-BASS data will be crucial in modelling different realisations of turbulent magnetic fields. Templates based on existing observations for different radiation processes [134] like synchrotron and thermal bremsstrahlung will be used as filters to study the contribution of unpolarised SR alone, providing new insight into turbulent magnetic fields. This is a well-established methodology previously used to study Galactic foregrounds [135–137]. This work is already underway as a further extension to this project.

What can be improved in the Galactic halo modelling proposed in this thesis? What happens to UHECR propagation and the dipole for a Galactic halo of a few 100s of kpc?

Current models of magnetic fields for the Galactic halo often use an exponential profile for the halo and can only describe the local Galactic halo up to a vertical height ~ 20 kpc from the mid-plane [35, 64, 154]. We have a growing body of evidence that the thermal pressure in Galactic halos of external galaxies drops as a power-law and assuming that magnetic fields and thermal gas are in equipartition the magnetic field strengths should follow a similar behaviour [42]. This scenario could also be applicable also to the Milky Way and magnetic fields in an extended halo region could influence the propagation of cosmic rays. The X-ray and radio observations have been hinting at the presence of an extended halo for both the Milky-way [52] and external Galaxies [42]. Moreover, recently models suggesting Cen A as a potential source of UHECRs have been suggested [54, 121], in this model the magnetised extended haloes of the Galaxies sitting in the Council of Giants seems to be reflecting off the UHECRs produced in Cen A which in-turn is observed at Earth. For the future, investigating a power-law profile for the magnetic field for the Milky Way's Galactic halo (extending out to 250 – 300 kpc) will be a priority. This future model could be utilised not only to study the effect it will have on UHECR arrival directions but also the propagation of an extragalactic dipole.

Appendices A

A.1 Example of a pure dipole

Analogous to Fourier transforms, spherical harmonics are a special tool to analyse anisotropy on a celestial sphere. Lower order harmonics are useful to study large-scale structures whereas higher order harmonics provide useful insight into small-scale structures.

The entire anisotropy function $f(\theta, \phi)$ can be understood if all spherical harmonic coefficients are known, here θ and ϕ are angles as shown in the top left figure in Figure A.1. Given below is the mathematical expression of the multipole expansion.

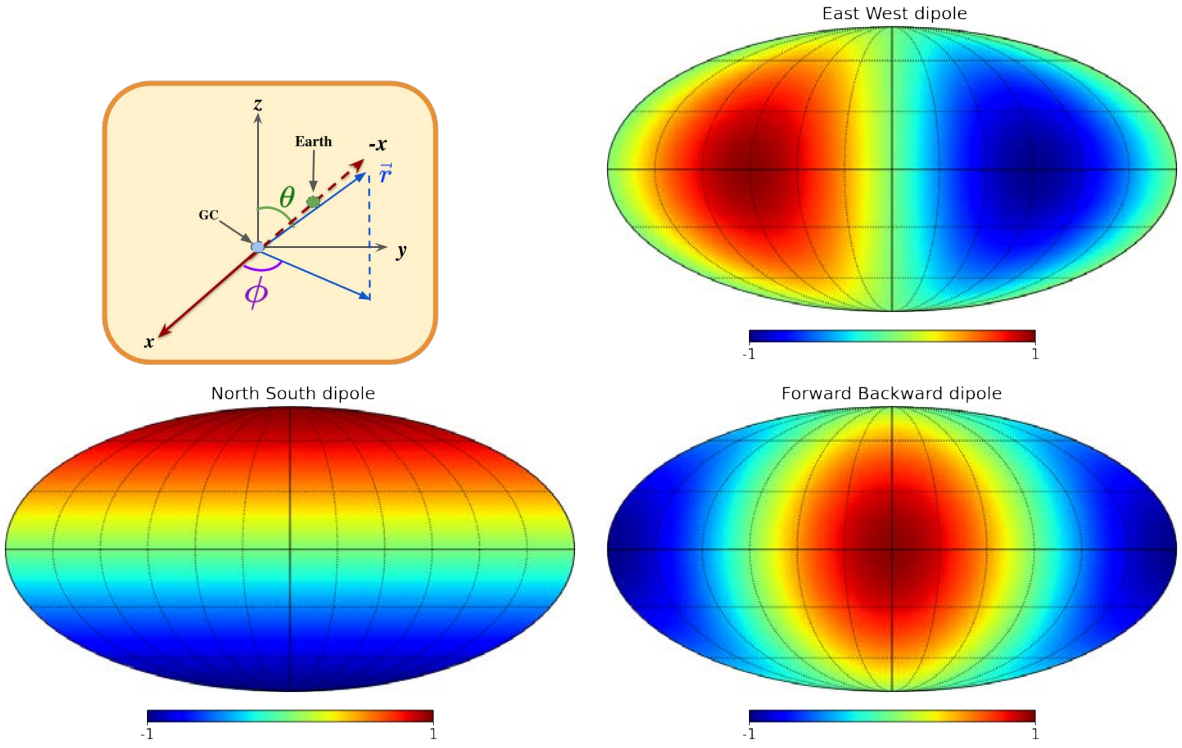

Figure A.1: The spherical coordinate system (**top-left**) r, θ, ϕ shown with respect the Cartesian coordinate system x, y, z.The three cases of a pure dipole, with the east west (**top right**), north-south (**bottom left**) and forward backward (**bottom right**) dipole.

$$f(\theta, \phi) = \sum_{l=0}^{l=\infty} \sum_{m=-l}^{m=+l} C_l^m Y_l^m(\theta, \phi) \tag{A.1}$$

Definitions: θ is the angle between the vector $\vec{r}$ and the z axis and ϕ is the angle between the $x-y$ axis,
$Y_l^m(\theta,\phi)$ are the spherical harmonics with l being the degree and m being the order of the polynomial and C_l^m are constant coefficients.

For a dipole $l = 1$ and then $m = -1, 0, 1$ which gives the spherical harmonic $Y_l^m(\theta,\phi)$. In the case of a pure dipole ($l = 1$) the anisotropy function $f(\theta,\phi)$ can be written in 3 components corresponding to the 3 values of $m = -1, 0, 1$ given by:

$$f_{\rm NS} = \delta \cos\theta,\ f_{\rm EW} = \delta \sin\theta \sin\phi \text{ and } f_{\rm FB} = \delta \sin\theta \cos\phi,$$

here, $f_{\rm NS}$,$f_{\rm EW}$ and $f_{\rm FB}$ are the anisotropy functions for the north-south, east-west and forward-backward dipole directions also shown in Figure A.1.

For a monopole $l = 0$, the anisotropy function $f(\theta,\phi) = 1$ which implies that there will be a flat skymap with intensity.

Note: the Healpix anafast package was utilised to calculate the angular power spectrum from the skymaps [123].

For the case when both monopole and dipole are present, the power is dominated by the monopole ($l = 0$) followed up by the dipole ($l = 1$). This is clearly visible if the angular power spectrum for each mode is plotted.

A.2 Potential due to point charge on a dielectric sphere full derivation

To study the effect of the diffusion coefficient on the CR dipole one can look at an analogous problem of calculating the dipole strength due to a point charge inside a dielectric medium from electrostatics. In Figure A.2, a sketch depicting a dielectric sphere of radius a situated at a fixed distance (d) from a point source (q) is depicted. Here, the dielectric sphere is equivalent to the Galaxy, with the point source being analogous to a UHECR source with d being similar to the distance between the Galactic center and the UHECR source.

In Figure A.2 the radial distance '$\vec{R}$' is measured from the charge and can be re-written as a function of distance 'd', radial distance '$\vec{r}$' measured from the center of the dielectric sphere and angle 'θ'.

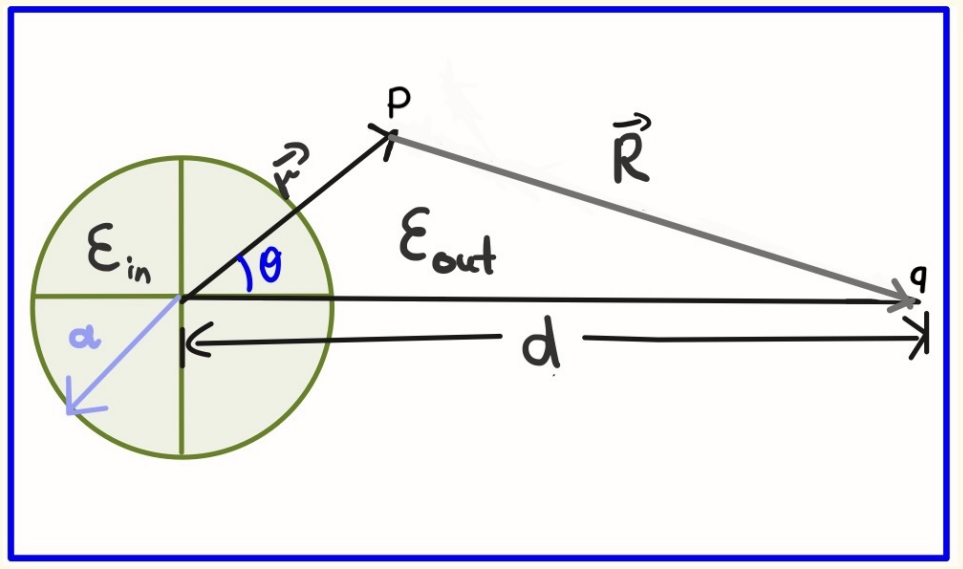

Figure A.2: A schematic representation of the electrostatic case with the charge q at a distance d from the center of the dielectric sphere of radius a. The dielectric constants inside and outside the sphere being ϵ_{in} and ϵ_{out}. $\vec{R}$ and $\vec{r}$ are the distances measured from the source charge q and center of the dielectric sphere respectively, with P being the point at which the potential is measured [149].

$$R = \sqrt{r^2 + \mathrm{d}^2 - 2\, r\, \mathrm{d} \cos\theta}$$

or,

$$\frac{1}{R} = \frac{1}{d} \frac{1}{\sqrt{\left(1 - 2\frac{r}{d}\cos\theta + \left(\frac{r}{d}\right)^2\right)}}. \tag{A.2}$$

The above expression is the same as the generating function for the Legendre polynomials:

$$\sqrt{\frac{1}{1 - 2xt + t^2}} = \sum_{n=0}^{\infty} P_{\mathrm{n}}(x) t^n,$$

In the expression Eq. A.2, r/d maps to t and x maps to $\cos\theta$, assuming that $r << d$, the expression above can be written in terms of Legendre polynomials $P_n(\cos\theta)$ as:

$$\frac{1}{R} = \sum_{n=0}^{\infty} \frac{r^n}{d^{n+1}} P_n(\cos\theta). \tag{A.3}$$

The potentials inside and outside of the dielectric sphere can be given by equations Eq. A.4 and Eq. A.5 respectively.

$$V_{\text{in}} \approx q\, \frac{1}{\epsilon_{\text{in}}} \sum_{n=0}^{\infty} \mathrm{A} \frac{r^n}{d^{n+1}} P_n(\cos\theta), \tag{A.4}$$

here, potential inside the dielectric medium (V_{in}) is only dependent on the source charge.

$$V_{\text{out}} \approx q \frac{1}{\epsilon_{\text{out}}} \sum_{n=0}^{\infty} \left(\frac{r^n}{d^{n+1}} + B \frac{1}{r^{n+1}} \right) P_n(\cos\theta), \tag{A.5}$$

here, '$P_n(\cos\theta)$' is the Legendre polynomial up-to n^{th} order. Note that the potential outside the dielectric sphere experiences an additional reactionary potential due to the dielectric sphere along with potential due to the source and is therefore a function of both. 'A' and 'B' are constants that can be calculated by solving for the boundary conditions for radial and tangential directions listed below:

Radial dielectric ($E^{\text{die}}_{\text{in/out}}$) field:

$$\epsilon_{\text{in}} \frac{\delta V_{\text{in}}}{\delta r} = \epsilon_{\text{out}} \frac{\delta V_{\text{out}}}{\delta r}$$

Solving at the boundary $r = a$,

$$\epsilon_{\text{in}} \frac{\delta V_{\text{in}}}{\delta r}\bigg|_{r=a} = q \sum_{n=0}^{\infty} A \frac{n\, a^{n-1}}{d^{n+1}} P_n(\cos\theta), \tag{A.6}$$

and

$$\epsilon_{\text{out}} \frac{\delta V_{\text{out}}}{\delta r}\bigg|_{r=a} = q \sum_{n=0}^{\infty} \left(\frac{n\, a^{n-1}}{d^{n+1}} - B\,(n+1) \frac{1}{a^{n+2}} \right) P_n(\cos\theta). \tag{A.7}$$

Equating Eq. A.6 and Eq. A.7, one can write A as:

$$A = 1 - \frac{n+1}{n} \frac{d^{n+1}}{a^{2n+1}} B. \tag{A.8}$$

Tangential electric ($E^{\theta}_{\text{in/out}}$) field:

$$\frac{1}{r} \frac{\delta V_{\text{in}}}{\delta \theta} = \frac{1}{r} \frac{\delta V_{\text{out}}}{\delta \theta},$$

Similarly, solving for the tangential condition at $r = a$

$$\frac{1}{r} \frac{\delta V_{\text{in}}}{\delta \theta}\bigg|_{r=a} = q \frac{1}{\epsilon_{in}} \sum_{n=0}^{\infty} A \frac{a^n}{d^{n+1}} P'_n(\cos\theta)(-\sin\theta) \text{ or,} \tag{A.9}$$

$$\frac{1}{r} \frac{\delta V_{\text{out}}}{\delta \theta}\bigg|_{r=a} = q \frac{1}{\epsilon_{\text{out}}} \sum_{n=0}^{\infty} \left(\frac{a^n}{d^{n+1}} + B \frac{1}{a^{n+1}} \right) P'_n(\cos\theta)(-\sin\theta). \tag{A.10}$$

Equating Eq. A.9 and Eq. A.10 for A:

$$A = \frac{\epsilon_{\text{in}}}{\epsilon_{\text{out}}}\left(1 + B\frac{d^{n+1}}{a^{2n+1}}\right). \tag{A.11}$$

Equating Eq. A.8 to Eq. A.11, the constant B can be given by:

$$B = \frac{a^{2n+1}}{d^{n+1}}\frac{n(\epsilon_{\text{out}} - \epsilon_{\text{in}})}{n\epsilon_{\text{in}} + (n+1)\epsilon_{\text{out}}}. \tag{A.12}$$

A similar calculation can be done for A which gives:

$$A = \frac{1}{d^{n+1}}\frac{(2n+1)\epsilon_{\text{in}}}{n\epsilon_{\text{in}} + (n+1)\epsilon_{\text{out}}}. \tag{A.13}$$

Putting values of A and B in Eq. A.4 and Eq. A.5, the inside and outside potentials can be expressed as:

$$V_{\text{in}} \approx q \sum_{n=0}^{\infty} \frac{2n+1}{n\epsilon_{\text{in}} + (n+1)\epsilon_{\text{out}}}\frac{r^n}{d^{n+1}} P_n(\cos\theta) \text{ and} \tag{A.14}$$

$$V_{\text{out}} \approx q \frac{1}{\epsilon_{\text{out}}}\sum_{n=0}^{\infty}\left(\frac{r^n}{d^{n+1}} + \frac{n(\epsilon_{\text{out}} - \epsilon_{\text{in}})}{n\epsilon_{\text{in}} + (n+1)\epsilon_{\text{out}}}\frac{a^{2n+1}}{d^{n+1}}\frac{1}{r^{n+1}}\right) P_n(\cos\theta) \tag{A.15}$$

Bibliography

[1] Vasundhara Shaw, Arjen van Vliet, and Andrew M. Taylor. *Galactic halo magnetic fields and UHECR deflections*. 2022. DOI: 10.48550/ARXIV.2202.06780. URL: https://arxiv.org/abs/2202.06780 (cited on pages iii, xi, 28, 29, 63, 91).

[2] Rainer Beck and Richard Wielebinski. „Magnetic Fields in Galaxies“. In: *Planets, Stars and Stellar Systems* (2013), pp. 641–723. DOI: 10.1007/978-94-007-5612-0_13 (cited on pages 1–3, 33).

[3] Rainer Beck. „Magnetism in galaxies – Observational overview and next generation radio telescopes“. In: *Proceedings of the International Astronomical Union* 6.S274 (2010), pp. 325–332. DOI: 10.1017/S1743921311007228 (cited on page 1).

[4] Ettore Carretti et al. „Giant magnetized outflows from the centre of the Milky Way“. In: *Nature* 493.7430 (Jan. 2013), pp. 66–69. DOI: 10.1038/nature11734 (cited on pages 1, 12, 16, 18, 33, 53, 59, 63, 64, 121, 122).

[5] Marijke Haverkorn and Volker Heesen. „Magnetic fields in galactic haloes“. In: *Space Sci. Rev.* 166 (2012), pp. 133–144. DOI: 10.1007/s11214-011-9757-0 (cited on pages 2, 6, 15, 33).

[6] R. Beck. „Magnetism in the spiral galaxy NGC 6946: magnetic arms, depolarization rings, dynamo modes, and helical fields“. In: *AAP* 470.2 (Aug. 2007), pp. 539–556. DOI: 10.1051/0004-6361:20066988 (cited on page 2).

[7] FS Tabatabaei et al. „High-resolution radio continuum survey of M 33-III. Magnetic fields“. In: *A & A* 490.3 (Nov. 2008), pp. 1005–1017. DOI: 10.1017/s1743921309031251 (cited on pages 2, 64, 96).

[8] Lawrence M. Widrow. „Origin of galactic and extragalactic magnetic fields“. In: *Reviews of Modern Physics* 74.3 (July 2002), pp. 775–823. DOI: 10.1103/revmodphys.74.775 (cited on pages 2, 3).

[9] R. Beck et al. „Multifrequency observations of the radio continuum emission from NGC 253. I. Magnetic fields and rotation measures in the bar and halo.“ In: *A & A* 292 (Dec. 1994), pp. 409–424 (cited on pages 2, 10).

[10] V. Heesen et al. 2023. DOI: 10.48550/ARXIV.2302.06617. URL: https://arxiv.org/abs/2302.06617 (cited on pages 2, 10).

[11] JL Han et al. „Antisymmetric rotation measures in our Galaxy: evidence for an A0 dynamo.“ In: *A&A* 322 (1997), p. 98 (cited on pages 2, 15).

[12] JL Han, RN Manchester, and GJ Qiao. „Pulsar rotation measures and the magnetic structure of our Galaxy“. In: *MNRAS* 306.2 (1999), p. 371. DOI: 10.1046/j.1365-8711.1999.02544.x (cited on pages 2, 15).

[13] Rainer Beck. „Galactic Dynamos and Galactic Winds“. In: *Ap&SS* 320 (2009), p. 77. DOI: 10.1007/s10509-008-9825-4 (cited on pages 3, 16).

[14] Kandaswamy Subramanian. „The origin, evolution and signatures of primordial magnetic fields“. In: *Reports on Progress in Physics* 79.7 (May 2016), p. 076901. DOI: 10.1088/0034-4885/79/7/076901 (cited on page 3).

[15] Kanhaiya L. Pandey et al. „Reionization constraints on primordial magnetic fields“. In: *Mon. Not. Roy. Astron. Soc.* 451.2 (2015), pp. 1692–1700. DOI: 10.1093/mnras/stv1055 (cited on page 3).

[16] K-T Kim et al. „Discovery of intergalactic radio emission in the Coma–A1367 supercluster“. In: *Nature* 341.6244 (1989), pp. 720–723 (cited on page 3).

[17] Kandaswamy Subramanian. „From Primordial Seed Magnetic Fields to the Galactic Dynamo“. In: *Galaxies* 7.2 (2019). DOI: 10.3390/galaxies7020047 (cited on page 3).

[18] Michael S Turner and Lawrence M Widrow. „Inflation-produced, large-scale magnetic fields“. In: *Physical Review D* 37.10 (1988), p. 2743 (cited on page 3).

[19] Bharat Ratra. „Cosmological'seed'magnetic field from inflation“. In: *Astrophysical Journal, Part 2-Letters (ISSN 0004-637X), vol. 391, no. 1, May 20, 1992, p. L1-L4. Research supported by California Institute of Technology.* 391 (1992), pp. L1–L4 (cited on page 3).

[20] Rainer Beck and Richard Wielebinski. „Magnetic Fields in Galaxies“. In: *Planets, Stars and Stellar Systems* (2013), pp. 641–723. DOI: 10.1007/978-94-007-5612-0_13 (cited on pages 3, 13).

[21] Chiara Caprini, Ruth Durrer, and Géraldine Servant. „The stochastic gravitational wave background from turbulence and magnetic fields generated by a first-order phase transition“. In: *JCAP* 2009.12 (2009), pp. 024–024. DOI: 10.1088/1475-7516/2009/12/024 (cited on page 3).

[22] D. R. G. Schleicher et al. „Magnetic fields in the first galaxies: Dynamo amplification and limits from reionization“. In: *Magnetic Fields in the Universe III - From Laboratory and Stars to Primordial Structures*. Jan. 2012, p. 165 (cited on page 3).

[23] Ruth Durrer and Andrii Neronov. „Cosmological magnetic fields: their generation, evolution and observation“. In: *The Astronomy and Astrophysics Review* 21.1 (June 2013). DOI: 10.1007/s00159-013-0062-7 (cited on page 3).

[24] Andrii Neronov and Ievgen Vovk. „Evidence for Strong Extragalactic Magnetic Fields from Fermi Observations of TeV Blazars“. In: *Science* 328.5974 (Apr. 2010), pp. 73–75. DOI: 10.1126/science.1184192 (cited on page 3).

[25] Axel Brandenburg and Kandaswamy Subramanian. „Astrophysical magnetic fields and nonlinear dynamo theory“. In: *Physics Reports* 417.1-4 (Oct. 2005). DOI: 10.1016/j.physrep.2005.06.005 (cited on page 3).

[26] Christoph Federrath. „Magnetic field amplification in turbulent astrophysical plasmas“. In: *Journal of Plasma Physics* 82.6 (Nov. 2016). DOI: 10.1017/s0022377816001069 (cited on page 3).

[27] Russell Kulsrud et al. „Dynamos and cosmic magnetic fields“. English (US). In: *Physics Reports* 283.1-4 (Apr. 1997), pp. 213–226. DOI: 10.1016/S0370-1573(96)00061-0 (cited on page 3).

[28] M. J. Reid and E. M. Silverstein. „OH Masers and the Galactic Magnetic Field“. In: *APJ* 361 (Oct. 1990), p. 483. DOI: 10.1086/169212 (cited on pages 5, 6).

[29] Malcolm S. Longair. *High Energy Astrophysics*. 2011 (cited on pages 6, 7, 13, 14, 45, 50, 69).

[30] R. Beck et al. „Magnetic fields and cosmic rays in M 31“. In: *A & A* 633 (Dec. 2019), A5. DOI: 10.1051/0004-6361/201936481 (cited on page 7).

[31] Jin-Lin Han and Richard Wielebinski. „Milestones in the observations of cosmic magnetic fields“. In: *Chinese Journal of Astronomy and Astrophysics* 2.4 (2002), p. 293 (cited on page 8).

[32] G. V. Panopoulou et al. „Revisiting the Distance to Radio Loops I and IV Using Gaia and Radio/Optical Polarization Data“. In: *APJ* 922.2 (Dec. 2021), p. 210. DOI: 10.3847/1538-4357/ac273f (cited on pages 9, 55, 58).

[33] Pablo Fosalba et al. „Dust Polarization From Starlight Data“. In: 609 (Nov. 2001). DOI: 10.1063/1.1471821 (cited on page 9).

[34] W. Pietsch et al. „X-ray observations of the starburst galaxy NGC 253:II. Extended emission from hot gas in the nuclear area, disk, and halo“. In: (2000) (cited on page 10).

[35] Ronnie Jansson and Glennys R. Farrar. „A New Model of the Galactic Magnetic Field“. In: *APJ* 757.1, 14 (Aug. 2012), p. 14. DOI: 10.1088/0004-637X/757/1/14 (cited on pages 10, 15–17, 37, 124).

[36] Katia Ferrière and Philippe Terral. „Analytical models of X-shape magnetic fields in galactic halos“. In: *A & A* 561 (Jan. 2014), A100. DOI: 10.1051/0004-6361/201322966 (cited on pages 10, 16).

[37] Thomas P. Robitaille and Barbara A. Whitney. In: *APJ* 710.1 (Jan. 2010), pp. L11–L15. DOI: 10.1088/2041-8205/710/1/l11 (cited on pages 10, 20).

[38] Adam K. Leroy et al. „A z = 0 Multiwavelength Galaxy Synthesis. I. A WISE and GALEX Atlas of Local Galaxies“. In: *APJS* 244.2, 24 (Oct. 2019), p. 24. DOI: 10.3847/1538-4365/ab3925 (cited on pages 10, 20, 28, 29).

[39] Judith Irwin et al. „Continuum Halos in Nearby Galaxies: An EVLA Survey (CHANG-ES). I. Introduction to the Survey“. In: *AJ* 144.2, 43 (Aug. 2012), p. 43. DOI: 10.1088/0004-6256/144/2/43 (cited on page 10).

[40] Marita Krause et al. „CHANG-ES“. In: *A & A* 639 (July 2020), A112. DOI: 10.1051/0004-6361/202037780 (cited on page 10).

[41] Rainer Beck. „New constraints on modelling the random magnetic field of the MW“. In: *Astron Astrophys Rev* (2016). DOI: https://doi.org/10.1007/s00159-015-0084-4 (cited on pages 10, 36, 64).

[42] Joel N. Bregman et al. „Hot Extended Galaxy Halos around Local L^* Galaxies from Sunyaev - Zeldovich Measurements“. In: *APJ* 928.1 (Mar. 2022), p. 14. DOI: 10.3847/1538-4357/ac51de (cited on pages 10, 35, 56, 64, 93, 124).

[43] P. A. R. Ade et al. „Planck intermediate results - IX. Detection of the Galactic haze with Planck“. In: *A&A* 554 (2013), A139. DOI: 10.1051/0004-6361/201220271 (cited on pages 11, 12, 121).

[44] Gregory Dobler et al. „The Fermi Haze: A Gamma-ray Counterpart to the Microwave Haze“. In: 717.2 (July 2010), pp. 825–842. DOI: 10.1088/0004-637X/717/2/825 (cited on page 11).

[45] Meng Su, Tracy R. Slatyer, and Douglas P. Finkbeiner. „Giant gamma-ray bubbles fromfermi-lat: active galactic nucleus activity or bipolar galactic wind?“ In: *APJ* 724.2 (Nov. 2010), pp. 1044–1082 (cited on pages 11–13, 18, 30, 33, 55, 121).

[46] Meng Su and Douglas P. Finkbeiner. „Evidence for Gamma-Ray Jets in the Milky Way“. In: 753.1, 61 (July 2012), p. 61. DOI: 10.1088/0004-637X/753/1/61 (cited on pages 11, 63, 122).

[47] Roland M. Crocker and Felix Aharonian. „Fermi Bubbles: Giant, Multibillion-Year-Old Reservoirs of Galactic Center Cosmic Rays“. In: *Physical Review Letters* 106.10 (Mar. 2011). DOI: 10.1103/physrevlett.106.101102 (cited on page 12).

[48] Douglas P. Finkbeiner. „Microwave Interstellar Medium Emission Observed by the *Wilkinson Microwave Anisotropy Probe*“. In: *APJ* 614.1 (Oct. 2004), p. 186. DOI: 10.1086/423482 (cited on page 12).

[49] Roland M. Crocker et al. „A unified model of the fermi bubbles, microwave haze, and polarized radio lobes: reverse shocks in the galactic center's giant outflows". In: *APJ* 808.2 (July 2015), p. 107. DOI: 10.1088/0004-637x/808/2/107 (cited on page 12).

[50] P. Predehl et al. „Detection of large-scale X-ray bubbles in the Milky Way halo". In: (Dec. 2020) (cited on pages 12, 13, 18, 33, 36, 55, 64, 121, 122).

[51] A. Fletcher et al. „The magnetic field of <ASTROBJ>M 31</ASTROBJ> from multi-wavelength radio polarization observations". In: *A & A* 414 (Jan. 2004), pp. 53–67. DOI: 10.1051/0004-6361:20034133 (cited on page 13).

[52] A. Gupta et al. „A huge reservoir of ionized gas around the milky way: accounting for the missing mass?" In: *APJ* 756.1 (Aug. 2012), p. L8. DOI: 10.1088/2041-8205/756/1/l8 (cited on pages 13, 35, 64, 93, 124).

[53] Yakov Faerman, Amiel Sternberg, and Christopher F. McKee. „Massive Warm/Hot Galaxy Coronae. II. Isentropic Model". In: *APJ* 893.1, 82 (2020), p. 82. DOI: 10.3847/1538-4357/ab7ffc (cited on pages 14, 64).

[54] A. M. Taylor, J. H. Matthews, and A. R. Bell. *UHECR Echoes from the Council of Giants*. 2023 (cited on pages 14, 20, 28, 29, 56, 91, 93, 122, 124).

[55] Rüdiger Pakmor et al. „Magnetizing the circumgalactic medium of disc galaxies". In: *MNRAS* 498.3 (Nov. 2020), pp. 3125–3137. DOI: 10.1093/mnras/staa2530 (cited on page 14).

[56] J. Han. „Observing Interstellar and Intergalactic Magnetic Fields". In: 55.1 (Aug. 2017), p. 111. DOI: 10.1146/annurev-astro-091916-055221 (cited on pages 15, 33).

[57] Ahmed Boulares and Donald P. Cox. „Galactic Hydrostatic Equilibrium with Magnetic Tension and Cosmic-Ray Diffusion". In: *APJ* 365 (Dec. 1990), p. 544. DOI: 10.1086/169509 (cited on page 15).

[58] C. G. T. Haslam et al. „A 408 MHz all-sky continuum survey. I - Observations at southern declinations and for the North Polar region." In: 100 (July 1981), pp. 209–219 (cited on page 15).

[59] C. G. T. Haslam et al. „408 MHz all-sky map". In: *Astronomy Data Image Library* (Dec. 1995) (cited on page 15).

[60] Katia M. Ferrière. „The interstellar environment of our galaxy". In: *Reviews of Modern Physics* 73.4 (Dec. 2001), pp. 1031–1066. DOI: 10.1103/revmodphys.73.1031 (cited on page 15).

[61] P. M. W. Kalberla and J. Kerp. „Hydrostatic equilibrium conditions in the galactic halo“. In: *A & A* 339 (Nov. 1998), pp. 745–758 (cited on page 15).

[62] X. H. Sun et al. „Radio observational constraints on Galactic 3D-emission models“. In: *A & A* 477.2 (Jan. 2008), pp. 573–592. DOI: 10.1051/0004-6361:20078671 (cited on page 15).

[63] B Ruiz-Granados, JA Rubiño-Martín, and E Battaner. „Constraining the regular Galactic magnetic field with the 5-year WMAP polarization measurements at 22 GHz“. In: *A&A* 522 (2010), A73. DOI: 10.1051/0004-6361/200912733 (cited on page 15).

[64] T. R. Jaffe et al. „Modelling the Galactic magnetic field on the plane in two dimensions“. In: *MNRAS* 401.2 (Jan. 2010), pp. 1013–1028. DOI: 10.1111/j.1365-2966.2009.15745.x (cited on pages 15, 124).

[65] M. S. Pshirkov et al. „Deriving the global structure of the galactic magnetic field from faraday rotation measures of extragalactic sources“. In: *APJ* 738.2 (Oct. 2011), p. 192. DOI: 10.1088/0004-637x/738/2/192 (cited on page 15).

[66] T. R. Jaffe et al. „Connecting synchrotron, cosmic rays and magnetic fields in the plane of the Galaxy“. In: *MNRAS* 416.2 (Sept. 2011), pp. 1152–1162. DOI: 10.1111/j.1365-2966.2011.19114.x (cited on page 15).

[67] L. Page et al. „Three-Year Wilkinson Microwave Anisotropy Probe (WMAP) Observations: Polarization Analysis“. In: *APJ Supplement Series* 170.2 (June 2007), pp. 335–376. DOI: 10.1086/513699 (cited on pages 15, 31, 37, 59).

[68] M. Krause. „Magnetic Fields and Star Formation in Spiral Galaxies“. In: *Rev. Mex. Astron. Astrof. Ser. Conf.* 36 (Oct. 2009), pp. 25–29 (cited on page 16).

[69] J. C. Brown et al. „Rotation Measures of Extragalactic Sources behind the Southern Galactic Plane: New Insights into the Large-Scale Magnetic Field of the Inner Milky Way“. In: *APJ* 663.1 (July 2007), pp. 258–266. DOI: 10.1086/518499 (cited on page 16).

[70] James M Cordes and T Joseph W Lazio. „NE2001. I. A new model for the galactic distribution of free electrons and its fluctuations“. In: *arXiv preprint astro-ph/0207156* (2002) (cited on page 16).

[71] Andrew M. Taylor and A. M. Hillas. *The Effects of the Galactic Magnetic Field on UHECR From Local Sources*. 2019 (cited on pages 18, 64, 86, 88, 122).

[72] J Xu and JL Han. „Magnetic fields in the solar vicinity and in the Galactic halo“. In: *MNRAS* 486.3 (2019), pp. 4275–4289 (cited on page 18).

[73] Victor F. Hess. „Über Beobachtungen der durchdringenden Strahlung bei sieben Freiballonfahrten“. In: *Phys. Z.* 13 (1912), pp. 1084–1091 (cited on page 20).

[74] Thomas K. Gaisser. *Cosmic rays and particle physics.* 1990 (cited on page 20).

[75] J H Matthews et al. „Fornax A, Centaurus A, and other radio galaxies as sources of ultrahigh energy cosmic rays“. In: *MNRAS: Letters* 479.1 (June 2018), pp. L76–L80. DOI: 10.1093/mnrasl/sly099 (cited on page 20).

[76] Carmelo Evoli. *The Cosmic-Ray Energy Spectrum*. Dec. 2020. DOI: 10.5281/zenodo.4396125. URL: https://doi.org/10.5281/zenodo.4396125 (cited on page 22).

[77] Kulikov G. V. and Kristiansen G.B. „On the size spectrum of extensive air showers“. In: *JETP* 35.635 (Oct. 1958) (cited on page 21).

[78] Kenneth Greisen. „End to the cosmic-ray spectrum?“ In: *Physical Review Letters* 16.17 (1966), p. 748 (cited on page 22).

[79] Georgi T Zatsepin and Vadem A Kuz'min. „Upper limit of the spectrum of cosmic rays“. In: *Soviet Journal of Experimental and Theoretical Physics Letters* 4 (1966), p. 78 (cited on page 22).

[80] A. M. Hillas. „The Origin of Ultra-High-Energy Cosmic Rays“. In: *Annual review of astronomy and astrophysics* 22 (Jan. 1984), pp. 425–444. DOI: 10.1146/annurev.aa.22.090184.002233 (cited on page 23).

[81] Rafael Alves Batista et al. „Open Questions in Cosmic-Ray Research at Ultrahigh Energies“. In: *Frontiers in Astronomy and Space Sciences* 6 (2019). DOI: 10.3389/fspas.2019.00023 (cited on page 23).

[82] A. U. Abeysekara et al. „The 2HWC HAWC Observatory Gamma-Ray Catalog“. In: *APJ* 843.1 (June 2017), p. 40. DOI: 10.3847/1538-4357/aa7556 (cited on page 24).

[83] W.D. Apel et al. „Energy spectra of elemental groups of cosmic rays: Update on the KASCADE unfolding analysis“. In: *Astroparticle Physics* 31.2 (Mar. 2009), pp. 86–91. DOI: 10.1016/j.astropartphys.2008.11.008 (cited on page 25).

[84] „The Pierre Auger Cosmic Ray Observatory“. In: *Nuclear Instruments and Methods in Physics Research Section A: Accelerators, Spectrometers, Detectors and Associated Equipment* 798 (Oct. 2015), pp. 172–213. DOI: 10.1016/j.nima.2015.06.058 (cited on page 25).

[85] M. Fukushima. „Telescope Array Project for Extremely High Energy Cosmic Rays“. In: *Progress of Theoretical Physics Supplement* 151 (Jan. 2003), pp. 206–210. DOI: 10.1143/PTPS.151.206 (cited on page 25).

[86] A. di Matteo and L. Anchordoqui. *2022 report from the Auger-TA working group on UHECR arrival directions*. 2023. DOI: 10.48550/ARXIV.2302.04502. URL: https://arxiv.org/abs/2302.04502 (cited on pages 25, 28).

[87] Beetjedwars from nl. *Air Shower Illustration — Wikipedia, The Free Encyclopedia*. [Online; accessed 30-August-2021]. 2010. URL: https://commons.wikimedia.org/wiki/File:AirShower.svg (cited on page 26).

[88] A. Coleman et al. „Ultra-high energy cosmic rays The intersection of the Cosmic and Energy Frontiers". In: *Astroparticle Physics* 149 (2023), p. 102819. DOI: 10.1016/j.astropartphys.2023.102819 (cited on pages 26, 93).

[89] Rafael Alves Batista et al. „CRPropa 3—a public astrophysical simulation framework for propagating extraterrestrial ultra-high energy particles". In: *JCAP* 2016.05 (May 2016), pp. 038–038. DOI: 10.1088/1475-7516/2016/05/038 (cited on pages 26, 27, 36, 73, 105, 108).

[90] Rafael Alves Batista et al. „CRPropa 3.2 — an advanced framework for high-energy particle propagation in extragalactic and galactic spaces". In: *JCAP* 2022.09 (2022), p. 035. DOI: 10.1088/1475-7516/2022/09/035 (cited on pages 26, 27, 36, 73, 105, 108).

[91] Arjan Koning, S Hilaire, and M Duijvestijn. „TALYS: Comprehensive nuclear reaction modeling". In: vol. 769. May 2005. DOI: 10.1063/1.1945212 (cited on pages 26, 27).

[92] Pierre Auger Collaboration et al. „Observation of a large-scale anisotropy in the arrival directions of cosmic rays above 8×10^{18} eV". In: *Science* 357.6357 (Sept. 2017), pp. 1266–1270. DOI: 10.1126/science.aan4338 (cited on pages 26, 95, 102, 106, 107, 117, 119).

[93] P. Abreu et al. „Arrival Directions of Cosmic Rays above 32 EeV from Phase One of the Pierre Auger Observatory". In: *APJ* 935.2, 170 (Aug. 2022), p. 170. DOI: 10.3847/1538-4357/ac7d4e (cited on pages 26, 28, 78, 79, 83, 86–88, 91, 95, 106, 122).

[94] Rogerio de Almeida et al. „Large-scale and multipolar anisotropies of cosmic rays detected at the Pierre Auger Observatory with energies above 4 EeV". In: *PoS* ICRC2021 (2021), p. 335. DOI: 10.22323/1.395.0335 (cited on page 27).

[95] A. Aab et al. „An Indication of Anisotropy in Arrival Directions of Ultra-high-energy Cosmic Rays through Comparison to the Flux Pattern of Extragalactic Gamma-Ray Sources". In: *APJ* 853.2 (Feb. 2018), p. L29. DOI: 10.3847/2041-8213/aaa66d (cited on pages 27, 28, 78, 83, 87, 88).

[96] R. U. Abbasi et al. „Search for Large-scale Anisotropy on Arrival Directions of Ultra-high-energy Cosmic Rays Observed with the Telescope Array Experiment“. In: *APJ* 898.2 (July 2020), p. L28. DOI: 10.3847/2041-8213/aba0bc (cited on page 27).

[97] A. Aab et al. „Searches for anisotropies in the arrival directions of the highest energy cosmic rays detected by the pierre auger observatory“. In: *APJ* 804.1 (Apr. 2015), p. 15. DOI: 10.1088/0004-637x/804/1/15 (cited on page 28).

[98] Pedro Abreu et al. „The ultra-high-energy cosmic-ray sky above 32 EeV viewed from the Pierre Auger Observatory“. In: *PoS* ICRC2021 (2021), p. 307. DOI: 10.22323/1.395.0307 (cited on pages 28, 86).

[99] Arjen van Vliet et al. „Extragalactic magnetic field constraints from ultrahigh-energy cosmic rays from local galaxies“. In: *MNRAS* 510.1 (2021), pp. 1289–1297. DOI: 10.1093/mnras/stab3495 (cited on pages 28, 29, 91, 122).

[100] Olivier Deligny. „The science of ultra-high energy cosmic rays after more than 15 years of operation of the Pierre Auger Observatory“. In: *Journal of Physics Conference Series*. Vol. 2429. Journal of Physics Conference Series. Feb. 2023, 012009, p. 012009. DOI: 10.1088/1742-6596/2429/1/012009 (cited on page 28).

[101] The Pierre Auger Collaboration et al. *The Pierre Auger Observatory Upgrade - Preliminary Design Report*. 2016 (cited on pages 29, 90, 91, 123).

[102] A. Castellina et al. „AugerPrime: the Pierre Auger Observatory Upgrade“. In: *EPJ Web Conf.* 210 (2019). Ed. by I. Lhenry-Yvon et al., p. 06002. DOI: 10.1051/epjconf/201921006002 (cited on pages 29, 90, 91, 93, 123).

[103] Luke O'C. Drury. „Origin of cosmic rays“. In: *Astroparticle Physics* 39–40 (Dec. 2012), pp. 52–60. DOI: 10.1016/j.astropartphys.2012.02.006 (cited on pages 29, 30).

[104] O. Deligny. *The energy spectrum of ultra-high energy cosmic rays measured at the Pierre Auger Observatory and at the Telescope Array*. 2020 (cited on page 30).

[105] M. Aguilar et al. In: *PRL* 113 (2014), p. 221102. DOI: 10.1103/PhysRevLett.113.221102 (cited on page 31).

[106] G. Ambrosi et al. „Direct detection of a break in the teraelectronvolt cosmic-ray spectrum of electrons and positrons“. In: *Nature* 552 (2017), p. 63. DOI: 10.1038/nature24475 (cited on page 31).

[107] O. Adriani et al. „Energy Spectrum of Cosmic-Ray Electron and Positron from 10 GeV to 3 TeV Observed with the Calorimetric Electron Telescope on the International Space Station“. In: *PRL* 119.18 (2017), p. 181101. DOI: 10.1103/PhysRevLett.119.181101 (cited on page 31).

[108] Waelkens, A. et al. „Simulating polarized Galactic synchrotron emission at all frequencies - The Hammurabi code“. In: *A & A* 495.2 (2009), pp. 697–706. DOI: 10.1051/0004-6361:200810564 (cited on pages 31, 37, 50, 56).

[109] A. W. Strong, E. Orlando, and T. R. Jaffe. „The interstellar cosmic-ray electron spectrum from synchrotron radiation and direct measurements“. In: *A&A* 534 (Sept. 2011), A54. DOI: 10.1051/0004-6361/201116828 (cited on page 31).

[110] and R. Adam et al. „Planck intermediate results. XLII. Large-scale Galactic magnetic fields“. In: *A&A* 596 (Dec. 2016), A103. DOI: 10.1051/0004-6361/201528033 (cited on pages 33, 54).

[111] and Y. Akrami et al. „Planck 2018 results. IV. Diffuse component separation“. In: *A&A* 641 (Sept. 2020), A4. DOI: 10.1051/0004-6361/201833881 (cited on pages 33, 64).

[112] J L West et al. „Helicity in the large-scale Galactic magnetic field“. In: *MNRAS* 499.3 (Oct. 2020), pp. 3673–3689. DOI: 10.1093/mnras/staa3068 (cited on pages 35, 36).

[113] Silvia Mollerach and Esteban Roulet. „Anisotropies of ultrahigh-energy cosmic rays in a scenario with nearby sources“. In: *Phy. Rev. D* 105.6 (Mar. 2022). DOI: 10.1103/physrevd.105.063001 (cited on pages 36, 86, 97).

[114] Hiroshi Ohno and Shinpei Shibata. „The random magnetic field in the Galaxy“. In: *MNRAS* 262.4 (1993), pp. 953–962 (cited on page 36).

[115] A. Chepurnov et al. „Velocity Spectrum for H I at High Latitudes“. In: *APJ* 714.2 (May 2010), pp. 1398–1406. DOI: 10.1088/0004-637X/714/2/1398 (cited on page 36).

[116] M Iacobelli et al. „Studying Galactic interstellar turbulence through fluctuations in synchrotron emission-First LOFAR Galactic foreground detection“. In: *A&A* 558 (2013), A72 (cited on page 36).

[117] G. Giacinti, M. Kachelrieß, and D.V. Semikoz. „Reconciling cosmic ray diffusion with Galactic magnetic field models“. In: *JCAP* 2018.07 (July 2018), pp. 051–051. DOI: 10.1088/1475-7516/2018/07/051 (cited on page 36).

[118] Igor V. Moskalenko, Andrew W. Strong, and Troy A. Porter. *Isotopic composition of cosmic-ray sources*. 2007 (cited on page 37).

[119] George B. Rybicki and Alan P. Lightman. *Radiative Processes in Astrophysics*. 1986 (cited on pages 40, 41, 44, 50).

[120] K. C. Westfold. „The Polarization of Synchrotron Radiation.“ In: (July 1959) (cited on pages 40, 41, 43, 46).

[121] James H. Matthews and Andrew M. Taylor. „Particle acceleration in radio galaxies with flickering jets: GeV electrons to ultrahigh energy cosmic rays“. In: *MNRAS* 503.4 (2021), p. 5948. DOI: 10.1093/mnras/stab758 (cited on pages 41, 46, 124).

[122] Planck Collaboration et al. „Planck 2015 results. XXV. Diffuse low-frequency Galactic foregrounds“. In: 594, A25 (Sept. 2016), A25. DOI: 10.1051/0004-6361/201526803 (cited on pages 44, 54).

[123] K. M. Gorski et al. „HEALPix: A Framework for High-Resolution Discretization and Fast Analysis of Data Distributed on the Sphere“. In: *APJ* 622.2 (Mar. 2005), pp. 759–771. DOI: 10.1086/427976 (cited on pages 46, 57, 115, 126).

[124] Planck Collaboration et al. „Planck intermediate results. XIX. An overview of the polarized thermal emission from Galactic dust“. In: *A & A* 576, A104 (Apr. 2015), A104. DOI: 10.1051/0004-6361/201424082 (cited on pages 46, 54).

[125] Planck Collaboration et al. „Planck 2015 results. XXV. Diffuse low-frequency Galactic foregrounds“. In: 594, A25 (Sept. 2016), A25. DOI: 10.1051/0004-6361/201526803 (cited on pages 51, 54).

[126] A. Kogut and D. J. Fixsen. „Foreground bias from parametric models of far-ir dust emission“. In: *APJ* 826.2 (July 2016), p. 101. DOI: 10.3847/0004-637x/826/2/101 (cited on pages 54, 55).

[127] Planck Collaboration et al. „Planck intermediate results - XLII. Large-scale Galactic magnetic fields“. In: *A&A* 596 (2016), A103. DOI: 10.1051/0004-6361/201528033 (cited on page 54).

[128] M. Wolleben. „A New Model for the Loop I (North Polar Spur) Region“. In: *APJ* 664.1 (July 2007), pp. 349–356. DOI: 10.1086/518711 (cited on pages 55, 58).

[129] Saumyadip Samui, Kandaswamy Subramanian, and Raghunathan Srianand. „Efficient cold outflows driven by cosmic rays in high-redshift galaxies and their global effects on the IGM“. In: *MNRAS* 476.2 (May 2018), p. 1680. DOI: 10.1093/mnras/sty287 (cited on page 56).

[130] A R Bell and J H Matthews. „Echoes of the past: ultra-high-energy cosmic rays accelerated by radio galaxies, scattered by starburst galaxies“. In: *MNRAS* 511.1 (2022), pp. 448–456. DOI: 10.1093/mnras/stac031 (cited on pages 56, 91, 122).

[131] R. Beck. „Magnetism in the spiral galaxy NGC 6946: magnetic arms, depolarization rings, dynamo modes, and helical fields“. In: 470.2 (Aug. 2007), pp. 539–556. DOI: 10.1051/0004-6361:20066988 (cited on pages 64, 96).

[132] CGT Haslam et al. „A 408 MHz all-sky continuum survey. II-The atlas of contour maps“. In: *A&ASS* 47 (1982), p. 1 (cited on page 64).

[133] M. Irfan. et al. „C-Band All-Sky Survey: a first look at the Galaxy“. In: *MNRAS* 448.4 (2015). DOI: 10.1093/mnras/stv212 (cited on page 64).

[134] SE Harper et al. „The C-Band All-Sky Survey (C-BASS): template fitting of diffuse galactic microwave emission in the northern sky“. In: *MNRAS* 513.4 (2022). DOI: 10.1093/mnras/stac1210 (cited on pages 64, 65, 124).

[135] A. Kogut et al. „Microwave emission at high galactic latitudes in the four-year DMR sky maps“. In: *ApJ* 464.1 (1996), p. L5 (cited on pages 65, 124).

[136] M. Peel et al. „Template fitting of WMAP 7-year data: anomalous dust or flattening synchrotron emission?“ In: *MNRAS* 424.4 (2012), pp. 2676–2685. DOI: 10.1111/j.1365-2966.2012.21358.x (cited on pages 65, 124).

[137] A. Peter et al. „Planck intermediate results. XXII. Frequency dependence of thermal emission from Galactic dust in intensity and polarization“. In: *A&A* 576 (2015) (cited on pages 65, 124).

[138] Theodore G. Northrop and Edward Teller. „Stability of the Adiabatic Motion of Charged Particles in the Earth's Field“. In: *Phys. Rev.* 117 (1 Jan. 1960), pp. 215–225. DOI: 10.1103/PhysRev.117.215 (cited on page 69).

[139] Diego Harari et al. „Lensing of ultra-high energy cosmic rays in turbulent magnetic fields“. In: *Journal of High Energy Physics* 2002.03 (Mar. 2002), pp. 045–045. DOI: 10.1088/1126-6708/2002/03/045 (cited on page 73).

[140] J P Boris. „Aacceleration calculation from a scalar potential.“ In: (Jan. 1970) (cited on page 74).

[141] Jay P. Boris and Ramy A. Shanny. „Proceedings of the Conference on the Numerical Simulation of Plasmas (4th) Held at the Naval Research Laboratory, Washington, D.C. on 2, 3 November 1970“. In: 1971 (cited on page 74).

[142] J. R. Cash and Alan H. Karp. „A Variable Order Runge-Kutta Method for Initial Value Problems with Rapidly Varying Right-Hand Sides“. In: *ACM Trans. Math. Softw.* 16.3 (Sept. 1990), pp. 201–222. DOI: 10.1145/79505.79507 (cited on page 74).

[143] Pasquale Blasi, Scott Burles, and Angela V Olinto. „Cosmological magnetic field limits in an inhomogeneous universe“. In: *APJ* 514.2 (1999), p. L79 (cited on page 78).

[144] PP Kronberg et al. „Discovery of new faint radio emission on 8° to 3'scales in the coma field, and some galactic and extragalactic implications“. In: *APJ* 659.1 (2007), p. 267 (cited on page 78).

[145] A. Aab et al. „Depth of Maximum of Air-Shower Profiles at the Pierre Auger Observatory. II. Composition Implications“. In: *Phys. Rev. D* 90 (2014). 13 pages, 7 figures ; see paper for full list of authors, p. 122006. DOI: 10.1103/PhysRevD.90.122006 (cited on page 79).

[146] Antoine Letessier-Selvon. „Highlights from the Pierre Auger Observatory“. In: *Brazilian Journal of Physics* 44.5 (Oct. 2014), pp. 560–570. DOI: 10.1007/s13538-014-0218-6 (cited on page 82).

[147] R. U. Abbasi et al. „Indications of intermediate-scale anisotropy of cosmic rays with energy greater than 57 eev in the northern sky measured with the surface detector of the telescope array experiment“. In: *APJ* 790.2 (2014), p. L21. DOI: 10.1088/2041-8205/790/2/l21 (cited on page 93).

[148] Sergey Troitsky et al. „Telescope Array anisotropy summary“. In: Aug. 2017, p. 548. DOI: 10.22323/1.301.0548 (cited on pages 93, 107).

[149] Vladimir N. Zirakashvili. „Cosmic ray anisotropy problem“. In: *International Journal of Modern Physics A* 20 (2005), pp. 6858–6860 (cited on pages 99, 101, 119, 123, 127).

[150] Markus Ahlers and Philipp Mertsch. „Origin of small-scale anisotropies in Galactic cosmic rays“. In: *Progress in Particle and Nuclear Physics* 94 (May 2017), pp. 184–216. DOI: 10.1016/j.ppnp.2017.01.004 (cited on pages 102, 105, 106).

[151] Markus Ahlers. „The Dipole Anisotropy of Galactic Cosmic Rays“. In: *Journal of Physics: Conference Series* 1181 (Mar. 2019), p. 012004. DOI: 10.1088/1742-6596/1181/1/012004 (cited on page 102).

[152] Alena Bakalová, Jakub Vícha, and Petr Trávníček. *Modification of the Dipole in Arrival Directions of Ultra-high-energy Cosmic Rays due to the Galactic Magnetic Field*. 2023 (cited on pages 119, 123).

[153] B.I. Bleaney and B. Bleaney. *Electricity and Magnetism, Volume 1: Third Edition*. Electricity and Magnetism. OUP Oxford, 2013 (cited on page 119).

[154] V. Heesen et al. In: *A&A* 670, L23 (Feb. 2023), p. L23 (cited on page 124).